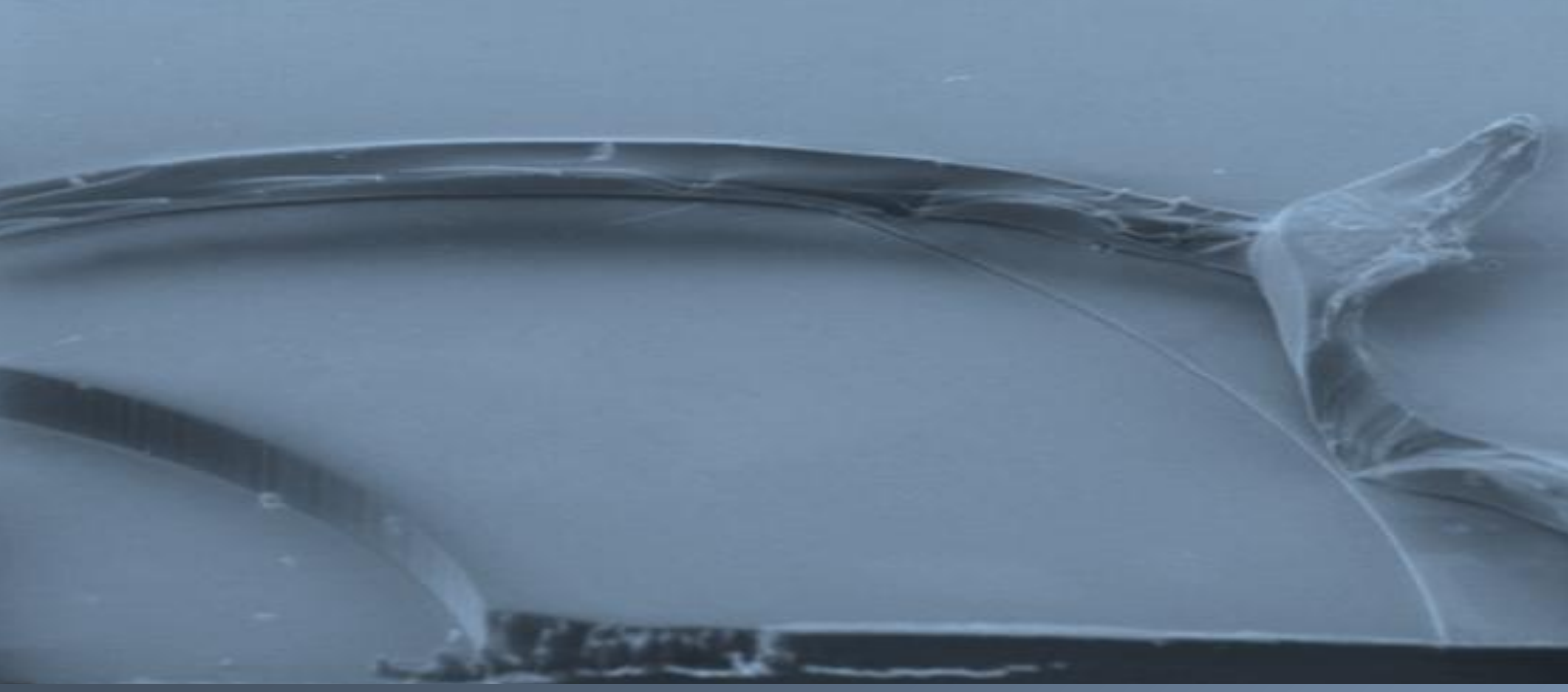

Modular integration and on-chip sensing approaches for tunable fluid control polymer microdevices

PhD Dissertation

Jaione Etxebarria Elezgarai, 2015

(c)2015 Jaione Etxebarria Elezgarai

Modular integration and on-chip sensing approaches for tunable fluid control polymer microdevices

Jaione Etxebarria Elezgarai

Arrasate, 2015

Supervisors:

Dr. Aitor Ezkerra Fernández
Dr. Victoria Laura Barrio Cagigal

Motibazioa

Azken hamarkadetan *Lab-on-a-Chip* (LOC) eta *Micro Total Analysis Systems* (μ-TAS) bezalako sistema mikrofluidikoek potentzial izugarria eskaini dute aplikazio mediko eta biologikoetan. Sistema hauek eskaintzen dituzten abantaila nagusiak koste baxuak, erreakzio erantzun azkarrak eta erreaktibo eta lagin biologikoen erabilera minimoak dira, besteak beste. Hala ere, LOC bezalako sistema hauetan jariakinen bolumen (μl) eta emari (μl/min) baxuak zehaztasunez kontrolatzea ezinbesteko baldintza da, dosifikazio edo diluzio akatsak ekidin, eta protokolo biologiko arrakastatsu eta diagnosi egokiak lortzeko. Beraz, jariakinen kontrol on bat izatea oinarrizko baldintza bat da, benetako aplikazioetan LOC-en erabilera bermatzeko. Gainera, jariakinen manipulazio zehatz hau gero eta garrantzitsuagoa bilakatzen ari da mundu osoan zehar, ekonomikoki garrantzitsuak diren aplikazio ugarik helburu hauxe bera bilatzen dutelako. Hala nola, erdieroaleen industriak, petrolio-findegiek, instrumentazio analitikoek, elikagaien farmazia industriek, energia eremuak, mikroerreaktore sistemek, etab. Hori dela eta, mikrofluidikan ematen ari diren azken aurrerapenek garapen teknologiko berri askorentzat onura garrantzitsuak eskaini ditzakete.

Mediku-diagnosietan esaterako, erreakzio azkarrak eta laginen erabilera minimoa erabiltzea eskaini dezake mikrofluidikak. Kasu honetan, fabrikazio kostu txikiak lortu ezkero, diagnosiaren eskenatokia eskala klinikotik pazienteen inguruetara transferitu ahal da, diagnosirako beharrezko denbora asko murriztuz eta pazientearen bizi kalitatea hobetuz. Analisietarako urrats ugari behar dituzten arlo biologiko hauetan, hala nola laginaren prestaketa, arazketa, detekzioa..., emariak kontrolatzeko elementuak gakoa suposatzen dute.

Kimika arloan mikrokanalen sareak sortzeko aukera ematen du mikrofluidikak, non erreakzioak balbula, ponpa, sentsore eta antzeko elementuekin kontrolatu ahal den, makro eskalan bezalaxe. Aplikazio honen barruan jariakinen kokapen zehatza erabakigarria izaten da askotan, baita erreaktibo biren sinkronizazioa ere, non emariak kontrolatzea ardura garrantzitsuenetariko bat den.

Azken hamarkadan mikrofluidika ospea lortzen hasi da zelula eta partikulen manipulazioan. Zelulen manipulazio on baterako emarien kontrol oso zorrotza bermatu behar da txipen barruan, eta adibidez emaria oso egonkorra izan behar da ebakidura-tentsioak gutxitzeko, eta zeluletan kalteak ekidinez hauen hazkuntza optimizatzeko.

Modu berean, tanten formazioan oinarritzen den mikrofluidika ere oso erakargarria bilakatzen ari da, hala nola, biologia eta kimikan. Tantekin lan egitean, hauen formazio abiadura, maiztasun eta monodispertsitatea egokiak izateko, emari oso egonkorrak izatea premiazko baldintza bat da. Beraz, pultsurik gabeko emariak behar dira, emari hauen gainean berehalako kontrola izatea ere beharrezkoa izanik.

Beraz, aplikazio komertzial gehienetan kontrol mikrofluidikoa beste esparruekin konbinatzean (esaterako ingeniaritza, fisika, kimika, mikroteknologia, fabrikazio teknologiak edota bioteknologia), miniaturizatutako sistema analitiko berritzaileak eta ekoizpen kontzeptu berriak sortzeko aukera zabaltzen da.

Hala ere, literaturan ez da oraindik ageri benetan integragarria den emari kontrolatzailerik, guztiz polimeroz egindako LOC batean dimentsio edo muntaia akatsik gabe integratu daitekeena, eta era berean pausu gutxitan fabrikatzeko erraza dena, ekonomikoki errentagarria, eta industriako masa-ekoizpen teknikekin bateragarria. LOC aplikazioetarako bereziki erronka nagusia da emaria kontrolatzeko sistema monolitiko berri bat sortzea, bere osotasunean plastikozko materialetan integratu daitekeena, erraz erabiltzen dena, eta errepikakorra, fidagarria, merkea eta erabili eta botatzekoa izango dena.

Literaturan aurki daitezkeen kontrolerako kontzeptu gehienek silizio eta beira bezalako material tradizionalez egindako balbula eta sentsoreak erakusten dituzte, edo berrikiago, elastomeroz edo silizio-polimero hibridoz egindakoak. Kontzeptu gehienek kontrolerako elementuen funtzionamendua aztertu dute, hala nola, eragiteko metodoa, isurien presentzia, bolumen hilak, erantzun denbora, etab. Baina material eta fabrikazioaren inguruko aurrerapen gehiago beharrezkoak dira elementu hauek LOC sistema konplexuetan errazki integratu nahi badira.

Laburpena

Doktore tesi honetan mikroemariak kontrolatzeko elementuak diseinatu eta garatu dira, eta ondoren gailu horiek batera integratu dira likido emari kontroladore bat sortzeko asmotan. Helburu nagusia gailuen fabrikazio arkitektura modular bat frogatzea da, non LOC prototipoak garatzeko beharrezko fase guztiak harmonizatuz, COP termoplastikozko mikrogailu merkeak pausu gutxi batzuetan garatuko diren, kalitate industriala bermatuz. Honi esker, prototipotik produkturako trantsizio azkar, erraz, errentagarri eta arriskurik gabea lortu daitekeelarik.

Lehenengo helburua laborategi mailan LOC-etako elementu nagusiak material termoplastiko baten fabrikatzea ahalbidetuko duen teknika berri bat garatzea da, industrian aurki daitezkeen fabrikazio tekniken antzeko kalitatea ziurtatuz. Horretarako, mikrokanalak, mikrobalbulak eta mikrosentsoreak bezalako elementuak Hot Embossing urrats bakar batean fabrikatu dira. Ondoren, disolbatze-teknika bidez gailuak itsatsi eta metal-geruza finak depositatzeko teknikak erabiliaz, kalitateko altuko gailu merkeak lortu dira. Gainera, garatutako fabrikazioaren integrazio potentzial izugarriak mikrofluidikan erabiltzen diren beste elementu asko gehitzea baimentzen du, eta masa-ekoizpen teknikekin bateragarria denez, prototipotik produkturako trantsizioa asko errazten du.

Bigarren helburua COP polimeroa erabiliaz mikrobalbula erabat monolitikoa sortzea da, non balbularen mintza material bereko lamina zurrun batez osatua egongo den. Pneumatikoki eragingo den mikrobalbula honek bi xede izango ditu, ireki/itxi eran funtzionatzea bata, eta irteerako emaria erregulatzea bestea. Balbularen diseinu parametro nagusiak aztertzeko asmotan, hemezortzi diseinu ezberdin aukeratu dira. Lehenik eta behin diseinu horietarako simulazioak gauzatu dira materialen eta jariakinen mekanika kontutan hartuta, eta bigarrenik, diseinu guztien karakterizazio esperimentala egin da. Hemendik ikusi ahal izan da teorikoki egindako hurbilketak diseinu bakoitzaren errendimendu kualitatiboa aurreikusteko balio duela, eta gainera interesatzen den emari tarteak lortzeko parametroen aukeraketa egiteko tresna erabilgarria dela. Azkenik, LOC sistemetan normalki aurkitu ohi diren emariak (200

nl/min – 6 ml/min) eskaintzen dituen diseinu jakin bat aukeratu da, indar balio onargarriekin itxi daitekeena (2 bar inguru).

Hirugarren helburua likidoen emariak neurtzeko mikrosentsore kalorimetriko bat garatzea da, guztiz COP termoplastikoan egina eta emaria neurtzeko elementuak kanala estaltzen duen laminaren kanpoaldean kokatuta izango dituena. Hogei diseinu ezberdin proposatu dira diseinu parametro bakoitzaren eragina esperimentalki ikertzeko, eta hauen artean sentikortasun handienekoa aukeratu da, errepikakorra, zehatza eta fidagarria dela frogatzeko. Honela, sentsoreetan hoberena 2 µl/min-ra arteko emariak neurtzeko gai dela ikusi da, 30 nl/min-ko zehaztasunarekin. Sentsorearen neurtze-tartea handitzeko, bypass egitura bat integratu da sentsoreak neurtzen duen mikrokanalaren ondoan. Emari handietarako garatu den sentsore honek ere ezaugarri bikainak ditu, 300 µl/min-ra arteko emariak neurtzeko gaitasuna erakutsiz %5 baino errore txikiagoarekin. Sentsorearen irakurketek islatu bezala, lamina isolatzaileen kanpoaldeko sentsorearen integrazioa oso arrakastatsua izan da. Gainera, teknologia hau txiparen edozein zonaldetan erraz kokatu daiteke, tokian tokiko emariaren jarraipena baimenduz.

Hurrengo helburua aurreko bi elementuak bateratu eta likidoen emaria kontrolatzeko sistema bat sortzea da, garatutako fabrikazio teknikaren egokitasuna integratutako gailuetan frogatzeko. Sortutako sistema automatizatu honekin 230 µl/min-ra arteko emariak ematea lortu da, %5 baino errore txikiagoarekin. Beraz, lan honetan aurkeztutako fabrikazio teknikak arrakastaz funtzionatzen duten elementu mikrofluidikoak ekoiztea gaitzen duela ikusi da, bai elementu bakoitza bere kabuz erabiltzeko, eta baita LOC sistema konplexuetan integratzeko ere.

Azkenik, garatutako teknologiaren ahalmena erakusteko, emari oso txikiak kontrolatzean oinarritzen diren hiru aplikazio bideratu dira, horietariko bi mikrosentsorean oinarrituak, eta hirugarrena likido emari kontroladorean oinarritua:

- Lehenengo aplikazioan likido-fronteak detektatzeko sentsore-itsasgarri baten hurbilketa bat egin da, sentsorearen berotze-elementua sentsore anemometriko baten gisa erabilita. Sentsore-itsasgarri hau erraz muntatu daiteke txip mikrofluidikoaren gainean, inolako lerrokatze baldintza hertsirik gabe, eta LOC

protokoloetako urratsen jarraipena fidagarritasunez egiteko erabili daiteke, aire burbuila edo ihes-isuri kasuak ere detektatzea ahalbidetuz.

- Bigarren aplikazioaren helburua zelulen hazkuntzarako erabilitako mikrogailu baten barnean mantenugaien egonkortasuna jarraitu eta kontrolatzea da, horretarako emari handietarako mikrosentsore kalorimetrikoa erabiliz. HUVEC (Human Umbilical Vein Endothelial Cells) zelulen hazkuntza dinamikoa 0.1 dyna/cm^2-ko ebakidura-tentsiopean (50 μl/min) gauzatu da 20 ordutan zehar. Saiakera honetan frogatu ahal izan da erabilitako materialek ez dutela inongo eragin negatiborik izan zelulen hazkuntzan, eta ez dela nabaritu ez bolumen hilik, ezta harrapatutako aire burbuilarik ere. Gainera, sentsorea eta irakurketetarako beharrezko elektronika kostu baxukoak direnez, teknologia honek erabili eta botatzeko sentsoreak ekoizteko ahalmena eskaintzen du. Ezaugarri hau oso erakargarria da zelulen hazkuntza bezalako aplikazioetarako, non beharrezko ekipamendua ingurune gogorretan kokatuta egoten den normalean (% 95ko hezetasuna, eta % 5ko CO_2 kontzentrazioa).
- Azkenik, likido emari kontroladorea uraren emaria kontrolatzeko erabili da, eraginkortasun handiko hexadekano tanten sorkuntza uretan lortzeko (O/W), non emarien kontrola eta egonkortasuna oso garrantzitsuak diren. Gailuak bermaturiko sistema egonkorrari esker, hexadekano tanten sorkuntza monosakabanatua lortu da emari bien tarte zabal baterako, errendimendu bikaina eta teknologia honen ahalmenak beste behin erakutsiz.

Eskerrak

Ez nuke lan hau bukatu nahi berau aurrera eramateko lagundu edota ondoan izan dudan jendeari nire eskerrik zintzoenak eman gabe. Aipatu gabe utziko ditudan lagun asko ere egongo dira seguru asko, xehetasunez begira hasi ezkero, hain baita luzea bidea …

Lehenik eta behin eskerrak Ikerlani, mikrofluidikaren mundua ezagutzea posible egin zidalako lehenengo, eta tesi hau egiteko aukera paregabea eskaini zidalako gero. Bereziki esker mila nire zuzendaria izan den Aitor Ezkerrari, bera barik lan hau ez litzatekeelako berdina izango. Beti kritiko azaldu delako, gauzak ondo ulertu eta ganoraz pentsatzen "irakatsi" didalako. Eta *nahitxe askotan amorro momentuk sortarazi dostazun (igual argazkilaritza kurtso bat ez dotelako ein ☺), kariño asko hartu dotsudalako*, eta zuzendari hobe bat bilatzea benetan zaila izango litzaidakeelako. Ildo berean eskerrak Javier Berganzo eta Jorge Elizalderi, bide luze honetan sarritan zuen laguntzaz gozatu ahal izan dudalako. Eta nola ez, Mikrosistemak departamentuko lankide guztiei eskerrak, beti giro oso ona eduki dugulako gure artean, eta horrela lan egitea benetan ikaragarri eskertzen delako: Marta, Aitor B., Iker, Ikerne, Ane, Ana, Irati, Jon, Mikel, Maria T., Maria A., Kepa, Jesus, Iñigo, Florian, Fernando, Lourdes, Vanessa, Borja, Janire, Tugze, Román, Werther, Marios, Verónica, Naiara, Josune, Miren, Rafa, Roberto, Anduaga, Besteiro, … Hauen artean aipamen berezia merezi duen Lioneli, benetan ederra delako zure bizi-poza hurbiletik sentitzea, eta oso pertsona *ikaragarrixe zazelako*, *asko-asko botaten dot faltan zure presentzixi nire eguneroko bixitxan!*

Holandan ezagutu dudan jende guztiari, baina batez ere Roald, David, Roland, Shaskia, Bart, Matia, Hoon, Han, Jaqueline, Brigitte, eta Monicari, …

Nire gurasoei, hautatu dudan bidea egiteko aukera eskaini didatelako, eta nigandik pertsona langile eta burugogor bat egiteagatik. Nire ahizpa eta anaiari, edozer dela ere laguntzeko prest aurkeztu zaretelako beti, *ezta gehixa esan biharrik,asko matxe zatxuet*.

Lurtxooooo!! mila esker zuri be *mogolloi balixo dozulako eta gozada bat dalako zure lakoxe lagun bat eukitxi!* Ondarru eta Arrasateko lagunei, bizitzako zailtasunak ahazteko ezinbestekoak zaretelako: *mendi irteerak, poteuk, eskurziñoik, parrandak,kontzertuk, antzerkixak, mozkorrak, barre algarak, penak eta negarrak ... matxe-matxe zatxuet danok!!!!*

Azkenik Davidi, zu ondoan izatea ez delako bat ere erraza hitzez azaltzea, beti irribarre bat aterako didazulako edozein dela egoera ere, zurekin denetarako kontatu dezakedalako, asko maite zaitudalako eta *aspaldixan zeu ezautzi ixan dalako pasa gaztan onena!*☺

Errealitatetik Ideiak Amestu,

Ametsetatik Errealitatea Ideiatu,

Ideietatik Ametsak Errealizatu.

(Káshbäd)

CONTENTS

1. GENERAL INTRODUCTION - 1 -

1.1. INTRODUCTION - 1 -

1.2. MOTIVATION, SUMMARY and OBJECTIVES OF THE THESIS - 1 -

2. STATE OF THE ART - 5 -

2.1. MICROVALVES - 5 -

2.1.1. Pneumatic microvalves - 6 -

2.1.2. Thermopneumatic microvalves - 10 -

2.1.3. Piezoelectric microvalves - 13 -

2.1.4. Electrostatic microvalves - 13 -

2.1.5. Electromagnetic microvalves - 15 -

2.1.6. Electrochemical microvalves - 17 -

2.2. MICROFLUIDIC SENSING - 19 -

2.2.1. Thermal flow sensors - 24 -

2.2.1.1. Anemometers or hot-wire/hot-film sensors - 25 -

2.2.1.2. Calorimetric flow sensors - 30 -

2.2.1.3. Time-of-flight flow sensors - 36 -

2.2.2. Bypass structures integrated in flow sensors. High flow rate sensing - 38 -

2.3. LIQUID HANDLING SYSTEM. MFCS (Mass Flow Control System) - 39 -

2.4. EVOLUTION OF USED MATERIALS - 40 -

2.4.1. Material selection - 41 -

2.5. FABRICATION - 42 -

2.5.1. General manufacturing methods for thermoplastics - 42 -

2.5.2. Bonding techniques - 45 -

2.5.3. Metallization. Metal thin film processes - 47 -

3. SECTION I – FABRICATION - 51 -

3.1. INTRODUCTION - 51 -

3.2. HOT EMBOSSING - 53 -

3.2.1. Master mould fabrication - 54 -

3.2.1.1. SU-8 master mould - 55 -

3.2.1.2. PDMS master mould - 56 -

3.2.1.3. Fluorinated (meth)acrylate master mould, MD700 - 57 -

3.2.2. Home-made embossing procedure - 58 -
3.2.2.1. Results and discussion of mould material selection - 60 -
3.2.3. Optimized hot embossing procedure - 67 -
3.2.3.1. Results of optimized procedure - 68 -
3.3. DRILLING - 71 -
3.4. BONDING - 72 -
3.4.1. Initial thermal bonding process - 73 -
3.4.2. Improved thermal bonding process - 74 -
3.4.3. Solvent bonding process - 74 -
3.4.3.1. Results and discussion - 75 -
3.5. METALLIZATION OF DEVICES - 77 -
3.6. CONCLUSIONS - 79 -
4. SECTION II –MICROVALVE MODULE - 81 -
4.1. INTRODUCTION - 81 -
4.2. ARCHITECTURE AND WORKING PRINCIPLE - 82 -
4.2.1. Theoretical model of the valve - 84 -
4.2.1.1. Theoretical results - 86 -
4.3. CHARACTERIZATON AND EXPERIMENTS - 87 -
4.3.1. Setup and Experiments - 87 -
4.3.2. Results and Discussion - 89 -
4.4. CONCLUSIONS - 92 -
5. SECTION III – FLOW SENSING. MICROSENSOR MODULE - 93 -
5.1. INTRODUCTION - 93 -
5.2. CALORIMETRIC FLOW SENSOR - 95 -
5.2.1. Working principle - 95 -
5.2.2. Architecture of the sensor chip and proposed designs - 97 -
5.2.3. Characterization and experiments - 99 -
5.2.3.1. Setup and packaging - 99 -
5.2.3.2. Calibration - 102 -
5.2.3.3. Characterization modes - 103 -
5.2.3.4. Summary of tests - 103 -
5.2.4. Results and discussion - 104 -
5.2.4.1. Response profile and flow direction detection test - 104 -

5.2.4.2. CV characterization for calorimetric sensor - 106 -
5.2.4.3. CT characterization of the anemometric sensor - 111 -
5.2.4.4. Accuracy and Reproducibility tests - 114 -
5.2.4.5. Resolution test - 117 -
5.2.4.6. Detection range extension in CT mode - 118 -
5.3. BYPASS CHANNEL FOR HIGH FLOW RATE MEASUREMENT - 119 -
5.3.1. Introduction - 119 -
5.3.2. Device description - 120 -
5.3.3. Bypass-sensor characterization and experiments - 120 -
5.3.3.1. Setup and packaging for bypass-sensor characterization - 120 -
5.3.3.2. Experiments and results for bypass-sensor characterization - 121 -
5.3.4. Flow sensor readouts evolution - 125 -
5.4. CONCLUSIONS - 127 -
6. SECTION IV – LIQUID FLOW CONTROL SYSTEM - 129 -
6.1. INTRODUCTION - 129 -
6.2. ARCHITECTURE AND WORKING PRINCIPLE - 130 -
6.2.1. Architecture - 130 -
6.2.2. Working principle - 131 -
6.3. LFCS CHARACTERIZATION AND EXPERIMENTS - 131 -
6.3.1. Setup and packaging - 132 -
6.3.2. PID control tool - 135 -
6.3.3. Characterization of the LFCS - 136 -
6.4. CONCLUSIONS - 141 -
7. SECTION V – APPLICATIONS FOR THE REALIZED DEVICES - 143 -
7.1. INTRODUCTION - 143 -
7.2. LIQUID MENISCUS DETECTOR: POST-PRODUCTION STICKER-SENSOR - 144 -
7.2.1. Device description - 145 -
7.2.2. Setup and packaging - 147 -
7.2.3. Experiments - 148 -
7.2.4. Results and discussion - 149 -
7.2.4.1. Disposable meniscus detector sticker, PSA (h=2500 µm -10 µm) - 149 -
7.2.4.2. Reusable meniscus detector membrane (h=2500 – 10 µm) - 151 -

7.3. CALORIMETRIC MICRO FLOW SENSOR IN CELL CULTURING .... - 153 -
7.3.1. Fabrication of cell culture microdevices .... - 153 -
7.3.2. Experiments .... - 154 -
7.3.2.1. Cell culture on COP devices .... - 155 -
7.3.2.2. Cell viability fluorescence staining .... - 156 -
7.3.3. Characterization and results .... - 157 -
7.3.3.1. Cell culture .... - 157 -
7.3.3.2. COP sensor validation for cell culturing .... - 158 -
7.4. AUTOMATIC LFCS IN DROPLET GENERATION .... - 160 -
7.4.1. Droplet generator architecture and working principle .... - 160 -
7.4.1.1. Working principle .... - 160 -
7.4.1.2. Architecture .... - 161 -
7.4.2. Droplet generation setup .... - 163 -
7.4.3. Experiments .... - 166 -
7.4.4. Droplet generation results .... - 167 -
7.5. CONCLUSIONS .... - 177 -
8. MAIN CONCLUSIONS .... - 179 -
8.1. FURTHER WORK .... - 182 -
9. APPENDIX .... - 183 -
APPENDIX SECTION II – Microvalve .... - 183 -
APPENDIX SECTION III - Sensor .... - 189 -
i. Electronic circuitries for heating and sensing (4w and Wheatstone Bridge) .... - 189 -
ii. Analysis of each design parameter for the calorimetric flow sensor .... - 191 -
iii. Effects caused by poor membrane flatness on the bypass-sensors .... - 195 -
APPENDIX SECTION IV - LFCS .... - 201 -
i. PID control tool .... - 201 -
10. List of PATENTS and PUBLICATIONS .... - 215 -
11. BIBLIOGRAPHY .... - 217 -

1. GENERAL INTRODUCTION

1.1. INTRODUCTION

Microfluidic Lab on a Chip (LOC) and micro total analysis systems (µ-TAS) offer immense potential for medical and biological applications. Low cost, fast response time and a minimal use of reagents and samples are some of their principal advantages. Accurate control of low fluid volumes (µl) and precise flow control (µl/min) are of utmost importance for LOC devices in order to eliminate dispensing, dosing or dilution errors, which could impair the progress of an otherwise successful biological protocol and alter the final result or diagnostic. Fluid control is thus, fundamental to ensure the adoption of LOCs by real applications. Moreover, accurate flow handling is finding new niches of application of economic importance in the oil refining, analytical instrumentation, food and pharma and industries.

The capacity of microfluidic control to generate innovative products and production methods lies in its combination with other fields, such as biology, engineering, physics, chemistry and manufacturing technology. Point-of-Care devices in medicine, micro-bioreactors in biotechnology, massive paralellization of chemical micro-factories or condition monitoring of hydraulic systems in the automotive industry are some of the success cases that feature this combination of technologies.

1.2. MOTIVATION, SUMMARY and OBJECTIVES OF THE THESIS

As stated previously, handling of small flow rates is becoming increasingly crucial for diverse economically important applications. However, in the literature there is still lack of truly integratable flow control elements, that can be adequately integrated in full polymeric LOCs without dimensional or assembly errors, that are easy to fabricate in a few manufacturing steps, cost-effective, and compatible with industrial mass-production techniques. For lab on a chip applications in particular, the challenge remains at creating

liquid flow control systems that can be monolithically integrated and easily actuated, which is reproducible, reliable, low-cost and disposable.

The majority of approaches found in the literature feature microvalves and micro flow sensors made in traditional materials like silicon, glass-silicon, elastomers or hybrid polymer-silicon materials. The fabrication methods employed are mostly not compatible with other elements required to make a complex LOC system. Therefore, not only a fluidic control component but also a fabrication method that fulfils basic performance and cost constraints are missing in the literature.

In the present thesis, a response to all these constraints has been investigated, leading to a design and manufacturing approach that enable excellent quality and problem-free integration of components, such as valves, channels, flow sensors and bypasses. As a result, these can be produced as stand-alone components or combined in a complex flow controller, without changing their individual performance.

Hence, the main contribution of this thesis are a robust and accurate liquid flow controller and a modular approach with characteristics of “design for manufacturing”, whereby all stages of generation of the LOC prototype are harmonized for its manufacture in few steps and with industrial-like quality at low cost. An important result of this is an accelerated transition from prototype to product in a way that is lean, cost-effective and with reduced risk.

Breaking it down into objectives, the first objective is to develop the manufacturing procedure for the most common microfluidic elements in thermoplastic material (COP, Cyclic Olefin Polymer). This way, microvalves and microsensors have been fabricated together with microfluidic channels and bypass in a single Hot Embossing step, subsequently solvent-bonded and finally metallized. The enormous integration potential achieved will allow covering plenty of microfluidic structures and will facilitate the transition from prototype to product owing to dimensional quality and similarity with respect to injection (industrial reference) and the post-production approach for metal deposition.

The second objective is to create a monolithic membrane microvalve entirely made of COP. This is intended to operate both as on/off and flow regulating microvalve. To this end, first mechanic-fluidic model has been realized and then, the experimental characterization of an array of valves has been carried out. It has been found that the model can predict the qualitative performance and the flow regulation profile of each design. From here, a choice of architecture for the required performance can be simplified.

The third objective is to realize a micro calorimetric flow sensor in COP, with the sensing elements deposited outside of the sealing membrane. An array of designs has been manufactured in order to investigate the effect of each parameter experimentally and the design with the highest sensitivity has been selected and demonstrated to be reproducible, accurate and highly reliable. This sensor is capable of measuring flow rates up to 2 µl/min with an accuracy of 30 nl/min. In order to adapt the detection range to flow rates more typical of LOCs, a bypass construction has been integrated, also showing excellent performance for flow rates up to 300 µl/min with less than 5% error. The satisfactory performance of the external sensing electrodes on polymer layers proves the possibility to place them anywhere on the chip to monitor local flow conditions as a post-production step.

The fourth objective is to integrate the valve and the sensor module to obtain the Liquid Flow Controlling System (LFCS), where the suitability of the fabrication method has been demonstrated for an integrated device, featuring various microfluidic components and electrodes working together in an automated system. Successful regulation of flow rates up to 230 µl/min with less than 5% error has been achieved.

Finally, three microfluidic control applications have been demonstrated, two based on the micro flow sensor and one on the LFCS:

- A meniscus detector, which can be used as a flag to verify the completion of a particular fluidic step, or presence of leakage. This has been fabricated on a

sticker, which can be easily applied on the test chip with no alignment requirements.

- A device to monitor and control the stability of nutrients' flow in a dynamic HUVEC-type cell culture. After 20 hours of continuous operation, neither the material nor the calorimetric actuation were observed to affect the viability of the cells and neither dead volumes or trapped bubbles could be observed. Moreover, the low cost of the sensor and its associated electronics allows it to be disposable, which is especially relevant in cell culture, where the sensor needs to be placed in a corrosive environment (95% humidity and 5% CO_2).
- Control of high throughput water droplets generation in hexadecane, using the LFCS. In this application, the control and stability of the flow rate is extremely important. This device enabled a stable system and successful monodisperse droplet generation for a wide flow range, evidencing the excellent performance and huge potential of this technology.

The research carried out in this thesis has been funded under the Etortek Programme 2010-2013 of the Basque Government, which is aimed at the development of "Microtechnologies for In Vitro Diagnosis and Industrial Environments".

2. STATE OF THE ART

In the following sections, previous works about flow controllers and their principal elements will be reviewed. The most up-to-date and relevant of these, which also include microvalves and microsensors, will be summed up together with the materials and micro fabrication methods used over the past years. These items are believed to encompass all aspects dealt with in this thesis, both from the scientific and the economic standpoints, thus resulting in a suitable frame for the work presented.

2.1. MICROVALVES

Microvalves are critical for fluid flow control and thus, one of the most important components for the realization of fully integrated Lab-on-a-Chip (LOC) systems [1-5]. High potential applications for precise volume handling include chemical analysis, gas/liquid sample injection, flow regulation, chemical reactions, etc. [6], where the microvalve functions involve flow regulation, on/off switching and sealing of liquids, gases or vacuum.

Many different methods for creating a microvalve have been reported depending on their actuation method, which are summarized in Table 2.1. Microvalves are basically categorized into active and passive, and both use mechanical and non-mechanical moving parts, and the active microvalves also use external systems.

Table 2.1. Classification of microvalves.

<table>
<tr><th>Category</th><th>Type</th><th>Actuation</th></tr>
<tr><td rowspan="3">Active</td><td>Mechanical</td><td>Electromagnetic
Electric
Piezoelectric
Thermal</td></tr>
<tr><td>Non-mechanical</td><td>Electrochemical
Phase change
Rheological</td></tr>
<tr><td>External</td><td>Modular
Pneumatic</td></tr>
<tr><td rowspan="2">Passive</td><td>Mechanical</td><td>Check valves</td></tr>
<tr><td>Non-mechanical</td><td>Capillary forces</td></tr>
</table>

The majority of active microvalves involve a flexible membrane, which is exerted by one of the existing actuation methods. These actuations include pneumatic, thermopneumatic, thermomechanical, piezoelectric, electrostatic, electromagnetic, electrochemical and chemical and capillary forces. The external active microvalves usually employ external systems such as pneumatic actuation to exert on the membrane. Finally, most passive microvalves, also known as check valves, are mechanical parts or moving structures such as flaps, membranes, spherical balls, etc. All actuation methods and their working principles have been thoroughly reviewed previously [6, 7].

2.1.1. Pneumatic microvalves

In pneumatic microvalves a flexible membrane is pressurized in order to open or close the microvalve by using a source of pressurized air. Most works concentrate on the membrane characteristics, since this element determines the whole properties of the valve. Yuen et al. [8] presented a microvalve made of PMMA (Poly(methyl methacrylate)) fabricated by CNC (Computer Numerical Control) for human cell isolation and DNA amplification systems. The microvalve consists of two discontinuous microchannels that allow controlled flow employing a flexible plastic membrane sealed with an adhesive. Meanwhile the pressured liquid flows through one of the discontinuous microchannels, it causes the membrane to rise into the recess, and permits the liquid to flow across the microvalve which connects with the other microchannel, Figure 2.1.(a). The microvalve closes by positive action on the valve closing system, Figure 2.1.(b). Release of this system allows the microvalve to re-open. This way, the valve allows processing microliter and sub-microliter sized samples of whole blood without inhibition of biochemical reactions and without sample loss on the microvalve (dead volume less than 0.16 µl) or loss by evaporation.

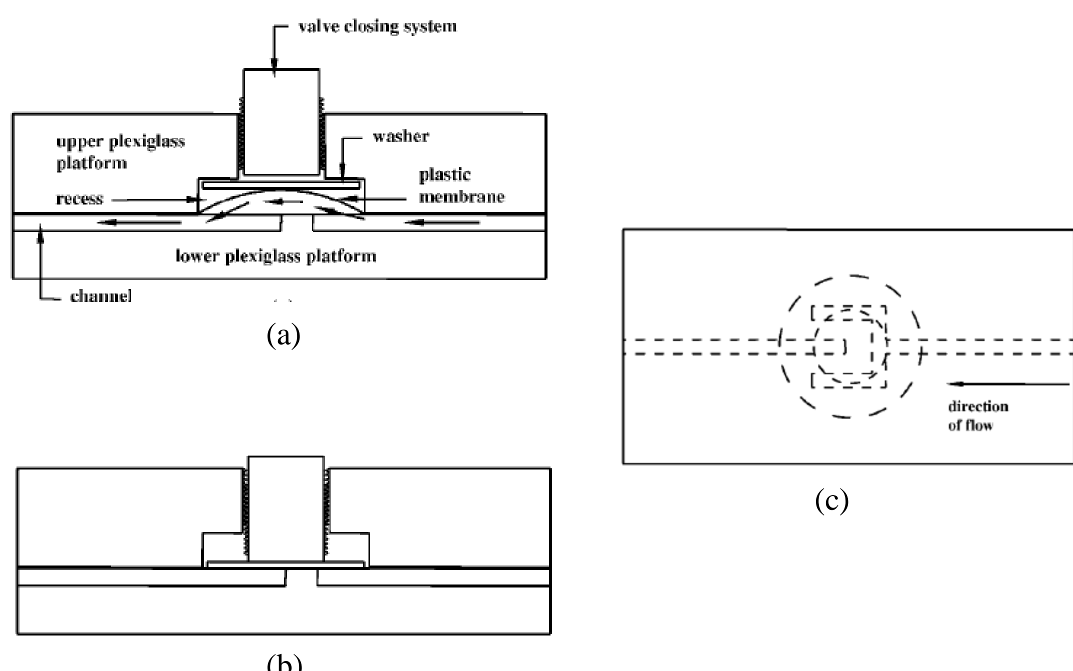

Figure 2.1. Operating principle of a semi disposable CNC machined PMMA pneumatic microvalve by Yuen et al. (a) Valve open, (b) Valve closed, (c) Bottom view.

Wang et al. [9] employed a previously reported microvalve [10] in order to achieve more efficient multidimensional protein separation in a microfluidic channel. The valve is a multilayer PDMS (Polydimethylsiloxane) valve featuring a low dead volume, and supposes a key component to prevent intermixing and contamination between two separation buffers.

Kanai et al. [11] introduced a microvalve for real-time monitoring of living cells, fabricating the valve chamber on silicon and assembled with a PDMS diaphragm. Examination of the leakage and sample injection accuracy showed a leakage less than 0.1 nl/min when the pneumatic valve was closed with 20 kPa, confirming a reproducible sample injection of the order of 1 nl using 10 kPa for the liquid.

The work reported by Luque et al. [12] describes a valve suitable for integration in a complex fluidic circuit. The device is fabricated from silicon and requires no bonding, being very compact and strong, decreasing the possibility to break down during

operation and totally removing leakages through the joints. It uses a fluid pressure compensation to allow the valve to work under high pressures. Two fluids apply pressure on each side of a membrane, Figure 2.2. The balance between both pressures determines the state of the valve, whether in equilibrium, open or closed. The fluid can be air, gas or liquid. Flow rates range from 1 μl/s to 100 μl/s with pressures of up to 5 bar.

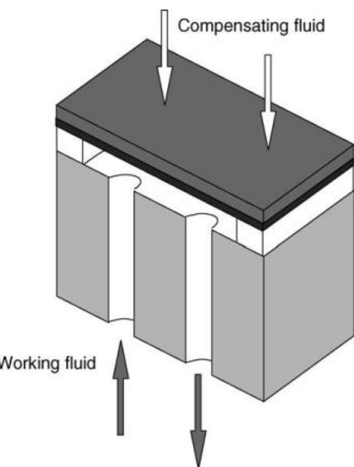

Figure 2.2. Silicon based pneumatic microvalve with flow compensation for high pressure environments.

Baek et al. [13] developed an on/off PDMS-based microvalve that regulates the flow using a thick centred membrane, as shown in Figure 2.3. The valve consists of one base relief plate of 10 mm and three PDMS layers of 200 µm. Through the pneumatic port, a slight vacuum is applied, the membrane with a thick centre (TC) is lifted upward, and the centre hole is opened allowing the fluid to flow to the outlet, Figure 2.3.(b). In contrast, if the compressed air enters through the pneumatic port and presses the membrane, the flow path closes as the TC membrane seals off the centre hole, Figure 2.3.(a). To integrate the freely moving thick centred membrane, regional bonding of the PDMS layer is required. The valve showed good on/off operation in accordance with the applied pressure, and the flow rate through the channel depends on the pressure applied to the liquid in the inlet, being able to provide tenths of microliter per minute flow rates. The main drawback of this valve is that the required regional bonding of the PDMS layer for the free motion of the TC membrane is difficult.

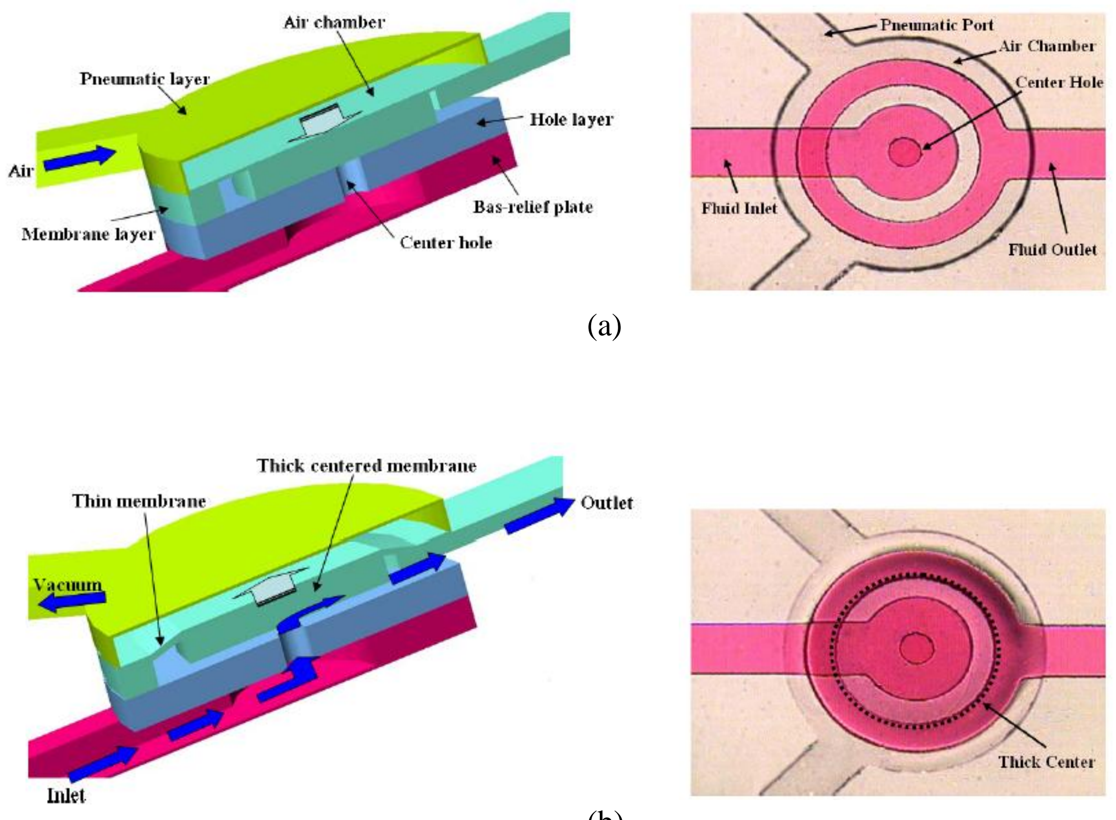

Figure 2.3. Pneumatically actuated operation of a thick centred microvalve made of PDMS. (a) Closing of the microvalve by compressed air; (b) Opening of the valve by vacuum.

The valve presented by Hua et al. [14] possesses a PDMS/parylene double-layer membrane, which is leak-proof upon actuation. The parylene side gives the membrane excellent chemical compatibility with typical aggressive chemicals, including tetrahydrofuran, toluene and dichloromethane as well as most solvents, acids, bases and oxidizers, and protecting the PDMS from damage. The 2 μm parylene layer is deposited by chemical vapour deposition and patterned using oxygen plasma. The microvalve shows linearity between flow and pressure and no leakage was observed below 1.4 bar.

A great number of pneumatic microvalves, combining rigid polymer substrates for control and fluid structures with flexible elastomer actuating membranes, have been realized using different surface treatments in order to achieve reversible or irreversible bondings [15-17]. Shanshi et al. [18] have developed a pneumatically actuated

microvalve, patterning the control and fluid channels on rigid PMMA substrates and using a PDMS membrane for control. Each patterned PMMA structure was silanized and irreversibly bonded to a plasma-treated PDMS membrane, forming a control half and fluid half structures. The two half structures were then reversibly sealed relying on the native adhesive force of the PDMS membrane. This fabrication process eases the difficulties in chip bonding and allows any of the halves to be replaced individually in routine analyses.

2.1.2. Thermopneumatic microvalves

In thermopneumatic microvalves generally a thermal actuation, provided by a resistor, is used to pressurize a secondary chamber and deflect a membrane in order to open or close the valve. The valve proposed by Yang et al. [19] employs thermal actuation through a secondary fluid, as shown in Figure 2.4. The secondary fluid heated with an electric resistor exerts pressure against the silicone membrane, causing it to deflect. They used a parylene layer to isolate the silicone membrane, avoiding the permeability that the silicone membrane presents to most fluids, such as the vapours arising from the heated secondary fluid.

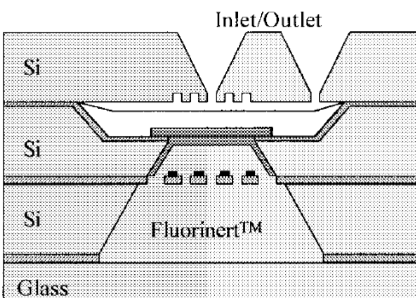

Figure 2.4. Schematic presentation of the thermopneumatic microvalve developed by Yang. The parylene membrane is employed to isolate the silicone membrane permeability from the vapours arising from the heated secondary fluid.

Baechi et al. [20] realized a microchannel network integrating up to 330 valves cm^{-2} and allowing parallel processing of nanoparticles with very high throughput. The bottom glass layer carries a metallic meander heater that heats the air in the cavity, deflecting the 3 µm thick silicone membrane. Short current pulses of 500 ms duration were used to heat the cavity, and fast rise time of 150 ms and fall time of 350 ms were measured, achieving flow rates of 95.8 µm/s and 8.3 µm/s when the valve was opened and closed respectively. Cooling channels were required to solve the thermal cross-talk problems between two valves.

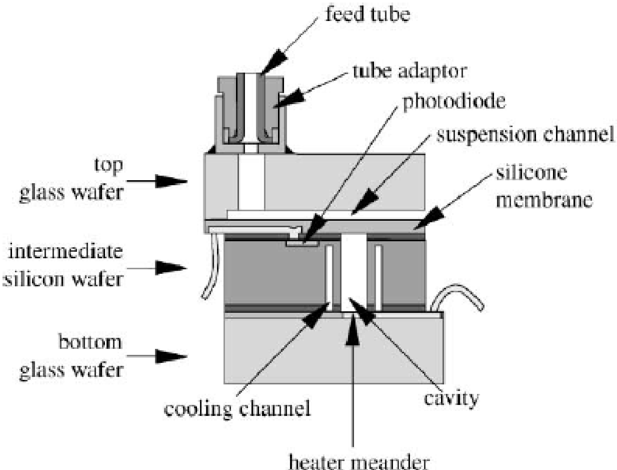

Figure 2.5. Thermopneumatically actuated microvalves developed by Baechi, used in a high density microchannel network combining glass, silicon structures with 3 µm thick silicone membrane.

The thermopneumatic microvalve from Rich et al. [21] comprises a silicon microstructure capped above and below by anodically-bonded glass plates, Figure 2.6. To overcome the limited deflection of the silicon membrane, they presented a corrugated silicon diaphragm, consisting of a 500 µm central boss supported by a 250 µm corrugated suspension, allowing greatly increased membrane deflection (> 50 µm) with small actuation forces, and therefore offering high-flow throughputs. The thermopneumatic actuation was implemented by means of heating volatile fluids, such as pentane or methanol, and deflecting the valve plate with the pressure generated by the vapours.

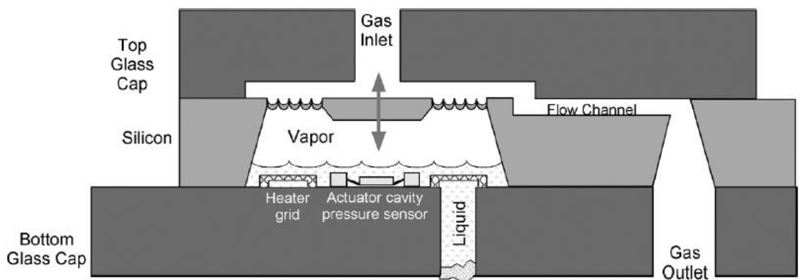

Figure 2.6. Thermopneumatically actuated glass-silicon microvalve developed by Rich. The proposed corrugated silicon membrane enhanced its deformation and the thermal optimization of the valve structure was carried out to enhance the response time and the power consumption.

Kim et al. [22] proposed a thermopneumatic microvalve made of PDMS and ITO-coated glass. The ITO is used to heat up the air of the PDMS thermopneumatic chamber, Figure 2.7, and the expanded air deflects the membrane to seal on the valve seat. The main drawback of this microvalve is the response time, requiring closing and opening times around 20 and 25 sec respectively.

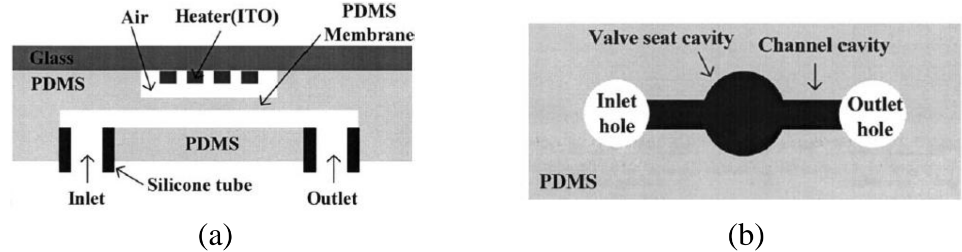

(a) (b)

Figure 2.7. Configuration of the thermopneumatic microvalve proposed by Kim, made of PDMS and ITO-coated glass. (a) Cross sectional view of the microvalve; (b) The cavity of PDMS replica.

2.1.3. Piezoelectric microvalves

Piezoelectric microvalves are generally composed of a membrane actuated at high frequencies by a piezoelectric actuator [23-25]. Spacecraft applications, where mass and size saving reduces costs, have found powerful applications with piezoelectric actuators, due to their advantages in power consumption, mass and size. For instance, Chakraborty et al. [26] introduced a microvalve specially designed to meet the rigorous performance requirements for a variety of spacecraft applications, such as micro-propulsion, in situ chemical analysis of other planets, or microbiology. The valve consists of a seat that contains the inlet and outlet, a corrugated diaphragm with a circular boss suspended by a silicon diaphragm or by four silicon bridges, and the piezoelectric actuator in a rigid housing.

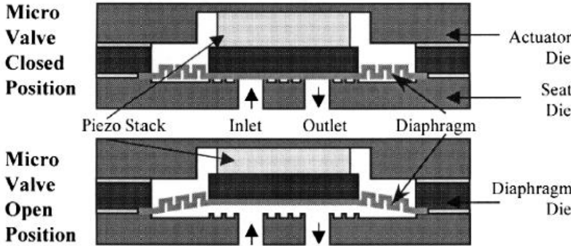

Figure 2.8. Piezoelectrically actuated microvalve proposed by Chakraborty for spacecraft applications.

2.1.4. Electrostatic microvalves

Electrostatic microvalves [27-29] are generally composed of an electrode-membrane actuated by the electrostatic force generated by a fixed electrode. The valve presented by Van der Wijngaart et al. [30] proposed a electrostatic valve for high pressure applications, employing a pressure balancing concept on both sides of the flexible electrode-membrane, Figure 2.9. Theoretically, the model also showed a large flow gap at low actuation voltage in comparison with former designs that a small stroke length

resulted in a high flow restriction, limiting the flow that the valve can control. However, the complexity of the design is an important disadvantage that also supposes a difficult fabrication of it.

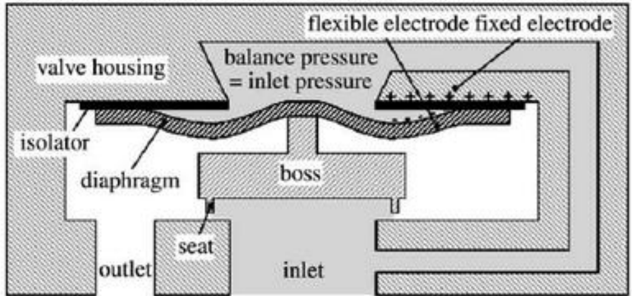

Figure 2.9. Electrostatically actuated flexible electrode-membrane microvalve concept by Van der Wijngaart. The present study could not be applied to a flexible electrode-membrane and a pair of Si-SOI wafers were employed.

The electrostatic micromachined pump for medical applications designed and simulated by Teymoori et al. [31] combines glass, silicon and the membrane. The electrostatic actuation allowed a smaller size of the device with no clogging and leakage, and satisfied all medical delivery requirements, such as compatibility, flow rate controllability and low power consumption, providing a flow rate of 9.1 µl/min with no residual stress.

Han et al. [32] have recently reported a strategy for operating pneumatic microvalves with microscale electrostatic actuator in order to offer a portable solution. The footprint of each actuator is less than 0.5 mm^2 and it is fully composed of PDMS and multi-walled carbon nanotubes, operating at electric potentials less than 300 V while regulating microchannels pressurized up to 4 kPa with no drift issue in the actuation potential. The actuator consists of a circular elastomeric membrane with an embedded electrode, suspended above a microfluidic chamber. A second electrode is embedded beneath the floor of the chamber. They attached a cylindrical post on the top of the membrane in order to reduce collapse due to sticking, and connected the above of the membrane to a venting channel to avoid pressure build-up in the cavity, Figure 2.10.

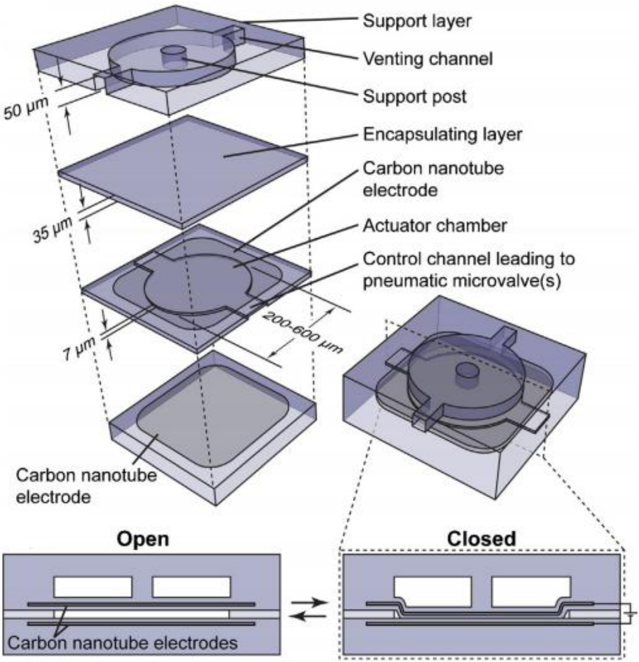

Figure 2.10. Monolithic PDMS electrostatic actuator proposed by Han, containing carbon nanotube electrodes.

2.1.5. Electromagnetic microvalves

In electromagnetic microvalves the actuation is realized by means of a magnet placed on the membrane and a solenoid which is fixed near the magnet. De Bahilís et al. [33] described a magnetic microactuator in a valve construction consisting of a Nd-Fe-B permanent magnet, a silicon nitride membrane and electroplated copper coil, Figure 2.11.

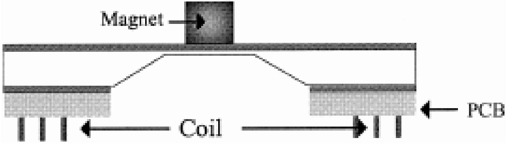

Figure 2.11. Structure of the magnetically actuated silicon nitride membrane proposed by De Bhailís. The silicon device was glued on top of a PCB with an electroplated solenoid for actuation.

Bae et al. [34] presented the intraocular pressure regulating valve for glaucoma active implant, made of silicon layers, placing them layer by layer using wet and dry etching. Then, the magnet and the solenoid were glued using an epoxy. The main challenges lied on the actuation method that had to be biocompatible, the size of the final implant device, and avoiding clogging problems.

Liu and Li [35] have recently presented a electromagnetic actuator for gas flow rate control with low powering and no leakage, which is different from others previously published. The normally-closed microvalve is composed of a miniature electromagnetic actuator and a valve body. The electromagnetic actuator is an inhalation electromagnet with a moving iron post and possesses a thin PDMS-base, which acts as the valve diaphragm used as a solid hydraulic medium, Figure 2.12. The method provides a simple and cheap choice to avoid the bulky and expensive external pressure control solenoid manifolds, allowing the easy assembly into portable and disposable devices. The dynamic tests for on/off control mode showed fast open response (~17 ms), small leak rate as low as 0.026 sccm at 200 KPa (N_2) pressure.

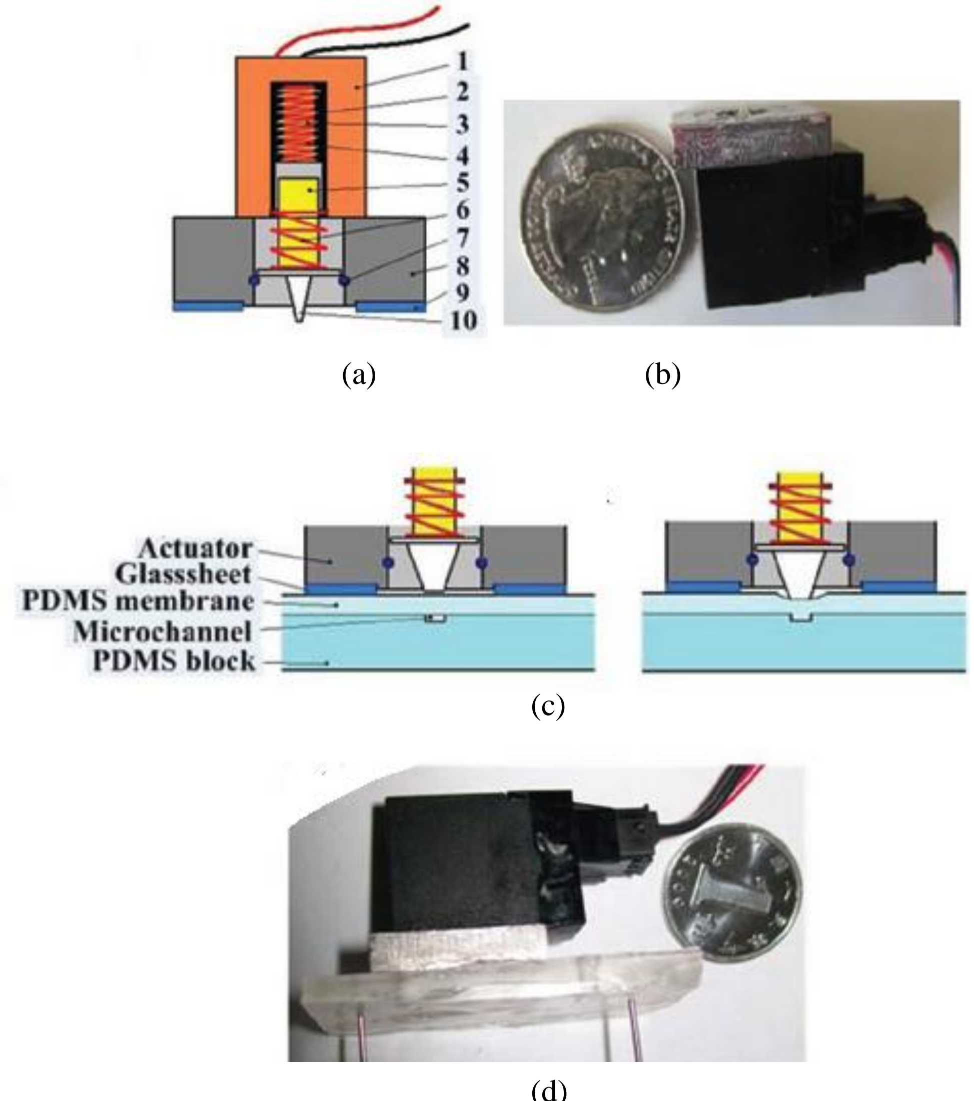

Figure 2.12. Electromagnetic microvalve proposed by Liu and Li. (a) Schematic design of the electromagnetic actuator; (b) Picture of the actuator; (c) Schematic design of the microvalve in its open and closed state; (d) Picture of an encapsulated microvalve.

2.1.6. Electrochemical microvalves

The chemical and electrochemical actuation methods comprise a reduced number of approaches based on chemical reactions, providing actuation with or without moving parts. For instance, Suzuki and Toneyama [36] integrated on-chip micropumps and check valves that function by means of a hydrogen bubble that is generated or

extinguished electrochemically. The bubble clogged in a valve compartment in the middle of the flow channel, blocking the passage of the fluid. Essential elements of the device consisted of a thin-film three electrode system, and the micro flow channels and containers for electrolyte solutions were formed on a PDMS substrate. Eddington et al. [37] described the use of an anionic stimulus responsive hydrogel that provides the requires actuation pressure to deform a flexible membrane above a fluid reservoir chamber, for valving and dispensing functions. Yamahata et al. [38] presented a PMMA micropump based on the magnetic actuation of a magnetic liquid, using two soft silicone membranes integrated in the microfluidic structure to form two check-valves. These valves convert the periodic motion of a ferrofluidic plug into a pulsed quasi-continuous flow. The ferrofluid is actuated by the mechanical motion of an external Nd-Fe-B permanent magnet. This way, successful pumping of up to 30 µl/min was achieved with backpressures of up to 25 mbar.

Amongst the microvalves published to present, pneumatically actuated membrane valves have been successfully used in many applications due to their low cost and simple fabrication. A variety of devices has been demonstrated for silicon [39-41], and glass-silicon [20, 42], as well as for elastomers [10, 43-45] and polymers [46-49]. Besides, the tendency of the last decades point to a change in the materials used for the construction of the microvalves, becoming polymeric materials, and specially thermoplastics, more and more attractive [50-52].

Nevertheless, far beyond the already researched features about the microvalves performance, such as actuation, leakages, dead volumes, response time, chemical compatibility, etc, further improvements in materials and fabrication of the microvalves are required in order to be easily incorporated in complex LOC systems. This necessity grows even more when it is interested to fabricate cheap and disposable LOC systems by industrial fabrication methods.

For the easy incorporation of the valve in the systems, firstly, the valve should be simple to fabricate, and for this it should ideally be monolithic with the rest of the device. As more number of components require different materials, higher will be the

steps required to fabricate the system. On the contrary, if the valve is composed of the same materials as the rest of the device, it can be fabricated in-parallel with the other components, thus in a single step. Unfortunately, most of the microvalve examples do not meet this criterion, requiring intensive fabrication processes.

One of the most reported microvalves entirely made of a single material is a pneumatic microvalve fabricated with PDMS, using soft-lithographic techniques [10]. This material can be adequate to carry out proof of concepts at laboratory scale, but is not suitable for mass-production manufacturing techniques. Therefore, there is still a need to develop fully polymeric, and preferable thermoplastic based, microvalves to demonstrate its good performance and incorporation possibilities into LOC systems.

2.2. MICROFLUIDIC SENSING

Sensors are essential in our everyday lives to fulfil the need of to collect and process some sort of information. The use of micro flow sensors is growing in many industrial areas such as chemistry, automotive and pharmacy industry, biology, medicine etc in order to condition monitoring and control or as preventive maintenance.

Lots of applications within the emerging fields of LOC and μ-TAS systems carry out the integration of the total sequence of lab processes, e.g. chemical reactions or diagnose of diseases. In these applications, the miniaturization of components is necessary in order to achieve low cost, fast response and minimal use of reagents. The inherent requirement for small and precise fluid volume handling makes flow sensors important components for this type of devices.

Many different flow sensing principles have been developed during the last years, some of them becoming miniaturized and incorporated into microdevices. The main flow sensor groups are distinguished by their measuring principles, being these of Mechanical, Thermal, Oscillatory -not suitable for miniaturization [53]-, Differential-Pressure and Coriolis type.

Mechanical Flow sensors rely on a drag force imposed by a moving fluid on a movable part or structure. Some groups have developed this type of sensors inspired on the natural capability of the crickets to detect the low-frequency sound waves [54-58]. Dijkstra et al. [59] presented a model, a design, a fabrication method and characterization to mimic the highly sensitive hairs of crickets to drag-forces, demonstrating the viability of the concept with capacitive measurements realized when using artificial sensory hairs made of SU-8 on suspended silicon-nitride membranes and chromium electrodes, Figure 2.13. Bruinik et al. [60] reported several advancements in fabrication and optimization of the design that contributed for 100-fold increase in acoustic sensitivity, obtaining higher capacitive outputs and measuring oscillating flow amplitudes down to 1 mm/s against the previous ranging from 100 to 1000 mm/s. The main modifications include longer SU-8 hairs, smaller inter-electrode gaps to increase the capacitive sensitivity, and the use of aluminium electrodes instead of chromium ones. Another measuring strategies based in microcantilever was presented by Ma et al. [61]. They realized a “weather-station” device, where the bending-up of the cantilevers using a LCR meter was used to determine the flow rate of the wind, together with temperature and humidity measurements using a Pt resistor (RTDs) and cantilevers covered with water-absorbent polyimide layer. When the polyimide layer absorbs the ambient humidity, it causes a moisture-dependent bending of the cantilever. This device consists of a polysilicon wafer, silicon-nitride membrane, Pt/Cr resistors, polyimide layer and Au/Cr electrical leads, Figure 2.14. The main disadvantage of this flow sensor is that exhibits a hysteresis effect. Attia et al. [62] introduced a microflow sensor made of PDMS (or PEGDA) and based on a deformable spring-like structure that has a large dynamic range, being able to scale down to nl/min range measurements. They demonstrate microscope-based stop flow lithography to fabricate deformable microstructures, such as spring-like sensors, inside microchannels with reproducible mechanical properties and dimensions, being the sensors able to measure in a range of 4 orders of magnitude.

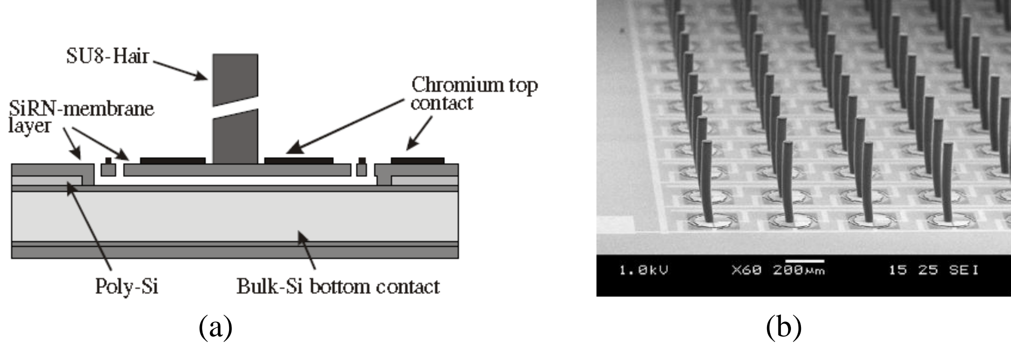

Figure 2.13. (a) Biomimetic mechanical flow-sensor, where sensory hairs have been realized in SU-8 on top of suspending silicon-nitride membranes. (b) Array sensory hairs.

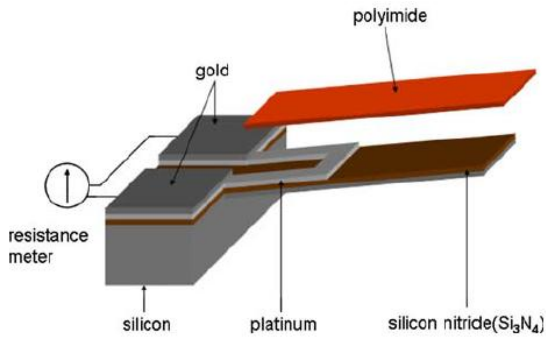

Figure 2.14. Schematic illustration of a micro-cantilever based weather station: temperature, humidity and flow sensor.

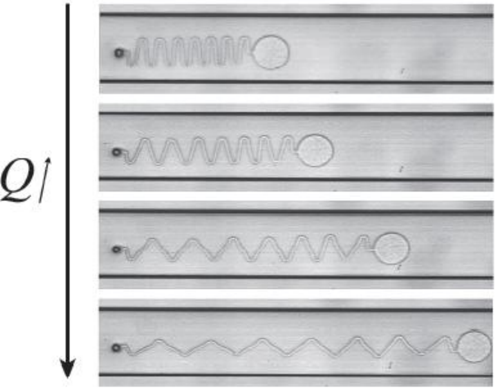

Figure 2.15. Deformation of the photopolymerized spring-shaped component of the flow sensor upon increasing flow rate.

Differential pressure flow sensors seem to be very promising to miniaturize. They usually have a restriction integrated into the channel, and two sensors placed before and after this restriction to measure the pressure difference in that points, being this measurement directly proportional to the volume flow rate. Ritcher et al. [63] proposed a flow sensor for liquid sensing, consisting of a common piezoresistive pressure sensor with an orifice between 100-400 µm in the sensor diaphragm. The orifice forms a flow restriction and thus, the sensor directly measures the pressure drop at the orifice. Oosterbroek et al. [64] presented a sensing system fabricated in silicon and glass, consisting of capacitive pressure sensors together with a microchannel as an hydraulic resistor, Figure 2.16. The pressure on both sides of microchannel is sensed, which is directly related to the flow rate. The main disadvantages were that the viscosity changes may influence the sensor signal, so temperature controlling systems are required for high precision, and also that clean fluids without particles may be used. Nevertheless, they demonstrated measurement of ethanol in µl/s range. Liu et al. [65] presented a high-speed liquid flow sensor based on pressure difference measurements and used together with a solenoid valve in order to realize a self-adjusted system that can dispense reagent accurately, being the sensor able to measure flow rates up to 80 µl/s with accuracies lower than 5%.

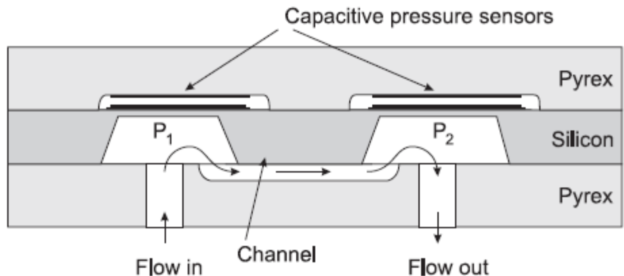

Figure 2.16. Schematic view of the capacitive pressure/flow sensor by Oosterboek et al.

The Coriolis mass-flow sensors do not posses any moving parts, and work by exerting a force onto the flowing fluid inside the channel in the perpendicular direction to that of the flow. This is usually done by vibrating the channels at their resonant frequency. This way, when no fluid is flowing, the two vibrating sensors synchronized each other. In

contrast, when the fluid flows, the vibration twists the channel in proportion to the mass flow rate. The sensors placed on the inlet and outlet of each tube, measure the caused twist and thus, the mass flow rate can be measured accurately. Enoksson et al. [66] introduced the first miniaturized Coriolis flow sensor made of silicon, Figure 2.17. The tube structure was exited electrostatically into a resonance bending or torsion vibration mode, and the liquid flow past through the tube induced a Coriolis Force, resulting in a linearly proportional twisting angular motion, perpendicular to the excitation. Here, the detection of the twisting was done optically, using a lateral photodetector placed at 1 m distance. The flow sensor was also able to measure density and direction of the flow, as well as mass-flow rates as low as 0-0.5 g/s. Haneveld et al. [67] reported the first true miniaturization of a micromachined Coriolis mass flow sensor, consisting of a silicon nitride resonant tube of 40 µm diameter and 1.2 µm wall thickness. They demonstrated linear performance of the sensor and flow measurements for both gas and liquid in the order of 10 mg/hr when Lorentz forces were applied for the resonating actuation of the sensor, and measuring the out-of-plane local displacements of the tube by a PolyTec laser vibrometer. They observed that misalignment among the sensor and the actuation magnetic field results in a sensor output signal offset. To further develop this work, they integrated capacitive readouts to detect the small Coriolis vibration of the sensor tube, and avoid using external measuring equipment [68]. They showed accurate mass-flow measurements between 0-1.2 g/hr, with an error in the order of 2% of the full scale.

The main drawbacks of Coriolis mass-flow sensors are that they are mostly used for measuring large flow rates and they require rather complex drive and detection electronics.

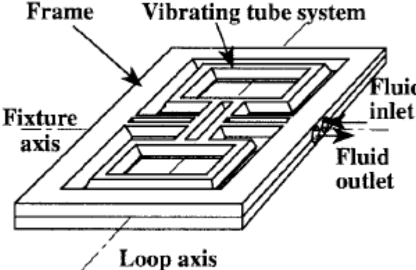

Figure 2.17. The combined Coriolis mass flow and density sensor resonator by Enoksson, consisting of two serially connected tube loops arranged symmetrically in plane. The double-loop size (without frame) is 9x18x1 mm.

Although lots of miniaturized examples for different measuring principles have been reported until the date, not all principles are equally suited for downscaling, some of them often being of little use in micro domain due to large size, complex construction and integration difficulties, high dead volume, or limited sensitivity at lowest flow rates. Thus, most micro flow sensors described so far rely on the thermal method. Since they do not posses any moving parts, they present simple structure and fabrication.

2.2.1. Thermal flow sensors

Thermal flow sensors have been extensively analyzed during the last decades [69, 70], since they are economically more attractive and can offer high turndown, being able to measure from low to high flow rates with the same device, reliably, without moving parts, a negligible pressure drop, fast response time and ease of fabrication.

Flow sensors are transducers comprised of heaters and temperature sensors, where the heat generated at the heater element interacts with the surrounding and a flowing fluid through the microchannel carries away some heat, causing a temperature distribution near the heater and in the flowing fluid. The three main types of thermal flow sensing principles are anemometric or hot-wire, calorimetric, and time-of-flight.

2.2.1.1.Anemometers or hot-wire/hot-film sensors

Anemometers are generally comprised of a single element which is heated by an electrical current and the heat dissipated by the surrounding fluid is measured as a function of the flow. Two modes are usually used to operate the anemometers, the constant power simple model (CV), and the constant temperature mode (CT). The CV is fed with constant voltage and the temperature or resistance of the hot element is measured, which decreases with increasing the flow rate of the fluid. The CT requires a feed-back loop to know and correct the temperature of the heater. The constant voltage mode is slower and less sensitive than the constant temperature, and response times can also be larger by orders of magnitude [71].

A great amount of hot-wire and hot-film examples have been developed, in wide a variety of substrates and metal thin wire/films. Most existing micromachined sensors have been developed using silicon substrates, because the silicon technology was already developed, and piezoresistive elements can be realized in silicon by selective doping.

Soundararajan et al. [72] presented a hot-wire anemometer to mimic capillaries under physiological conditions and know the shear stress generated by a fluid on the channel walls. They employed backside wire bonding technique to insulate the sensor element, made of polysilicon doped with phosphorous using a silicon substrate, from biological fluids. They demonstrated shear stress measurements with dimensions and Re number commonly encountered at the capillary level, solving the shear stress measurements in complicated arterial geometry in presence of unsteady flows.

Kaltsas et al. [73] introduced a fabrication method to realize a thermal flow sensor in SU-8, a non conductive material, significantly minimizing heat diffusion to the substrate and increasing the sensitivity and response time. For the flow sensing, they used both anemometric and calorimetric configurations, and the sensor consisted of three thin Pt

strips directly connected to copper tracks of the SU-8 substrate, using the central heater for anemometric measurements.

Kaanta et al. [74] presented a flow sensor that does not require calibration in order to in situ measure the flow rate in a micro-gas chromatography system where the solute elutes. By using multiple detector elements that were heated at constant temperature mode and measured simultaneously, they achieved extremely fast responses that allowed for direct measurement of sample peaks. The flow sensor is made using silicon and glass substrates and Cr/Ni suspended filament as the heater element.

Bailey et al. [75] realized a nano-scale thermal anemometry probe to measure velocity fluctuations at ultra-small scales, using platinum nano-wire suspended between two current contacts. The sensor consists of Ti/Pt nano-wire on silicon substrate. The measurements in a turbulent flow showed a similar behaviour to conventional hot-wires, but with enhanced resolution and response time.

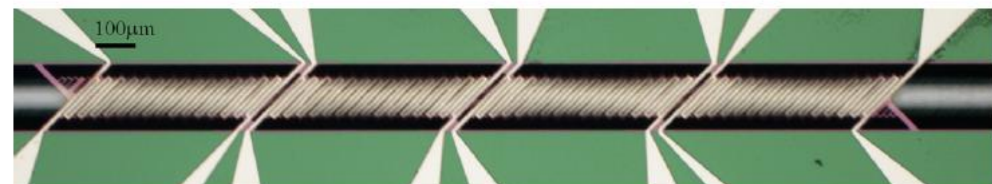

Figure 2.18. Highly sensitive anemometric flow sensor with multiple active regions, by Kaanta et al.

Ito et al. [76] employed a Ti/Pt suspended metal film with vertically aligned carbon nano-tube fins and using silicon as substrate, in order to improve the operation of the anemometer. The use of carbon nanotubes enhances the heat transfer to the fluid, apart from the heat enhancement that the suspended film provides reducing the heat loss to the substrate. By means of a theoretical model they concluded that using CNT higher sensitivities, lower power consumption and further miniaturization are possible.

Li et al. [77] assembled three microsensors, a temperature sensor, a Ti/Au hot-film anemometric flow sensor and glucose biosensor, on a flexible Kapton film using standard microfabrication. This film was spirally rolled into different diameters and easily assembled at the tip of commercial catheters, resulting in a lab-chip with microsensors on tube wall, Figure 2.19. The use of Kapton contributes for good flexibility, mechanical robustness, biocompatibility and low cost material. Moreover it possesses low thermal conductivity, reducing thermal losses caused by conduction and lowering the power consumption to avoid fluid heating over the sensor. The constant temperature anemometer was able to measure flow rates between 2-10 ml/min.

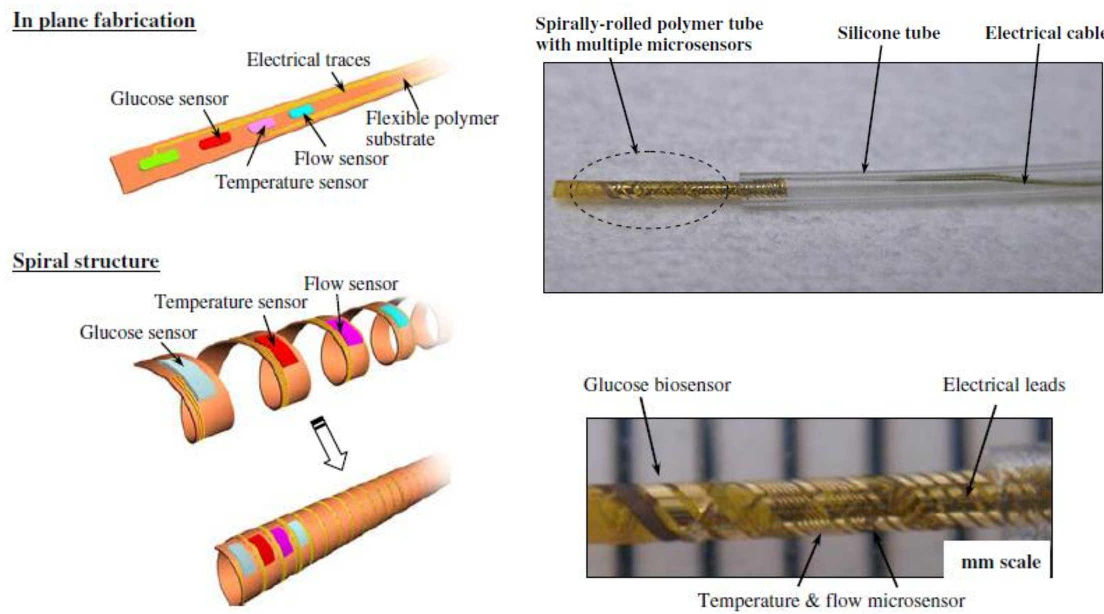

Figure 2.19. A flexible Kapton spiral assembled in a commercial catheter tube, integrating a temperature sensor, a hot-film anemometric flow sensor and a glucose biosensor, by Li.

Yu et al. [78] proposed another biocompatible and flexible anemometric flow sensor for in vivo intravascular shear stress measurements in rabbits. Ti/Pt was used for the sensing elements deposited on silicon wafers, and parylene was employed to provide insulation to the electrode leads and give more flexibility the device, allowing to better adapt to the arterial system.

Dominguez et al. [79] described a wind sensor for Mars atmosphere, employing the constant temperature anemometer principle composed of four hot points together with a reference sensor. The sensor was implemented to measure wind speeds in 0-80 m/s range. The atmosphere in Mars is very thin and heat convention is quantitatively smaller than in earth, and in relative terms the heat conductive losses from the silicon chip would be significant. Consequently, in order to improve the thermal isolation between the active sensor chip and passive supporting structure, a pedestal structure of Pyrex was used due to its low thermal conductance, rendering a silicon chip supported by high aspect ratio and small cross section Pyrex legs, Figure 2.20.

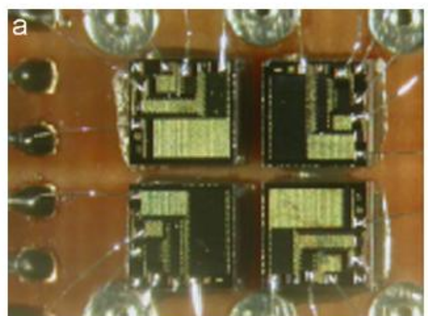

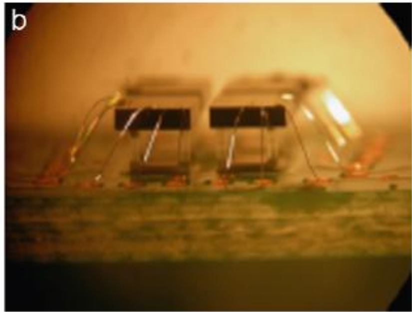

Figure 2.20. Wind anemometric flow sensor for Mars atmosphere, by Dominguez, integrating four hot points suspended on top of Pyrex supporting legs to diminish heat losses.

Liu et al. [80] presented an anemometric flow sensor using a flexible polyimide substrate to print the electronic circuits, in comparison against the former polyimide-based flow sensors that presented complex and fragile structures that did not include electric circuit on a chip [58, 77, 81]. The sensing elements were made by thin-film sputtering of Cr/Ni/Pt on top of the polyimide, rendering a simple structure, low-cost and flexible sensor that features good mechanical characteristics and sensing capabilities and which can be easily attach on object surfaces, Figure 2.21. Furthermore, the polyimide possesses a low thermal conductivity, almost two orders of magnitude lower than that of silicon, that allows decreasing the heat losses, and it is a standard material for flexible printed circuit boards. In the sensing elements, Ni was used to

increase the temperature coefficient of resistance (TCR) of it, and thus the sensitivity of the measurements. They characterized the sensor in constant voltage (CV), constant current (CC) and constant temperature (CT) operating modes, concluding that for the CT mode the frequency response is faster and the sensitivity higher comparing to the other two modes. This way, they achieved air flow rate measurements up to 15 m/s, with 0.1 m/s resolution.

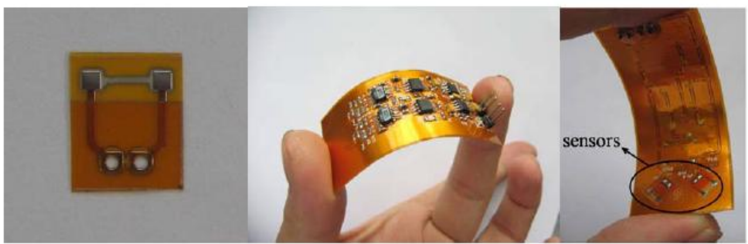

Figure 2.21. Anemometric flow sensor printed in a flexible polyimide PCB with sensing elements made of Cr/Ni/Pt, by Liu.

Adamec et al. [82] also proposed an anemometric flow sensor to detect wind direction with self heating of the sensing elements, employing four Ni elements arranged in a differential bridge configuration on top of silicon substrate and using silicon nitride as isolation layer between the Ni tracks and the substrate. The power consumption caused by heat loss in the simultaneously heated elements was used to measure the velocity, and the temperature distribution among opposing element pairs was employed to determine the direction of the airflow. This way, they measured airflow angles within 2% error for airflow velocities up to 20 m/s.

Ahrens et al. [83] presented a micro flow sensor for dynamical flow measurements (oil) in hydraulic systems under high pressures. The flow sensor consists of a microchannel made of two polysulfone shells with a thin polyimide membrane in between that supports three gold track structures forming an electrical heater or anemometer and two temperature sensors to detect the direction of the flow. The whole device is assembled by epoxy-based adhesive bonding technology. Although the whole device is immersed into the pressurized system, a splitting system was used to direct only a small bypass flow through the channel, remaining a laminar flow inside the device microchannel in

order to avoid any change in oil viscosity. The small heat capacity of the sensor elements results in a fast response time, allowing dynamical flow measurements at frequencies up to about 1200 Hz, and thus offering the possibility for condition monitoring of hydraulic systems. This sensitivity would aloud interesting applications in the field of preventive maintenance, for example.

The main points for anemometric flow sensors are that *(1)* employing multiple wires the direction of the flow can be detected, *(2)* the wire/film must be thin in order to minimize the heat capacity and make the sensor fast, *(3)* in case of the wires in the inner face of the channels, the thermal conductivity of the supporting structure must be as small as possible to enhance the sensitivity of the sensor, and *(4)* the higher the resistivity of the wire/film, higher is also the sensitivity of the sensor.

2.2.1.2.Calorimetric flow sensors

The calorimetric flow sensors usually consist of central heater with two temperature sensors placed symmetrically upstream and downstream around the heater. The measuring principle is based on the asymmetric temperature profile around the heater, caused by the flowing fluid, being the output signal the temperature difference measured at upstream and downstream sensors. Since during the measurements the downstream sensor is heated and the upstream sensor cooled, the calorimetric method allows detecting the direction of the flow rate.

They are basically mass flow sensors, since the amount of heat to be detected is carried away by convection to the fluid and is proportional to the mass flow, and dependent of the specific heat of the carrying fluid.

The output of calorimetric flow sensors are characterized by a linear dependency on the flow rate at low flow rates, afterwhich there is a peak in the voltage followed by an exponential decline. An example of such output can be seen in Figure 2.22, obtained by

Lammerink et al. [84] by the electrical resistance of a chromium-gold thin film deposited on top of a silicon nitride carrier.

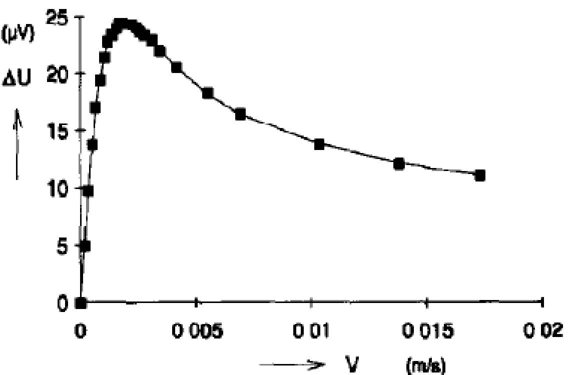

Figure 2.22. Output of a calorimetric flow sensor, by Lammerink.

This output was obtained as follows, considering the heat distribution around the heater as shown in Figure 2.23.

By applying a constant voltage (CV) to the heater element, the surrounding liquid is heated. Then, temperature distribution around the heater is proportional to the fluid flow, and is measured by means of resistance change at the temperature sensors. The electric resistivity of most materials depends strongly on the temperature. Therefore, as the temperature of the sensor increases, so does the resistance, and vice versa. The magnitude of the output voltage measured is related to the difference in the values of resistance upstream and downstream.

When no flow exists, the temperature profile is symmetrically distributed around the heater, as is the case of the line *a*. In this situation, there is no difference in the resistance of the sensors as they are both at the same temperature, and therefore there is no difference in the voltage across the Wheatstone Bridge.

However, under flow conditions, the heat is transported away from the heater and there is a change in the heat distribution around it. The cooling rate of the heater depends on

the velocity of flow at the sensor location, which is linear to the liquid flow while working in laminar flow regime.

As the symmetry of the heat distribution is broken, the two sensors will measure a difference in temperature, which can be used to determine the direction and velocity of the flow. As shown in line *b* and *c*, the temperature of the heater decreases as the flow rate increases, and the difference in temperature at the two sensors changes according to the flow rate.

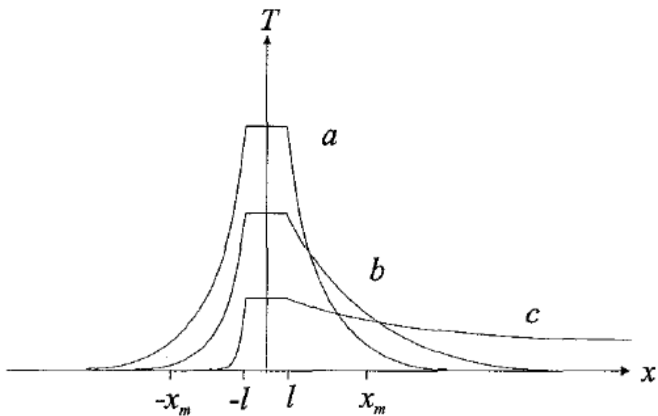

Figure 2.23. Heat distribution in a calorimetric flow sensor at constant voltage.

When the heater is maintained at constant temperature (CT) for a calorimetric flow sensor, the heat distribution is as shown in Figure 2.24. Due to the fact that the temperature of the heater remains constant over all flow rates, the temperature measured by the downstream sensor is much increased at high flow rates compared to that in line *c* in Figure 2.23. The heat distribution at the upstream sensor remains similar, and after a certain flow rate the sensor is no longer able to sense any heat coming from the heater. Looking at this, the difference in resistance between the two sensors should increase with flow over a larger range and then level off, resulting in a voltage output of similar description.

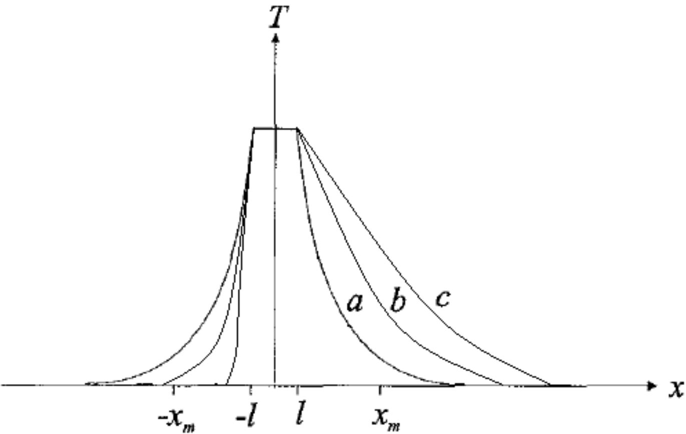

Figure 2.24. Heat distribution in a calorimetric flow sensor at constant temperature.

Shin et al. [85] presented a study of the performance of a calorimetric flow sensor integrated with a silicon microreactor for gas flow measurements. The sensor was made of a silicon microchannel that was annodically bonded to a pyrex substrate that carried the aluminium sensor elements. They found that the sensitivity of the sensor depends strongly on the sensors design factors. For example, the sensitivity is increased when using sensor elements with higher resistivity, shorter distances between the heater and the sensing elements, and higher input power to the heating, being the first condition the one that influences the most. Although no insulating layer was used to decrease the heat conduction through the pyrex, good sensitivity of the sensor was achieved in the range of 0-20 sccm.

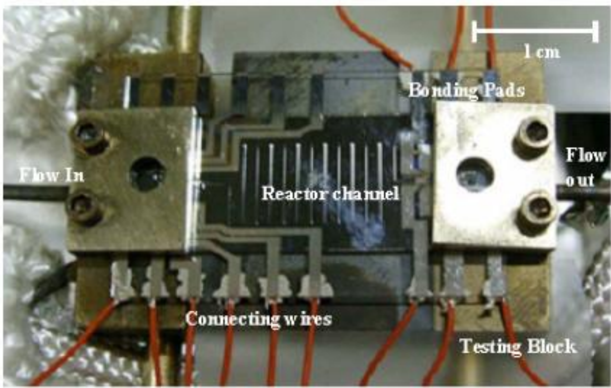

Figure 2.25. Calorimetric micro flow sensor on the testing block, by Shin.

Dijkstra et al. [86] realized a calorimetric water flow sensor based on freely suspended silicon-rich silicon-nitride semicircular microchannels made below the substrate surface, allowing the planar integration of the Pt sensor structures on the substrate. Thus, the sensing elements are in close proximity to the fluid, but not in contact, Figure 2.26. They observed linear sensor response for water flow rates up to 300 nl/min with sensitivities in the order of 0.2 µV/(nl/min).

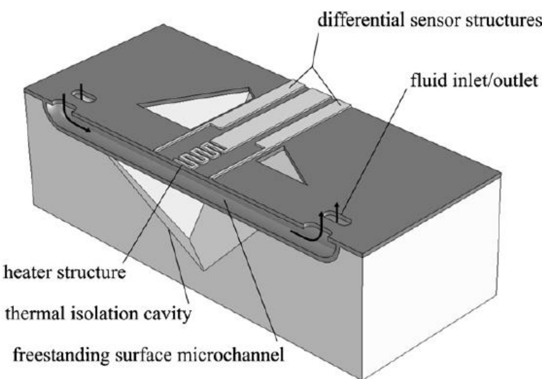

Figure 2.26. Cross-section of calorimetric flow sensor design by Dijkstra.

Tanaka et al. [87] also introduced a calorimetric flow sensor placing the sensors elements on the covering membrane outside the fluid microchannel, Figure 2.27. The sensor is highly resistant to corrosive liquids because only a glass substrate is in direct contact with the liquid, and the Pt sensing areas are arranged in non-wetted areas. For the calorimetric operating mode, they contributed in compensating for the diffusing heat that does not contribute to measurement and causes saturation of the calorimetric measurement as the flow rate increases. For that, the difference of temperatures was normalized by dividing the difference by the sum of temperatures measured by two sensors. The results for flowing water showed linear measurements between 10-500 µl/min, but with a considerable drift on the signal during the time.

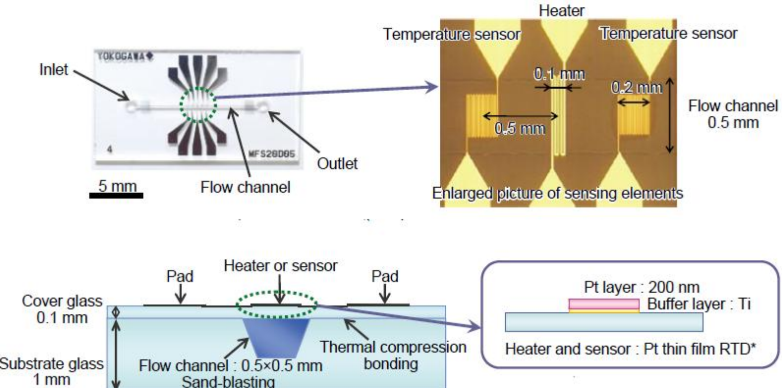

Figure 2.27. A calorimetric flow sensor for microreactor by Tanaka. The sensor consists of a finalized glass device with a microchannel and Pt sensing elements placed in the outer side of the cover glass.

Palmer et al. [88] also developed a non-wetted flow sensor configuration, placing the Ti/Pt sensor elements outside the channel, using silicon as bulk material in order to realize an easily integratable sensor into silicon-based microsystems, Figure 2.28. The sensors can be used with corrosive gases, and was tested using nitrogen flow rates and calorimetric principle, achieving a maximum flow signal and sensitivity of 0.95 mV and 29 µV/sccm respectively, with a power consumption of less than 40 mW. They also analyzed the configuration of the heater and sensors along the channel to obtain different sensitivities and extend operation ranges.

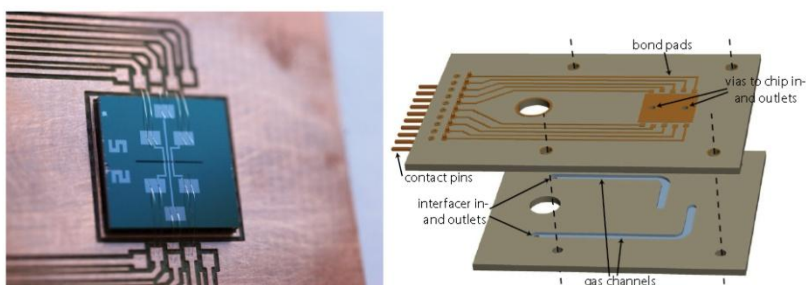

Figure 2.28. A highly integratable silicon flow sensor device glued and wire bonded to the PCB interface, by Palmer.

Vilares et al. [89] integrated a calorimetric flow sensor in a completely polymeric based microfluidic chip consisting of a PMMA substrate, microchannels and inlet/outlet connections made of SU-8, and the Pt sensing elements placed in the inner wall of the SU-8 covering, protected by a SU-8 5 layer to avoid direct contact with flowing liquid. Due to the need to control small volumes of fluid, they chose calorimetric configuration because the excellent sensitivity for small fluids. Using low actuation temperatures (40-60ºC) the sensor was tested in CV and CT modes. For the CV, flow rates ranging between 40 nl/min-2 µl/min were measured in both directions, while for the CT the sensor measured from 0 µl/min to 25 µl/min.

Regarding to sensor configurations, different arrangements exist as for the anemometric sensors. *(1)* Elements placed in the inner face/wall of the microchannel, *(2)* on the outer face of the channel, and *(3)* as a free-standing bridge in the middle of the flowing channel. The first two have the advantage of robustness and easier fabrication, but the disadvantage of slower response times and lower sensitivities, due to thermal loses through the substrate.

2.2.1.3.Time-of-flight flow sensors

In time of flight sensors a short thermal pulse is fed to the fluid surrounding the heater, and a temperature sensor located downstream detects its delay. By measuring the time between the pulse and the response of the sensing element, the flow rate can be determined. At least one heater and one downstream thermal sensor are required, where ideally the heater is thermally isolated from the substrate to eliminate interference from thermal conduction effects.

Rodrigues et al. [90] proposed a design for a TOF flow sensor made of silicon, silicon nitride for insulation, a PECVD oxide layer as sacrificial layer, aluminium and polysilicon with six free-standing microfilaments. The free standing elements allow improvements as fast response and low power consumption, due to size reduction and thermal isolation from the bulk. The dynamic simulations showed good response times.

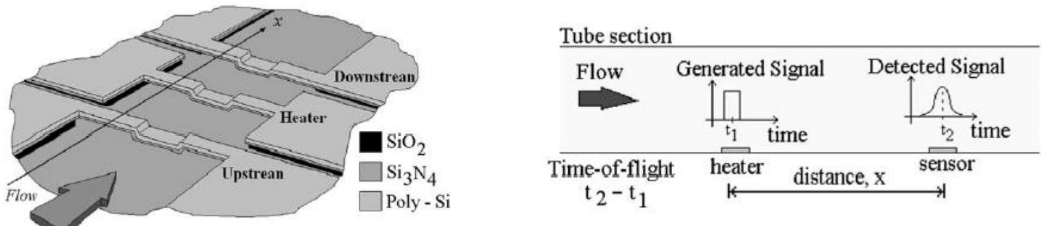

Figure 2.29. Flow measurement by time of flight principle.

Tanaka et al. [87] used TOF operating principle together with the calorimetric, placing a second temperature sensor downstream, in order to further extend the measurable flow rate. The heater was driven by a pulse wave pattern, giving a small amount of heat to the fluid past the heater at that instant, and the flow rate is determined by the time difference needed to detect the heat pulse in the two downstream sensors. By integrating TOF principle they were able to cover higher flow rate ranges, satisfying the necessities of large-scale petrochemical plants (0.1-10 ml/min for water).

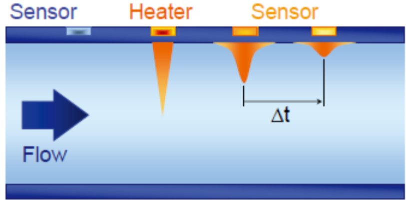

Figure 2.30. Illustration of TOF principle, by Tanaka.

Palmer et al. also combined calorimetric and TOF principles, achieving about two times wider detectable flow ranges compared with calorimetric mode [88]. However, for high sensitivity and large operational range the pulses should be as short as possible but their energy being high. The response time for this method is very low, in the millisecond range.

Berthet et al. [91] introduced a glass/silicon/glass microsensor with suspended MEMS heater and detector bridges across the microchannel. The sensor implements a stochastic time-of-flight measurement, allowing accurate signal detection with high signal-to-noise ratio for small variations (pulses) in the heater temperature. They achieved a linear response and eliminated dependence on fluid properties by operating the sensor in a regime in which longitudinal diffusion effects are negligible, and performing the measurements using several sequential detector bridges.

The evolution of the materials used for the development of micro flow sensor shows the same direction as for the microvalves. The technology started using MEMS silicon micromachining technologies that enabled the fabrication of small components, and it is gradually evolving to simpler materials such as polymers, that offer possibility for simple, cheaper and easily fabricating devices.

2.2.2. Bypass structures integrated in flow sensors. High flow rate sensing

Most of the thermal flow sensors can only measure small flow rates accurately. Thus, bypass constructions are usually employed to measure larger flows [83, 92, 93], where the flow is divided into two parts between the sensing tube where the flow is measured and a bypass channel where the majority of the flow passes. The bypass is normally designed in a way that the flow through the sensor and the bypass is always proportional. This way, the sensor can deliver an output voltage signal that is proportional to the total circulating flow rate.

The bypass principle is based on the laminar flow theory. This way, the flow in the sensing tube is proportional to the flow in the bypass channel, and this is achieved only if the tubes are small enough. Otherwise, the relation is non-linear, achieving often quadratic flow characteristics.

It is important to note that, as the flow measured in the sensing channel is used to determine the total flowing through the device, any deposition in the sensing or bypass

channels changes the diameters of the tubes, thereby also changing the accuracy of the measurements. This is why sensors incorporating a bypass structure often use clean and filtered fluids to avoid clogging in both tubes.

2.3. LIQUID HANDLING SYSTEM. MFCS (Mass Flow Control System)

Mass flow controllers are closed-loop devices that set, measure and control the particular flow of a gas or a liquid. This is essential in many industrial processes, chemical reactions, automotive, etc, but also in drug delivery systems, in vitro diagnostic devices or micro Total Analysis Systems.

Every flow controlling system is composed of two elements: the flow meter component and the regulating valve with its electronics for closed-loop control to drive the control valve and regulate the flow in order to generate the desired one fixed in the set point.

There is a wealth of miniaturized MFCS devices in the literature [94-96], and the trend leads towards modular systems that can be easily constructed by assembling different parts. However, microfluidic flow control seems to remain difficult to integrate on a monolithic disposable chip at low cost.

For example, Kohl et al. [97] realized a microfluidic controller for nitrogen measurements, consisting of a microvalve and a flow sensor, proposing two different designs. One is a modular system, allowing flexibility to combine different microfluidic components on a microfluidic chip. In the other, the microfluidic components (SMA microvalve and anemometric flow sensor) were fully integrated in a polyimide membrane on top of a silicon wafer in order to minimize the system size and dead volumes. For the housing of the whole device they used adhesive bonding and contact pads of the SMA valve were laser welded to the connection pins to obtain low resistances in the contacts. The microfluidic controller using a PI controller operates up to 300 kPa and gas flows of 600 sccm, achieving a control tolerance of 1% between 25% and 70% of maximum flow.

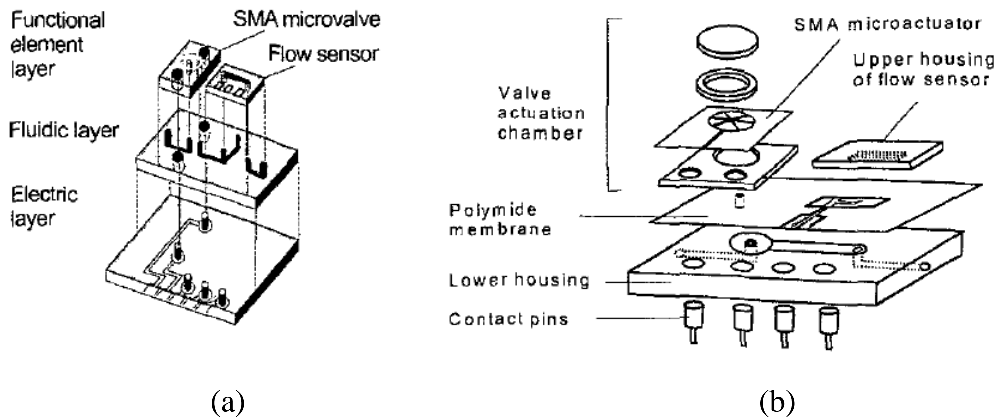

(a) (b)

Figure 2.31. Microfluidic controller by Kohl. (a) Schematic layout of a microfluific controller with a modular design; (b) and with an integrated design.

2.4. EVOLUTION OF USED MATERIALS

Since the beginning of the Lab-on-a-Chip devices, in the early nineties [3], the predominant substrate materials have been glass and silicon [98]. The main reason was that the manufacturing of these materials had been previously developed by the semiconductor industry while the surface properties were characterized and developed by the chromatography industry.

There are several properties that make glass very attractive as a substrate in microfluidic devices. Among others, good electroosmotic and optical properties, chemical stability and very high level of biocompatibility. In contrast, its fabrication increases the production cost and complicates the manufacturing [98].

Silicon has also been a popular choice, largely due to the high level of development of micromachining techniques in the microelectronics industry. However, the high cost is an important drawback for industrial production, which has led to the search for alternative materials [98].

An adequate substrate material should meet several requirements, such as availability in pure form at low cost, chemical, optical, thermal and electrical requirements for the desired application, as well as to be easily processable. Polymers are a close match to these criteria and thus, their use has increased against silicon and glass. Furthermore, the wide range of polymers available caters for the specificities of each application [99].

Most commonly polymeric materials used to fabricate these microfluidic devices are polymethylmethacrylate (PMMA), polycarbonate (PC), polydimethylsiloxane (PDMS), polyester (PET), polystyrene (PS) and SU-8 photosensitive polymer [100]. Among all, SU-8 can be easily structured by standard lithography, obtaining well defined structures ranging from nanometers to hundreds of micrometers .Unfortunately, SU-8 has the disadvantages of high optical propagation losses in the ultraviolet region, and a high permeability to water [101, 102]. PDMS is probably the most popular polymer used in soft lithography, due to its easy fabrication and bonding processes. It provides increased permeability to O_2 and CO_2 than any other polymer (which facilitates the cell culturing in the chip) and is optically transparent from the UV to the near IR region, which is important for optical detection methods. However, the microchannels can be deformed during use (excessive flexibility of the material), it swells on contact with organic solvents, it is hydrophobic, and surface treatments are often unstable over the time [103, 104]. Rigid polymers such as PMMA and PC can be employed to manufacture less deformable structures. However, their application is limited in some applications of LOC due to low stability against organic solvents [105].

2.4.1. Material selection

As described in the previous section, the popularity of thermoplastics has grown significantly over the last years due to the lower material and manufacturing costs [106]. The emerging cyclic olefins, like COP or COC, have become attractive [105, 106] because of their high optical quality, in the visible and near UV region [107], high bio-compatibility [108, 109], low autofluorescence, low water absorption [110-113] and

high chemical resistances, including organic solvents [106, 110, 111]. Moreover, cyclic olefins are easy to manufacture and they allow surface treatments that remain stable over time [114-116].

Other materials, such as elastomers have also been encouraging for a number of reasons such as low cost and simple fabrication processes. However, the hydrophobicity and porosity of the surfaces make these devices incompatible with many chemical and biochemical fluids unless surface modification treatments are employed [117, 118]. Swelling of elastomer devices in most organic solvents is also a serious drawback. Moreover, PDMS soft lithography is well adapted for small laboratory scale production for prototypes, but is not still feasible for industrial mass-scale production. All of these make thermoplastics superior to elastomers for low cost LOC applications.

2.5. FABRICATION

In the following sections, the most common techniques for manufacturing plastic devices reported in the literature have been detailed.

2.5.1. General manufacturing methods for thermoplastics

In recent years, special attention has been paid to the manufacturing of COP/COC devices by means of patterning techniques such as injection moulding, hot embossing (HE) and nanoimprint lithography (NIL) [119, 120]. Whilst HE and NIL are suited for the production of small amounts of complex structures, injection moulding is used for large scale polymer manufacturing, as in that scenario it is fast and a low cost technique [121].

Another frequently used technique is the hot embossing, where most commonly the wafer or sheet format of the material is used [122-124]. The technique consists in pressing a structured master mould against the thermoplastic wafer, which is previously

heated above its glass transition temperature. The optimum process parameters depend on the mould material, the design and dimension of the structures to be replicated and the grade of the thermoplastic employed. However, pressure, time and temperature are the most important factors that influence in the final quality of the patterned structures, and variations of these parameters during the process have been thoroughly studied in terms of properties of the resulting device part [125]. In general, pressure and temperature used in hot embossing processes are lower compared to these employed in injection moulding.

The most traditional master moulds used in HE have been metallic, fabricated by either CNC-machining or LIGA-type methods [126], whose fabrication involve polishing steps that are expensive and time consuming. Other materials, such as SU-8, have also been used, but the limited number of replications has supposed serious disadvantage. To overcome the mould breaking problem, anti-sticking coats, like an aluminium layer on top of a SU-8 mould, have been employed to facilitate the de-moulding [108]. In hot embossing, the distance that the COP flows through the mould is substantially lower than in the injection moulding, resulting in stress reduction and shrinking effects [127].

Another replication technique, gravity moulding, was described by Mosaddeagh and Angstadt (6013 grade), where gravity is used to make a molten substrate (241 ºC) flow into the mould, avoiding costly pressing equipment [128]. In this case, interfacial effects and the viscosity played a role for the proper mould filling and obtaining a good replication of the microstructures. The replicas obtained with this method showed better results for PS and PMMA than that for COP, because the later tended to stick to the silicon oxide mould employed.

Finally, two other commonly used techniques for direct structuring are laser ablation and micromilling, which have been understood to be appropriate techniques for COP/COCs due to the hardness and chemical resistance of the material. In laser ablation, the interaction of a laser beam of high intensity with the material causes it to evaporate in the laser focal point [129]. This technique has been reported to be successful for PMMA, but not for COP/COC, where only some results have been

presented using “ArF-excimer” laser (k = 193 nm) and the ablation depth of COP was observed to be 3.4 times lower than that of PMMA [130]. However, this lower ablation depth can be used to further control the depth of the structures of the devices. They observed that for structures not deeper than 200 µm, no residue was deposited on top of structured surface, but for deeper structures, some material (~ 100 nm) was deposited and ultrasonic treatment in isopropanol was observed to be ineffective to eliminate these residues. Bundgaard et al. employed CO_2 laser, and concluded that well-defined structures were not possible to produce in COP, which suffers from limitations [131].

One disadvantage of the ablation technique is that it can cause changes in the chemical properties of the polymer surface compared with the chemical properties of the polymer bulk [132]. This can be difficult to control, and product performance may be affected in an unpredictable way in applications where the surface plays an important role, for example, electrokinetic separations.

On the other hand, micromilling involves modelling a substrate moving it against a rotating tool (for example, a drill). The dimensions of the tool employed affect directly both the resolution as well as the wall roughness.

Table 2.2 summarizes the manufacturing techniques for COC/COPs in terms of performance, adequacy for fast prototyping and minimum feature size.

Table 2.2. Summary of different manufacturing methods for COP where +++ means excellent, ++ means good, + means acceptable and – means inappropriate

Process	Throughput	Fast prototyping	Feature size
Injection moulding	+++	-	++
Hot embossing	+	+	++
Nanoimprint	+	+	+++
Laser ablation	++	+++	+
Micromilling	-	+++	+

2.5.2. Bonding techniques

Manufacturing of LOC systems involves a covering step of the microfluidic cavities with a membrane or another microfluidic part in order to finalize the chips without clogging the channels, collapsing the cavities, changing their physical parameters or altering their dimensions. Depending on the requirements of the microfluidic system, there are several aspects to consider when selecting an appropriate bonding technique, such as surface chemistry, material compatibility, bonding strength, etc.

Bonding techniques can be categorized as indirect or direct. Indirect bonding involves an adhesive and the bonding forces between the surfaces are charge interactions. Direct bonding comprises thermal bonding, solvent bonding, localized welding and surface treatment and modification bonding and the binding is due to molecular entanglement [106].

Adhesive bonding is one of the most common techniques, where a layer of adhesive is used to attach the two pieces of polymer [133]. For instance, an adhesive cured by UV light was used at room temperature to join three COP parts of a LOC system [134]. However, this implies a risk that the adhesive layer may flow into the cavities, leading to clogging of the channels.

Since Cyclic Olefins are thermoplastics, they have been most frequently joined by thermal bonding [107-109, 120, 135]. For this, the best choice is to use parts of COPs with slightly different glass transition temperatures, and so only one layer softens, preventing the deformation of the other part's microstructures [120, 136]. Yang et al. carried out thermal bonding of Zeonor substrates by heating them to the glass transition temperature of the polymer, and exerting pressure of 0.5 N for 5 minutes [124, 137]. Then, the applied force was removed and the substrates were annealed at T_g + 10 °C for 10 min. With this step the bond strength was observed to be increased, so that the

fluidic channel could support a flow rate of 10 µl/min [124]. However, the thermal joints typically provide relatively low bond strengths due to the low surface energy of thermoplastics. Hence, several tests have been performed to improve the bonding strength. For instance, it has been observed that the activation by oxygen plasma is more effective to improve the bonding strength of COP substrates compared to nitrogen or oxygen-nitrogen plasma treatment [138].

UV/ozone surface treatments can also increase the bond strength under certain conditions [139]. Improvement of the polymeric chains diffusion due to the surface treatments is because of a closer contact between the contact surfaces. When parameters such as temperature and pressure are not optimized in thermal bonding techniques, deformation of the channels can occur. Some experiments have shown that temperature is the most important parameter. Thus, whilst too high temperatures lead to deformation of the channel, including bending of the device, too low temperatures are not sufficient to establish the bonding [125].

Another more suitable technique to achieve high bond strengths, required by some COP microfluidic devices, is the union with solvents [123, 140-144], where the solubility of the polymer allows better entanglement of the polymer chains as they become more mobile through the bonding interface.

Specific advantages of solvent bonding are homogeneous distribution of mechanical loads, good aesthetics, economic assembly, good sealing and insulating properties. On the other hand, the potential limitations are the entrapment of solvent in the joints, stress cracking or crazing, possibility of joining dissimilar materials only if both are soluble in a common solvent or in a mixture of solvents, the differences in thermal expansion of components that are not compensated in dissimilar material bonding, reproducibility/process control and high solvent evaporation time due to its entrapment in the polymer matrix.

Summarizing, to achieve high adhesion resistance the solvent must meet the following requirements: a) it must be a good solvent; b) it should not degrade the plastic; and c) it must not evaporate too quickly.

2.5.3. Metallization. Metal thin film processes

The most common thin film processing techniques are evaporation methods or the sputtering process. The thin film process can be physical or chemical in nature.

In chemical vapour deposition (CVD), a reaction of gaseous components at a surface leads to the deposition of a solid film. Depending on the conditions, the methods can be classified into low pressure chemical vapour deposition (LPCVD), plasma enhanced chemical vapour deposition (PECVD) and atmospheric pressure chemical vapour deposition (APCVD). In CVD there are often dangerous or volatile byproducts created during this process, so labs must be equipped to dispose of the resultant chemicals. Heating the substrate may enhance the growth of the thin film during chemical vapour deposition. The materials which are most commonly deposited by CVD are silicon oxide, silicon nitride, silicon carbide and crystalline silicon.

Physical vapour deposition (PVD) is the process of depositing atoms on a target surface by evaporating or sputtering. This technique is mainly used for metals, but can also be used to deposit insulators like silicon dioxide and silicon nitride as well as piezoelectric materials like zinc oxide [145].

In PVD evaporation the target material is heated until it evaporates or sublimates. Once the substance is a gas, it is released into a chamber that contains the substrate on which the thin film will form. The substance hits the substrate and forms a thin film. There are a number of different machines that can be used to evaporate target materials. These machines can heat a target material on a heated coil, plate, or in a heated chamber. Substances can also be evaporated if they are hit by a beam of high intensity electrons or photons, such as those emitted by a laser.

In the sputtering process, Figure 2.32.(a), also called sputter deposition or reactive magnetron sputtering, argon plasma is generated between two parallel plates placed in a vacuum chamber within a specialized machine, which form a capacitor. Argon ions are accelerated towards the negative plate, and remove the neutral atoms from the surface of the plate by virtue of their kinetic energy. The sputtered atoms from the source during the initial bombardment move towards the other plate of the capacitor. The sputtering ensures that the thin film is evenly distributed on its surface and guarantees a more conformal deposition than the evaporation. Sputter deposition may be used for the deposition of dielectric, piezoelectric and other layers.

Magnetron sputtering is a type in which, in addition to use a DC or RF source, power is based on the use of a magnetic field transversal to electric field in the target surface, placing a permanent magnet inside the cathode (target containing the metal to be deposited), Figure 2.32.(b), and the plasma is concentrated precisely in this zone with a high magnetic field, Figure 2.32.(c). The application of the transverse magnetic field leads to major changes in the basic process of sputtering. The secondary electrons generated in the target do not bombard the substrate because they are trapped in cycloidal trajectory near the target, thereby decreasing the temperature at which the substrate is heated and thus decreases also damage due to radiation. This allows coating of substrates that cannot withstand high temperatures (such as plastics) or sensitive surfaces. In this type of sputter, deposition rates are also higher than in the traditional sputtering. Nevertheless, due to the shapes of field lines, the plasma does not attack all parts of the cathode surface equally, which reduces the life of the target.

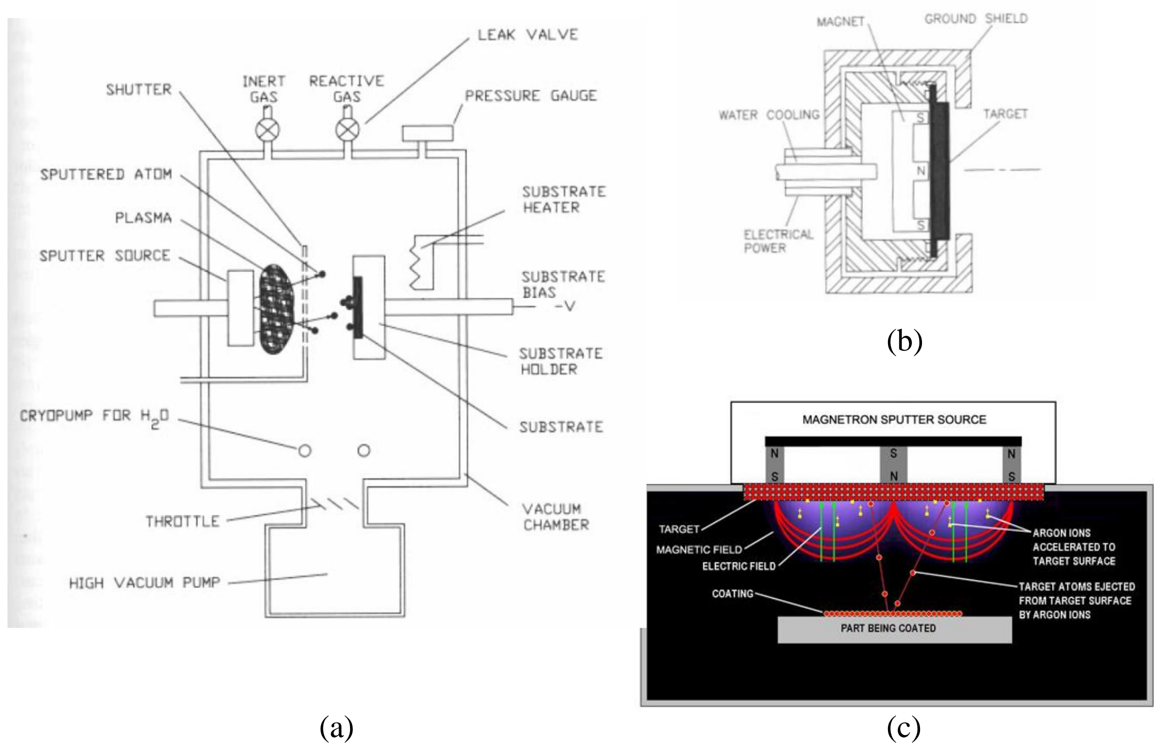

(a) (b) (c)

Figure 2.32. Metal thin film deposition via sputtering, a physical vapour deposition process. (a) General features of a sputter coater; (b) Cross sectional view of a planar magnetron sputter source; (c) Drawing of a magnetron sputtering process.

3. SECTION I – FABRICATION

3.1. INTRODUCTION

The design and manufacturing of each microfluidic component maintains a common focus on the later integration. The goal is to prove a modular approach with characteristics of “design for manufacturing”, whereby all stages of generation of the LOC prototype are harmonized to manufacture with industrial-like quality at low cost. The result is an accelerated transition from prototype to product in a way that is lean, cost-effective and with minimum risk. Thus, a methodology has been developed that can monolithically produce all elements commonly found in LOC devices i.e. channels, chambers, valves and electrodes in the final material with excellent dimensional control, bonding quality and high repetitivity. In this Chapter, the work carried out to generate a harmonized fabrication method will be described. The general method, which is an optimized Hot Embossing procedure followed by bonding and metal deposition, is depicted in Figure 3.1.

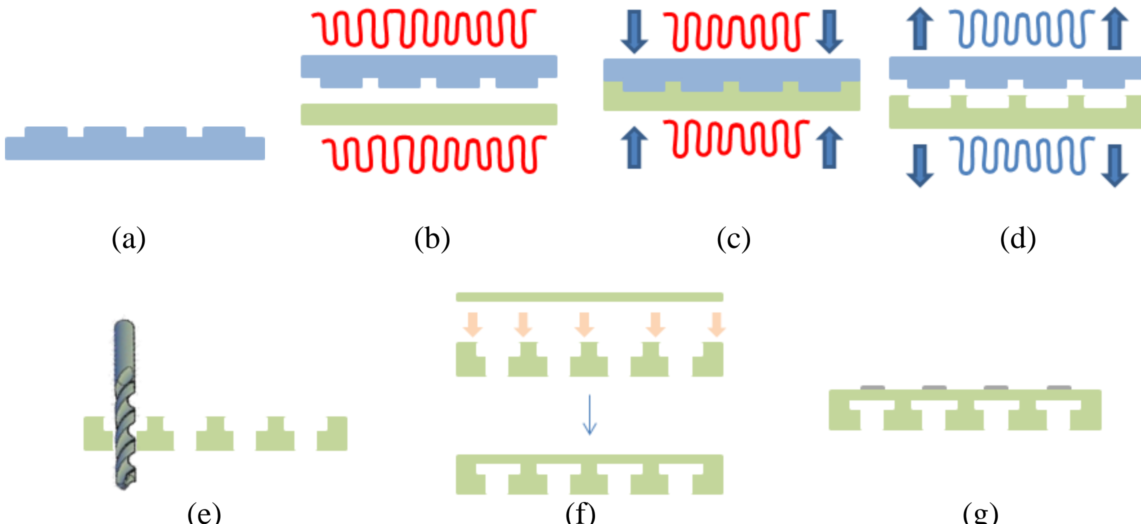

Figure 3.1. General fabrication process. (a) Master mould fabrication; (b) Heat both mould and COP substrate (c) Apply embossing force on the substrate by pressing the mould, under vacuum (d), Cool substrate and mould down to de-embossing temperature (e) Drill fluidic inlet and outlet ports; (f) Seal

structures with a COP membrane (g) Deposit metal on top of the membrane.

As described in Figure 3.1, the LOC patterning method chosen is Hot Embossing (HE) of COP, since it bears similarities with the industrial method of reference (i.e. injection moulding) and it offers the advantages of low cost, relatively simple replication, excellent dimensional control down to nanometre scale [146] and satisfactory aspect ratio (2:1). Furthermore, HE is suited for the production of LOCs from proof-of-concept to short-series (≈100 units- usually initial tests and optimization of LOC protocol) and it is a good choice for production of microfluidic devices in laboratory environments, even with low-cost pressing systems [99, 133, 147-151]. With respect to the material, Cyclic Olefin Polymer (COP) has recently emerged as an attractive material [105, 106] due to its high optical clarity (into deep-UV range) [107], high bio-compatibility [108, 109], low auto-fluorescence, low water absorption [110-113] and good chemical resistance, also against organic solvents [106, 110, 111].

Sealing the microstructures with a cover layer is another key step, which should be performed reproducibly without causing channel clogging, bubble trapping or changes in mechanical, fluidic or optical properties. Current COP bonding methods present these limitations, including low bonding strength, durability and non-homogeneous channel surface properties [144]. Depending on the requirements of the microfluidic system, there are several considerations to take into account when selecting an appropriate bonding technique, amongst others chemistry, material compatibility and bonding strength. In this work, thermal and solvent bonding have been investigated. As it will be shown later, the latter has been chosen because of its simpler, faster, lower cost and stronger bonding characteristics. Moreover, solvent bonding overcomes several specific problems observed when employing thermal bonding, namely clogging, non-uniform wafer contraction and distortion of cover membrane planarity.

With regard to metallization, this has been made on the cover membrane, as shown in Figure 3.1. The main reason is that the membrane is flat, making it possible to deposit metal patterns reproducibly, either by traditional (evaporation, sputter) or industrial

methods (inkjet/screen/contact printing, roll-to-roll). This approach has been previously shown for electrochemical sensors on the inner face of the cover membrane [152, 153]. However, in this work thermal resistors for flow sensing have been placed on the outside of the covering membrane, as a post-production step applied to the finished LOC. This approach reinforces the modularity of the fabrication method, separating the aggressive polymer structuring from value-adding features (sensors, heaters, excitation/detection OLEDS), minimizing manufacturing incompatibilities, alignment problems and development costs. Although this approach spans across many LOC value-enhancing features, it is acknowledged that it is not universal, as it is not applicable to metallic components requiring direct contact with the sample.

3.2. HOT EMBOSSING

Hot Embossing (HE), described in Figure 3.2, commonly consists in the replication of a given pattern onto a thermoplastic substrate at a temperature higher than its glass transition temperature (T_g). The pattern, which is engraved in a master mould, is pressed against the substrate for replication. After the prescribed time, the substrate and the master mould are cooled below T_g, while the pressure is maintained. When the desired de-moulding temperature (T_d) is reached, the mould and the polymer are separated.

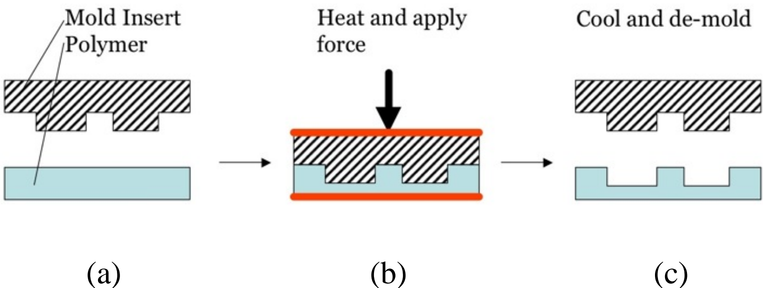

Figure 3.2. Hot embossing process. (a) Mould and substrate heated just above T_g of the thermoplastic; (b) Embossing force applied on the substrate via mould, under vacuum conditions and keeping embossing temperature (c) Cooling down of substrate and mould, followed by de-embossing.

It is well known that thermoplastic substrates are subject to contraction while cooling, before and after the de-moulding step. In order to prevent dimensional distortion, leading to misalignment of parts, variations in LOC internal volumes and underperformance of passive/inertial features (capillary valves, separators, mixers), it is important to i) guarantee a uniform and repetitive contraction across the substrate and ii) quantify this in order to apply corrective measures in the mould. Since COP is an isotropic material, quality will mostly depend on the properties of the master mould material and the HE process parameters. Additional sources of defects appear during de-moulding, where the forces exerted to separate the parts are the main cause [154-157]. Again, quality depends on the master mould material, since these forces are of mechanical (mismatch in Coefficient of Thermal Expansion) and adhesive nature (between contact surfaces). Hence, in the following sections, the mould material investigation process will be presented, showing the results obtained for each material employed.

3.2.1. Master mould fabrication

Master moulds are traditionally metallic and fabricated by costly and time consuming methods, such as CNC-machining or LIGA [126]. These can be interesting for large production of replicas, but this is rarely the case in the proof-of-concept or initial test/optimization stages. Furthermore, it should be noted that changes are often required at this point, which would increase the cost of the LOC optimization process significantly. The investigation presented in this section is aimed to determine the best mould material and processing for high-quality, reproducible HE.

Three materials commonly employed in the literature for NIL and HE have been tested [158-160], namely, PDMS silicone elastomer (Sylgard 184, Dow Corning Corp.), MD700 Fluoropolymer (Fluorolink® PFPE, Solvay Solexis S.p.A.) and SU-8 Epoxy photoresist (MicroChem Corp.). In the next sub-sections the fabrication processes for moulds in these three materials will be explained in detail.

3.2.1.1.SU-8 master mould

The mould fabrication protocol in SU-8 is a modified version of an existing protocol [161]. As shown in Figure 3.3, the manufacturing process consists of a sequence of spin coating, soft baking, UV exposure and post-exposure baking steps on an initially clean, dehydrated and plasma treated 700 µm-thick, 4 inch, Pyrex® wafer. The process finishes with a developing and hard baking step to ensure full polymerization of the mould, preventing possible changes in mould dimensions during HE and defects in the replicas.

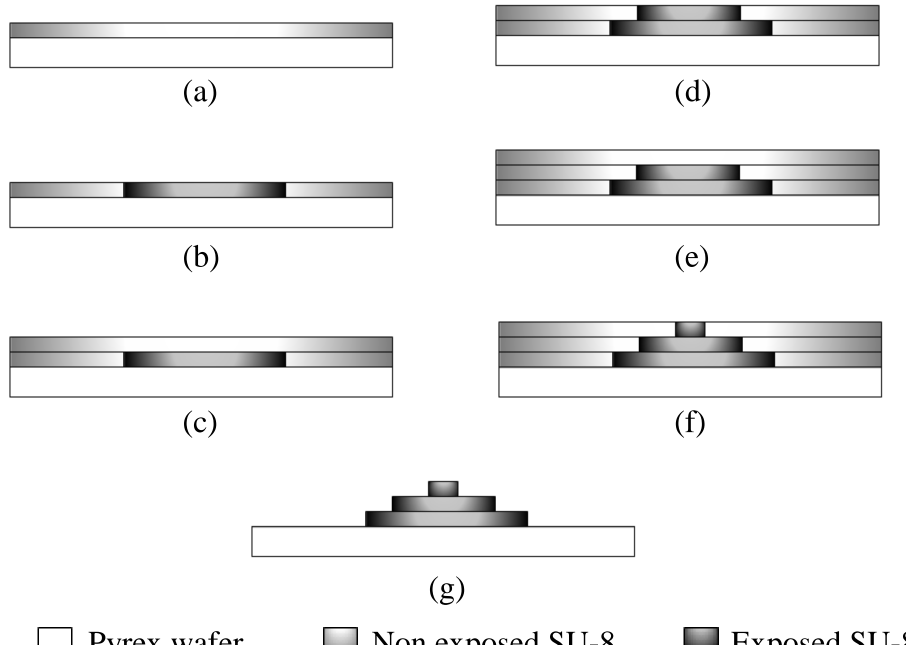

Figure 3.3. Schematic of master mould fabrication process for the microvalve module. Successive spin coating, soft baking (a, c, e), UV exposure and post-exposure baking (b ,d ,f) steps on top of a previously cleaned and dehydrated Pyrex® wafer have been carried out. Finally the entire mould is developed (g) and subsequently hard baked to ensure the full polymerization of the mould.

For any SU-8 layer, the soft bake is performed at 65ºC for 4 min and at 95ºC for 7 min, using a progressive temperature ramp to avoid cracking. Next, the layer is UV exposed

with a dose of 200 mJ·cm^{-2} and post baked at 65ºC for 2 min and at 95ºC for 4 min. Once all the layers have been processed, the wafer is developed in a Propylene Glycol Monomethyl Ether Acetate (PGMEA) bath to obtain the desired mould structure. Finally, the mould is hard-baked in an oven at 170ºC for 16 h. Figure 3.4 shows the finished mould for an array of microvalve devices.

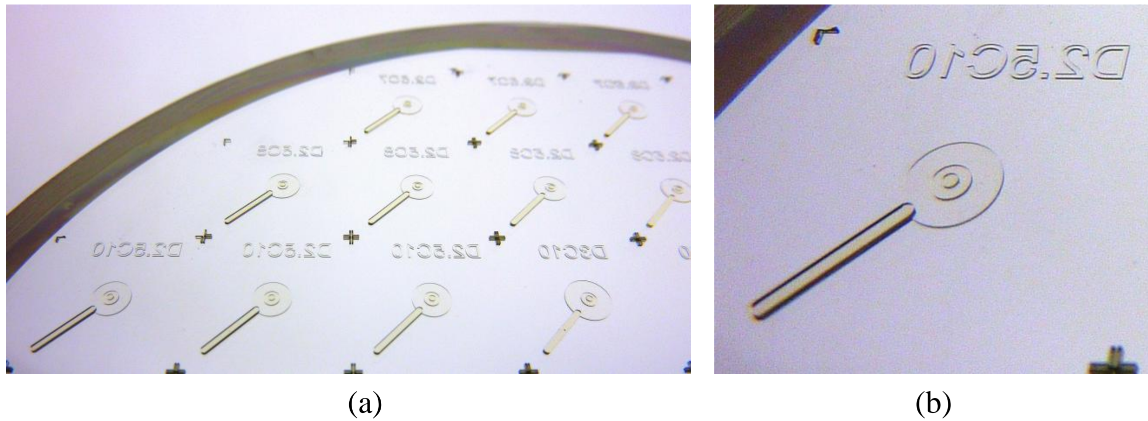

(a) (b)

Figure 3.4. (a) SU-8 master mould with different valve designs for hot embossing. (b) Close-up view of one valve mould structure.

3.2.1.2.PDMS master mould

For the PDMS mould, the curing agent and the polymer base is mixed in a 1:5 proportion and degassed for 30 minutes in a vacuum desiccator to remove air bubbles introduced during mixing. Once degassed, the PDMS mix is poured on to a negative SU-8 mould, which is previously placed inside an aluminium ring and fixed using adhesive tape in order to shape the PDMS mould as a thick cylindrical slab. The assembly is degassed again for 30 minutes in the vacuum desiccators to eliminate the bubbles trapped during pouring. Next, the assembly is placed on a hot plate at 70ºC for 2.5 hours in order to cross-link the PDMS and the resulting mould peeled away. Before HE, the PDMS is fully cross-linked and dehydrated at 180ºC for 6h. Figure 3.5 shows the finished PDMS mould for an array of microvalve devices.

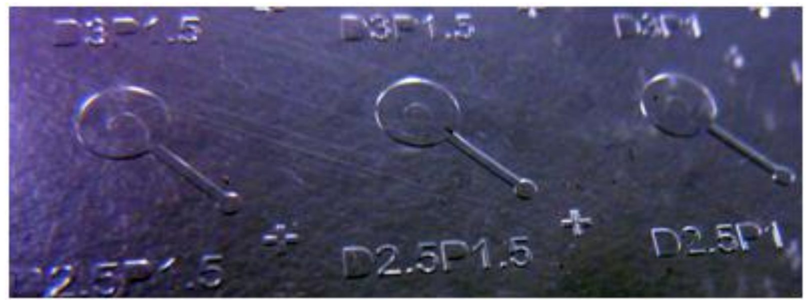

Figure 3.5. PDMS master mould with different valve designs for hot embossing.

3.2.1.3. Fluorinated (meth)acrylate master mould, MD700

For the MD700 mould, the polymer base is mixed with 1% photoinitiator (Darocur 1173, Ciba Specialty Chemicals) and the mixture is degassed for 30 minutes in a vacuum desiccator to remove the bubbles introduced during mixing. Once degassed, mix is poured on to a negative SU-8 mould, which is previously placed inside an aluminium ring and fixed using adhesive tape in order to shape the MD700 mould as a thin cylindrical slab. The assembly is degassed again for 30 minutes in the vacuum desiccator to eliminate the bubbles trapped during pouring. Next, a Pyrex wafer is placed on top of the liquid polymer to which it will bond during curing, providing rigidity to the mould. This wafer is previously dehydrated at 180ºC for 30 min, spin-coated with 3-methacryloxypropyltrimethoxysilane adhesion primer and soft baked at 180ºC for 3 min. Finally, the assembly is cross-linked by exposing it to a UV dose of $1 J/cm^2$ in a N_2 atmosphere and peeled away from the SU-8 mould. Before HE, the mould is degassed at 60ºC and 20 mbar (absolute pressure) for 10h. Figure 3.6 shows the finished MD700 mould for a LOC device consisting of channels, valves and chambers.

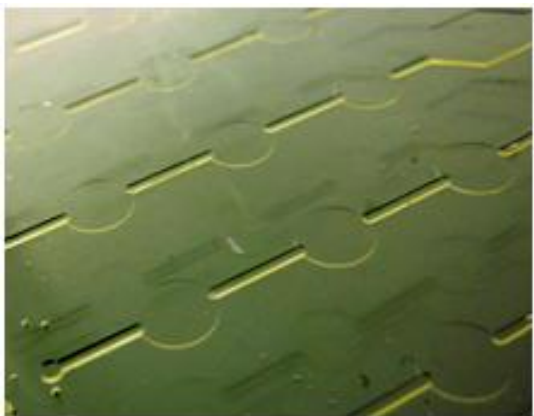

Figure 3.6 MD700 master mould with a LOC structures comprising channels, valves and chambers.

3.2.2. Home-made embossing procedure

The first HE tests are carried out in a low cost home-made system. It allows an even application of temperature and pressure, but the de-embossing process has to be performed manually on a hot plate with the aid of a razor and tweezers. Processing is considerably faster than in a commercial HE machine, shortening the time required to select the best mould material and obtain an initial estimation of the optimum HE parameters.

The process starts by vacuum packing the master mould and the COP substrate together, sandwiched between two 4-inch Pyrex wafers. Vacuum packing avoids generation of bubbles and free-flow of COP during the process. Previously, the COP is degassed for 8 hours at 60ºC and 10 mbar (absolute pressure). As a general rule, embossing should take place at 15ºC to 20ºC above T_g ($T_{g,COP}$= 138ºC) and de-moulding at 10ºC below T_g, but this has to be empirically optimized for each polymer [162]. As a compromise for the initial tests, the mid-range embossing temperature, 155ºC, and a previously reported COP de-moulding temperatures of 120ºC were chosen [163]. With regards to moulding pressure, high values help reduce de-moulding forces, since thermal shrinkage is

reduced [164]. Thus, the maximum pressure available in the system, 6 bar, will be employed.

Once packed, the assembly is heated above the T_g, first to 145ºC, pressure is applied and heating continued up to 155ºC. These parameters are kept constant for 1h, after which the assembly is cooled down to near de-moulding temperature, 125ºC, while maintaining the pressure. When the temperature reaches 125ºC, the system is de-pressurized down to atmospheric, causing a sudden temperature decrease to 120ºC. The assembly is removed fast from the HE system and placed on a hot plate at 120ºC for de-moulding. Fast transfer is required in order to avoid sudden temperature contrasts which can lead to thermal stresses, hindering the release of the master mould from the polymer substrate and/or causing defects in the patterned structures.

Manual de-moulding, consists in the release of the master mould by means of a razor. The components of the applied forces are important for the discussion of results. As shown in Figure 3.7, there is a vertical force (upwards, z axis) and q radial force (from the outer diameter to the centre of the wafers, r direction). Table 3.1 and Figure 3.8 summarize the process parameters for hot embossing in the three master mould materials employed.

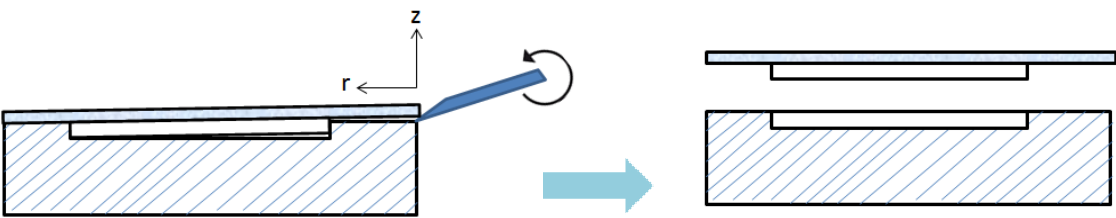

Figure 3.7. Manual de-moulding method carried out on a hot plate, after using the home-made HE system.

Table 3.1. HE parameters used for mould material election in a home-made HE system.

Process step	T (ºC)	P (bar)	Time (h)
Heating	Up to 145	1	-
Pressure apply	145	6	-
Heating	Up to 155	6	-
Embossing	155	6	1
Cooling	up to 125	6	-
Vent	125→120	1	-

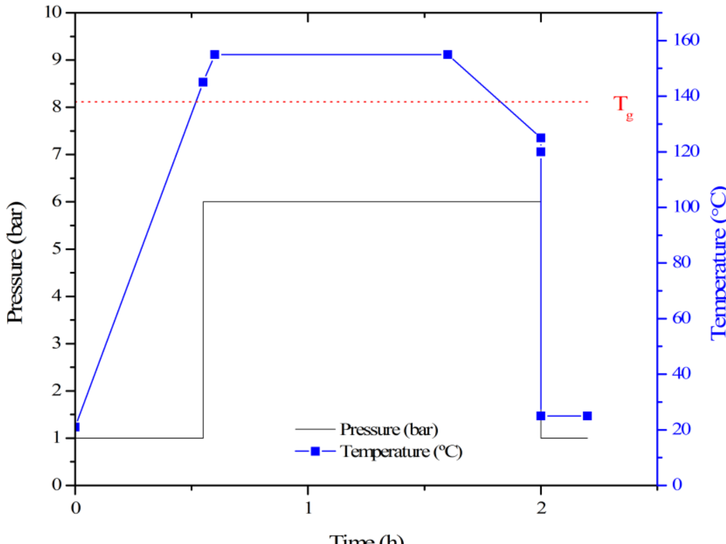

Figure 3.8. Schematic of HE process, used for mould material election in a home-made HE system.

3.2.2.1.Results and discussion of mould material selection

Several master mould characteristics have been evaluated, namely, type of defect, dimensional control and durability. In particular, for the dimensional control analysis the contraction of the replicas is measured using a high-precision automatic dicing machine (Disco DAD321, Japan). The results obtained are shown in Table 3.2. The main conclusion is that the mould should show, above all, high mechanical strength to avoid fracture, chipping-off and deformation.

Table 3.2. Results from HE using a home-made HE system, master moulds made of SU-8, PDMS and MD700.

Material	Defect	Dimensional control			Durability (uses)	Quality of mould
		Contraction	Wafer	Batch		
SU-8	Mounds	0.67% ± 0.036%	✓	✓	~ 10 ± 4	Good
PDMS	Deformed	0.82% ± 0.56%	×	×	> 20	Too soft
MD700	Debris in	0.79% ± 0.39%	×	×	1	Too brittle

In the case of PDMS, it should be mentioned that, despite this being the most commonly used mould material, it is not suitable for high aspect ratio patterning (≥3), as it deforms due to its low elastic modulus (1,5 MPa). Consequently, the patterns engraved into the polymer present a considerable level of deformation, which is worse in the high aspect ratio zones i.e. dicing marks, as depicted in Figure 3.9.(a). Figure 3.10 shows the cross section of these marks, measured with a profilometer on the original PDMS mould and the COP replica. As a conclusion, PDMS is valid only for low aspect ratio structures, for which lower pressures, higher temperature and longer times can be employed. Other works in the literature show that a modified PDMS with a higher elastic modulus could be employed [165], reinforcing the need for high mechanical strength.

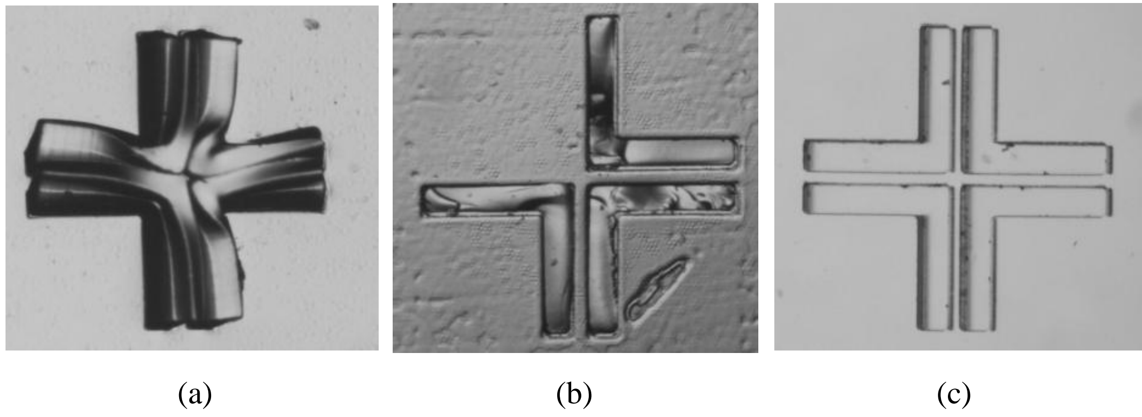

(a) (b) (c)

Figure 3.9. Results for high aspect ratio (≥3) pattern replication into COP using various mould materials; (a) Pattern in COP employing the PDMS master mould shows deformation of the patterned structure due to the high elastic modulus of PDMS; (b) Pattern in COP using the MD master mould shows good replication of the structure, but the MD mould was broken and debris can be seen inside the patterned structure; (c) Pattern in COP with the SU-8 master mould, showing perfect replication.

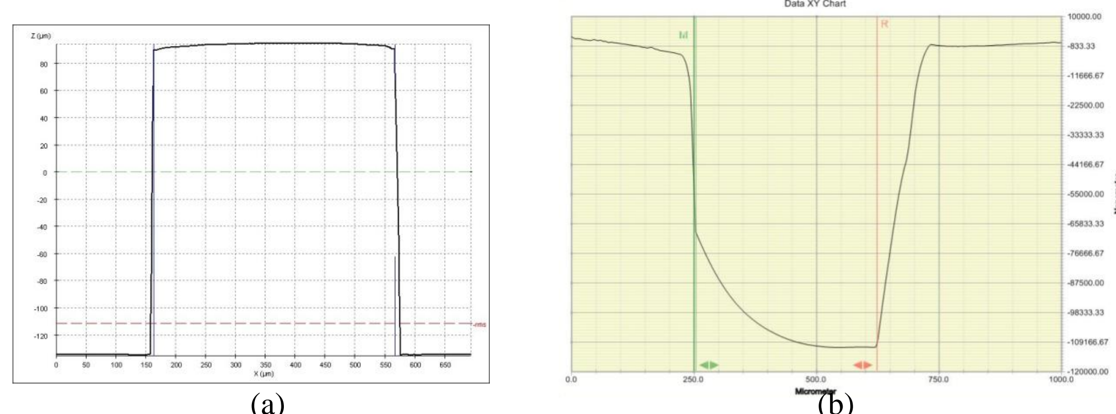

(a) (b)

Figure 3.10. Comparison between (a) a structure in the PDMS master mould and (b) its replica in COP. Large underfilling and bad wall profile can be observed.

In the case of MD700, the structures are replicated much better than with PDMS, as shown in Figure 3.9.(a) and Figure 3.9.(b). This could be expected from its elastic modulus, which is two orders of magnitude higher. However, MD700 is also very brittle and debris is left inside the replicas, as depicted in Figure 3.9.(b) and Figure 3.11. The main explanation for this phenomenon is the compressive stress generated during cooling, which results from the mismatch in the Coefficient of Thermal Expansion (CTE) of COP and MD700 [154, 157, 166, 167]. In this scenario, the shear stress required to de-mould is much higher than the tensile strength of the mould, causing it to chip-off.

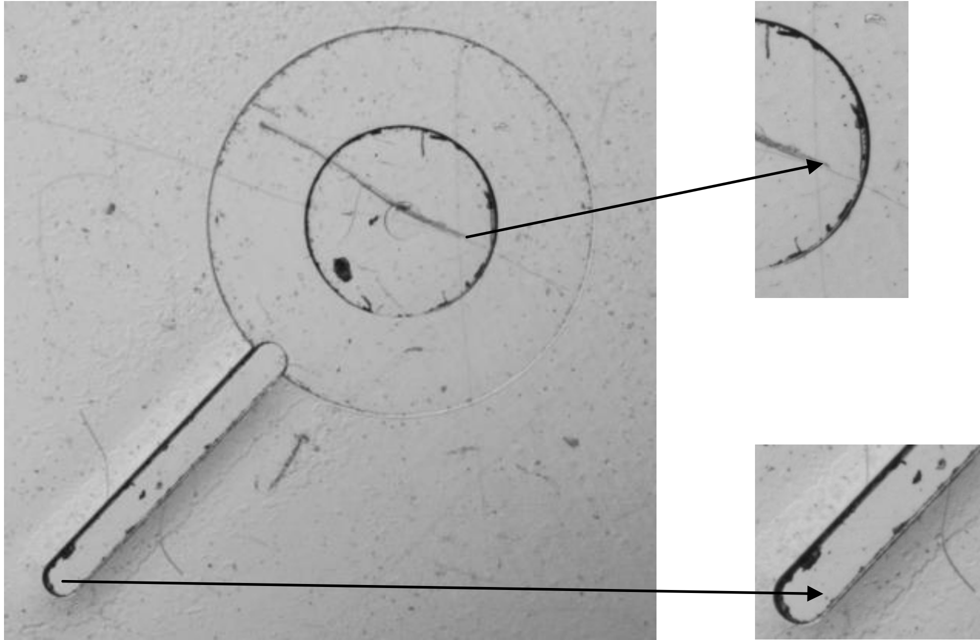

Figure 3.11. Results for pattern replication into COP with a MD700 master mould. Debris can be found inside the embossed COP structures due to material chipping-off during de-moulding.

In the case of SU-8, this exhibits glass-like mechanical properties when fully cross-linked [162], meaning that it has a higher elastic modulus than MD700 but it is less brittle. Besides, its CTE is very similar to that of COP [158], meaning that contraction rates are similar and stress is lower. As a result, SU-8 is the best mould material for COP that ensures good replication without breaking. However, replica measurements show small mound-like defects appearing at the edges, Figure 3.12. This implies that the shear stress generated during de-moulding exceeds the yield stress of COP. From their location and alignment in the direction of the de-moulding lever, it is reasonable to conclude that these are not only due to the CTE difference, but also because of the non-uniformly distributed forces occurring during manual de-moulding [151, 168].

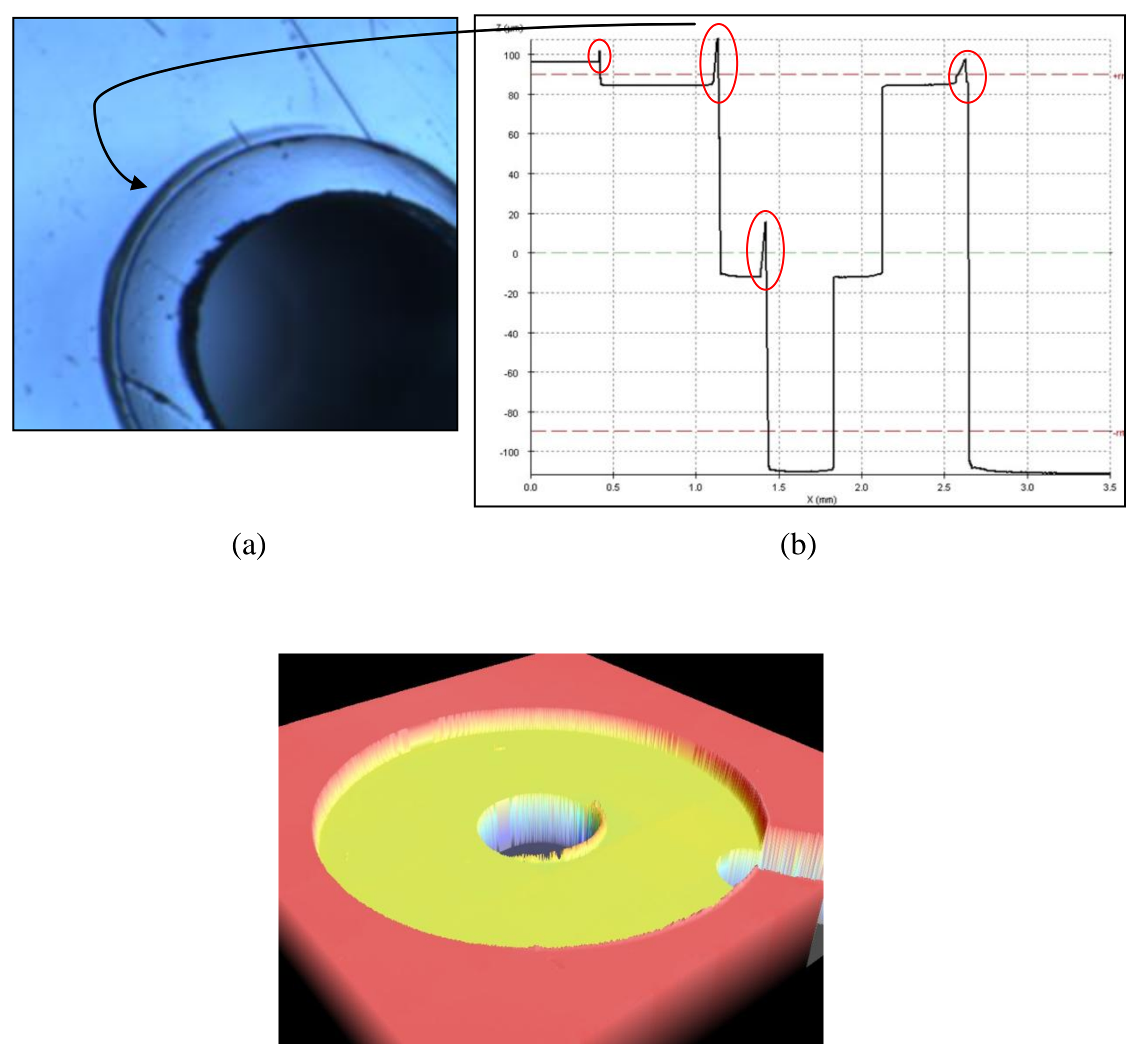

(c)

Figure 3.12. Results for pattern replication into COP with a SU-8 master mould. (a) Close up view of a mound-like defect at the outer edge of a microvalve, (b) Profile of the valve with mounds, which can reach up to 20 µm. (c) Confocal Topography of the microvalve with a mound at the edge of the inner diameter.

From the discussion, it can be concluded that SU-8 is the material with best overall replication quality, including exceptional dimensional control (similar to that of injection moulding, the industrial reference), acceptable durability and only slight defects in the replicas. However, this latter point must be minimized further in order to achieve mass production-like quality. As it is found, this not only depends on the mould

but also on an optimum processing, which reduces the stresses generated between mould and substrate during cooling (find optimum de-moulding temperature) and avoids high and localized de-moulding forces.

Prior to the explanation of the optimized HE process, the fabrication recipe for each SU-8 device mould is shown in Table 3.3. As it can be seen, for the last device (IV) that integrates all the previous (I-III), the layer-by-layer structuring makes it possible to maintain a coherent process for any integrated device.

Table 3.3. Summary of the recipes employed to fabricate the used master moulds.

(I) MICROVALVE MODULE	**(II) SENSOR MODULE**
Dehydration, pyrex wafer	Dehydration, pyrex wafer
O_2 plasma treatment, pyrex wafer	O_2 plasma treatment, pyrex wafer
Process SU-8 5 seed layer	Process SU-8 5 seed layer
Process gap layer, thickness= desired gap	Process channel, 80 µm
Process seat layer, 80 µm	Development, 3 min + 2 min + IPA
Process drilling layer, 80 µm	Hard bake, 170ºC for 16 h
Development, 7 min + 3 min + IPA	TOTAL height: 85 µm
Hard bake, 170ºC for 16 h	
TOTAL height: 220 µm	
(III) SENSOR + BY-PASS MODULE	**(IV) MODULE INTEGRATION LIQUID FLOW CONTROLLER**
Dehydration, pyrex wafer	Dehydration, pyrex wafer
O_2 plasma treatment, pyrex wafer	O_2 plasma treatment, pyrex wafer
Process SU-8 5 seed layer	Process SU-8 5 seed layer
Process sensor channel + by-pass channel (1/3), 80 µm	Process valve's gap layer + sensor channel (1/2) + valve's seat (1/3) + bypass-channel (1/4), thickness= desired gap
Process by-pass channel (2/3), 80 µm	Process sensor channel (2/2), + valve's seat (2/3) + bypass-channel (2/4), 40 µm
Process by-pass channel (3/3), 80 µm	Process valve's seat (3/3) + bypass-channel (3/4), 80 µm
Development, 7 min + 3 min + IPA	Process bypass-channel (4/4), 80 µm
Hard bake, 170ºC for 16 h	Development, 7 min + 3 min + IPA
TOTAL height, Sensor channel: 85 µm By-pass channel: 270 µm	Hard bake, 170ºC for 16 h
	TOTAL height, Microvalve's gap= desired Sensor channel: 75 µm Microvalve's seat= 165 By-pass channel: 250 µm

3.2.3. Optimized hot embossing procedure

The optimized HE process is aimed to minimize mound-like defects, by applying perpendicular de-moulding forces at the optimum de-moulding temperature. The tests are performed in an EVG®510HE hot embossing machine, which has a fixture for mounting the mould on a vertically displacing hot-plate. A previously degassed COP wafer is fixed to the bottom hot plate by means of a screwed ring, Figure 3.13. Initially, the same embossing temperatures (155 ºC) and time (60 min) as in the home-made machine were applied, as well as the maximum available force, 7,5 kN.

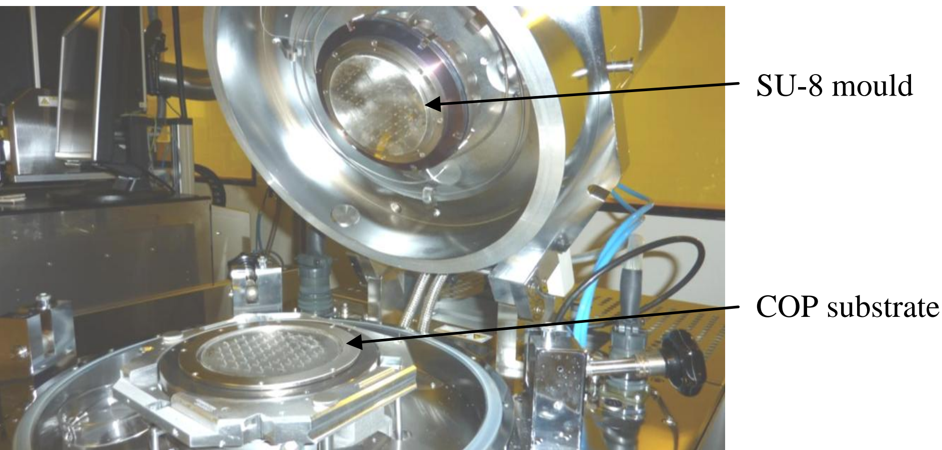

Figure 3.13. EVG®510HE hot embossing machine.

In order to optimize the de-moulding temperature, increasing values are tested, measuring the resulting defects after each test. Temperature values in the vicinity of T_g have been applied, on the grounds that close to this, the contraction of the material is lower and the shear stress is reduced. As it will be shown in the next section, the optimum is found to be slightly above T_g, where the polymer can still reflow and lead to a pattern recovery that reduces the severity of the defects [169, 170]. The optimized hot embossing process is shown in Figure 3.14.

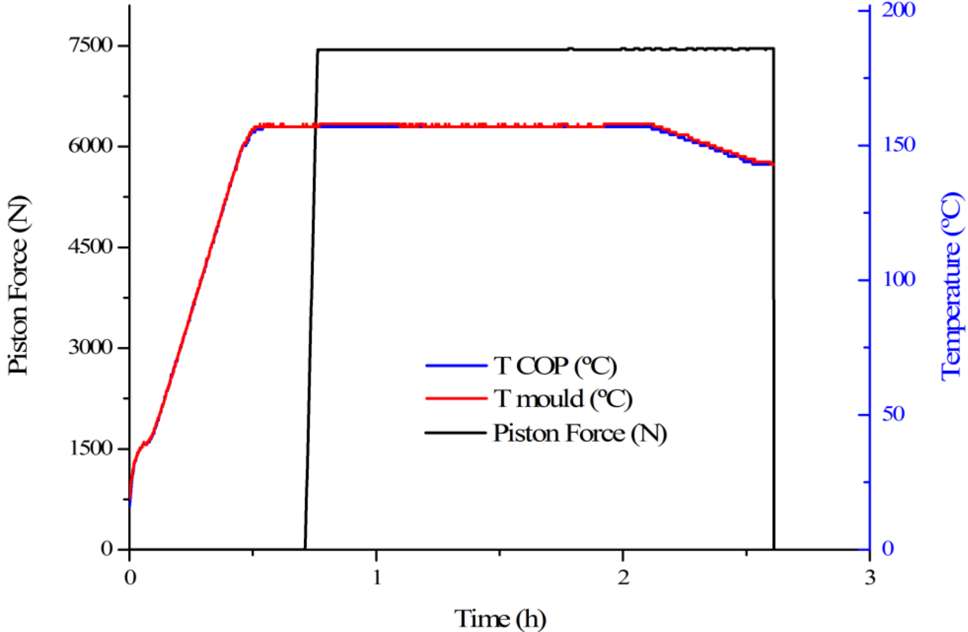

Figure 3.14. Optimized HE process with minimized mound generation by de-moulding slightly above T_g (T_d=143ºC).

3.2.3.1.Results of optimized procedure

The replicas obtained during the optimization are shown in Figure 3.15 for increasing values of T_d. Measurements confirm that as T_d increases, the mounds' height reduces. However, the walls of the replicas show to be tapered (a), implying that the mould is not completely filled. One possible explanation is the higher pressure exerted on the wafer (7kN ➔ 9bar), for which the embossing temperature either is not high enough or the embossing time is not sufficient. Therefore, in the final tests, the embossing temperature and time have also been increased (155ºC ➔ 157ºC and 60 min ➔ 80 min), resulting in more perpendicular walls (b,c).

Finally, at a T_d of 143ºC a negligible mound height (<1 μm) is repetitively achieved, (c), topography shown in Figure 3.16. The contraction of the devices with respect to the mould is measured and compared at chip and wafer level. The obtained value, 0.66% ± 0.015%, is within the specifications of the manufacturer (0.5-0.7 %) for injection

moulding [111], evidencing the quality of the process and its compatibility with mass production means. For replicating the different microfluidic elements presented in this work, this contraction value has been used as a scaling factor for the moulds.

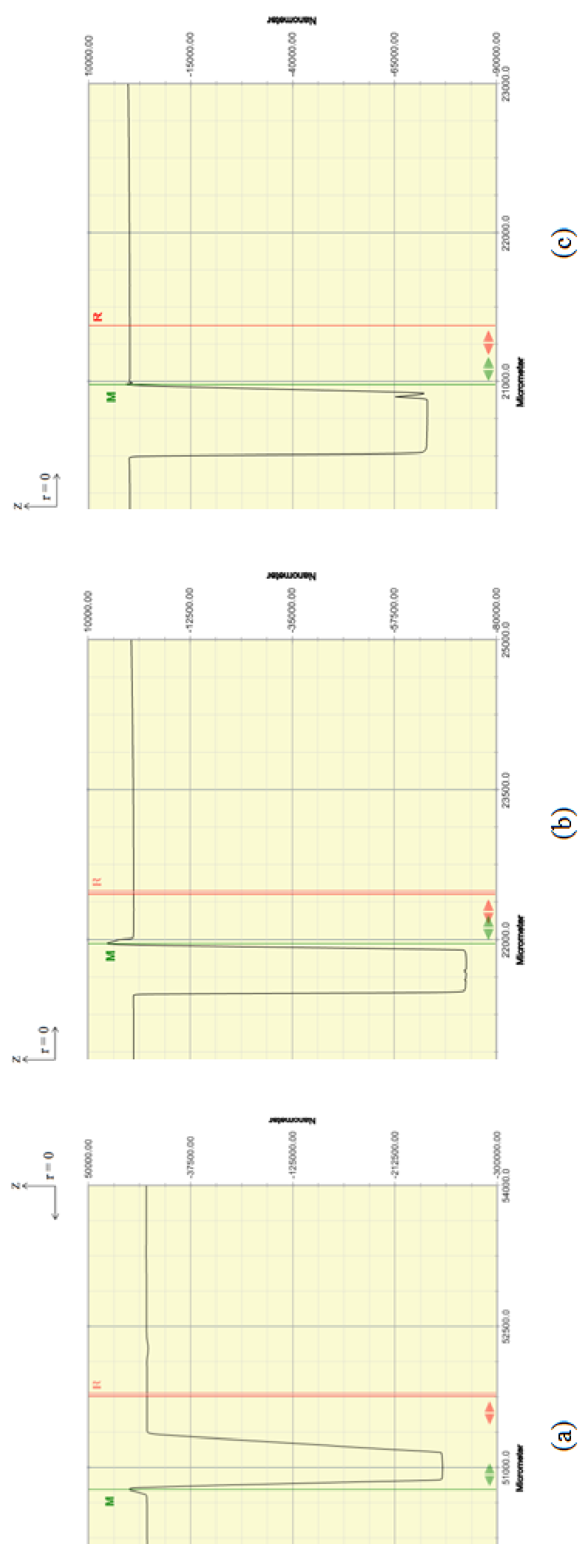

Figure 3.15. Hot embossing tests at different de-moulding temperatures (a) Embossing at 155ºC, F= 7.5 kN, t= 60 min, de-moulding at 130ºC: the defect is about 14.5 μm; (b) Embosing at 157ºC, F= 7.5 kN, t= 80 min, de-moulding at 138ºC: the defect is about 5.7 μm (c) Embossing at 157ºC F= 7.5 kN, t= 80 min, de-moulding at 143ºC: the defect is less than 1 μm.

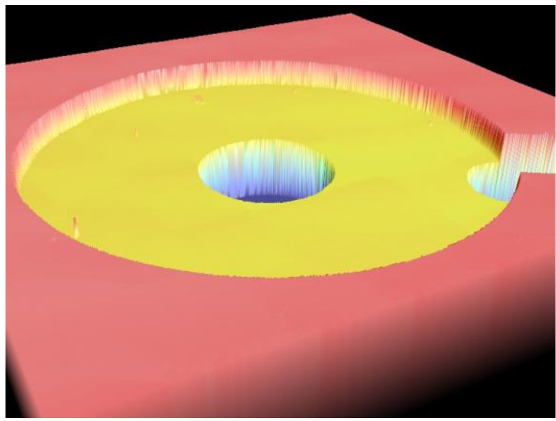

Figure 3.16. Confocal Topography of a replica for microvalve module obtained by the optimized HE process. Negligible mounds appear owing to the equilibrium between mound generation and recovery of pattern.

3.3. DRILLING

Once the structures are patterned, inlet and outlet key-holes need to be made to connect the devices to the external fluidic source, Figure 3.17. Care must be taken when selecting the type of bit to be used, since COP is a complex material to machine, showing tendency to crack, fray and produce uneven borders with common polymer fabrication techniques like routing or laser cutting. In this work, drilling is selected for simplicity, using high precision bits of Ø 0.5 mm. It is found that low speed bits generate considerable burr at the edges of the ports. This affects the subsequent bonding process severely, leaving large non-bonded areas around them. For the particular case of the valve, where the outlet port is drilled at the valve seat, burr may also impair its normal functioning. Particularly, burr prevents proper closure of the valve membrane or it may bond to it during bonding, impairing flow regulation. Finally, a high speed drill (Farnell DU65.10-Drill, Carbide Ø 0.5 mm) is selected, which has considerably reduced the problem.

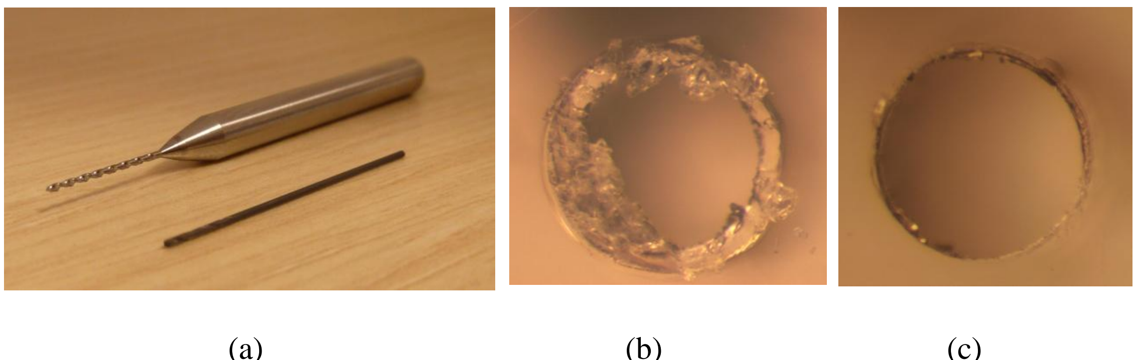

(a) (b) (c)

Figure 3.17. (a) Different bits tested for inlet/outlet drilling. (b) burr around a port by low speed bit drilling (c) clean edges by high speed bit drilling.

3.4. BONDING

Upon drilling, the structures are sealed at wafer level, using a 100 µm thick COP membrane, in order to finalize the chips. It should be mentioned that this is a very delicate process, since the sealing membrane will also be employed as a flow regulation element (valve) and as a support for the metallized sensor. This implies that the bonding must render a flat surface and be gentle enough to maintain the thin clearance against the valve seat (10 µm – 40 µm).

Current bonding methods have limitations, including channel blockage, channel distortion, poor bonding strength and durability and non-homogeneous channel surface properties [144]. In this work, thermal and solvent bonding is investigated. As it will be shown in the following sub-sections, the latter showed better capabilities for production of monolithic devices.

3.4.1. Initial thermal bonding process

In the preliminary tests, sealing of the structures was realized by conventional thermal bonding. The basic principle of the process is to heat two polymer parts near their glass transition temperature, then apply a suitable amount of pressure and hold until they bond.

Several tests were made to determine thermal bonding parameters. The manufacturing process starts by sandwiching the polymer wafers, i.e. patterned COP wafer and a 100 µm COP membrane, between two Ø100 mm and 0.7 mm thick Pyrex wafers and heating to 138 ºC at a rate of 5 ºC/min. After heating, a pressure of 3 bar was applied while keeping the bonding temperature constant for one hour. Once the substrates had cooled down to room temperature the pressure was removed.

This process was found to be particularly unsuitable for the microvalve module. Only designs whose chamber height was at least 80 µm could be fabricated without collapse of the membrane. It is believed that thermal stress leads to membrane deformation values greater than 80 µm, making it collapse against the valve seat and bond to it, as shown in Figure 3.18.

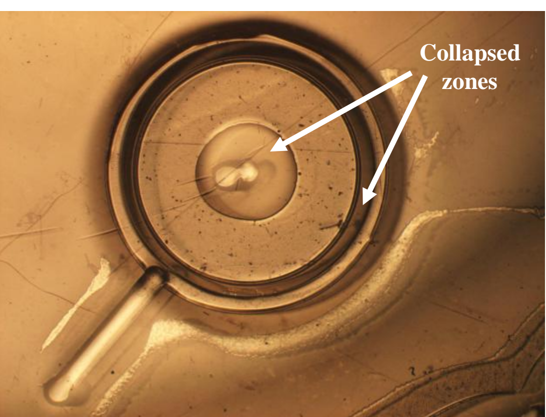

Figure 3.18. Image of a microvalve module after thermal bonding. Collapsed areas can be seen in the centre and in the outer edges of the microvalve.

3.4.2. Improved thermal bonding process

One possible way to avoid membrane deformation is to fix it to the Pyrex bonding supports during the process. The strength of this temporary bonding should be higher than the thermal stresses. The concept is taken from a previously patented process [171], whereby the supporting Pyrex and COP membrane are subjected to a UVC dose of 1000 $J \cdot cm^{-2}$ to create a temporary bonding.

This improved process allowed fabrication of a wider range of devices, including valves with chamber heights ≥ 20 µm and chamber diameters ≤ 3 mm. However, non-bonded areas were observed, as a result of bad contact between the COP wafer and the membrane on the rigid substrate. In order to overcome these limitations and to fabricate shallower chamber heights, a solvent bonding process is also investigated.

3.4.3. Solvent bonding process

This technique is aimed to promote bonding between the parts by dissolving the interface between them with a suitable solvent, causing the polymer chains to intertwine. Once the solvent evaporates, the chains lose their mobility and a monolithic COP-to-COP bond is created. This requires that the solvent be able to release the chains without degrading the polymer and evaporate slowly to allow enough manipulation time.

Various solvents were tested, most of them with undesired results. These include chlorobenzene, chloroform, toluene, orto-Xylene, para-Xylene, limonene, dichlorobenzene and trichlorobenzene. The optimum recipe consists in dispensing 4 ml of chlorobenzene, spinning the wafer at 1000 rpm, with an acceleration of 1000 rpm/s for 120 seconds. This leaves a dry and slightly sticky surface. Next, the assembly is placed in a laminating machine (manufactured by EVG during the Lab on Foil project), which fixes the rigid parts by means of vacuum and gently laminates the membrane

over these, achieving highly repetitive planarity. Then, the assembly is sandwiched between two Pyrex wafers and pressure is maintained by means of clamps. Solvent evaporation is enhanced in a vacuum desiccator.

3.4.3.1.Results and discussion

The solvent bonding method allows fabrication of devices with excellent bonding strength, unimpaired optical properties, fast processing and planarity. Particularly, the most critical module of the liquid flow controller, a microvalve with a minimum gap of 10 µm was obtained with a remarkably low and repetitive absolute deformation of the membrane at the centre, i.e. Ø 0.04% (±0.013%) for the 2.5 mm diameter membrane, Ø 0.024% (±0.014%) for the 3 mm diameter membrane and Ø 0.016% (±0.011%) for the 4 mm diameter membrane. Figure 3.19 shows SEM images of a replica obtained by solvent bonding, where the narrow gaps can be seen underneath the flat membrane.

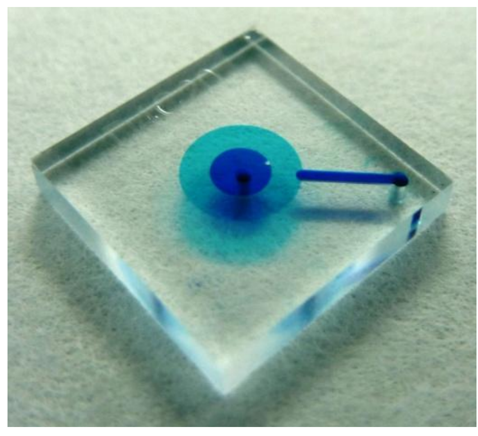

(a)

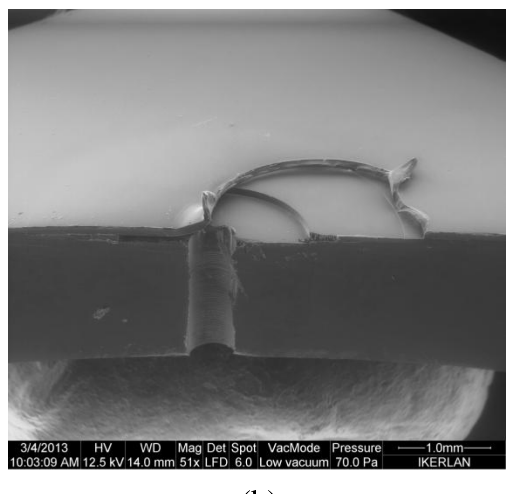

(b)

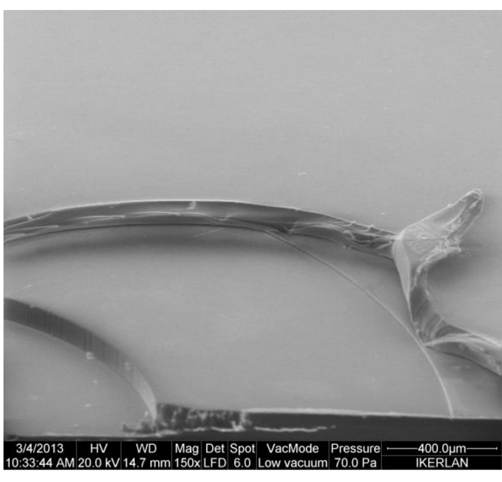

(c)

Figure 3.19. (a) COP microvalve module with 40 µm chamber height by solvent bonding. The microvalve is filled with methylene blue to improve inspection (b) Image of a torn microvalve to expose the 10 µm chamber height (c) Close-up image of the suspended membrane, showing no collapse against the seat.

As explained previously, other solvents were also tested but the results were not satisfactory. The observations are listed as a series of requirements for a correct choice of solvent.

- Find equilibrium in evaporation velocity. The solvent must neither evaporate too quickly, providing enough time for manipulation, but nor too slowly to reduce the evaporation time and be able to process quicker. Chloroform showed a too high evaporation rate, leading to non-bonded areas.

- Avoid mechanical stresses. Some solvents tend to generate mechanical stresses in the polymer after evaporation, leading to cracking of the membrane and peeling off from the replica after some time. Toluene causes substantial cracking at the bonding interface.

- Avoid cloudiness of the bonding surface. Despite high bonding strength, this phenomenon would prevent quality inspection or using optical measurement techniques, which are typical in LOC devices. Orto-xylene and para-xylene caused this effect, despite being supplied as chemically compatible with COP.

- Ensure sustained bonding strength. Even if some solvents can successfully dissolve the polymer, the resulting bond strength might reduce over time, leading to subsequent peeling of the LOC devices. Limonene resulted in peeling after 1-2days, without application of pressure or force.

- Prevent polymer swelling. Some solvents are absorbed very easily into the bulk of the polymer causing swelling. This may even lead to distortion of the structures, which is irreversible once the polymer has evaporated. Dichlorobenzene and trichlorobenzene caused softening and swelling, thereby preventing bonding of the membrane.

3.5.METALLIZATION OF DEVICES

The final step of the fabrication process involves the deposition of the Ni electrodes by sputtering. Since Ni is a magnetic material, magnetron sputtering is used, where the power is based on the use of a magnetic field transversal to the target surface, in addition to an RF source. For patterning, metal lift-off is employed, using a sacrificial layer of OIR photo-resist. First, an O_2 plasma is applied on the wafer for 2 min at 90 W in order to clean the surface and promote adhesion of the photoresist to the membrane. Next, the OIR is spin coated and soft-baked on a hotplate. Then, the resist is exposed to a UV dose of 350 $mJ \cdot cm^{-2}$, developed in a MF400 bath for 40 s and rinsed with DIW.

Prior to sputtering, an O_2 plasma is applied again at 90 W in order to clean the surface of the wafer and promote adhesion of the Ni to the membrane. 100 nm of Ni is deposited at 350 W in 360 seconds. Finally, the wafer is immersed in acetone to remove

the OIR and reveal the electrodes' pattern and rinsed with methanol and DIW. The resulting electrodes are shown in Figure 3.21.

As explained previously, preservation of the membrane planarity is highly important, particularly due to the frequent thermal steps required to fabricate the electrodes. Although care has been taken to avoid excessive heating, surface profile measurements of the microvalve module show a minor increase of the deformation with respect to the solvent step, being Ø 0.47% ±0.183% for 3 mm diameter membrane vs. the previous Ø 0.024% ±0.014%. This deformation can be considered negligible in terms of device performance, as will be discussed in the following Chapters.

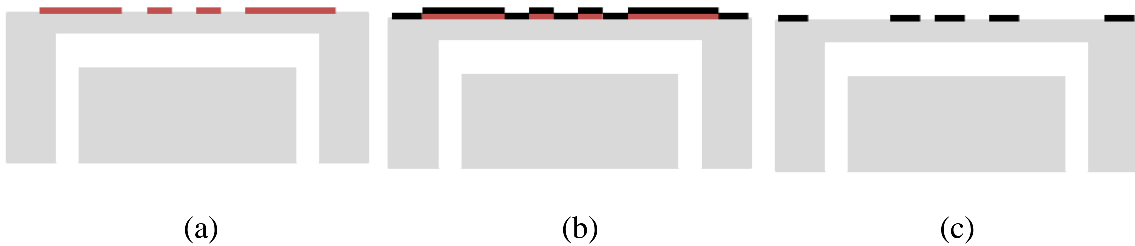

(a) (b) (c)

Figure 3.20. Schematic diagram of thin film deposition by lift off. (a) Deposition of sacrificial layer by photolithography; (b) Deposition of the nickel film by sputtering; and (c) Lift off.

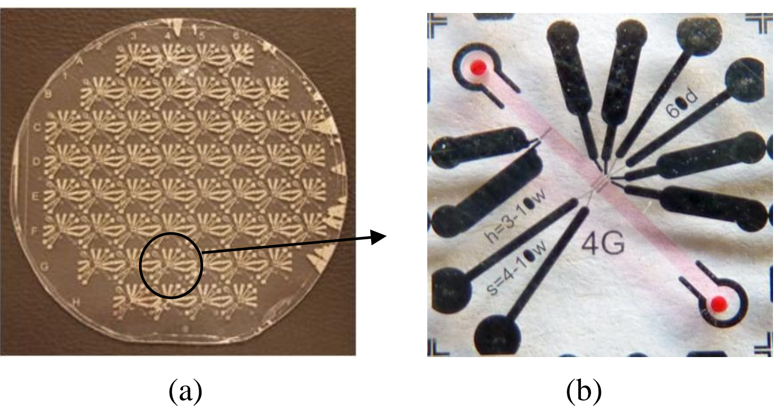

(a) (b)

Figure 3.21. (a) Nickel thin film structures on top COP wafer, for simple channel flow sensor module.

3.6. CONCLUSIONS

- In this chapter, a modular fabrication process is successfully accomplished, using a simple and low-cost hot embossing method, which renders virtually defect-free devices with uniform contraction at batch level, achieving values similar to those of industrial processes like injection moulding. This is achieved through a series of improvements over existing procedures, like the use of a mould material with a CTE close to that of COP (e.g. SU-8) and de-moulding above its T_g to reduce shear stress and take advantage of polymer reflow.

- The devices are finished off by solvent-bonding of a sealing membrane, resulting in a monolithic component with excellent flatness at wafer level, Ø 0.024 % (±0.014 %), allowing fabrication of microvalves with uniform valve seat clearances as low as 10µm.

- Ni deposition on top of the finished devices is successfully accomplished without substantial change to the deformation of the membranes and maintaining highly repetitive values at wafer level, Ø 0.47% (±0.183%).

- The quality of the modular fabrication evidences the enormous integration potential achieved, covering a wide range of typical structures for microfluidics, microfluidic control and sensing in a mass-production-compatible way and proving the possibility to accelerate the transition from prototype to product.

4. SECTION II –MICROVALVE MODULE

4.1. INTRODUCTION

Microvalves are one of the basic elements of microfluidic control and represent one of the most researched topics in microfluidics over the past 30 years. However, there is not yet any example that can be truly integrated in complex LOC systems, which is robust, simple, versatile, low-cost and free from assembly errors. The lack of integrated valves has generally implied the use of alternatives, such as capillarity, that only sustain simple protocols. Therefore, it is necessary to dispose of valves that help link or isolate areas within LOCs in order to adapt more of the steps and protocols currently being developed in "microfluidic" biology.

Microvalves are basically categorized into active and passive, the former being best suited for complex LOCs. Actuation principles include pneumatic [8, 9, 11-14], thermopneumatic [13-17, 19-22, 172], thermomechanical, piezoelectric [23-26], electrostatic [27-31], electromagnetic [33, 34, 173-176], electrochemical and chemical [36-38, 177-180] and passive capillary force microvalves [181-184]. Amongst these, pneumatically actuated membrane valves have been successfully used in many applications due to their low cost and simple fabrication. A variety of devices has been demonstrated for silicon [39-41] and glass–silicon [20, 42] as well as for less traditional materials such as elastomers [10, 43-45] and polymers [46-49]. Within the latter, cyclic olefin polymer (COP) has recently emerged as an attractive material [105, 106] due to its high optical clarity (into deep-UV range) [107], high bio-compatibility [108, 109], low auto-fluorescence, low water absorption [110-113] and good chemical resistance, also against organic solvents [106, 110, 111].

Most valves in the literature are of the on/off type, which are simpler to construct and actuate. In fact, flow modulation would require the valve to have a sensitive control system, but also design parameters to control its flow modulation range, modulation profile and the closing pressure. This way, a versatile concept would be available that could tailor the valve's characteristics to the intended application. As an example, flow-

modulating valves would allow mass-parallelization in continuous flow microfluidics (such as droplet generation), and increase the useful life of pumps (pressure dispensers) by minimizing variations in their workload.

In this chapter, the design and performance of a full-COP valve will be shown, which is intended to work both as on/off and modulating valve. Following the modular approach of this thesis, the features of the design will enable its use both as an individual or an integrated component. To this end, a membrane-type microvalve has been chosen, since these are simple to construct, characterize and tailor and they are compatible with the fabrication process previously described.

In the following sections, the architecture of the valve will be introduced and the influence of its design parameters described by means of a simple theoretical model. Next, a library of 18 designs will be characterized, proving the possibility of generating a wide range of behaviours from the aforementioned design parameters. Finally, the measured and predicted performance will be compared for a selected number of designs, in order to validate the model as a design tool for future applications.

4.2. ARCHITECTURE AND WORKING PRINCIPLE

Membrane-type microvalves work by deflecting their membrane towards the bottom of a channel or chamber, as a result of an externally applied pressure. By controlling this pressure, a partial or total blocking of the flow is achieved, which effectively describes the principle of modulation.

In Figure 4.1 a schematic overview of the proposed active microvalve design is presented. As it can be observed, two different sections are distinguished. On the one hand, a valve chamber is defined by the outer diameter of the valve (*D*) and the clearance between the membrane and the seat (*gap* or *G*). On the other hand, the valve seat is delimited by the inner diameter (*C*).

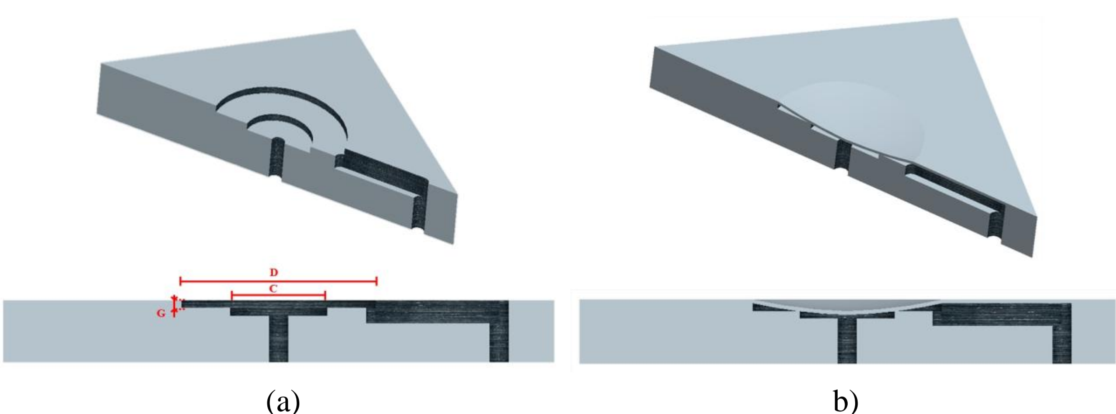

Figure 4.1. (a) Schematic drawing and cross-section of the normally-open microvalve, without the diaphragm. (b) Cross-section of a COP microvalve with a COP diaphragm in its closed state.

The portion of the membrane above the chamber cavity, delimited by *D*, is at the same time the active moveable part that regulates the flow by deflecting and reducing the fluidic section under the action of an external pressure source. As a result, the fluidic path gets narrower and the flow rate is reduced. When sufficient pressure is applied, the membrane collapses against the seat, closing the microvalve and stopping the flow, Figure 4.1.(b). Thus, this is a normally-open, out-of-plane microvalve.

The characteristics of the flow modulation and the closing pressure for each design will depend on the contribution of the diameters and gap. In principle, it can be stated that (i) D governs the elasticity of the membrane or the ratio between actuation pressure and deflection, (ii) C governs the span of the flow regulation range and (iii) G governs the maximum flow rate. However, the behaviour of a given valve will depend on the interaction between these elements, which can be difficult to predict. In order to understand this interaction and the resulting behaviour, a model of the valve is presented in the following section.

4.2.1. Theoretical model of the valve

In this section, the interaction between the flow and the membrane has been investigated and the main influential aspects have been considered to obtain a qualitative value of flow rate as a result of changes in the actuation pressure.

In order to describe the flow conditions, a simple 2D theoretical approximation has been made, based on the pressure drop through each element of the device as a result of their geometry. Thus, a series of microchannels has been chosen to facilitate modelling. As it will be shown later, this simplification allows for a quick and convenient qualitative result. From Figure 4.2, the entrance channel, L1, ends in a sudden contraction, C1, representing the entrance to the chamber. C1 is the initial gap size, which decreases gradually down to C2 at the valve seat, depending on the pressure exerted on the membrane. For simplicity of the forthcoming equations, the contraction along the portion of the chamber between the entrance and the seat, L2, is considered to be constant and equal to C2.

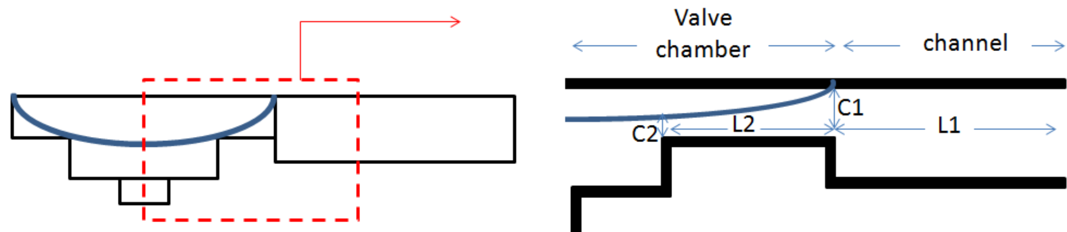

Figure 4.2. Schematic representation of the microvalve with the control box for the model. The “L” terms represent the length of the channels, and the “C” terms represent the contraction of the valve. C1 refers to the contraction ahead of the valve chamber and C2 refers to the clearance between the valve seat and the membrane.

For the model, the pressure difference applied across the channel is termed total pressure drop, because the pressure decreases from the source at the inlet, down to atmospheric at the outlet. According to this definition, each channel and contraction will

contribute to the total pressure drop depending on the resistance posed against the flow i.e. the larger the resistance, the larger the pressure drop. For a given total pressure drop and according to Figure 4.2, L1 has constant pressure drop because its dimensions do not vary. However, C2 decreases with membrane deflection, resulting in an increased pressure drop across both itself and L2.

The value of C2 has been calculated from the expression for the symmetrical bending of circular plates [185] at the appropriate radial distance from the centre of the membrane. The pressure drop for the channels and for the contract element has been calculated using expressions (1) and (2) [186].

$$\Delta P_L = \frac{fpL}{A}\left(\frac{1}{2}\rho U_L{}^2\right) \quad (1)$$

$$\Delta P_C = K\left(\frac{1}{2}\rho U_C{}^2\right) \quad (2)$$

$$f = \frac{24}{Re\ D_h}\left(1 - 1.3553\frac{h}{w} + 1.9467\left(\frac{h}{w}\right)^2 - 1.7012\left(\frac{h}{w}\right)^3 + 0.9564\left(\frac{h}{w}\right)^4 - 0.2537\left(\frac{h}{w}\right)^5\right) \quad (3)$$

Where, ΔP is the pressure drop, f is the friction factor, expression (3), p is the wetted perimeter, L is the channel length, A is the cross-sectional area of the channel, ρ is the density, U_L is the mean flow velocity at the channel, U_C is the velocity at the contraction and K is an experimental factor, which for sudden contractions has a typical value of K=1. It should be noted that the variation in pressure drop with this parameter is small compared to the drop associated with the length or the velocity.

The expressions represent the channel and the contractions as resistive elements, the resistance of each one being summed in series to obtain the total pressure drop. It should be noted that, since the channels are assumed rectangular, the velocity at L2 and C2 is the same and that at C1 and L1 it is proportional to the ratio between C1/C2. Therefore, the solution is obtained by iterating until a velocity at C2 is found that

satisfies the total pressure drop. Also, because the flow rate across C2 is proportional to the local velocity, it is possible to obtain a qualitative variation of flow rate as a result of changes in valve geometry, namely, gap size, chamber diameter, seat diameter and membrane deflection.

4.2.1.1.Theoretical results

The flow regulation behaviour has been analyzed for an array of six designs, having a valve diameter of 2.5 mm, two different seat diameters of 0.7 mm and 1 mm, and three *gap* heights of 10 µm, 20 µm and 40 µm. In all cases, a constant pressure drop of 1bar has been imposed, as well as a range of pressures on the membrane, from fully open to closure. The results are shown in Figure 4.3.

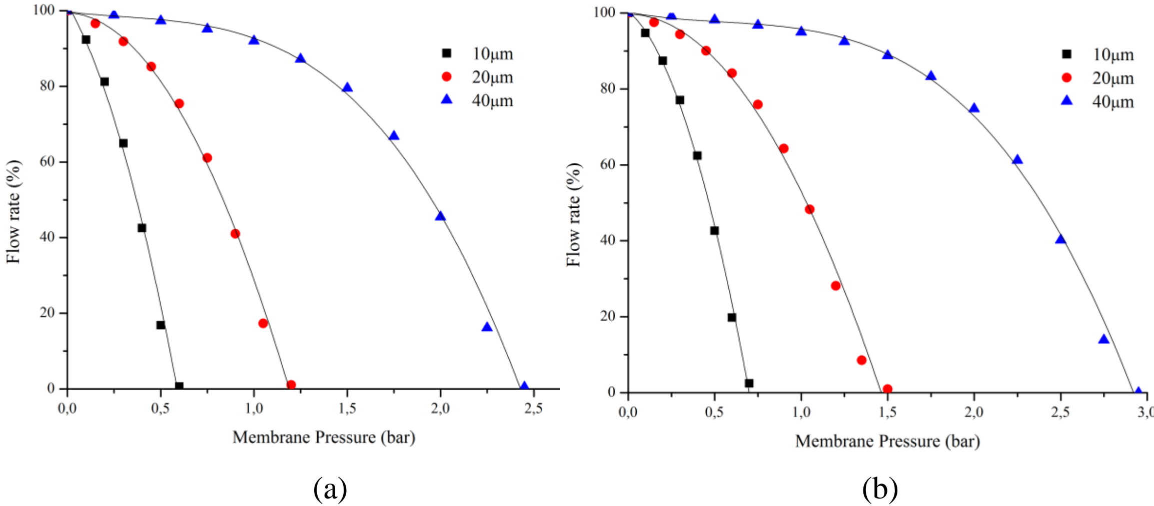

Figure 4.3. Theoretical variation of the valve's flow profile, for a valve diameter of 2.5 mm, as the *gap* size is reduced (▲=40 µm, ●=20 µm, ■=10 µm), when valve seat is a) 0.7 mm and b) 1 mm.

According to the equations, for a given seat diameter the initial gap size will influence the maximum flow rate, the pressure drop across the valve and its rate of increase as the membrane deflects. For larger *gap*s (40 µm curves), the pressure drop at the valve will be small for low values of membrane deflection, giving a parabolic flow rate decay.

Upon a certain level of deflection, the resistance at the valve will become dominant, resulting in a more linearly decaying flow rate. For smaller *gap* sizes (10 µm curves), the valve dominates over a wide range, resulting in a rather linear flow rate. Figure 4.3 depicts such behaviour as predicted by the equations. With respect to "seat diameter/valve diameter ratio (*C*/*D*)", its effect is easier to predict, simply resulting in a proportional change in closing pressure due to a change in the value of the membrane deflection per unit actuation pressure. Hence, from the previous prediction, we can design for (i) the maximum flow rate and its regulation profile through the *gap* size and (ii) the valve closing pressure range through the seat diameter/valve diameter ratio (*C*/*D*).

4.3. CHARACTERIZATON AND EXPERIMENTS

The prediction of the theoretical model provides a qualitative base to compare the relative performance of each valve design. In order to verify the capabilities of the microvalves for flow regulation and blockage, the performance has to be evaluated under flow conditions likely to be encountered in LOC devices.

4.3.1. Setup and Experiments

The setup includes a positive pressure flow controller (Fluigent MFCS™ FLEX, France), a flow microsensor to measure the flow rate passing through the microvalve (Sensirion CMOSens©, Switzerland) and a pressure controller (EFD1500XL, USA) to regulate the pneumatic actuation on the membrane. Pneumatic actuation has been chosen because it is capable of providing enough force for closure, as well as uniform and controlled displacement of the membrane.

These elements are connected to a PMMA packaging that houses the microvalve (MicroLIQUID, Spain), which allows fast replacement of devices with leak-free operation. This packaging is divided into two parts, the chip holder and the cover. The

chip holder (bottom piece) has a housing to accommodate the chip in a fixed position and the pressure connection to actuate the membrane. The cover (top piece) has the fluidic connections. The set-up and packaging are shown in Figure 4.4 and Figure 4.5, respectively.

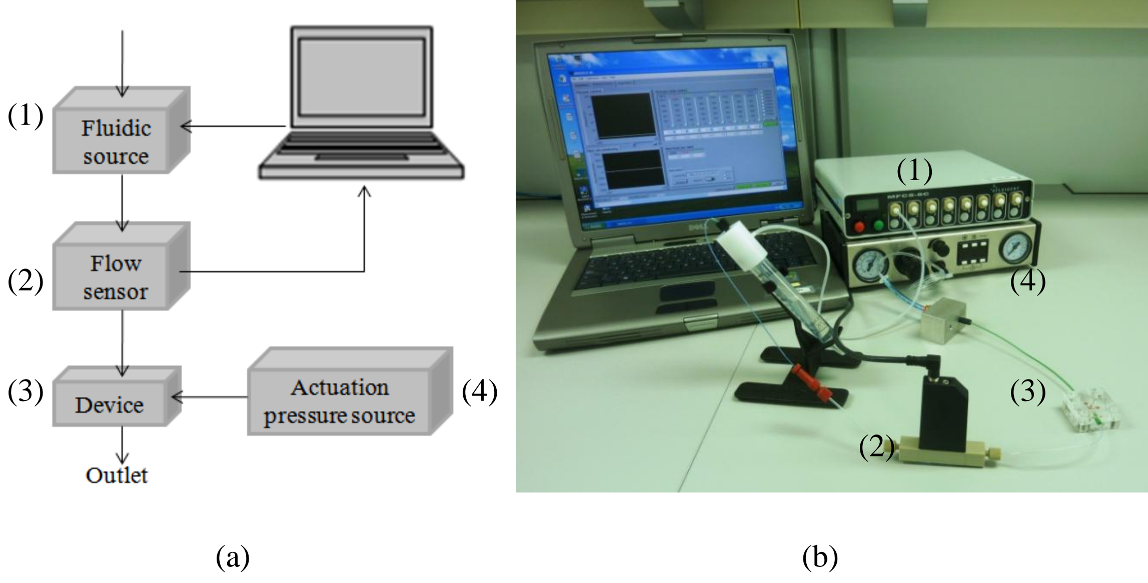

Figure 4.4. a) Block diagram of the experimental setup. b) Experimental setup involved for the characterization of microvalves.

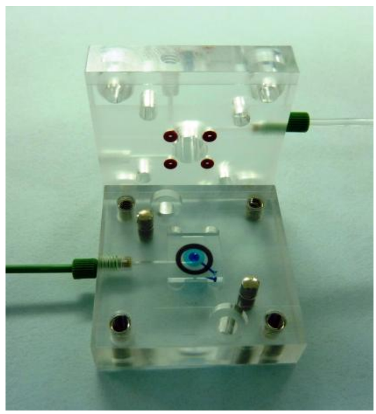

Figure 4.5. PMMA packaging showing the microvalve in place and the fluidic and pneumatic ports required for actuation.

For the characterization, an array of 18 designs has been employed, Table 4.1, and the predicted behaviour caused by the design features has been measured and verified. For all the experiments, a constant pressure drop of 1 bar has been imposed across the valve.

First, the maximum flow rate has been measured at zero membrane actuation pressure. Then, the pressure has been increased step-wise, measuring the resulting flow rate and obtaining the flow rate modulation profile and the pressure at closure.

Table 4.1. Proposed array of microvalves (18) for performance characterization.

Design	D (mm)	GAP (µm)	C (mm)
1	2,5	10, 20, 40	0.7
2	2,5	10, 20, 40	0.8
3	2,5	10, 20, 40	1
4	3	10, 20, 40	1
5	3	10, 20, 40	1,5
6	4	10, 20, 40	2

4.3.2. Results and Discussion

The characterization results are depicted in Figure 4.6. Due to effect of membrane flatness on performance, only valves with a maximum deformation of 3 µm at the centre have been employed (yield about 80% for the optimized solvent bonding). As a result, wafer-to-wafer repeatability is significantly improved, reducing the deviation of the measurements from 47% (no valve selection) down to 15% (with valve selection). A discussion on the effects of poor membrane flatness is shown in Appendix II.

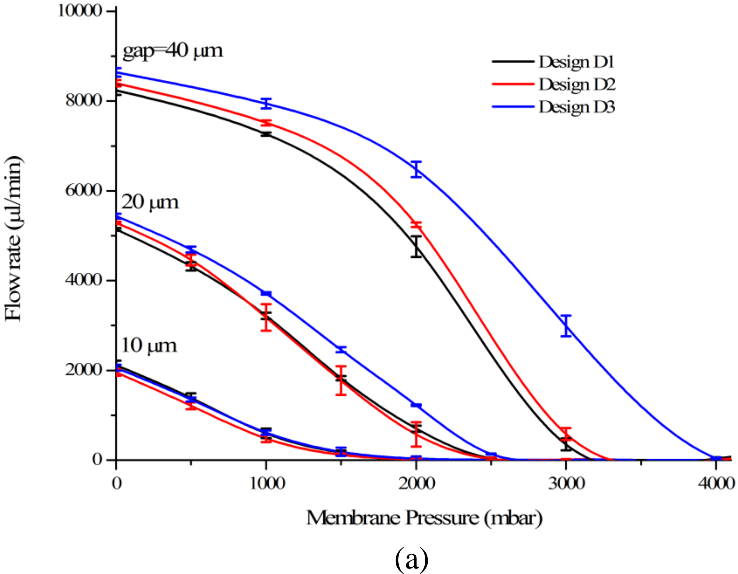

(a)

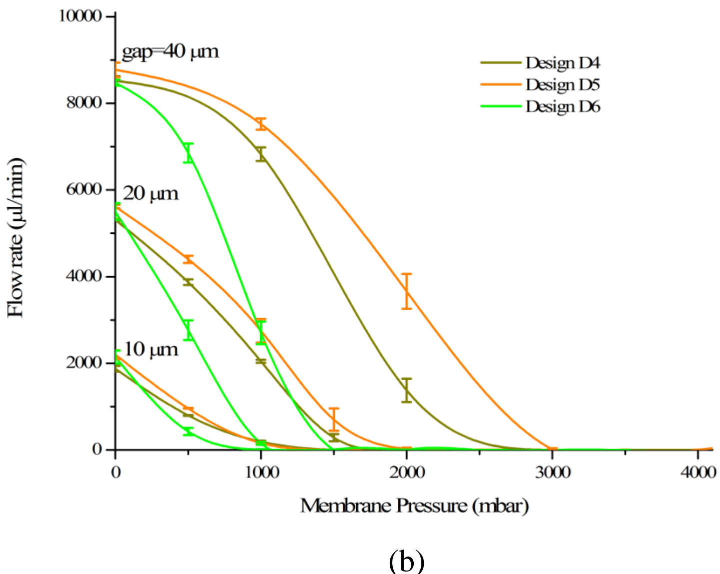

(b)

Figure 4.6. Characterization of microvalves at 1 bar pressure drop (a) Characterization for designs D1, D2 and D3 with *gaps* of 10, 20, 40 µm, membrane diameter (*D*) of 2,5 mm and seat diameters (*C*) of 0.7 mm, 0.8 mm and 1 mm respectively. (b) Characterization for designs D4, D5 and D6 with *gaps* of 10, 20, 40 µm, membrane diameter (*D*) of 3 mm for D4 and D5 and 4 mm for D6, and seat diameters (*C*) of 1 mm, 1.5 mm and 2 mm respectively.

The array of *gap*s, outer diameters and seat diameters employed highlights the separate effects of the valve's design features on performance: (i) maximum flow rates depend on the *gap*'s dimension, since it is the most restrictive and dominant element. (ii) the flow regulation profile is dependent on the ratio between the outer diameter (*D*) and the diameter of the valve seat (*C*), as the membrane deformation for a given load is dependent on *D*. (iii) closure pressure is dependent on C, since deflection is larger for a given pressure towards the centre of the membrane and on the gap, as it defines the distance the membrane must displace for closure against the seat. Repetitive results show that the microvalve can work properly as flow controller and all designs can be closed easily with low actuation pressures (1-4 bar).

With regard to the operation mode of the microvalve, for on/off behaviour, a higher *D*/*C* ratio is preferred since the closing pressure decreases. On the contrary, for flow regulation a lower *D*/*C* ratio is best, because the regulation profile features a smoother slope and a higher closing pressure, making control easier. If combined with a lower *gap*, the regulation profile becomes more linear, further improving flow control.

The results agree well with the theory, except around the closing pressure, which is substantially higher than predicted. In fact, the model assumes that the flow is interrupted when the membrane contacts the valve seat. However, this is not true for rigid components like the membrane of the valve, thus extra pressure is needed to force the membranes sufficiently against the seat, as observed.

The effect of increasing the valve seat (*C*) also follows the theoretical behaviour, resulting in a larger flow for similar membrane pressures, since the value of deflection, and thus closure, is lower as we move towards the edges of the membrane. In principle, this implies a wider regulation range. However, as it can be seen in Figure 4.6, in practice this difference reduces significantly as the *gap* decreases, which sets the lower limit for the flow tailoring capabilities predicted by the theory.

4.4. CONCLUSIONS

- In this chapter a microvalve architecture has been presented, whose design parameters (*gap*, *D*, and *C*) allow tailoring of the performance as on/off or flow regulation valve.

- A theoretical model that satisfactorily predicts the qualitative performance of the microvalve has been proposed. However, deviations from the real performance were observed around the closing pressures, were the rigid membrane requires extra pressure for closure.

- The pressure drop characteristics of the devices allow flow rate values well suited for LOC applications, providing improved performance for liquid flow regulation ranging from 200 nl/min up to 9 ml/min, in comparison with other works with flow rates as high as 1.3 l/min [175], ability to fully close the valve with negligible leakage of 0.2 µl/min, in comparison with other works that present non-negligible leakage of 3.9 µl/min [187] or a considerable leakage of 420 µl/min [188], improved repeatability owing to the repetitive membrane deformations obtained in the solvent bonding process [189], and faster response time [187].

- Summarizing, the microvalve represents a real alternative for microfluidic control, as it shows tunable and highly repetitive flow regulation capabilities, allowing to cater for varying flow control needs with a single valve concept and with high performance standards. And moreover, it evidences a large integration potential, owing to its monolithic construction in ordinary materials, which can simplify the complex task of embedding microfluidic control into LOCs.

5. SECTION III – FLOW SENSING. MICROSENSOR MODULE

5.1. INTRODUCTION

Flow sensors are fundamental control components to ensure robust and repetitive fluid volume delivery in Lab-on-a-Chip (LOC) devices. In general, such sensors must exhibit high performance and reliability, a convenient integration method with the LOC, fast response and low cost, all of which are enhanced by the contribution of the miniaturization of the sensor elements [69].

Among the flow sensing principles described in the literature, differential pressure transmitters, thermal flow sensors, vortex flow meters or electromagnetic flow meters can be found [87]. Within these, optical and acoustic principles can be rarely found [190], whereas pressure distribution and, particularly, thermal principles have been most explored [69, 70].

The extensive use of thermal sensors owes to their simple structure and fabrication, since they do not posses any moving parts. The three main methods employed to thermally sense the flow of gases and liquids are (i) hot-wire [58, 72-76, 191] and hot-film [77-80, 82, 83, 192-199] sensors where the forced convective cooling rate due to a fluid flowing is measured, (ii) calorimetric sensors [73, 82, 86, 89, 200-206], which detect the asymmetric thermal profile owing to fluid flow and, (iii) time-of-flight sensors where the time needed to detect a heat pulse generated at the heater is tracked [88, 91, 207, 208]. Above all other methods, calorimetric sensing has been reported to be the most sensitive technique to measure low fluid flows [69, 70, 209].

Regarding the materials employed to fabricate the thermoresistors, the most typical are Au [77, 83, 194, 195, 197, 198], Ni [74, 82, 200, 210], Pt [73, 75, 76, 78, 79, 86, 89, 91, 192, 196, 202, 204, 211-213] and polysilicon [72, 191, 193, 199]. Other materials, such as Al, Cu, Fe, Pa, Ag, and W can also be found [70, 214]. Pt is mostly used for biomedical flow sensing due to its biocompatibility and corrosion resistance [215-217], whereas Ni presents higher sensitivity due to its high TCR [74, 82, 200, 210]. The most

typical substrates for the sensors are silicon nitride [72, 74, 82, 191, 193, 196, 200-203], Pyrex [79, 91] and polymers, such as Kapton [77], Parylene [78, 192, 195, 211, 213], Polyimide [58, 83, 194, 197, 198] and SU-8 [73, 89].

In terms of sensor configuration with respect to the fluid, most are placed inside the microchannel, for example, as a free standing metal resistor at the center of the fluidic channel [84, 194], or as a patterned resistor on the inner wall of the channel [85, 89]. However, off-chip sensors, i.e. placed outside the microchannel, have also been demonstrated. These feature a non-wetted resistor configuration for gases [88] and liquids [87, 218] and offer a great advantage in that they can be post-produced on the LOC. This fact reduces complexity of integration and readout and facilitates their application at any location on the LOC, helping maximize robustness of the microfluidic protocol. Amongst their main disadvantages, these sensors have lower sensitivity than their on-chip counterparts.

In this chapter, an off-chip micro flow sensor on a finalized polymeric device is presented, featuring precise and reproducible flow rate measurements over a wide range. The device responds to the need for convenient and flexible integration of micro flow sensors in complex LOC systems. It enables customization of the sensor location and has low prototyping costs in comparison to devices in silicon [88] or glass [87, 218]. The sensor is a Ni-sputtered series of resistors on a microfluidic channel, fabricated in COP polymer by hot embossing and sealed by solvent bonding to a 100 µm thick COP membrane.

An array of twenty designs has been characterized against a commercial flow sensor in order to find the maximum sensitivity as a result of changes in configuration and dimensions. First, a flow sensor for low flow rate is presented, which covers flow rates up to 2 µl/min with an accuracy of 30 nl/min at low temperatures (up to 60ºC). Next, a higher range sensor is presented, featuring a bypass channel in order to avoid the sensor's early saturation, thus covering flow rates up to 300 µl/min. It should be mentioned that the scalable construction allows flow rate tuning by modifying the bypass-channel dimensions.

Two applications for the sensor are proposed in Chapter 7: (i) monitoring and control of stability of nutrients' flow in a cell culture device and (ii) a sticker sensor that can be reversibly applied to devices to reliably monitor the completion of microfluidic steps in a LOC protocol.

5.2. CALORIMETRIC FLOW SENSOR

In the following sub-sections, the basic architecture of the sensor and its working principle will be explained. Then, an array of twenty designs will be characterized to find the optimum configuration, followed by a discussion of results.

5.2.1. Working principle

The calorimetric flow sensor presented in this work consists of a central heater surrounded by two temperature sensors, placed an equal distance upstream and downstream. There are two ways to operate the sensor, with constant heater voltage or constant heater temperature.

At a constant heater voltage and no flow, the temperature profile around it is symmetrical, as depicted in Figure 5.1, curve *a*. As the fluid flows, the heat generated by the heater is dissipated, creating a temperature distribution at the membrane that is characteristic of that particular flow rate, Figure 5.1, curves *b*, *c*. This temperature distribution will in turn cause a difference in resistance of the sensors, which can be directly measured as a voltage signal and transduced to flow rate.

The temperature distribution near the heater offers the advantage of determining the direction of the flow, by the two surrounding sensors, in a simple way. On the downside, it also saturates faster than the anemometric flow sensors, at higher flow rates.

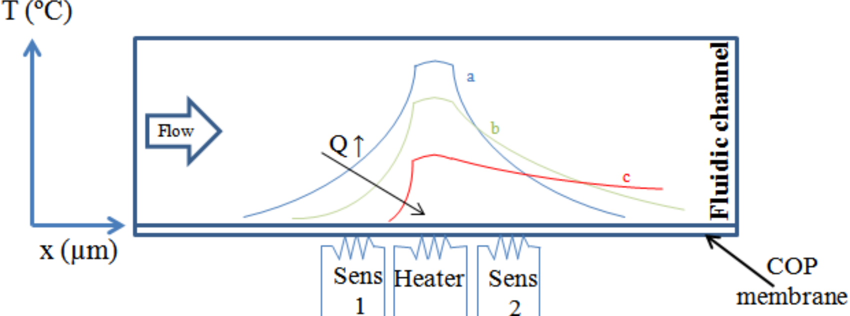

Figure 5.1. Illustration of a calorimetric flow sensor when operating the heater at constant voltage mode. (a) Symmetric heat distribution profile when the fluid is stopped. (b,c) Asymmetric profile when fluid flows.

In the constant heater temperature mode, Figure 5.2, the temperature profile is also symmetric at zero flow. As flow rate increases, the temperature measured at the downstream sensor is higher than in the constant heater voltage mode, resulting in a wider sensing range.

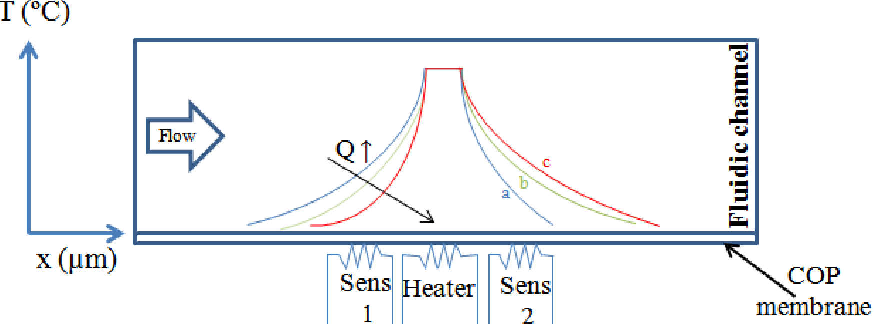

Figure 5.2. Heat distribution in a calorimetric flow sensor when keeping the heater at constant temperature.

The central heater can be also operated as anemometric hot film flow sensor. In this case, the heater is maintained at constant temperature. When the fluid starts flowing, the thermal diffusion from the heater to the surrounding fluid causes the heater to cool down. The temperature of the heater is monitorized the whole time and the power delivered to the heater is adjusted continuously in order to keep its temperature constant. As the cooling rate of the heater depends on the fluid flow rate, it can be measured as the power supplied to the heater and transduced to flow rate.

5.2.2. Architecture of the sensor chip and proposed designs

The sensor is deposited on top of a microfluidic channel of 80 µm height and 500 µm width, which has been hot embossed and sealed entirely in COP, the total size of the dye being 2 cm x 1 cm.

The selected geometry aims to increase sensitivity and it is optimized based on a previous on-chip sensor [89]. It consists of a series of long and thin electrodes arranged in meanders across the channel, Figure 5.3.(c), where the slenderness of the meanders minimizes the heating capacity for faster response [70]. In order to improve accuracy, the central heater has a four-wire configuration and the two sensing resistors have a Wheatstone bridge configuration.

According to literature, the distance between the sensors and the heater is commonly very short, ranging from 1 mm down to 10 µm [209]. Due to our interest in measuring low flows, several distances ranging from 20 µm up to 100 µm have been chosen, assuming that higher distances would cause the fluid to cool down before reaching the downstream sensor, and lower distances would increase cross-talk.

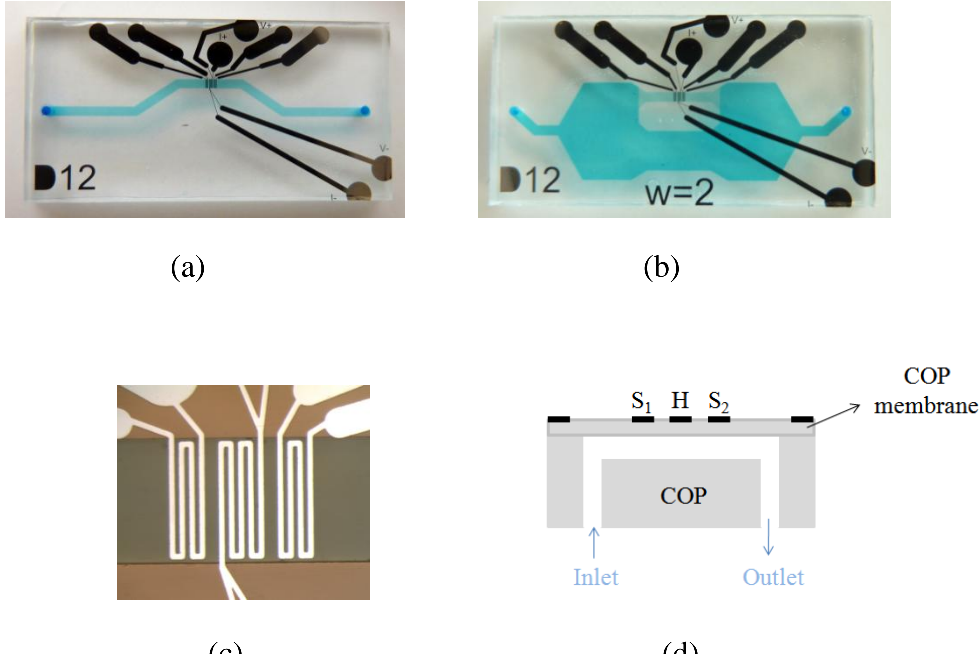

Figure 5.3. Architecture of the calorimetric micro flow sensor. (a) Image of a finished microsensor on a simple microchannel structure filled with a blue coloured solution (b) Image of a finished microsensor on a microchannel with a bypass structure (c) Close-up image of the Ni microsensor on a finalized microfluidic channel (d) Schematic structure of the micro sensor, showing the downstream sensor (S_1), the heater (H) and the upstream sensor (S_2).

To determine the optimum design, an array of 20 designs is proposed, where (i) the dimensions of the meanders, (ii) the width and length for the heater and sensors and (iii) the distance between the elements has been varied. Table 5.1 illustrates the different designs proposed, where *H* and *W* refer to the heater length and width, respectively, *D* refers to distance between heater and sensors and *S* and *W* refer to sensor length and width, respectively.

Table 5.1. Different designs with their respect heating and sensing areas, proposed to find the optimum configuration.

Design	Heater		Distance	Sensors		Area	
	H (µm)	W_H (µm)	D (µm)	S (µm)	W_S (µm)	H·10^{-3} (µm^2)	S_1/ S_2·10^{-3} (µm^2)
1	1500	10	20	2000	10	25	35
2	2500	10	20	2000	10	45	35
3	1500	20	20	2000	20	50	70
4	2500	20	20	2000	20	90	70
5	1500	10	40	2000	10	25	35
6	2500	10	40	2000	10	45	35
7	1500	20	40	2000	20	50	70
8	2500	20	40	2000	20	90	70
9	1500	10	60	2000	10	25	35
10	2500	10	60	2000	10	45	35
11	1500	20	60	2000	20	50	70
12	2500	20	60	2000	20	90	70
13	2500	20	40	2000	10	90	35
14	2500	20	60	2000	10	90	35
15	2500	20	80	2000	10	90	35
16	2500	20	100	2000	10	90	35
17	2500	20	40	4000	10	90	75
18	2500	20	60	4000	10	90	75
19	2500	20	80	4000	10	90	75
20	2500	20	100	4000	10	90	75

5.2.3. Characterization and experiments

5.2.3.1.Setup and packaging

In order to characterize the sensor, the device has been fitted in a packaging (microLIQUID, Spain), providing fluidic connection to the channel and powering and readout connections to the sensor, Figure 5.4. The packaging has a PCB mounted on it and a protective methacrylate piece to avoid convective heat dissipation, which could

impair the measurement. The setup, Figure 5.5, consists of a syringe infusion pump to generate a stream of DIW through the microchannel (SP101IZ, *WPI* World Precision Instruments, Inc.), a power supply (Agilent E3631A, U.S.A.) for constant voltage operation of the heating and sensing elements, a data logger for data acquisition (Agilent 34970A, U.S.A.) and a Wheatstone bridge board to convert the difference in resistance of the sensors into voltage signals. The fluidic outlet of the packaging is connected to a high precision flow sensor (CMOSens® SENSIRION, Switzerland) to measure the flow rate through the microchannel. The electrical circuit can be seen in Figure 5.6.

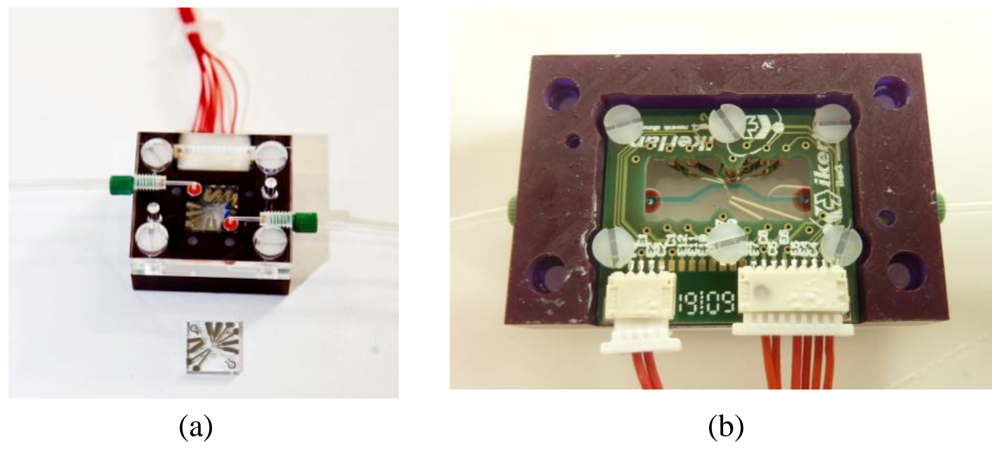

(a) (b)

Figure 5.4. Packaging used for the characterization of the micro flow sensor, enabling different dye dimensions of (a) 1x1 cm^2 and (b) 2x1 cm^2. The chip holder has electric connections made with spring loaded pins inserted in a printed circuit board (PCB). The bottom methacrylate has threaded fluidic connectors (Upchurch Scientific®) and O-rings to ensure leak tight seal.

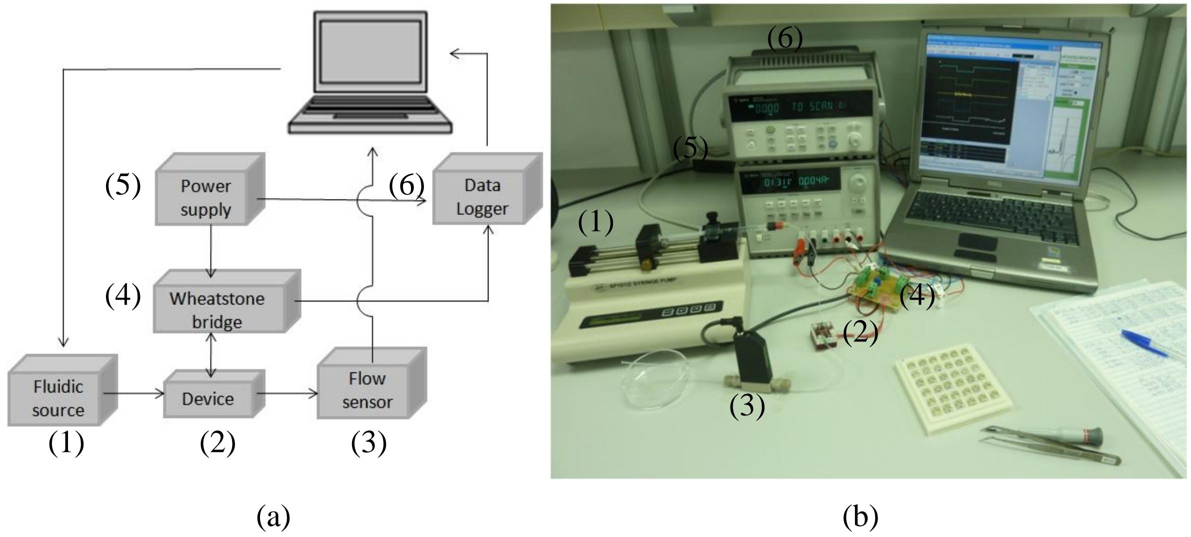

(a) (b)

Figure 5.5. Experimental setup used to characterize the calorimetric flow sensor. (a) Block diagram of the experimental setup; (b) Experimental setup for characterization.

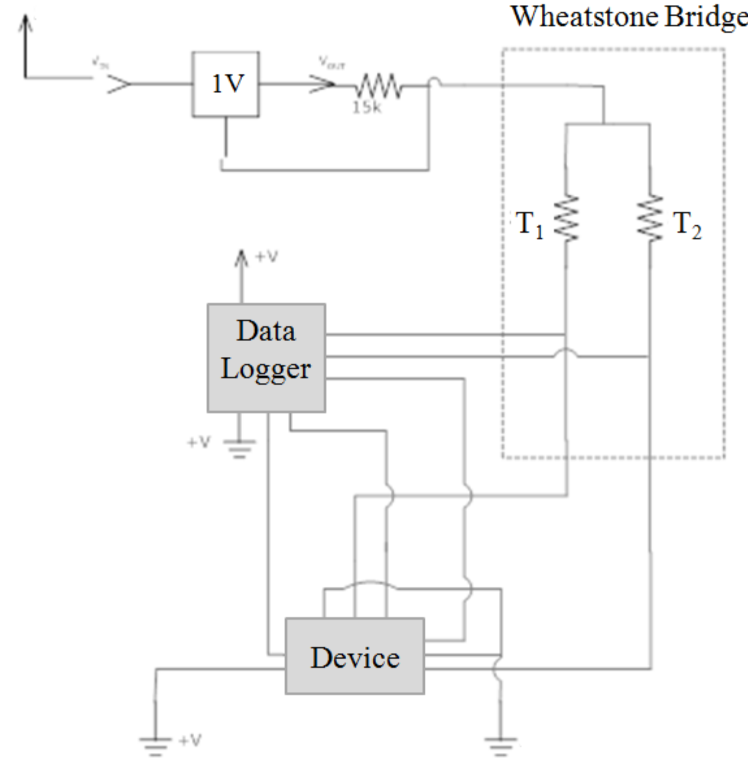

Figure 5.6. Schematic representation of the electrical circuit for readout.

In the following sections different possibilities to operate the heater will be introduced, as well as the calibration process which defines the relationship between electric resistivity and temperature and later with flow rate.

5.2.3.2.Calibration

Prior to the characterization, the TCR of the heater (linear relationship between T and resistance) has to be obtained. The measurements are performed in an oven, gradually increasing the temperature in steps of 10ºC, from room temperature to 60ºC. From this, the required input voltage for the desired heater temperature is determined, Figure 5.7.

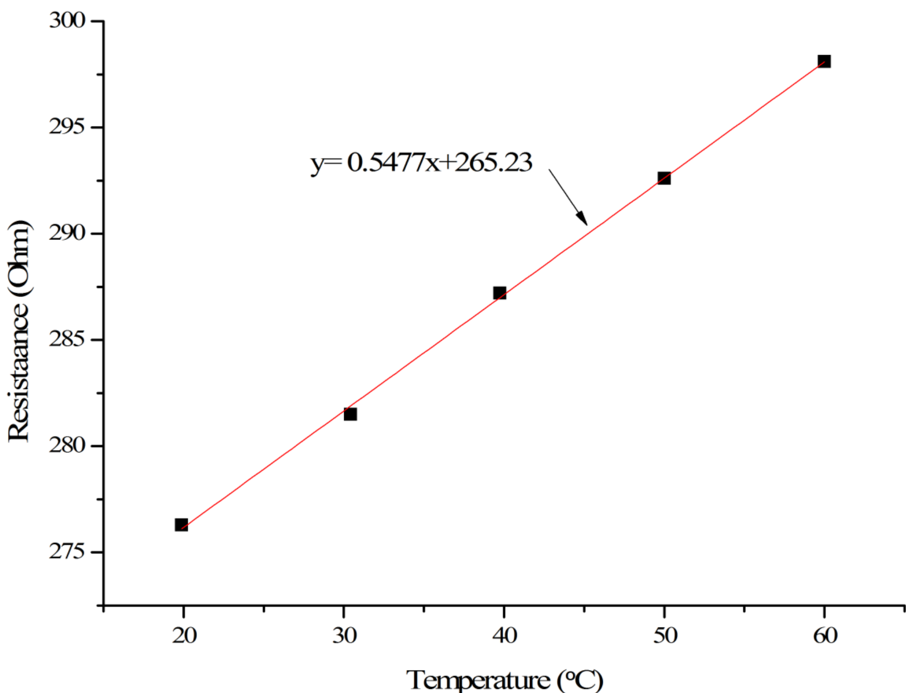

Figure 5.7. Example of the variation of the heater’s resistance as function of the temperature, design 12.

5.2.3.3.Characterization modes

The sensor is characterized in two actuation modes, namely as a calorimetric sensor with the three elements and as an anemometric sensor using only the heater element (hot wire).

For the calorimetric sensor, the constant voltage mode is employed. Here, the voltage to generate the desired temperature (40ºC, 50ºC or 60ºC) is fixed at zero flow and kept constant throughout the experiment (CV mode).

For the anemometric sensor, the desired heater temperature is maintained constant throughout the experiment, adjusting the power required to maintain the desired resistance at each flow rate value (CT mode).

5.2.3.4.Summary of tests

First, flow direction determination tests at 60ºC are carried out in CV and CT modes for the calorimetric and anemometric sensors, respectively, in order to demonstrate that the calorimetric flow sensor is able to detect flows direction, contrary to the anemometric flow sensor. It should be noted that the fluid affects the performance of the sensor as each has a different thermal diffusivity [219]. Therefore, for the characterisation, DIW is employed as a realistic approximation to the aqueous solutions regularly used in LOC systems.

For the calorimetric sensor, the optimum geometry and operating temperature are obtained from the characterization of the 20 designs in the array, at temperatures of 40ºC, 50ºC and 60ºC. Detection range, sensitivity and accuracy of the sensor are chosen as selection criteria. Next, reproducibility, validation of a general calibration equation (to avoid calibration of each device) and accuracy tests are carried out with the optimum design. In the reproducibility tests, the existence of hysteresis at chip level and an average calibration curve (voltage vs. flow rate) at wafer level are assessed. In the validation test, the average calibration curve is applied to three sensors outside the calibration group and measurements compared against a commercial sensor. In the accuracy test the capacity to discriminate between two close values is studied.

A similar procedure is followed for the anemometric sensor. Here, only the heater is required, for which the array reduces to four designs. Results indicate that CT mode widens the saturation limit, increasing the detectable flow range.

Finally, in an attempt to increase the saturation limit of the calorimetric configuration, the optimum design is also tested in CT mode, manually adjusting the values.

5.2.4. Results and discussion

5.2.4.1. Response profile and flow direction detection test

The characteristic outputs for the calorimetric (operated at CV mode) and anemometric (operated at CT mode) sensors are depicted in Figure 5.8, at 60ªC.

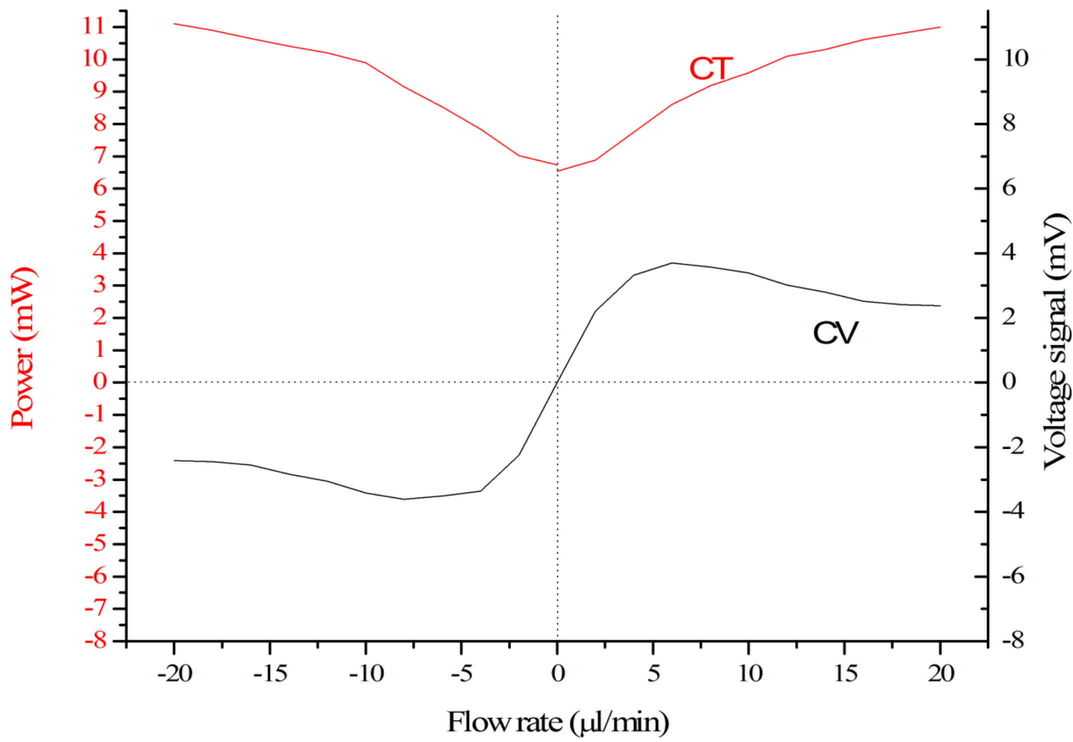

Figure 5.8. Characteristic response at 60ºC of the (i) calorimetric sensor in CV mode, dark line and (ii) anemometric sensor in CT mode, red line. The abscissa features output voltage signal vs. flow rate for the calorimetric sensor and heater power vs. flow rate for the anemometric sensor.

In the calorimetric configuration, dark line, it can be observed that the voltage does not rise past a given flow rate. This is because the saturation point has been reached, with the characteristic plateau and an exponential decrease (not shown) as a result of insufficient heat transport to the downstream sensor at high flow rates.

In the anemometric configuration, red line, the curve increases without saturating. This means that the anemometric CT configuration allows flow rate sensing over a larger range. However, comparison between both configurations shows that the calorimetric CV configuration is more sensitive at low flows, and could be used to accomplish a more accurate and sensitive micro flow sensor.

Moreover, with regard to flow direction, results confirm that the calorimetric sensor is able to detect it, the voltage sign changing with the direction. On the contrary, the

anemometric sensor could not differentiate between positive and negative flows. This is because there is no additional sensing element that can close the loop, resulting in identical power curves for both directions.

5.2.4.2. CV characterization for calorimetric sensor

The proposed array has been characterised at initial heater temperatures of 40ºC, 50º and 60ºC. The devices have been subjected to increasing flow rates of DIW, from 0 to 5 µl/min, while measuring flow rates with a commercial sensor and the voltage signal. From these, curve of flow rate vs. voltage signal has been obtained, Figure 5.9.

As it can be observed, between 0 µl/min – 2 µl/min the curve shows a linear portion. Beyond this, the sensor starts to saturate, until a plateau is reached (4 µl/min – 5 µl/min). Thus, the operation range will be limited to the 0 µl/min – 2 µl/min range.

Comparing the results between Figure 5.9.(a), (b) and (c), it can be concluded that the magnitude of the readout signal depends on the difference in resistance between the upstream and downstream sensors. This difference increases both when the heater temperature is higher for a fixed flow rate and when the flow rate is greater for a fixed heater temperature.

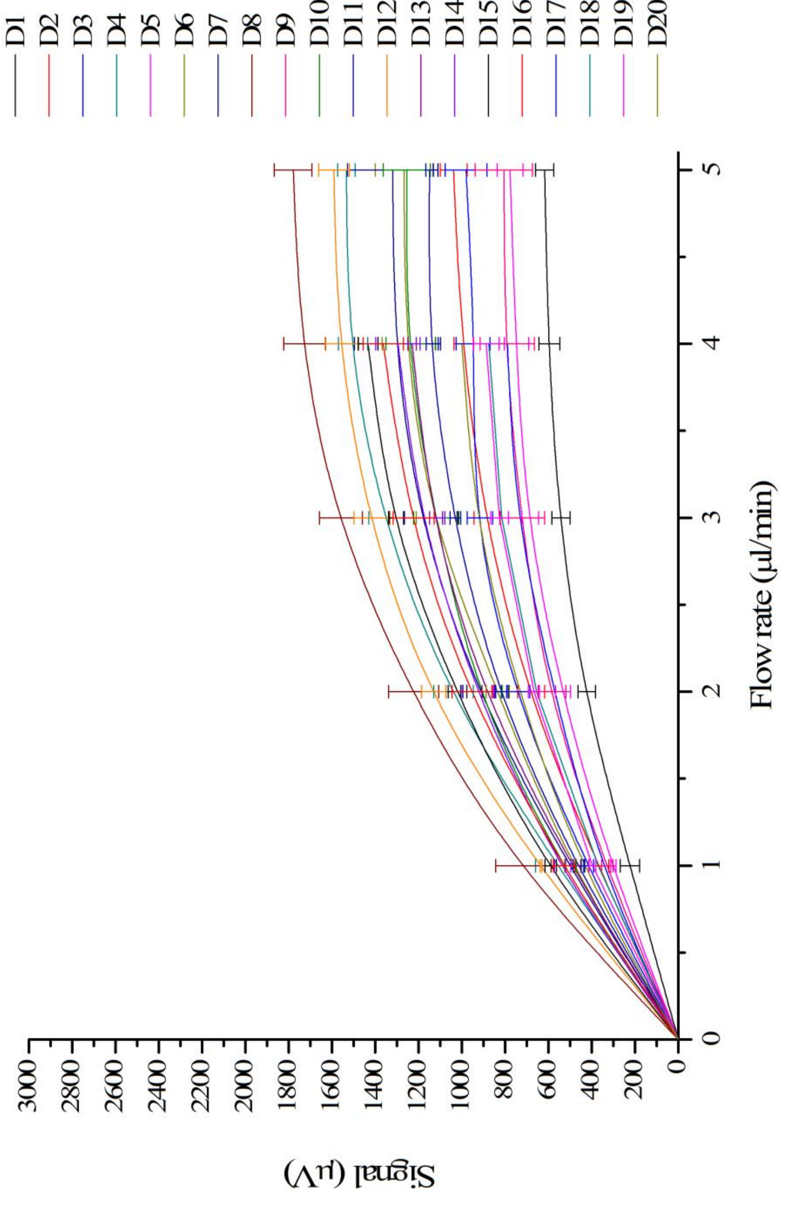

(a)

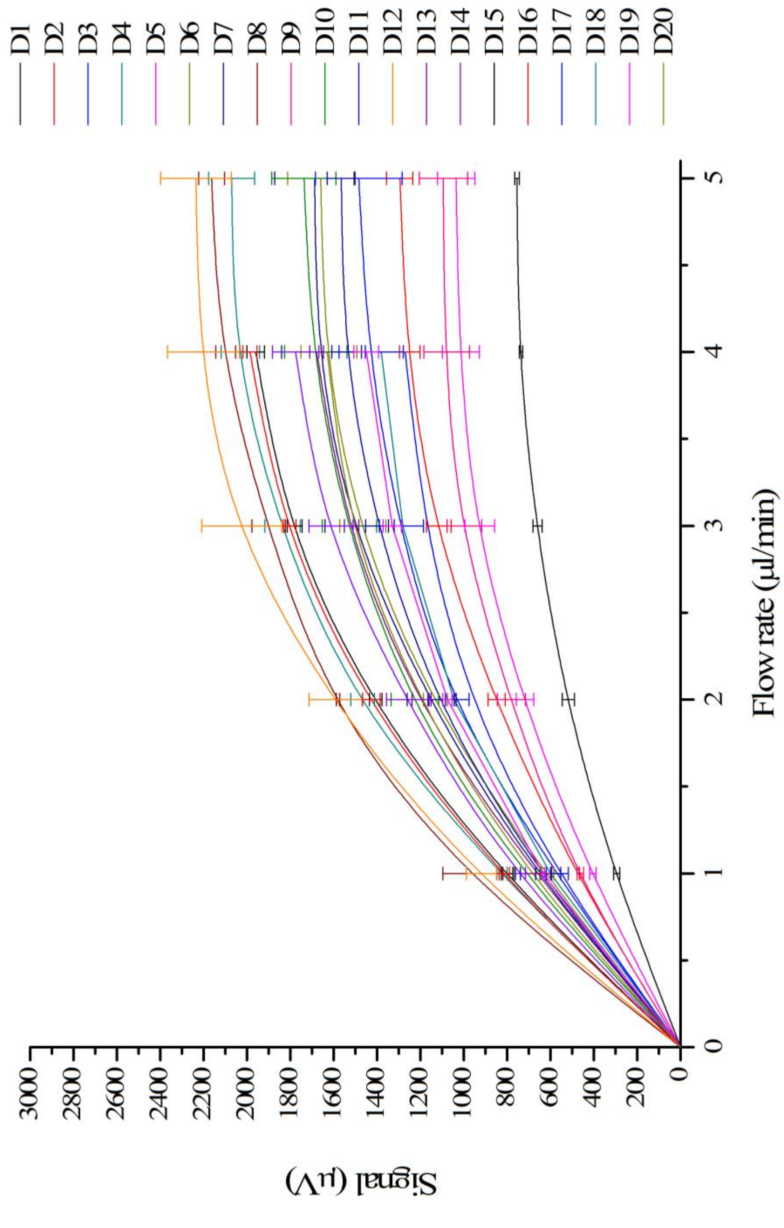

(b)

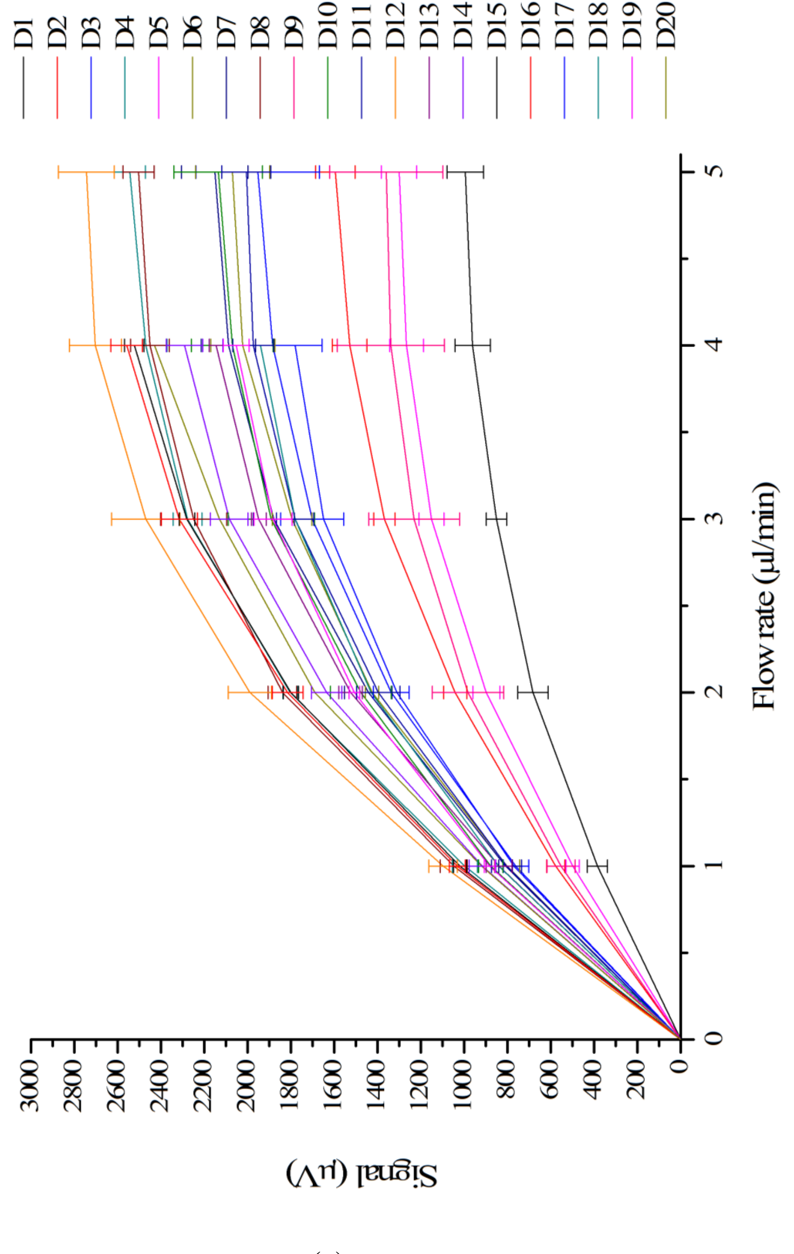

(c)

Figure 5.9. Characterization results for flow sensor array, in calorimetric configuration and CV mode, at initial heater temperature of (a) 40ºC, (b) 50ºC and (c) 60ºC. The voltage signal has been measured for an increasing flow of DIW.

The sensor sensitivity has been chosen as the selection criteria for the best design, defined as the slope of the linear portion (derivative of the sensor signal with respect to flow rate), which ought to be as high as possible in order to discriminate better two close values of flow rate. From Table 5.2, the best overall design is D12, although at lower temperatures D8 shows better performance.

Table 5.2. Characterization results for the proposed 20 designs in calorimetric configuration and CV mode. Sensitivity of each design, has been shown when operating the heater at initial temperature of 40ºC, 50º and 60ºC.

40ºC		**50ºC**		**60ºC**	
Design	**Sensitivity**	**Design**	**Sensitivity**	**Design**	**Sensitivity**
8	611.3	12	795.7	12	994.8
12	564.8	8	790.3	8	919.7
4	519.5	4	733.3	16	907.5
15	510.0	16	713.3	4	901.7
16	476.7	15	703.3	15	900.0
14	460.8	14	629.2	20	845.0
7	455.7	10	612.7	14	817.5
10	452.7	13	597.5	13	762.5
13	440.0	20	595.0	19	753.8
6	417.3	7	574.3	10	738.2
11	407.8	6	565.2	18	715.0
3	369.8	11	552.5	7	721.3
20	365.0	19	537.5	6	712.7
2	340.0	18	522.5	11	698.2
19	333.8	3	514.7	3	668.3
18	327.5	17	447.5	17	620.0
9	292.0	2	424.0	2	520.8
17	285.0	9	390.7	9	491.2
5	266.2	5	358.7	5	449.0
1	211.5	1	258.8	1	341.3

In Appendix III, the designs have been compared in terms of sensitivity against a given design parameter, in an attempt to determine their relative effect. The parameters analyzed have been (i) distance between the heater and the sensors (D) (ii) length of the heater (H), (iii) width of the heater (W_H), (iv) length of the sensing elements (S), and (v) width of sensing elements (W_S). The main conclusions are as follows:

- The increases in length of the heater (H) results in an increase in sensitivity. This is due to the increase in heater area, which transfers more heat to the liquid and from this to the sensor.

- The increase in the width of the heater (W_H) does result in a significant increase in sensitivity. This is due to the increase in cross-talk (heating of the sensing element through the membrane) and in heat transfer to the liquid cancelling out. In this case, increasing D is required to increase sensitivity.

- The decrease in the width of the sensor (W_S) does not result in an increase in sensitivity, expected from the increased resistance of the sensor. This is due to self heating of the sensor, which reduces the temperature difference between the sensor and the liquid.

- The increase in length of the sensor (S) has a similar negative effect than the decrease in width of the sensor (W_S).

5.2.4.3. CT characterization of the anemometric sensor

In this case, only the heater is employed (anemometric sensor), for which only the four heater configurations have been tested. The heater temperatures have been kept constant at 40ºC, 50ºC and 60ºC. The power needed to keep the heaters temperature constant has been obtained while the flow rate was increased from 0 µl/min to 20 µl/min, and the results have been shown in Figure 5.10.

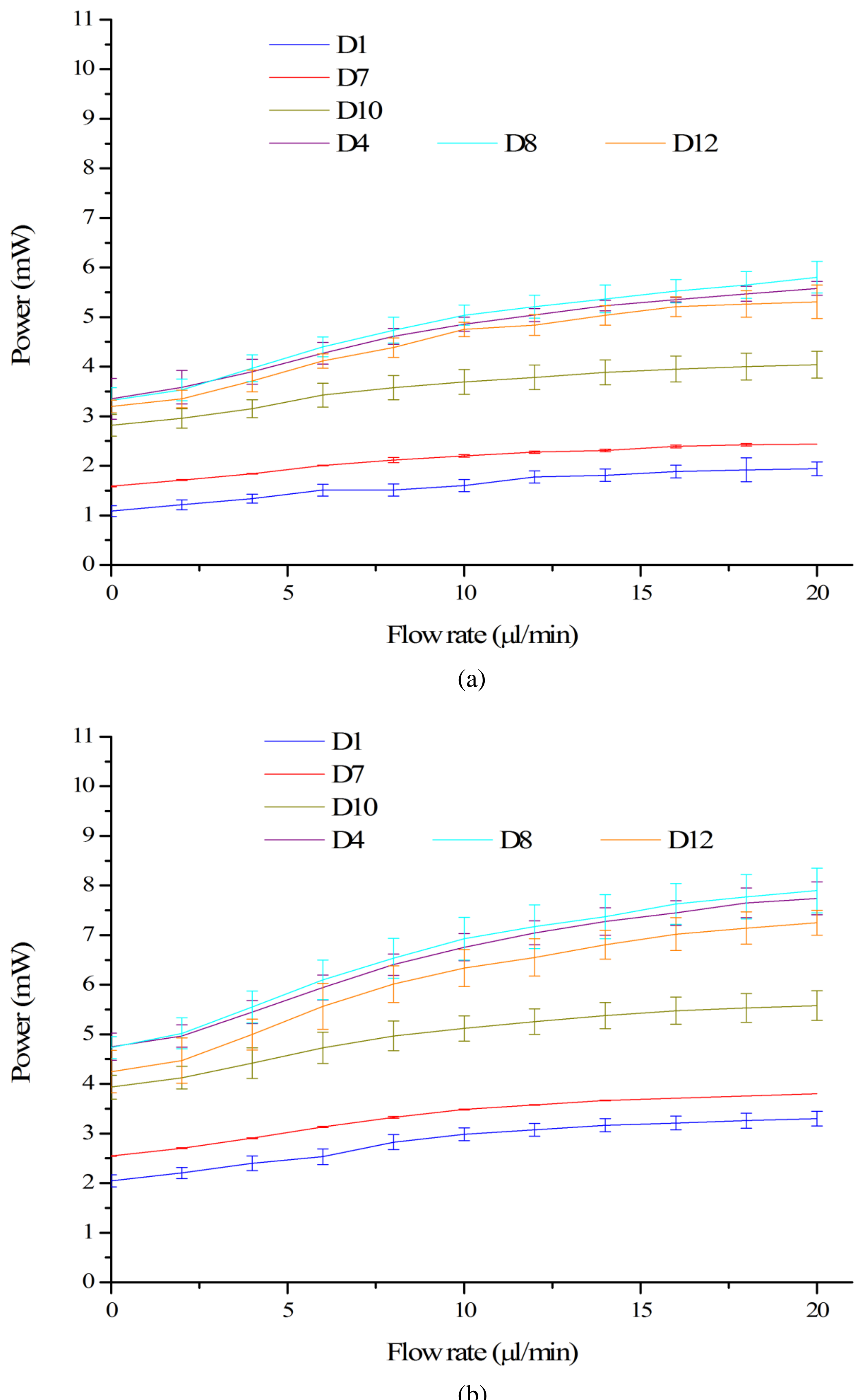
D1
D7
D10
D4
D8
D12
Power (mW)
Flow rate (µl/min)
(a)
D1
D7
D10
D4
D8
D12
Power (mW)
Flow rate (µl/min)
(b)

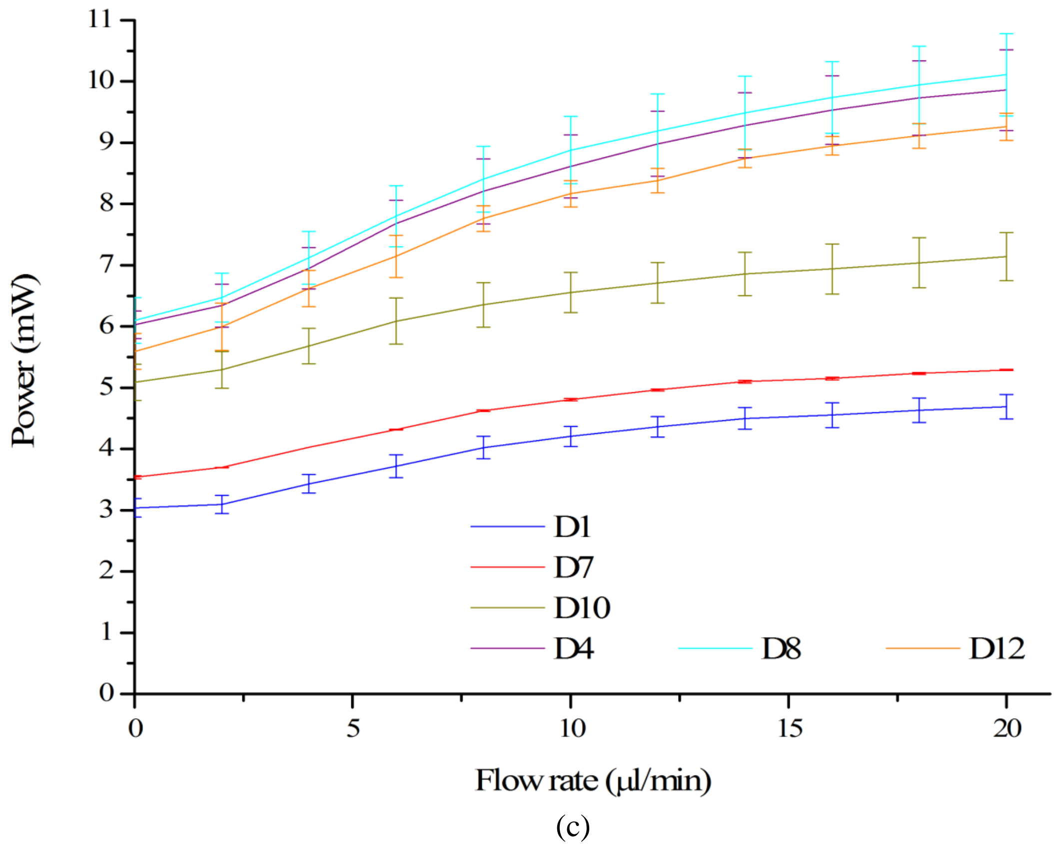

(c)

Figure 5.10. Characterization of the 4 heater designs as anemometric sensors in CT mode at (a) 40ºC; (b) 50ºC and (c) 60ºC.

From Figure 5.10, it can be observed that higher power is required as the heater area increases, due to the enhanced heat transfer to the liquid. This can be observed for designs D4, D8 and D12, featuring 2500 µm length, 20 µm width and heater area of $90 \cdot 10^3$ µm^2, more than two times larger than the other designs. The three designs for this configuration (D4, D8 and D12) show a similar response, since their heater is identical.

Comparing the results for similar heater areas, D7 (SH≈ $50 \cdot 10^3$ µm^2) and D10 (SH≈ $45 \cdot 10^3$ µm^2), it can be seen that D10 needs more power to keep the heater at constant temperature. This can be explained from its higher resistance, three times higher than D7, and consequently the drop in its resistance value is more significant for the same amount of heat transferred to the liquid. Therefore, the power needed to keep the heater at constant temperature is also higher.

Finally, saturation is observed near 15-20 µl/min, almost four times wider than the calorimetric configuration (~ 4-5 µl/min). However, the sensitivity is not as good as in the calorimetric configuration. As a result, accuracy and low flow measurements would be significantly worse. For these reasons, the calorimetric sensor has been selected to construct the final flow sensor, but a second device based on the CT mode (instead of CV) will be proposed to widen its flow sensing range.

5.2.4.4. Accuracy and Reproducibility tests

From the previous tests, it has been concluded that D12 in calorimetric configuration offers the best sensitivity. In the next sub-sections reproducibility and accuracy tests have been carried out to fully characterize the sensor's capabilities.

Five sensor devices have been subjected to increasing and decreasing flows of DIW, from 0 to 5 µl/min, while recording the flow rate with the commercial flow sensor, the voltage signal with the data logger and with the heater at 40ºC, 50ºC and 60ºC. A total of 10 measurements, 2 per device (first increasing and then decreasing), have been made to obtain the curve of flow rate vs. voltage signal, shown in Figure 5.11.(a).

As shown in Figure 5.11.(a), the sensor is accurate, as both increasing and decreasing flow curves match for all devices. This also implies that the individual sensor has a very small measurement error, although small variations amongst sensors can be seen. As mentioned previously, the sensor provides a linear relationship between flow rate and voltage signal in the 0-2 µl/min range. Because of its convenience, this will be the working range of the sensor, from which the calibration equation is obtained. Normally, a calibration curve for each device should be derived to maximize accuracy. However, it was considered interesting to derive a curve at batch level, Figure 5.11.(b), which would reduce calibration efforts with a small trade-off in accuracy. This is also done to show the reliability of the fabrication method developed in this thesis.

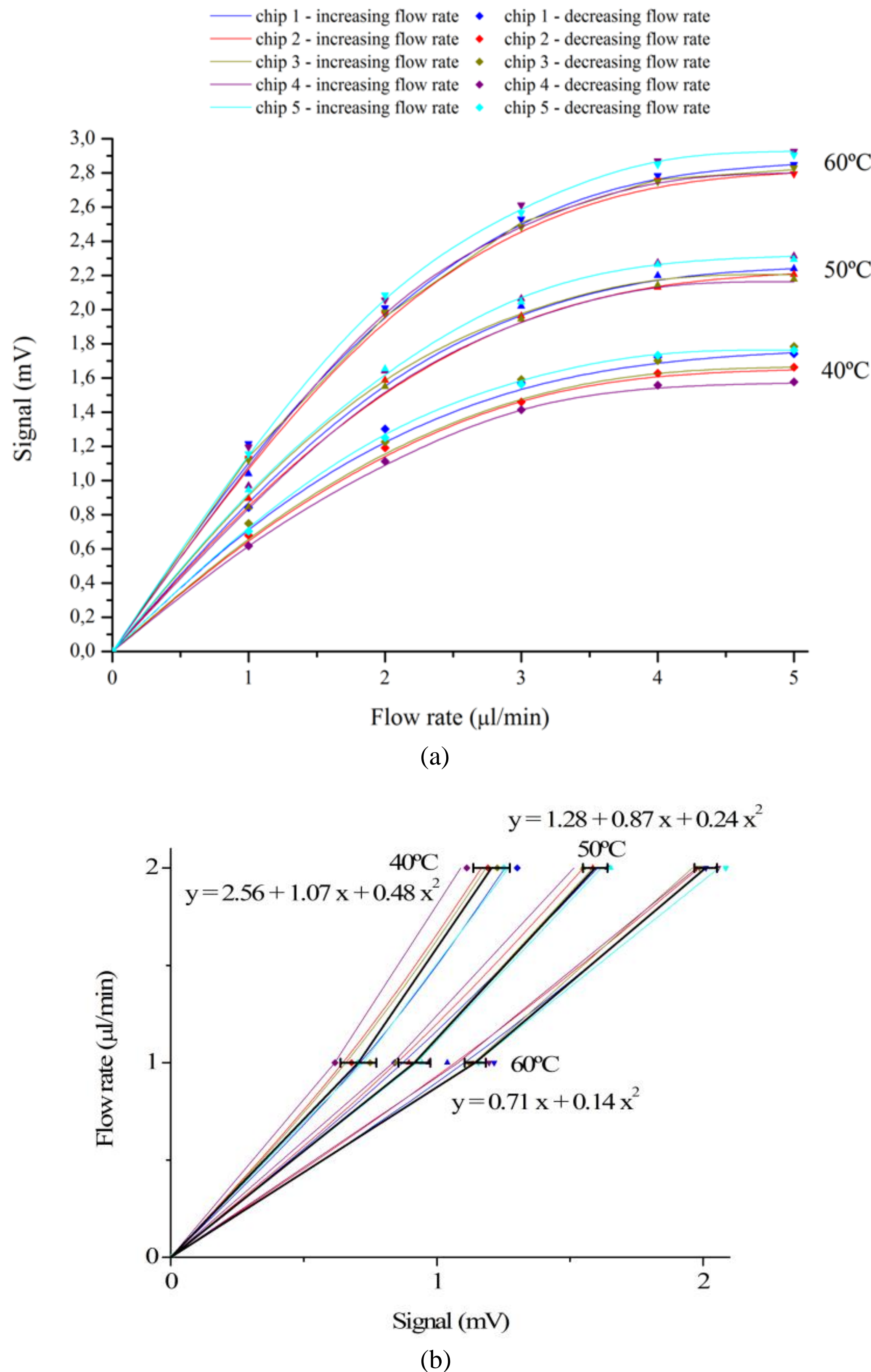

Figure 5.11. Accuracy and Reproducibility test carried out for the best sensor in calorimetric configuration and CV mode, at 40ºC, 50ºC and 60ºC. (a) Voltage signals from five devices with cyclic flow rates in 0 - 5 µl/min

range; (b) From the linear portions, the calibration equation of the 5-sensor batch has been calculated.

The convenience of this wafer-level calibration has been validated by applying it to three different devices in the wafer and comparing against a commercial flow sensor, Figure 5.12. The good match, particularly at 50ºC with 2.8% error (3.4% at 40ºC and 6.8% at 60ºC) indicates that the sensor is highly reproducible and that individual calibration could be avoided, except for high precision applications. From this, 50ºC has been found to be the optimum working temperature for subsequent applications.

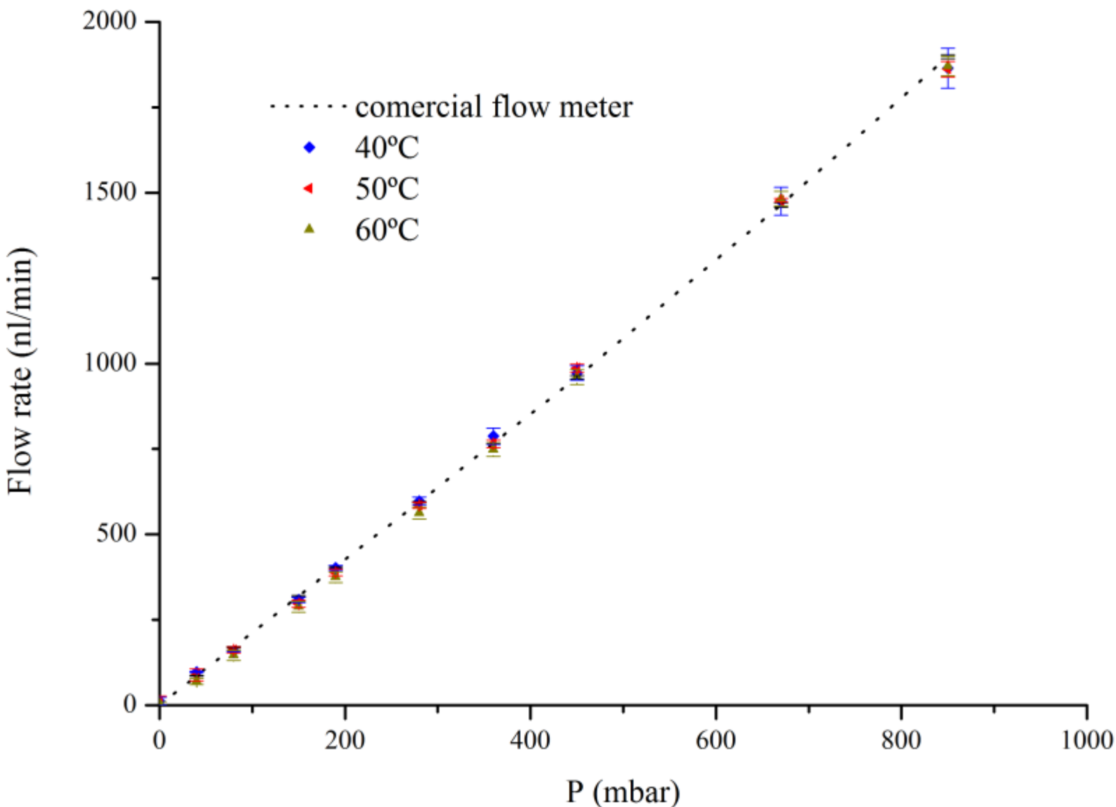

Figure 5.12. Validation wafer-level calibration equation, applied to three different chips in the wafer. Measurements have been compared against a commercial sensor, showing high reproducibility and accuracy.

5.2.4.5.Resolution test

The resolution of the sensor has been determined by increasing the flow rate at the smallest steps that the setup could deliver, 30 nl/min, to cover a range from 0 nl/min to 500 nl/min. Figure 5.13, shows the discrete measurements, which are clearly differentiated and show no deviation with respect to the sensor curve previously shown in Figure 5.11. From this, it can be expected that the resolution of the devices is better than 30 nl/min. The characterization tests show that the proposed micro flow sensor can be reliably used for monitoring flow rates with excellent precision, accuracy and reproducibility.

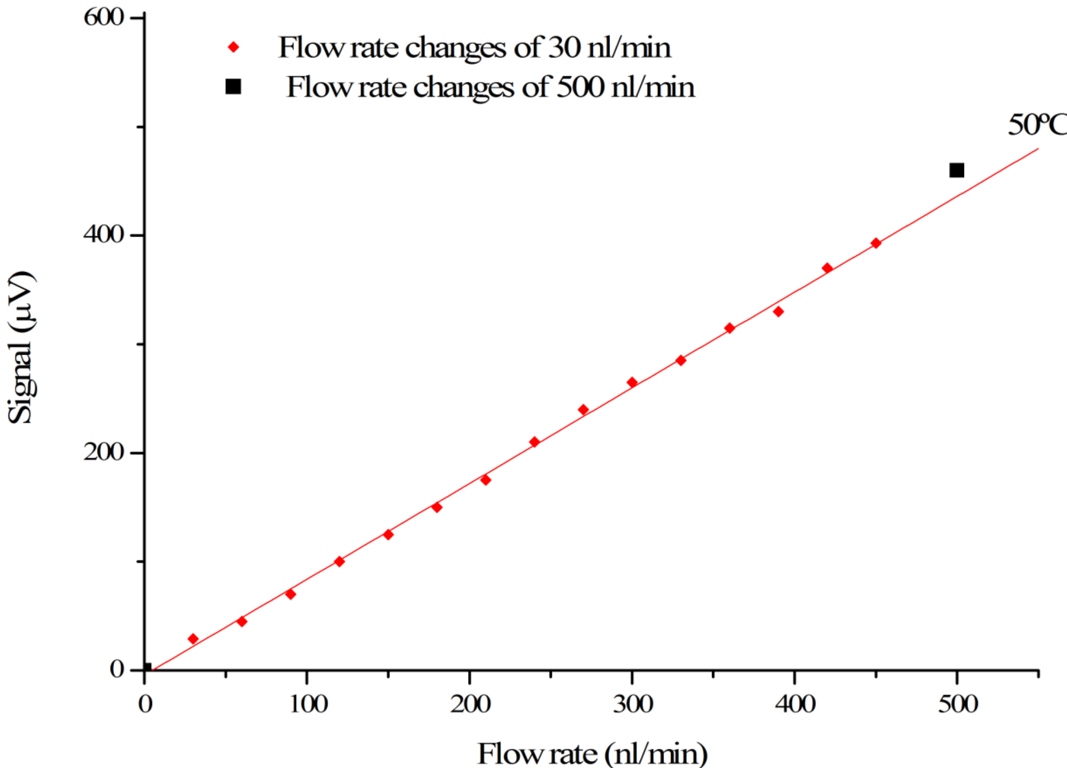

Figure 5.13. Accuracy test carried out for the best sensor in calorimetric and CV at 50ºC. The flow rate has been increased from zero to 500 nl/min in changes of 30 nl/min. The results show no deviation with respect to the previously obtained sensor curve.

5.2.4.6.Detection range extension in CT mode

So far, an optimum design has been found, which has showed excellent capabilities in calorimetric configuration, but with constant heater voltage. It has also been found that constant heater temperature extended the working range of the sensor. In this section, the possibility of applying this latter method to the best design has been investigated, with an aim to create a more versatile sensor. For this purpose, both operating modes have been compared at different working temperatures, 40ºC, 50ºC and 60ºC; the results are shown in Figure 5.14.

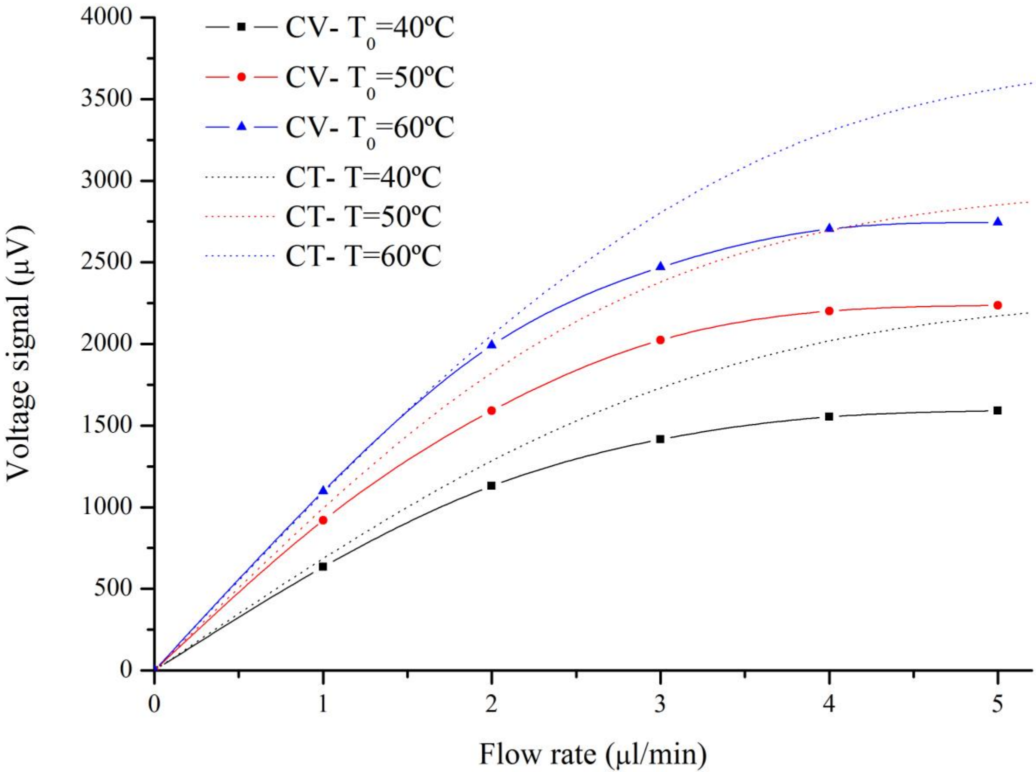

Figure 5.14. Comparison between the CV and CT operating modes for the best sensor in calorimetric configuration at 40ºC, 50ºC and 60ºC.

For the lowest range of flow rates (0-1 µl/min), the signals are very similar for both operating modes and the sensitivity remains practically the same. Beyond this range, a 30% improvement has been observed by applying constant heater temperature, since the saturation point has been delayed and the sensitivity is higher, especially as CV mode starts to saturate.

Therefore, it is concluded that calorimetric CT mode is the best option for the sensor, as it would extend its range of detectable flow rates or provide higher accuracy in similar bypass configurations. However, the effort required to build a closed-loop control system for continuous power adjustment could not be assumed in the time scale of this work, for which CV mode has been employed in the subsequent developments.

5.3. BYPASS CHANNEL FOR HIGH FLOW RATE MEASUREMENT

5.3.1. Introduction

The measurement range of the single channel sensor would be insufficient for most LOC devices. However, it is possible to extend it by adding a bypass channel, which could also be customized for a particular flow range. The bypass integration has been carried out taking into account that linearity of the calibration curve must be maintained and also dead volumes and bubble trapping must be avoided. Following the previous procedure, the calibration equation has been derived using seven devices with bypass and implemented into three other devices in the wafer to compare their performance against the commercial flow sensor at 50ºC. Satisfactory widening of the detection range to 3-300 µl/min with a measurement error lower than 5% has been achieved.

5.3.2. Device description

The previously obtained optimum has been patterned on top of a microfluidic structure consisting of a sensing channel (of identical dimensions as previously) and a bypass channel, as it can be seen in Figure 5.15. The width of the bypass channel (W) is aimed to cover different flow rate ranges. A proof of concept has been realized with a 2 mm wide channel, which would theoretically widen the detection range from 10 to 365 μl/min.

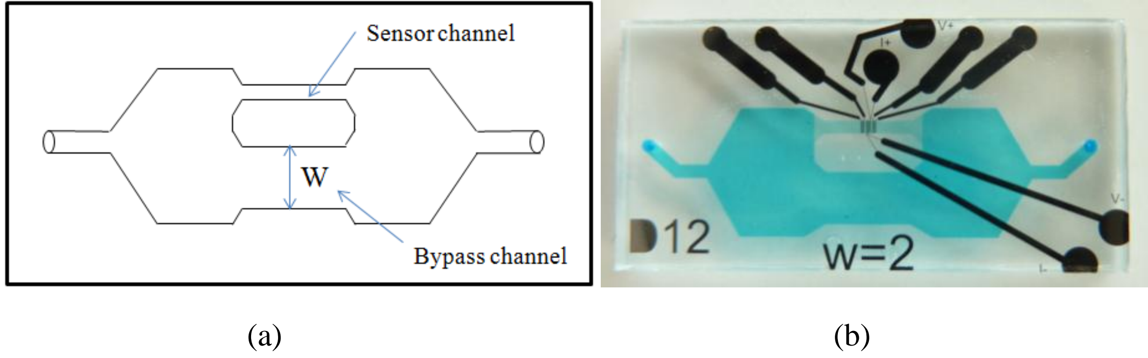

(a) (b)

Figure 5.15. Flow sensor integrated in a bypass construction to increase the detection range; (a) Schematic of the microfluidic structure comprising a bypass patterned together with a sensing channel (b) Image of the finished sensor in a 2x1 cm^2 dye, the bypass channel width being 2 mm.

5.3.3. Bypass-sensor characterization and experiments

5.3.3.1.Setup and packaging for bypass-sensor characterization

For the characterization of the bypass-sensor, the same setup as for the simple channel construction has been employed, although the syringe pump has been substituted by a Fluigent MFCS^{TM} FLEX (France) mass flow controller, Figure 5.16.

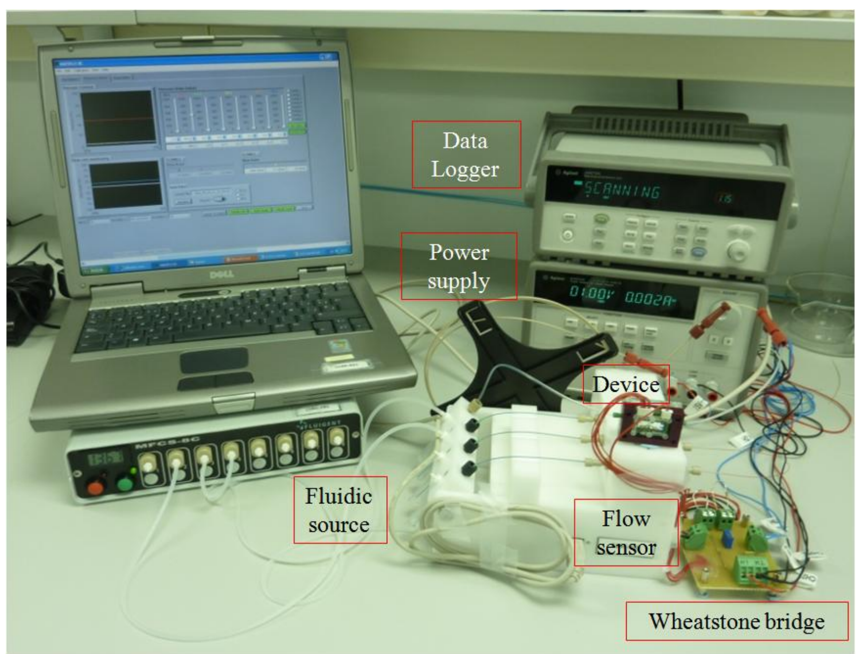

Figure 5.16. Bypass characterization setup, consisting of a fluidic source, a power supply, a data logger, a Wheatstone bridge and a packaging where all former elements are connected. A commercial mass flow is used to correlate the voltage signal measurements to the flow rate.

5.3.3.2.Experiments and results for bypass-sensor characterization

The TCR for high flow rate detection has been obtained in the same way as for the low detection sensor and the characterization has also been carried out in calorimetric configuration and CV mode.

As in the case of the valve, the planarity of the membrane affects the readout of the bypass-sensor. For this reason, profile measurements have been made and only the bypass-sensors with a deformation about of 80 µm (±10 µm) have been chosen for the characterization (80-90% yield). This selection has improved the wafer-to-wafer repeatability significantly, reducing measurements errors from 25.6% down to 12%. A discussion on the effects of poor membrane flatness is shown in Appendix III.

Seven devices have been characterized by applying an increasing pressure drop, from 0 to 1 bar. The generated flow rates and signals have been recorded as previously and are shown in Figure 5.17. From this, it can be observed that the 7 curves feature similar profiles as the single-channel sensor, with a linear portion followed by saturation region, but measuring flow rates up to 300 µl/min.

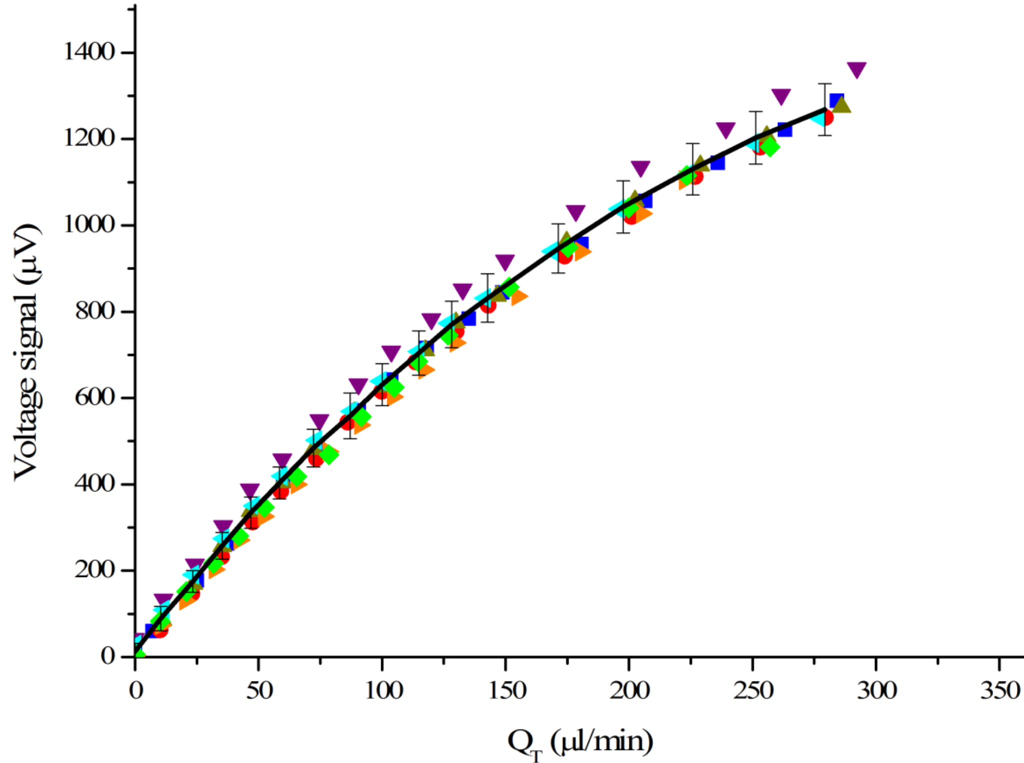

Figure 5.17. Characterization results for seven bypass sensors using a calorimetric configuration and CV mode at 50ºC. The pressure drop across the device has been increased from 0 to 1 bar.

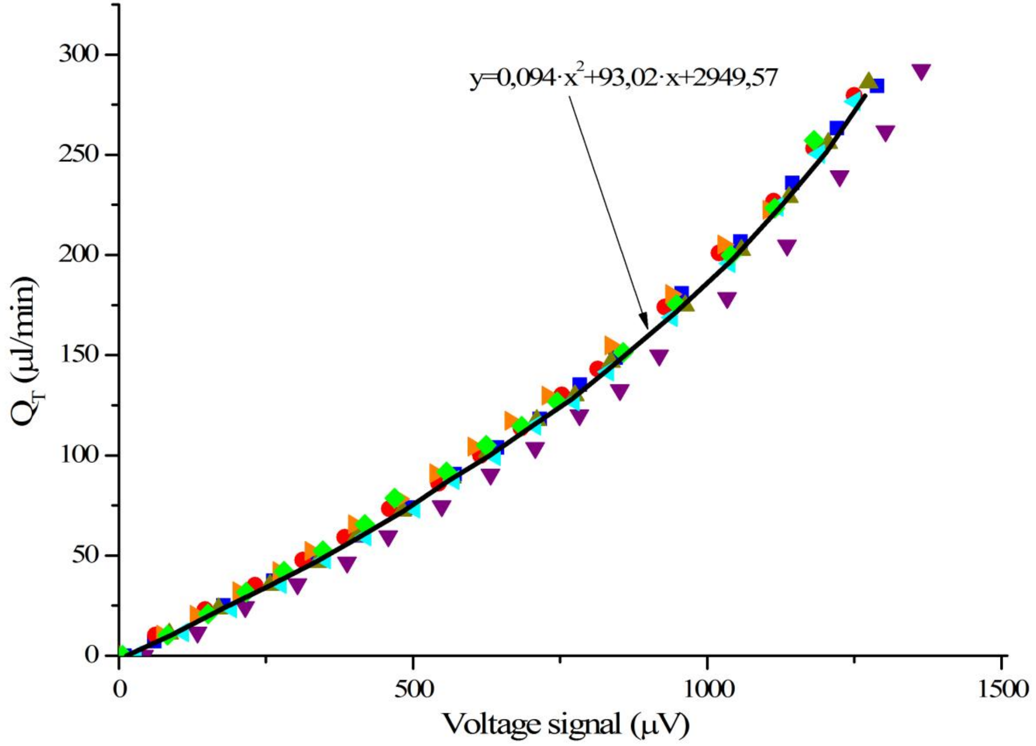

Figure 5.18. The average characterization curve obtained from seven bypass sensor.

The average characterization curve, Figure 5.18, has been calculated and applied to three different chips in the same wafer. Next, the flow rates have been validated against the commercial sensor, Figure 5.19. Again, it is acknowledged that for high precision applications, it is best to carry out an individual sensor calibration.

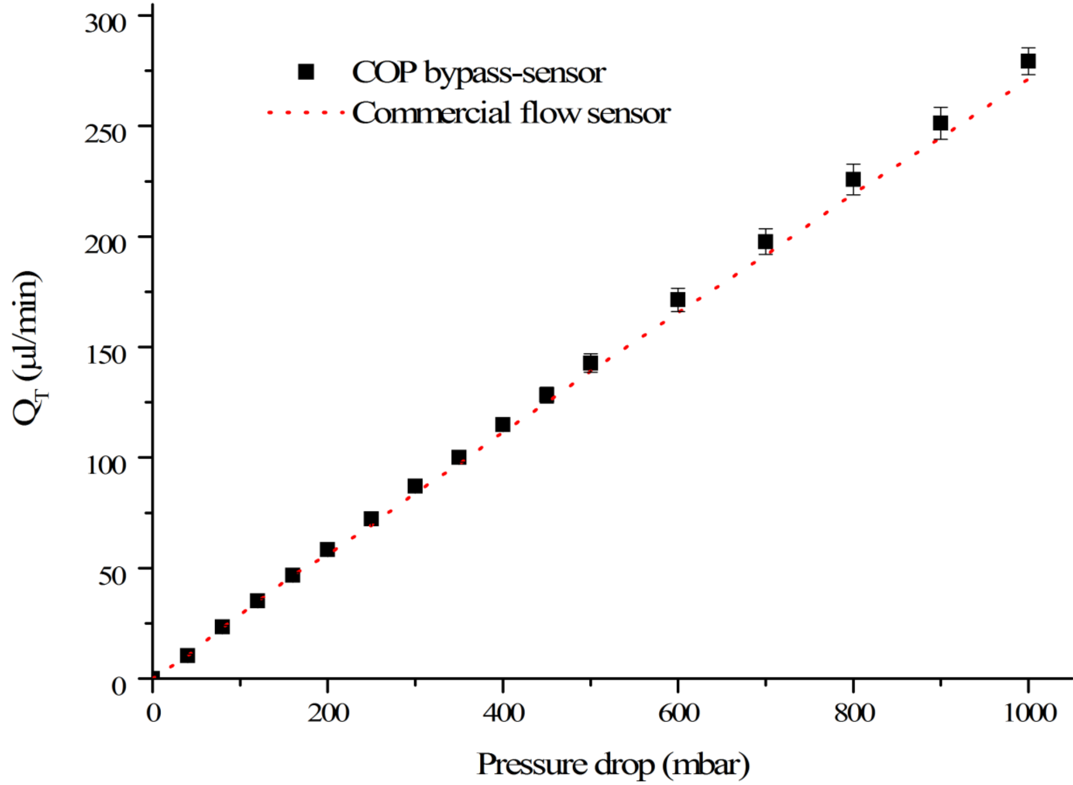

Figure 5.19. Validation of bypass' characteristic equation, which has been built from seven chips and used to measure flow rate in other three chips. The average of the flow rates measured has been compared to the measurements of a commercial flow sensor.

As it can be observed, satisfactory widening of the detection range has been achieved, namely a 100-fold increase, covering the 3-300 µl/min range with a measurement error less than 5%. In both low and high flow sensors, as fluid flow increases, the saturation point becomes closer and measurement errors become larger for the highest flow rates, owing to the lower heat transmission from the heater element to the fluid due to the velocity of the fluid [209]. Although the accuracy of the sensor is lower for the whole range, recalibration of the sensor for a certain range can be made for high-precision applications.

5.3.4. Flow sensor readouts evolution

The following experiment attempts to test the flow sensors performance with the time. For that purpose, a routine of flow rates has been defined, and for each flow rate the resulting voltage signal has been converted into flow rate by the calibration curve previously obtained, and results compared to the flow rate measured by the commercial flow sensor.

The routine has been realized five times, and results are shown in Figure 5.20. The first four cycles have been performed one after the other and the fifth cycle after 65 hours. Comparison between readouts and the commercial flow sensor shows great agreement among them, including the response after being 65 h continuously working. In Figure 5.21 can be seen that the error accomplished is less than 5% between 10-200 µl/min, and around 20% and 12% below 10 µl/min and beyond 200 µl/min, respectively.

This demonstrates that whenever the presented flow sensor operates at controlled environments of constant humidity and temperature, it is able to operate at least several days without observing any drift in the readouts.

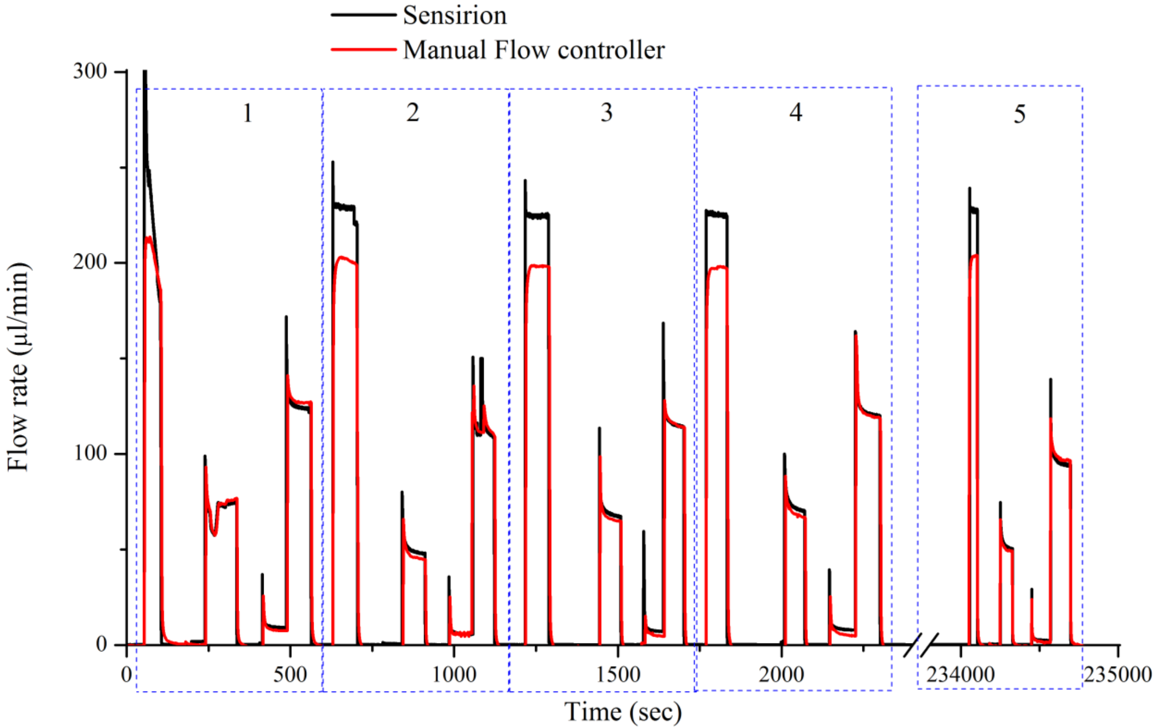

Figure 5.20. Flow sensor readout evolution with time. Five cycles of a routine of flow rates have been realized, performing the first four, one after the other, and the fifth cycle after 65h. For each step the flow rate has been obtained by converting the voltage signal into flow rate value, and it was compared against a commercial flow sensor measurements.

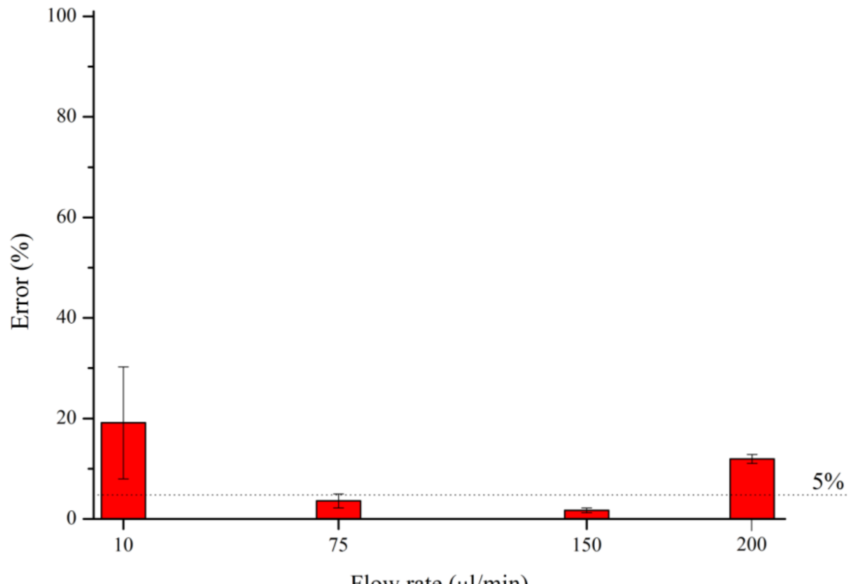

Figure 5.21. Measurement error for the flow sensor with respect to the commercial flow sensor in the readout evolution test, shown in percentage.

5.4. CONCLUSIONS

- The presented device is the first approach towards an off-chip monolithic flow sensor in polymer material. This construction allows patterning of sensors anywhere on the chip to determine local flow conditions, which are impossible to measure with conventional sensors.

- A high resolution and accurate sensor has been developed, which operates at low temperatures. Furthermore, its fabrication process is reliable enough to allow for a simpler calibration, using only a sample of devices in the wafer and applying the same calibration curve to any other chip in the wafer.

- Ni electrodes have enhanced the sensitivity of the off-chip sensor, while reducing costs. Its location outside the device also avoids direct contact with the sample, thus allowing sensitive or corrosive liquids to be used.

- A bypass construction has been introduced to delay the saturation point of the sensor and cover higher flow ranges, successfully demonstrating the detection range widening concept and enabling measurements between 3-300 µl/min with an error less than 5%, with no dead volumes and no trapped bubbles. Although the accuracy of the sensor is lower for the whole range, recalibration of the sensor for a certain range can be made for those high-precision applications.

- In general, the scalability characteristic makes the proven concept very interesting, providing improved performance for flow sensing in comparison with other works, for example in terms of the relation between the measuring range and the resolution, where 0-1 µl/min range with 250 nl/min resolution is available [192], or simply in the measuring range when comparing to 3-167 µl/min with 10 µl/min resolution [194], or others that afford too higher flow rates for LOC devices [77, 195, 201]. Comparing to other external configurations, this is the first monolithic approach fully fabricated in a thermoplastic material which offers similar

capabilities [218], or improved ones for a great amount of LOC applications [87, 88].

6. SECTION IV – LIQUID FLOW CONTROL SYSTEM

6.1. INTRODUCTION

Handling of small flow rates is becoming increasingly important for diverse, economically important applications, such as bioanalytical systems, pharmacy, food, analytical instrumentation, energy, micro reaction systems or petroleum refining industry, where accurate and repeatable mass flows are required.

Moreover, as mentioned in previous chapters, liquid control is fundamental for successful operation of LOC systems. However, as in case of microvalves, there is still no micro flow controller that can be adequately integrated in full polymeric LOCs, that is easy to fabricate and compatible with industrial mass-production techniques [97].

In this chapter, the modular components from the previous chapters have been integrated into a monolithic closed-loop liquid flow regulating system fully made of COP. Therefore, the device is composed of a hot embossed channel with a post-produced off-chip thermal flow sensor in bypass configuration and a flow-regulating microvalve.

The micro Liquid Flow Control System (LFCS) has proven excellent reproducibility and accuracy.

Therefore, it was verified that the modular approach is a realistic option for high-quality prototyping of microfluidic elements (chambers, channels, sensors and valves) in a monolithic, final material device, reducing the risk and cost associated with LOC optimization for mass production.

6.2. ARCHITECTURE AND WORKING PRINCIPLE

6.2.1. Architecture

In this section, the construction of the LFCS will be explained. The layout, highlighting the different elements and the finished device are shown in Figure 6.1. The parts coloured in red, blue and turquoise represent the measuring channel, the bypass and the sensor, while the green and black parts represent the microvalve module.

For the microvalve, design D4, having a membrane diameter of 3 mm with a seat diameter of 1 mm and a gap of 20 µm was chosen. This construction is considered the best option because it features a linear flow regulation profile that facilitates flow control and an affordable closing pressure of 2 bars.

With respect to the flow sensor, a bypass construction is required whose detection range is within the flow range that the microvalve can regulate. The bypass design introduced in the previous chapter is well within these limits and it consists of a sensing channel 75 µm high and 500 µm wide (shown in red) and bypass-channel 250 µm high and 2 mm wide (shown in blue). Finally, the optimum sensor configuration found in Chapter 5 has been deposited on the finalized device.

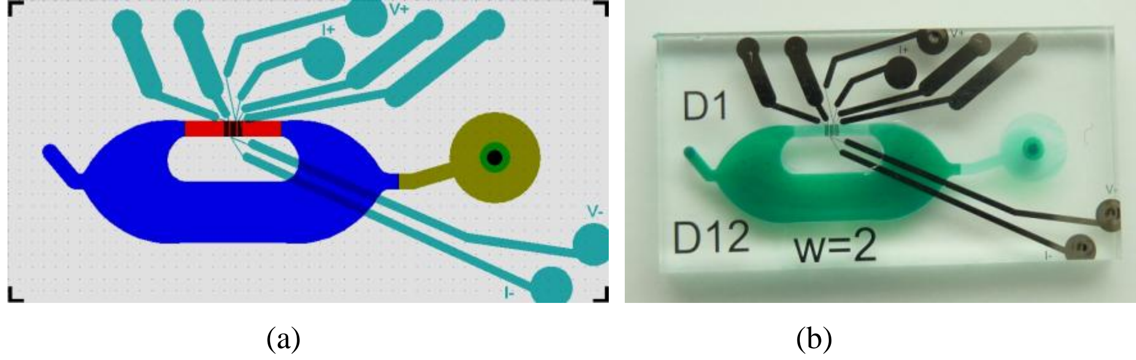

(a) (b)

Figure 6.1. Architecture of the microliquid flow controller, featuring all the elements introduced in the previous Chapters and according to the previously derived fabrication method a) layout of the device, where each colour refers to a different part of the device. b) Image of the finished liquid

flow controller in a 2 cm^2 dye, filled with diluted green-coloured solution.

6.2.2. Working principle

The working principle of the LFCS is depicted in Figure 6.2. First, a constant-pressure source is used to drive the liquid through the device. Then, the resulting flow rate is measured by the sensor module, which communicates the signal to the pressure regulator that controls the membrane via a computer-aided PID control (Labview). The closed-loop compares the signal against the set point and modulates the pressure on the membrane to arrive at the desired flow rate.

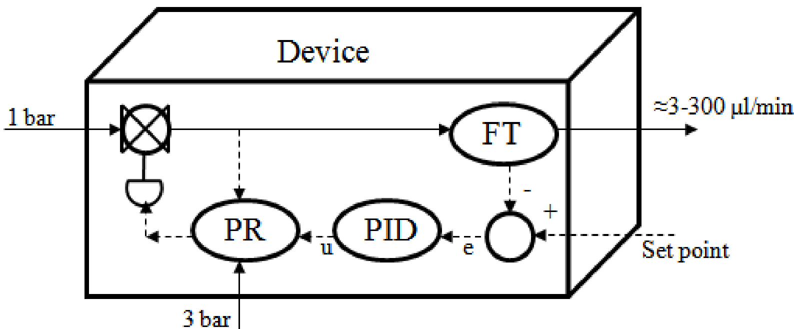

Figure 6.2. Block diagram of the LFCS working principle, where the flow sensor (FT) sends the flow rate value to the PID controller, which modulates the pressure on the valve (PR) to minimize the error (e) between the measured flow rate and the desired one.

6.3. LFCS CHARACTERIZATION AND EXPERIMENTS

In this section, a description of the setup and packaging used for the characterization are detailed, as well as the computer-aided control. Finally, the device characterization experiments are presented.

6.3.1. Setup and packaging

The setup consists of (i) a packaging, Figure 6.3, which provides fluidic connection to the device, pneumatic actuation to the valve and powering and readout connections to the sensor by means of a mounted PCB (microLIQUID, Spain), (ii) a pressure dispenser for moving the fluids (Ultra® 1400 EFD), (iii) a miniature pressure regulator to modulate the pressure on the membrane (Parker Hannifin S.L.), (iv) a data logger for data acquisition (Agilent 34970A, Agilent technologies), (v) a PCB, dedicated to driving the LFCS operation and (vi) computer-aided PID control loop feedback mechanism, programmed in Labview. The block diagram of the setup is shown in Figure 6.4 and the actual setup in Figure 6.5.

Figure 6.3. Image of the packaging with an LFCS device, which provides connection to all source and control elements.

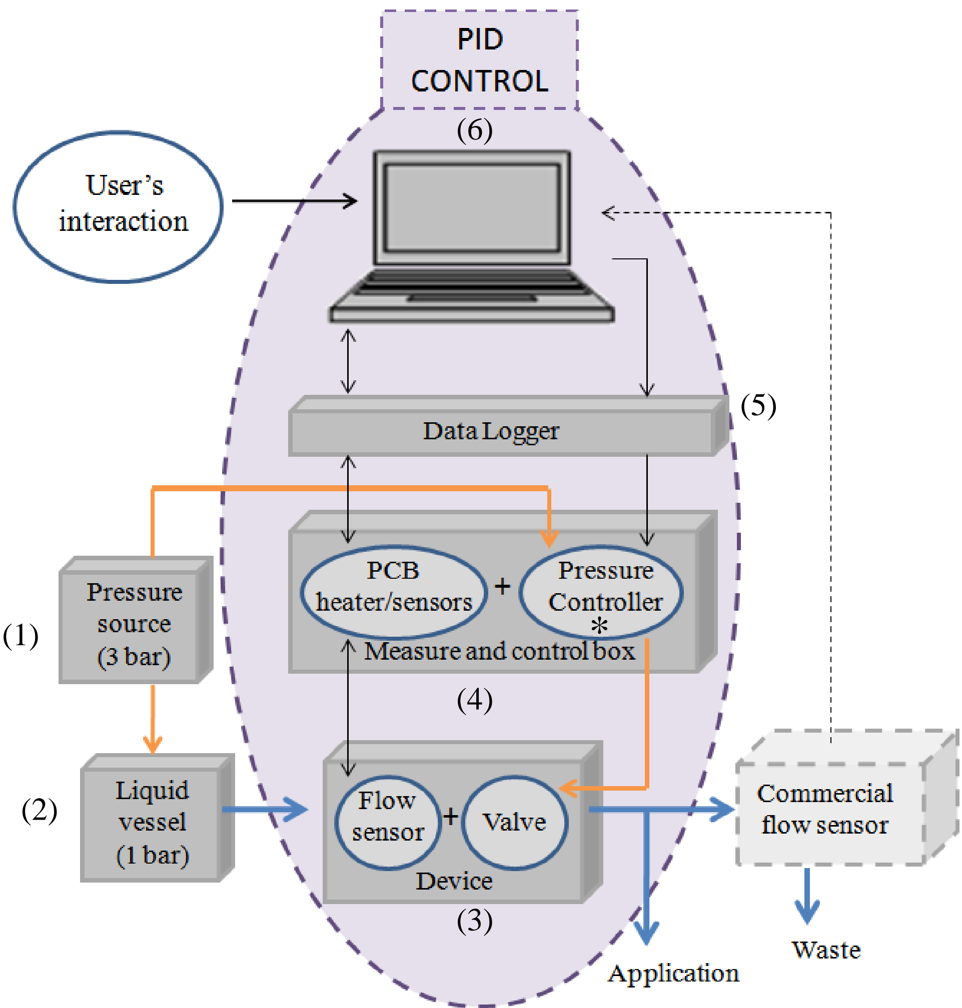

Figure 6.4. Block diagram of the experimental setup. The measure and control box features a pressure controller to regulate the actuation on the valve membrane and a PCB that integrates all control elements and connects them to the PID control. The orange rows refer to compressed air, black rows refer to electrical signal (input information or execution commands) and the blue rows refer to the liquid flow, whose flow rate is measured before ending in the waste. The user options include desired flow rate, sensor's working temperature and zero-flow signal balance.

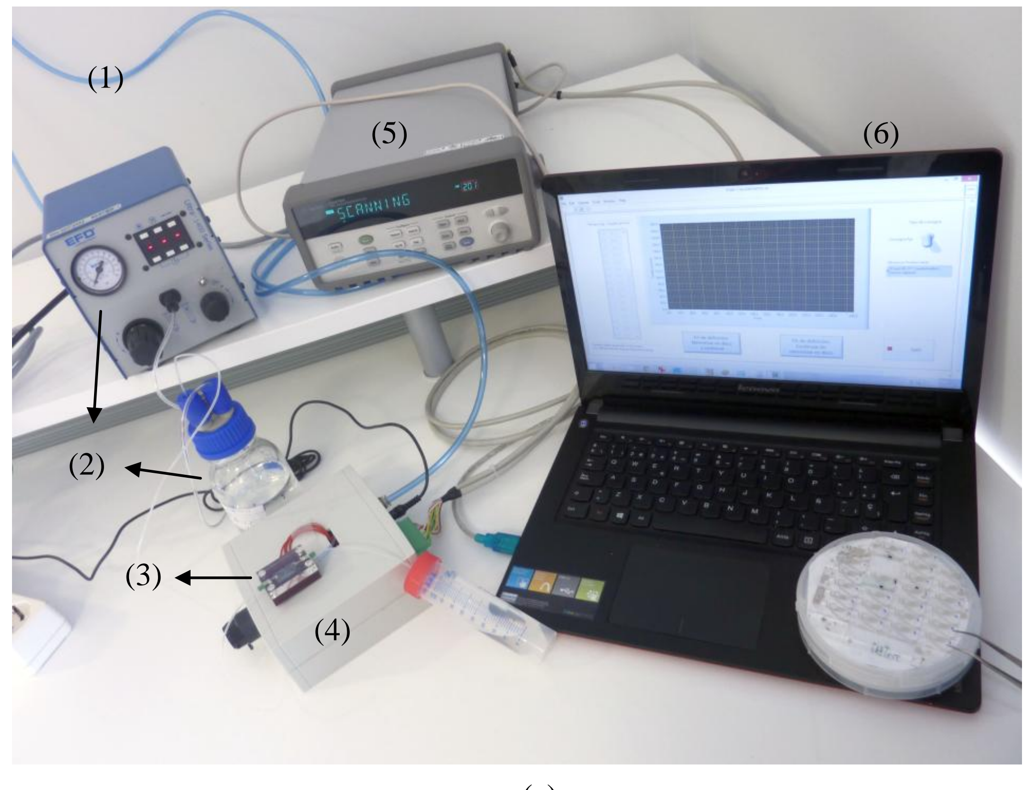

(a)

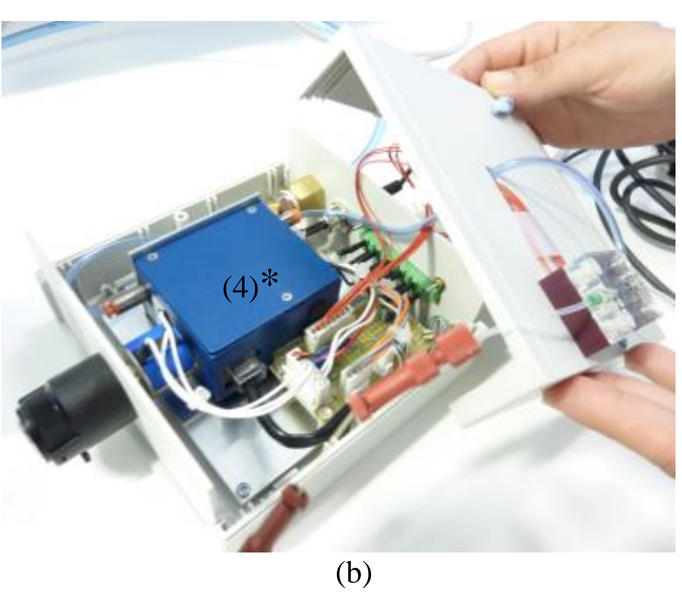

(b)

Figure 6.5. Setup for characterization of the LFCS, (a) consisting of (1) a main pressure source (3-6 bar), (2) a pressure dispenser for moving the fluids (Ultra® 1400 EFD) and a liquid vessel (1 bar), (3) The flow controlling device, (4) the measure and control box that contains a pressure regulator* to modulate the pressure on the membrane (Parker Hannifin S.L.) and a PCB to integrate all control components and connect them to

the PID control, (5) a data logger for data acquisition (Agilent 34970A, Agilent technologies) and (6) a Labview-based control program. (b) Image of the measure and control box with the pressure regulator (4)*, with the multi-turn potentiometer (black knob) for zero flow signal balance.

6.3.2. PID control tool

In order for the LFCS to perform accurately, a closed-loop feedback system is required, which translates the flow sensor readings into valve motion. In this section, the Labview program employed will be described in its most basic terms, focusing the explanation on the user's options.

The control and display program was made by implementing an Event-driven State Machine, which used to implement decision making algorithms, where the user's input determines which state to go next. The main options available are (i) Initialization State 1, (ii) Initialization State 2, (iii) Heater State, (iv) Measure State and (v) Stop State. The actions involved at each State are as follows, and the programming interfaces and the user interfaces are shown in the Appendix IV:

(i) Initialization State 1: the program asks to the user to input the calibration data (discrete points, not the equation) for the flow sensor. In order to convert the output voltage signal into flow rate more accurately, the program approximates the value with the least-squares method.

(ii) Initialization State 2: the user determines the flow rate routine that the LFCS must comply with, which can either be a sequence of flow rates or a constant value.

(iii) Heater State: the user introduces the TCR obtained during the sensor's characterization to translate input voltage into temperature. In the previous

chapter an optimum working temperature of 50 ºC was found. At this point, the user also needs to equilibrate the Wheatstone Bridge at zero flow, for which the multi-turn potentiometer was fitted.

(iv) Measure State: the flow meter starts working under the control of the PID. Initially, the microvalve is fully open and the fluid starts to run. Once the flow rate is measured, the PID controller compares it to that defined by the user and a command is sent to the pressure controller in order to modulate the membrane's position and correct the flow rate.

(v) Stop State: the user finishes the execution of the flow controller by simply clicking on the STOP button placed in the flow rate real time monitoring interface. To finish the application the program gives the opportunity to save all the data measured during the application, such as measured flow rate, exerted pressure against the microvalve, voltage measured at the Wheatstone Bridge, the resistance of the heater etc.

6.3.3. Characterization of the LFCS

To LFCS was characterized with a routine of increasing flow rates, as shown in Figure 6.6, in steps of 10 µl/min, which is considered thorough enough to evidence performance errors.

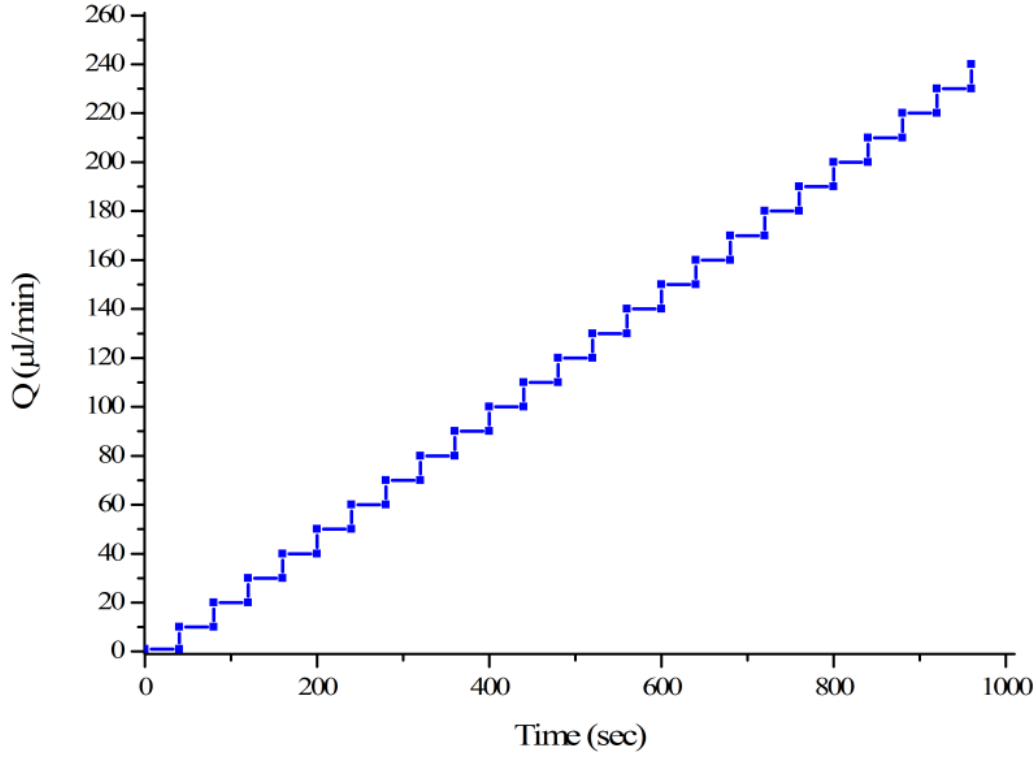

Figure 6.6. Flow rate routine for characterization, in increasing steps of 10 µl/min to evidence performance errors.

As it can be observed in Figure 6.7, the accuracy and reproducibility of the separate modules remains. Here, an error of less than 5% is achieved in the range between 30-230 µl/min, less than 15% below 30 µl/min (15% of the maximum flow rate), and around 30% for the stopped liquid, as is depicted in Figure 6.8.

With respect to response time, as it can be seen in Figure 6.9, the stabilization time is around 10 s, which can be too high for some applications. However, this stabilization time is mostly dependant on the software, which for this experiment has an established sensor reading and response command frequency of 1 sec. Thus, for demanding applications, this parameter can be simply changed in the software.

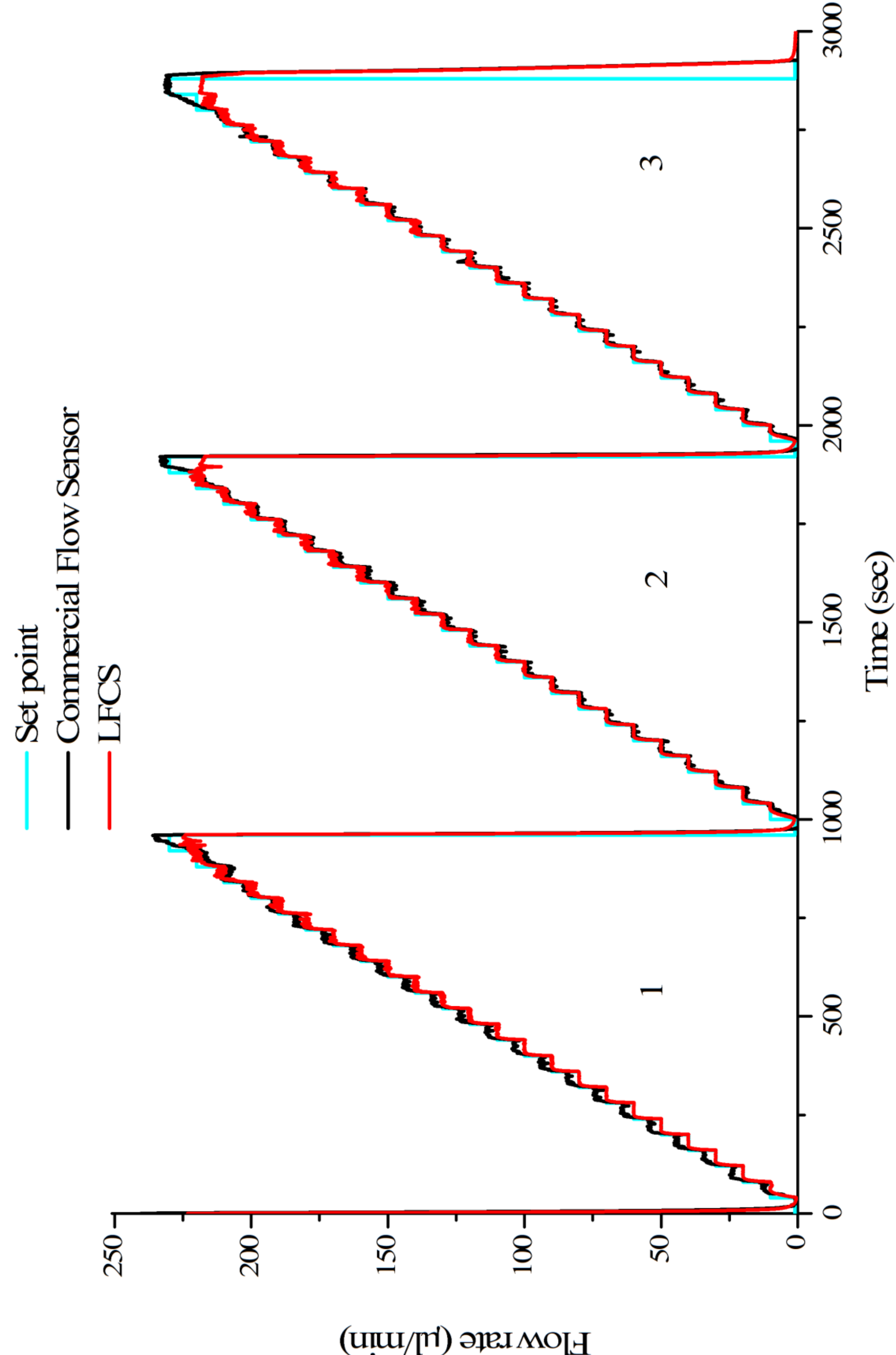

Figure 6.7. Characterization of the LFCS. Three cycles of increasing 10 µl/min steps, up to 230 µl/min, have been sequentially performed and the delivered flow rate is compared against commercial flow sensor measurements.

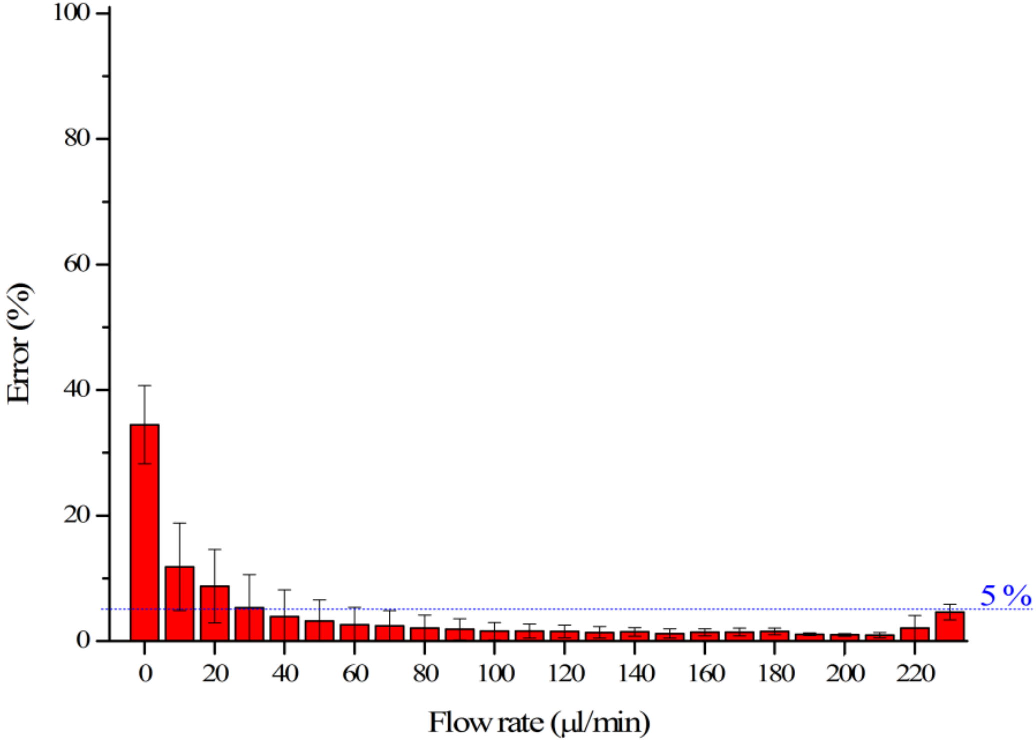

Figure 6.8. Measurement error of the delivered flow rate in the automatic LFCS with respect to the commercial flow sensor, where the average error accomplished in three cycles is shown in percentage.

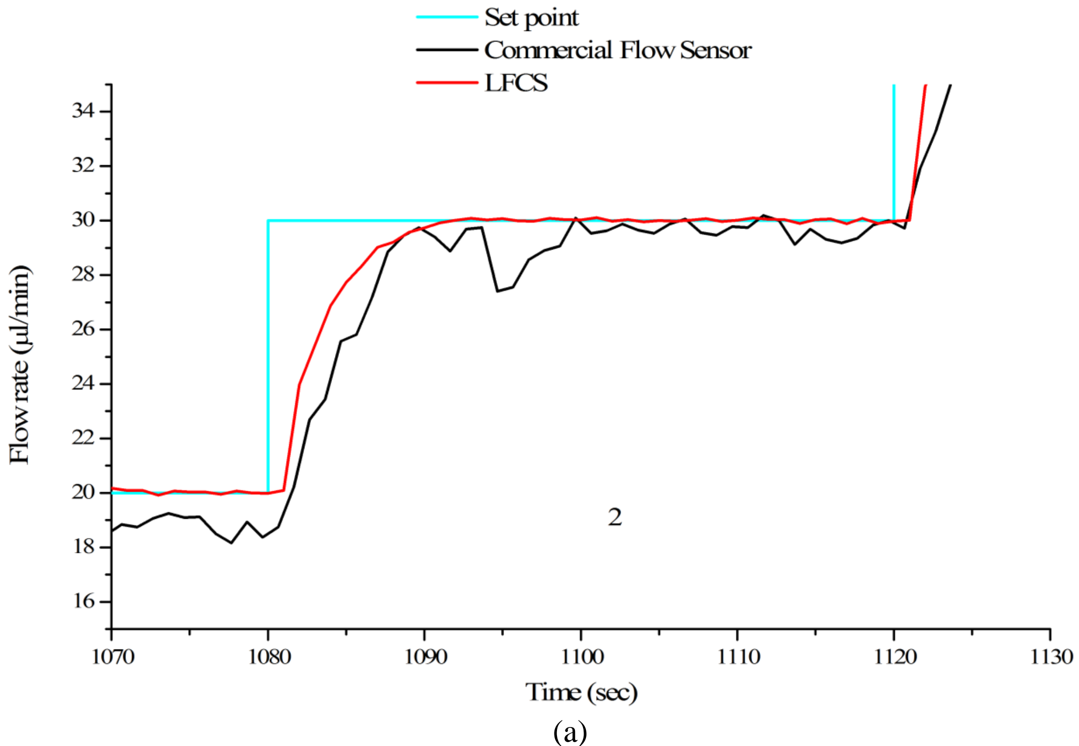

(a)

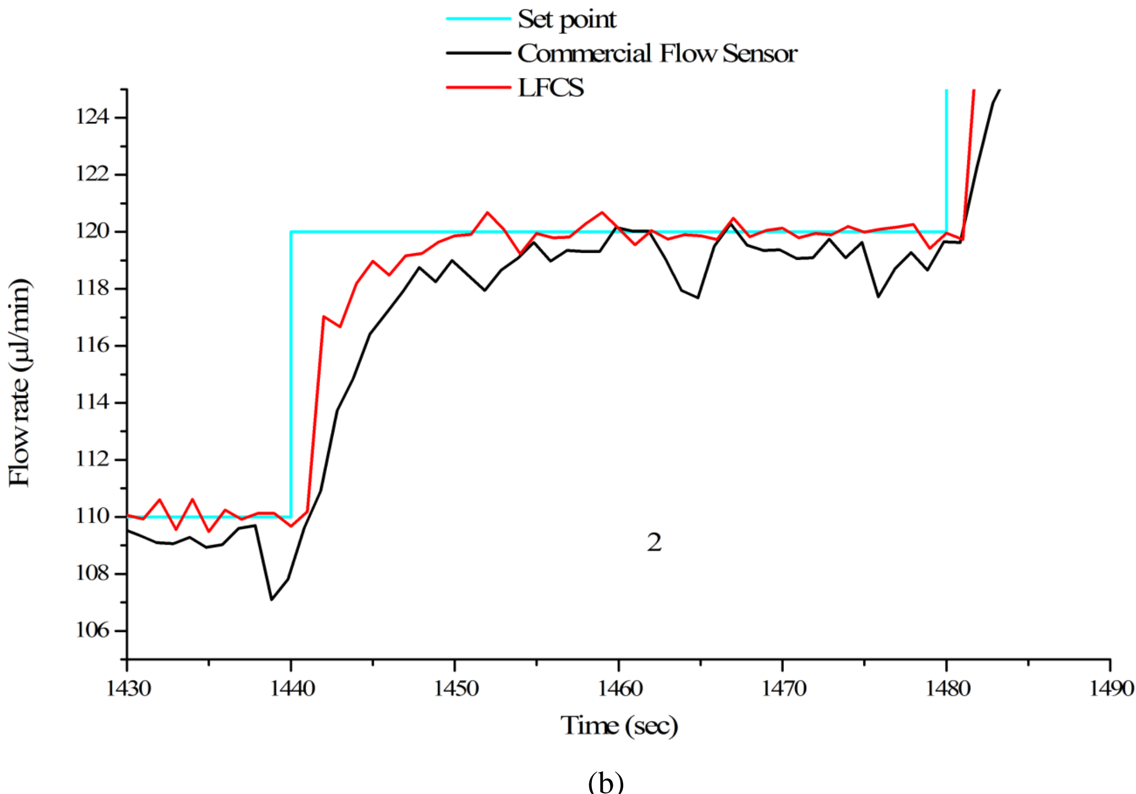

(b)

Figure 6.9. Response of the LFCS compared to the commercial flow sensor, when (a) flow rates of 30 µl/min are required and (b) when flow rates of 120 µl/min are required. Here, the long stabilization time (10 s) can be appreciated.

6.4. CONCLUSIONS

- The suitability of the fabrication method developed in this work has been demonstrated in an integrated device, featuring various microfluidics components and electrodes working together to provide new functionalities.

- Membrane deformations caused during different fabrication processes notoriously affects the performance of the developed devices. Nevertheless, any fabrication method that renders devices with uniformly distributed membrane deformations would be successful to obtain reproducible results, as the optimized one during this work. This way, good reproducibility and accuracy have been obtained for the LFCS, achieving an error <5% between 15-100% of the flow rate full range, <15% below 15%.

- For enhanced accuracies, especially for the lowest and highest flow rates, it is highly recommended to customize the bypass, scaling it in agreement with the range of interest. Another option is to recalibrate the sensor around the working range.

- LFCS stabilization time achieved for this proof of concept has been very high as a consequence of the data acquisition parameters used in the software (1 sec). For the demanding applications this parameter can be simply changed in the software in order to decrease stabilization times.

7. SECTION V – APPLICATIONS FOR THE REALIZED DEVICES

7.1. INTRODUCTION

After demonstrating the satisfactory performance of the developed devices, several applications are described in the following sections in order to show their potential for practical approaches found in LOC systems.

For the flow sensor two different applications have been carried out:

(i) A sticker anemometric sensor that can be reversibly applied to finalized devices to reliably monitor the completion of microfluidic steps in a LOC protocols.

(ii) Monitoring and control of stability of nutrients' flow in a cell culture device for an uninterrupted period of 20 hours, employing the calorimetric flow sensor for high flows (with the bypass).

The micro LFCS is used in a droplet generator system where the stability of the generated flow is a crucial condition. Hexadecane droplet formation in a continuous water phase has been tested in order to obtain monodisperse droplet formation for a great range of both flow rates.

The results in both applications indicate successful performance of the sensor, especially in highly sensitive environments, reporting full compatibility with biological applications such as cell culture experiments. Therefore, significant improvement that the off-chip sensor approach offers has been evidenced over existing sensor devices.

7.2. LIQUID MENISCUS DETECTOR: POST-PRODUCTION STICKER-SENSOR

The application consists of a detector which is able to detect a liquid meniscus when a liquid is passing through a channel. For this, the resistance variation that the metal wire senses, due to the change of the channel from being empty to be filled with a liquid, is used. This allows external and independent sensing in microfluidic systems, enabling direct sensing capabilities in a simple and easy way, e.g. as in Figure 7.1. Although some optical front-detectors can be found in literature [220, 221], the introduced idea fullfils the sensing demand that currently microsystems present, being reusable or disposable due to its low cost requirements, and presenting low space needs.

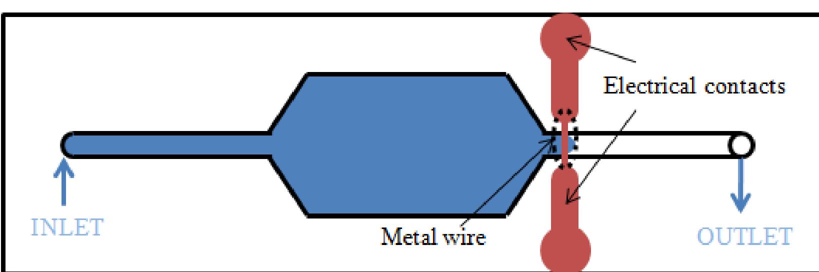

Figure 7.1. A microfluidic device with a liquid meniscus detector, used to know if the liquid has reach a specific position, so as to guarantee that a particular zone (e.g. reaction chamber) is fully filled, which can be highly useful when working with opaque microfluidic devices or systems.

The liquid meniscus detector is developed in two modes, disposable or reusable. In the disposable mode a PSA (Pressure Sensitive Adhesive) sticker sensor is metallized and bonded onto a finalized chip for one-zone meniscus detection, which offers fast, cheap and easy choice. In the reusable mode, the detector is pretended to be assembled in a movable membrane/platform, where the metal-wire can be moved between different detecting zones, allowing multiple measurements with a solely detector. In this case, the metal-wire is metallized on a 100 µm COP membrane and brought into contact with a finished LOC cartridge, where a good contact between both devices (LOC cartridge and the sensing membrane) is ensured.

7.2.1. Device description

The detector involves merely the heater element and not the two sensor elements, since when the channel turns from being empty to be filled only the heater's resistance is expected to change.

The sensor is better in detecting small changes in its resistance when its as-designed resistance is larger. Therefore, the best heater for this application is the one featuring a longer and thinner wire (*h510w*), as shown in Figure 7.2.(a) and (b).

The aforementioned meniscus detector modes consist of *(1)* Disposable meniscus detector with a metal wire metallized on top of PSA sticker with subsequent bonding onto the 100 μm COP channel cover, Figure 7.2.(a), (b) and (c), and *(2)* Reusable meniscus detector with a wire metallized on top of a 100 μm flexible COP membrane and brought into contact with a 100 μm COP channel cover, Figure 7.2.(d), (e), (f) and (g).

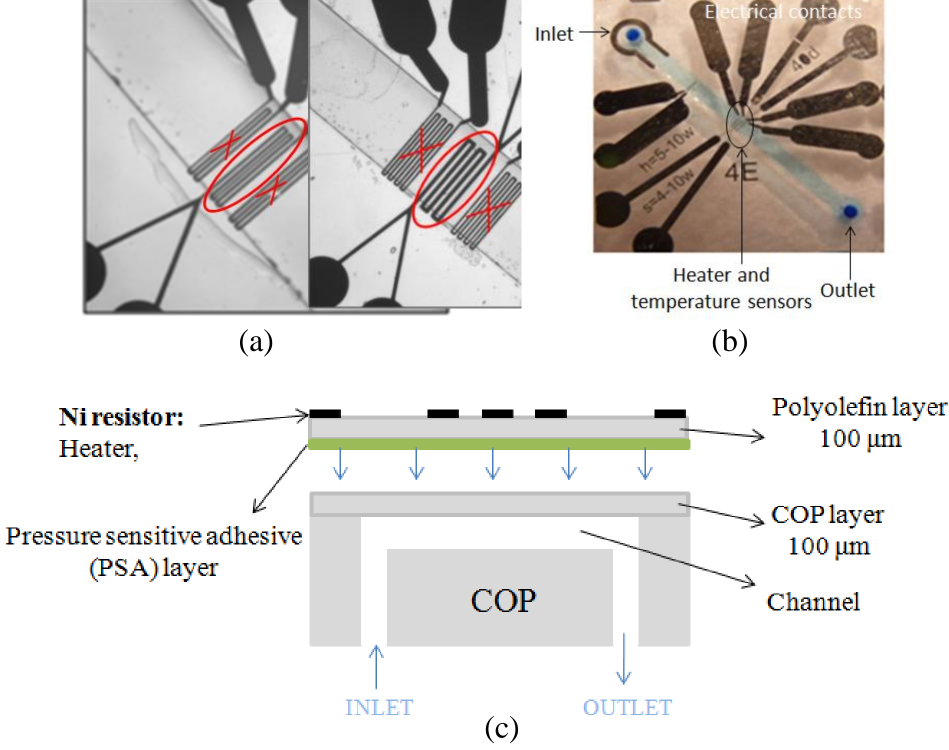

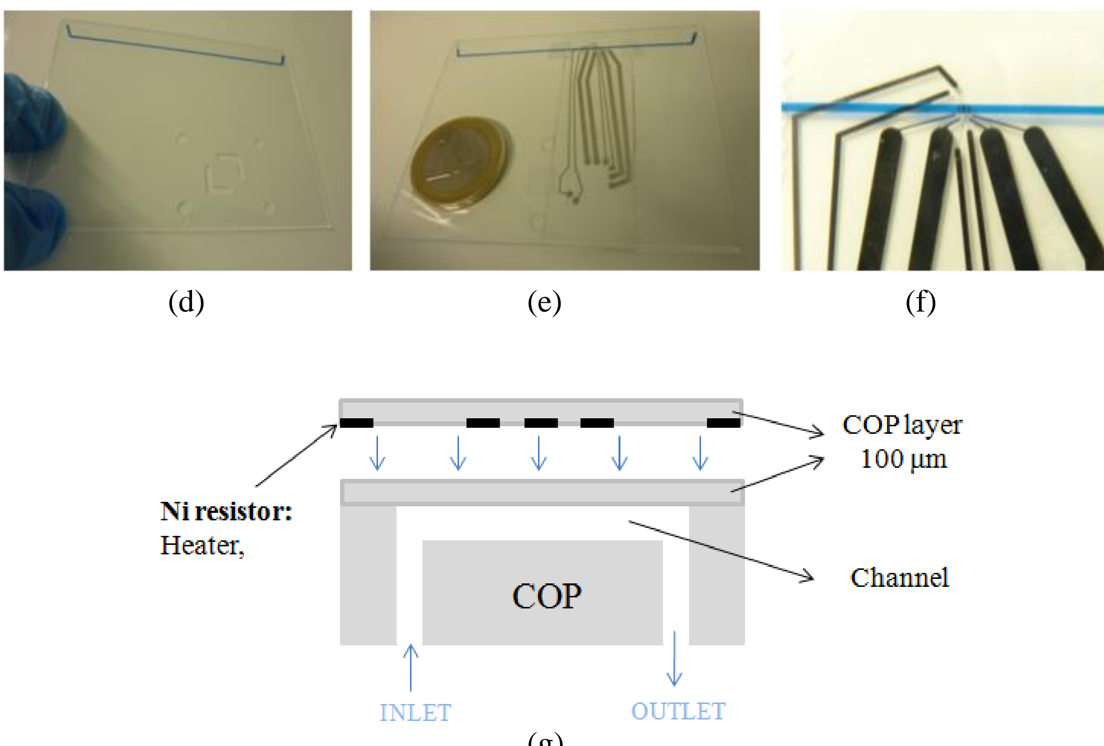

Figure 7.2. (a),(b) Layout of the *h510w* design liquid meniscus detector for the disposable mode (PSA sticker), where a finalized microchannel of 80 µm high and 500 µm width and around 100 nm thick nickel thin film is used; (c) Configuration for the disposable meniscus detector sticker (PSA); (d) Microfluidic cartridge used for the reusable mode experiments with a channel of 500 µm width and 100 µm high. (e) Microfluidic cartridge aligned together with a reusable meniscus detector membrane; (f) Close-up image of the alignment between the microfluidic channel and the reusable meniscus detector membrane of design *h510w*; (g) Configuration for the reusable meniscus detector membrane.

The microfluidic cartridge shown in Figure 7.2.(d) has been specially designed and fabricated by a previously developed method, using a craft cutter for fast prototyping with straightforward alignment method based in *origami* technique, followed by the bonding of the layers by thermo-compression [222].

7.2.2. Setup and packaging

The setup and packaging used to test the disposable detector is the same as the previously employed in Chapter 5. The reusable detector is tested in an already built point of care (POC) system, using the packaging and the setup shown in Figure 7.3 and Figure 7.4.

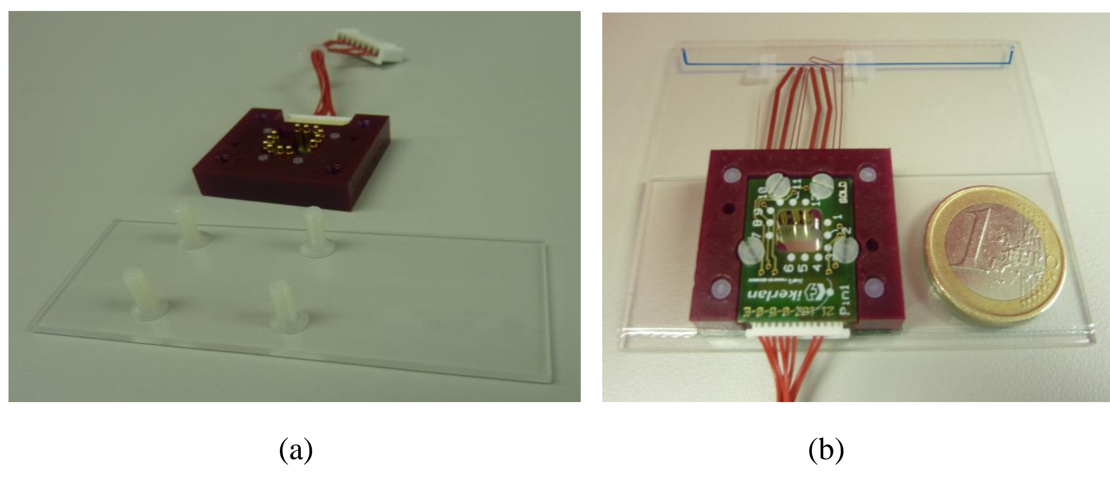

(a) (b)

Figure 7.3. Packaging for the reusable meniscus-detector in a POC system; (a) Packaging; (b) Packaging with the aligned cartridge-detector assembly.

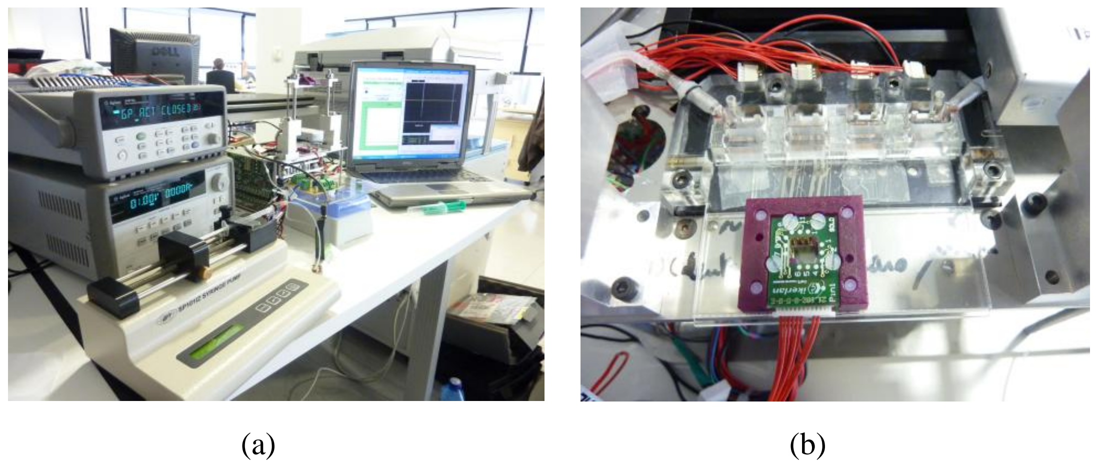

(a) (b)

Figure 7.4. POC platform used to test the reusable meniscus-detector; (a) Entire setup used for the experiments; (b) Close-up image of the platform with the packaging.

7.2.3. Experiments

Both detector modes are tested by fixing the heater around 40ºC and recording its resistance variation (ΔR_1, ΔR_2 and ΔR_T) due to different channel states, where States 1, 2 and 3 refer to the empty channel, filled channel with flowing DIW and filled channel with stopped DIW, respectively, as depicted in Figure 7.5.

For the disposable mode the effects of alignment between the PSA detector and the microchannel are tested in order to see if it affects on the detection capability. Thus, for PSA sticker experiments, the measurements have been conducted twice, for a properly aligned device and for the misaligned device.

During these assays, capability to detect presence of leakage is also tested during the State 3, by imposing small flow rates (0.5-2 µl/min through the microchannels).

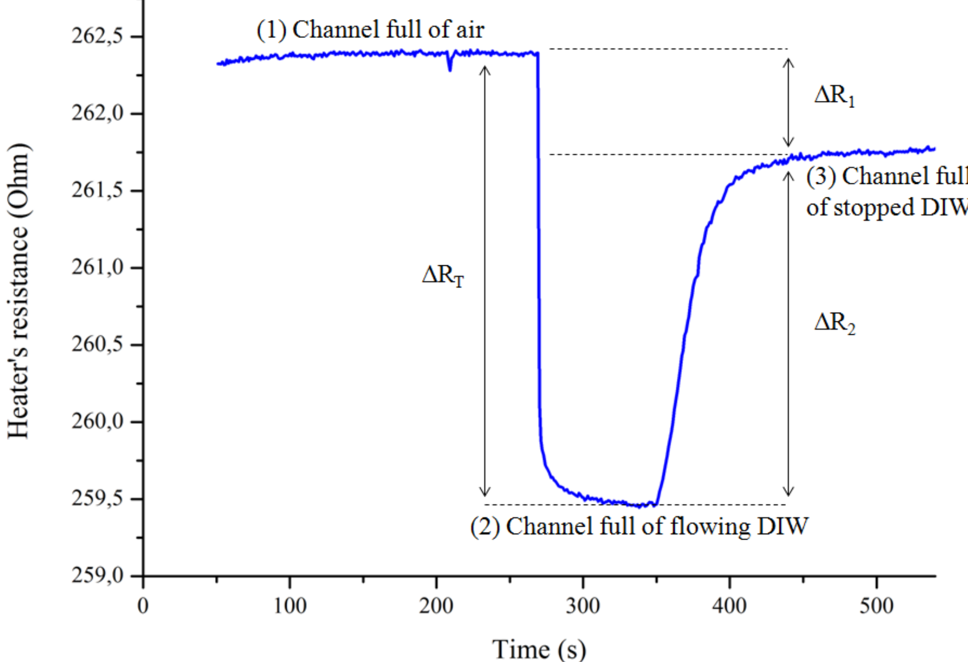

Figure 7.5. Resistance variations (ΔR1, ΔR2 and ΔRT) due to different channel states, where States 1, 2 and 3 refer to the empty channel, filled channel with flowing DIW and filled channel with stopped DIW, respectively.

All the carried out tests have been summed up in Table 7.1.

Table 7.1. Summary of the realized experiments with the two liquid meniscus detector modes.

<table>
<tr><td rowspan="3">Liquid Meniscus Detector (LMD)</td><td>Application</td><td>Metal wire feature analysis</td><td>Further analysis</td></tr>
<tr><td>Reusable meniscus detector membrane integrated within a POC system</td><td>Simplification by metallizing a membrane and pressing it against a finalized chip</td><td></td></tr>
<tr><td>Disposable one-zone-meniscus detector sticker</td><td>Metalized PSA bonded to a finalized chip</td><td>Effect of misalignment on measurement sensitivity</td></tr>
</table>

7.2.4. Results and discussion

7.2.4.1. Disposable meniscus detector sticker, PSA (h=2500 µm -10 µm)

The essay is realized in two devices, one with the heater properly aligned with respect to the channel, as can be seen in Figure 7.6, and the second with a misalignment of around 30%. The results for both alignment types have been depicted in Table 7.2, and the evolution of the resistances is shown in Figure 7.7.

According to the results, it can be seen that the properly aligned heater results in a better detection (about 25% higher). However, the leakage is almost imperceptible regardless of the alignment (≈0.2-0.3 Ohm for the properly aligned).

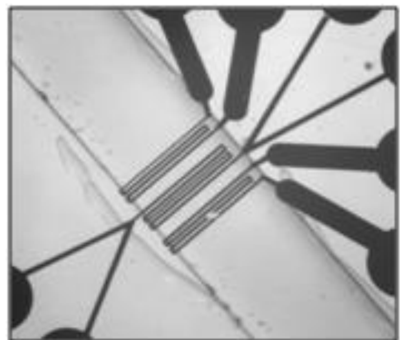

Figure 7.6. Liquid meniscus detector of design *h510w* metallized on top of PSA sticker and manually stuck above a 500 µm width and 80 µm height channel covered by 100 µm COP membrane, resulting in a great alignment with respect to the channel.

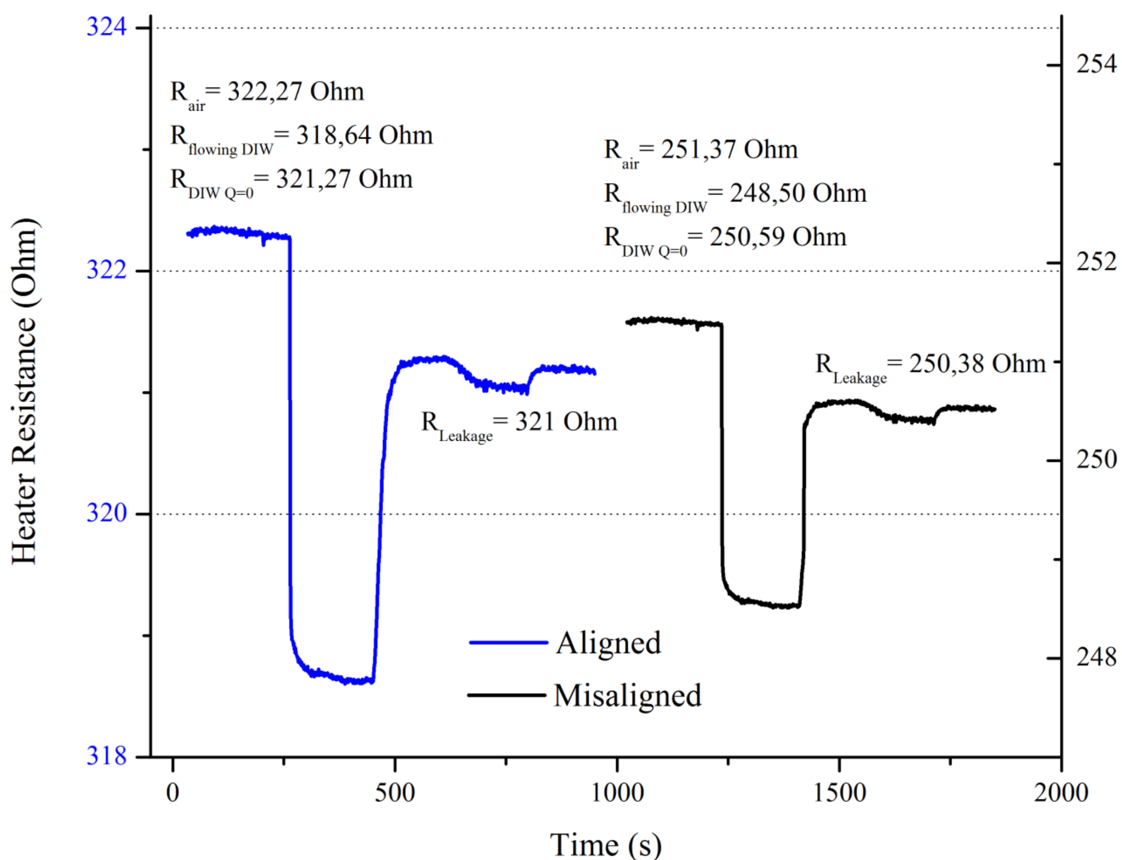

Figure 7.7. Liquid meniscus and leakage detection tests for a disposable PSA sensor sticker, employing the heater of design *h510w* and using a DIW flow rate of 100 µl/min and leakage of 2 µl/min, while the heater operates at 40ºC.

Table 7.2. Heater resistances at different channel states for the properly aligned and misaligned disposable meniscus detector stickers of design *h510w*, when working at 40ºC.

Working T (ºC)	R (Ohm) Empty channel	R (Ohm) circulating water	R (Ohm) Stopped water	ΔR_1: $\Delta R_{(1)\rightarrow(3)}$	ΔR_2: $\Delta R_{(3)\rightarrow(2)}$	ΔR_T: $\Delta R_{(1)\rightarrow(2)}$
aligned	322.27	318.64	321.27	1.00	2.63	3.63
misaligned	251.37	248.50	250.59	0.78	2.09	2.87

7.2.4.2. Reusable meniscus detector membrane (h=2500 – 10 μm)

For the simulation of the movable meniscus detector in a POC platform, the heater is set at 2V, and ΔR_1, ΔR_2 and ΔR_T are measured while the cartridges are subjected to flow rates between 0.5 - 300 μl/min. The results are summarized in Table 7.3 and ΔR_T depicted in Figure 7.8.

According to Table 7.3 for a flow rate of 0.5 μl/min, the reusable membrane detector is able to notice the liquid meniscus ($\Delta R_T > 0$), but the resistance of the heater remains at the same value when the flow is stopped ($\Delta R_2 \approx 0.01$). This means that the membrane-detector is not able to detect leakages until flow rates beyond 1 μl/min are imposed, when it is able to detect small leakages ($\Delta R_2 \approx$ 0.03). Beyond 5 μl/min, detection between circulating and stopped DIW can be seen.

Overall, the results show that any heater is able to notice the liquid passing the heater, and thus the proof of concept has been successfully verified. Moreover, for PSA-detector, it was seen that the alignment with respect to the channel is not a critical point, allowing a more comfortable approach for the user, with no need of microscope or aligners to bond the detector on a desired device.

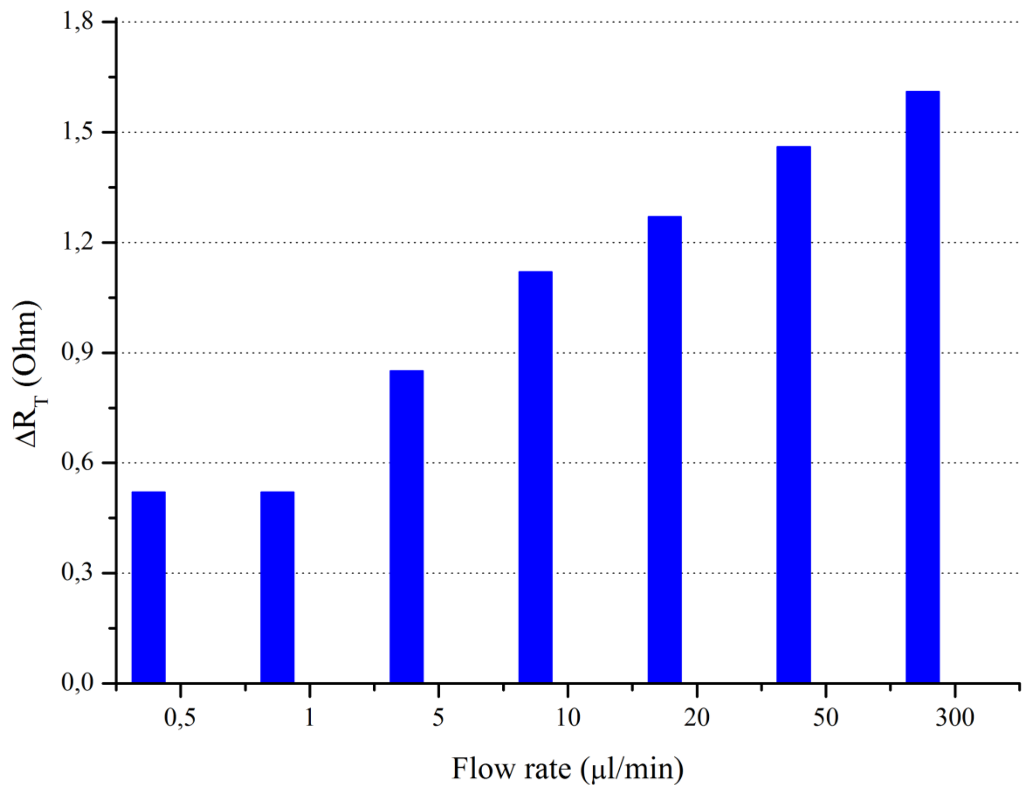

Figure 7.8. Summary and comparison of ΔRT values obtained when using a reusable meniscus detector membrane of design *h510w* aligned with an adequate cartridge to be used in the POC platform at different DIW flow rates (ranging from 0.5 µl/min up to 300 µl/min) while the heater operates at 2V constant voltage.

Table 7.3. Summary of ΔR1, ΔR2 and ΔRT values obtained for a reusable meniscus detector membrane of design *h510w* aligned with an adequate cartridge to be used in the POC platform at different DIW flow rates (ranging from 0.5 µl/min up to 300 µl/min) while the heater operates at 2V constant voltage.

Reusable membrane							
Flow rate (µl/min)	0.5	1	5	10	20	50	300
$\mathbf{\Delta R_1: \Delta R_{(1)\rightarrow(3)}}$	0.49	0.49	0.53	0.55	0.54	0.67	0.62
$\mathbf{\Delta R_2: \Delta R_{(3)\rightarrow(2)}}$	0.01	0.03	0.32	0.57	0.73	0.79	0.99
$\mathbf{\Delta R_T: \Delta R_{(1)\rightarrow(2)}}$	0.52	0.52	0.85	1.12	1.27	1.46	1.61

7.3. CALORIMETRIC MICRO FLOW SENSOR IN CELL CULTURING

The calorimetric flow sensor with the bypass has been tested by connecting it to a microfluidic cell-culture device for an uninterrupted period of 20 hours, and recording the nutrients flow rate. The results indicate successful performance of the sensor in this highly sensitive environment, featuring full compatibility with biological applications such as cell culture experiments. Moreover, the low cost approach of the microdevice and the required readout electronics allows the use of this technology for disposable flow sensor devices, being especially relevant in applications where the equipment requires harsh environments (e.g. 95% humidity and 5% CO_2 as in cell culture).

7.3.1. Fabrication of cell culture microdevices

Cell culture microdevices were made of three different 188 µm thick COP films [223], that were diced using a cutting plotter (GRAPHTEC FC8000-60) in order to get a flat bottom, a microchannel layer containing three microchannels of 1 mm wide and 188 µm high, and a cover with the required inlets and outlets respectively. Once aligned, the three layers were bonded by applying 140 ºC and a pressure of 3 bar. Figure 7.9 shows a picture of a typical fabrication result. Shear stress in the microchannels was calculated using a simplified formula for a rectangular channel:

$$\tau = \frac{6\mu Q}{h^2 w} \qquad \textbf{(4)}$$

Where µ (dyna·s·cm^{-2}) is the dynamic viscosity of the medium, Q (cm^3·s^{-1}) is the flow rate, h (cm) is the height of the microchannel and w (cm) is its width.

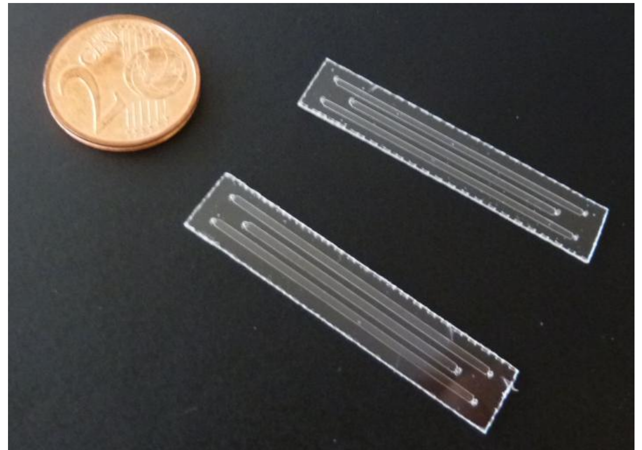

Figure 7.9. COP culture microdevice that comprises three microchannels of 1 mm width and 188 µmm height and the respective inlets and outlets.

7.3.2. Experiments

For the use of the flow sensor in cell culture applications, neither the sensor nor the measurement process should jeopardize the cell viability. The punctual heating of the culture medium over the culture conditions (37ºC) could affect negatively the cell viability if there is some thermal decomposition of some key medium elements such proteins, peptides, vitamins, hormones, etc. In addition, the materials used in the sensor fabrication could be a potential source of toxicity that could affect the cell viability. HUVEC cells (Human Umbilical Vein Endothelial Cells) are primary cells very sensitive to changes in the composition of the media and to the presence of toxic elements. To study these possible effects over the cell viability, HUVECs were seeded in a microfluidic culture chamber and placed downstream from the sensor in the fluidic set up.

7.3.2.1. Cell culture on COP devices

HUVEC cells from various donors (passages 3-5) were maintained and expanded following the ATCC recommendations for this particular cell line. HUVECs were grown in Endothelial growth media (EGM-2), formulated supplementing Endothelial basal media (EBM-2) (Lonza CC-3156) with EGM-2 bullet kit (Lonza CC-4176) following manufacturer indications.

To increase cellular attachment, cell culture devices were activated by exposing them to a radiofrequency generated oxygen plasma (Pico Plasma Cleaner, Diener). Next, ethanol was drained off by flushing sterile deionized water. Finally, any remaining liquid in the microchannels was completely drained off, afterwhich no sign of contamination was observed in any of the devices sterilized following this procedure.

Then, in order to let the cells attach, a cellular suspension of 2.5 10^6 cells/ml was seeded in a cell culture microdevices and placed overnight in a bioreactor (EBERS Medical Technology, TEB-1000, Spain) at culture conditions of 37ºC, 5% CO_2 and 95% humidity.

Finally, the cell culture microdevice, the COP flow sensor and a commercially available flow sensor (Sensirion, LG16-0430D) were connected in series and the whole setup was placed inside a bioreactor, except the commercial flow sensor due to its high cost and no guarantees to withstand culture conditions for long. Cells were cultured under a flow rate of 50 µl/min (0.1 dyna/cm^2) for 20 hours.

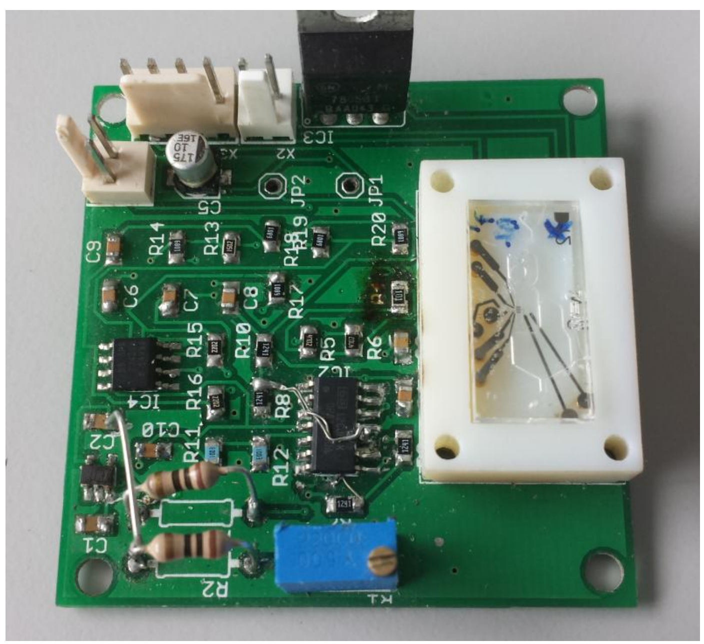

Figure 7.10. Integrated electronics and COP flow sensor housing for cell culture experiments.

7.3.2.2. Cell viability fluorescence staining

Cell viability inside the devices was assessed by fluorescence microscopy using a live-dead staining. Fluorescein diacetate (FDA), which is not fluorescent by itself, can freely diffuse into cells and nonspecific intracellular esterases cleavage the ester bonds in the FDA molecule, becoming strongly fluorescent in the green wavelength range. That enzymatic cleavage is only possible in cells with metabolic activity, thus FDA was used as a live cell marker. Propidium iodide (PI) is a DNA intercalating agent that is strongly fluorescent in the red wavelengths when it is binding to the DNA. Since PI is not permeable to live cells, it was used as a dead cell marker.

FDA/PI working solution of FDA (Sigma F7378), PI (Sigma P4170) was prepared in sterile Phosphate Buffer Saline (Lonza BE17-516F). Prior to staining, all the remaining media inside the devices was displaced with sterile PBS. Next, FDA/PI working solution was perfused inside the device, and incubated for 5 minutes at room

temperature. Finally, FDA/PI working solution was displaced with sterile PBS and fluorescence observed in a fluorescence microscope (Nikon Ti-Eclipse, Japan). Obtained images were processed using Image J software (NIH).

7.3.3. Characterization and results

7.3.3.1. Cell culture

After HUVECs being cultured for 20 hours under a shear stress of 0,1 dyna/cm² (in the range of the 50 µl/min) while the continuous nutrients flow measured using the COP and commercial sensors, the Live-Dead staining (FDA/PI) measurement of cells is shown in Figure 7.11. The typical cobblestone morphology of the HUVECs can be observed without signs of major stress or cellular damage, and thus most of the cells were alive after being exposed to the generated shear stress. This good morphology, the high cellular viability and the absence of depopulated areas could point to the suitability of this kind of sensor for cell culturing.

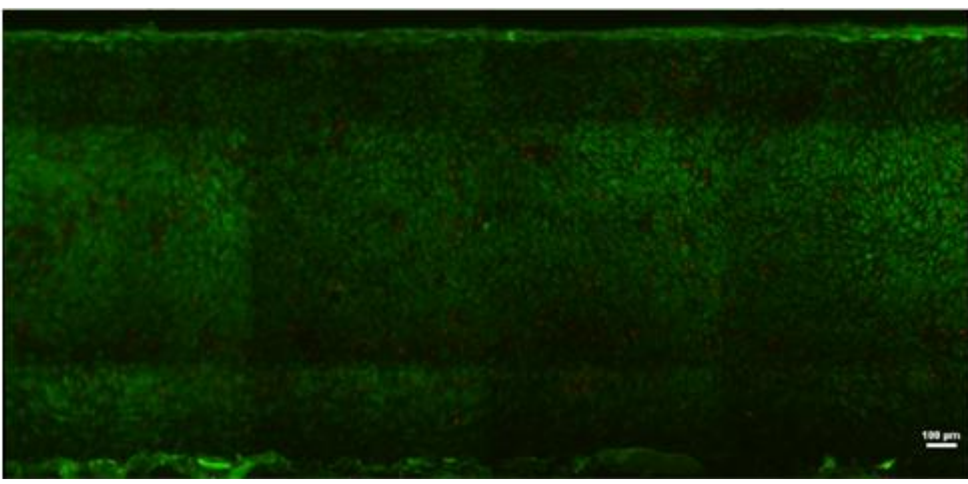

Figure 7.11. Chamber (white bar scales 50 µm). Live cells are labelled in green while dead cells are labelled in red.

7.3.3.2. COP sensor validation for cell culturing

The required electronic setup for powering of the flow sensor and the readouts based on the use of a Wheatstone bridge, discussed in Chapter 5, has been fully integrated on a single PCB, as shown in Figure 7.10. The price for all required electronic components was lower than 15 euro, even though they were bought in low quantities (2 complete sets per order). It is therefore believed that dedicated integrated electronics fabricated on mass production would be cheap enough to be included on a disposable final product. This is indeed very relevant, as electronics suffer severe damage over time under bioreactor conditions due to corrosion (95% humidity and 5% CO_2).

A set of experiments were carried out to perform a validation study of the COP based flow sensor. First, the sensor was connected in series with the microfluidic cell culture microdevice, and a commercially available flow sensor (Sensirion, LG16-0430D, which was placed outside of the bioreactor, as it was found to stop working after 2-3 weeks of testing due to electronic failure). Then, a flow rate of 50 µl/min was applied, and both flow sensor readouts stored during the dynamic culture for 20 hours.

As can be observed in Figure 7.12, a stable flow rate reading was obtained during the course of the experiment, in agreement with Sensirion´s readout. After 20 hours of constant flow, cell viability was assessed by fluorescence microscopy using a Live-Dead staining (FDA/PI). As can be observed in Figure 7.11, cells inside of the microfluidic culture chamber established a confluent monolayer, with a small number of dead cells. It can be therefore concluded that the sensor is suitable to be used for cell culture applications.

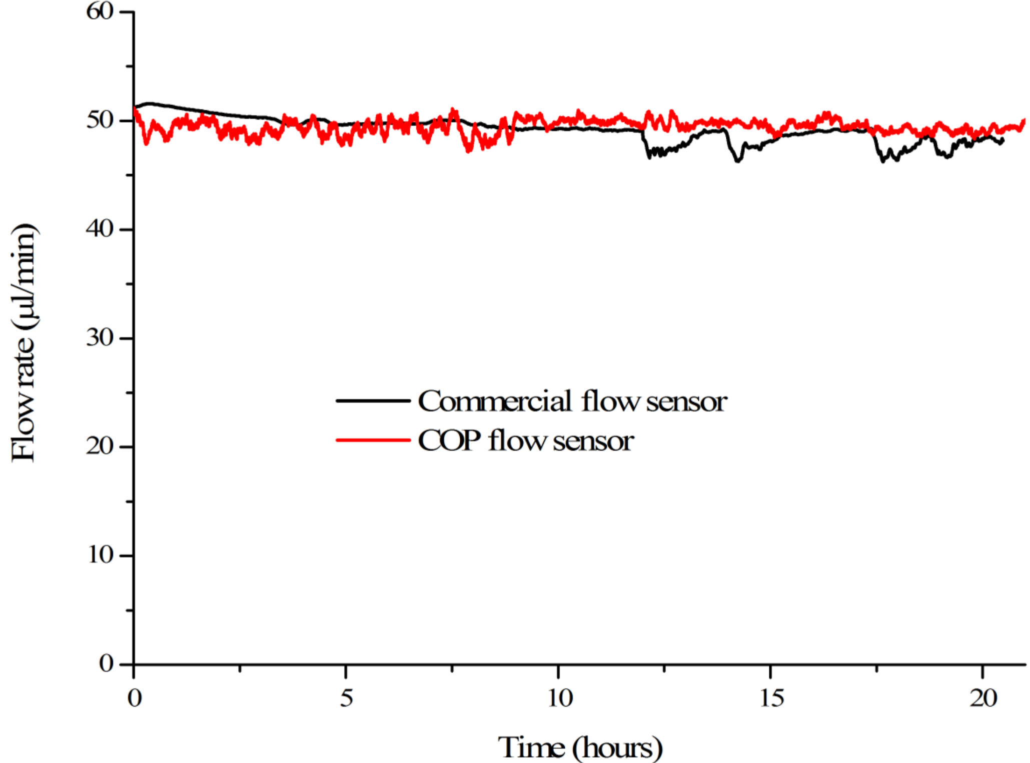

Figure 7.12. Flow rate readouts using commercially available sensor and the presented COP based sensor when an intended flow rate of 50 μl/min is applied for 20 hours.

7.4. AUTOMATIC LFCS IN DROPLET GENERATION

In recent years, demand on droplet-based microfluidics in chemistry, biology or biomedicine has increased in the same way as the interests in microfluidics have grown in the last two decades. The advantages that the droplet microfluidics offer compared to continuous phase microfludics include encapsulation, enhanced mixing due to internal recirculation, monodisperse particle generation and highly parallelized experiments for high throughputs [224-227].

Correct performance of droplet-microfluidics demand highly stable flows in order to acquire a homogeneous droplet size with proper generation speed (or frequency), since steady flows avoid oscillations of pressure inside the system that can break its steady state. Therefore the LFCS presented in this work meets the aforementioned requirements and makes this application suitable to effectively proof the system in a realistic scenario.

The following work was carried out in collaboration with Mesoscale Chemical Systems (MCS) group of MESA+ Institute for nanotechnology (University of Twente, Enschede, Netherlands) and Micronit Microfluidics B.V. (Enschede, Netherlands), where hexadecane (HD) droplet formation in a continuous water phase (W) was analyzed in a flow-focused droplet generator customized in glass material.

7.4.1. Droplet generator architecture and working principle

7.4.1.1. Working principle

Microfluidic droplet generators work by combining immiscible fluids and generating a shear force on the continuous phase causing it to break up into discrete droplets. Critical factors for the drop formation include the materials chosen for the device [228-230], the fluids used for droplet formation, the size of the nozzle restriction, the viscosity of the immiscible phases, the use of surfactants, and so on. Also, the dimensionless capillary

number, Ca, plays an important role in the droplet dynamics since the type of the flow depends on it. The capillary number is defined as follows:

$$Ca = \frac{\eta\, \nu}{\gamma} \quad \textbf{(5)}$$

where η (Pa·s) and ν (m/s) are the viscosity and the velocity of the continuous phase respectively, and γ (N/m) is the interfacial tension between the two immiscible phases. Above a critical capillary value, which is system dependent, droplet formation starts.

The surface wettability of the channel is critical to form aqueous-in-organic (W/O) or organic-in-aqueous (O/W) droplets. To prevent HD droplets to stick on channel walls, hydrophilic channels are required (untreated glass) and for water droplets hydrophobic channels are needed (coated glass). Therefore, surfactants are usually used to alter the channel surface wettability and prevent coalescence of the droplets.

7.4.1.2. Architecture

Droplet formation was tested in a single junction droplet generator device provided by Micronit Microfluidics. The microfluidic channels were structured in 1.1 mm glass layer and subsequently a 700 µm glass layer with holes was bonded on top of it, enclosing the channels and providing the microfluidic ports.

The droplet generator, depicted in Figure 7.13.(a) and (b), posses a channel of 100 µm width and 20 µm high, and the chip relies on a highly precise 10 µm restriction in a flow-focused configuration, where a sheet flow is created ahead of the restriction, as can be seen in Figure 7.14, generating a droplet.

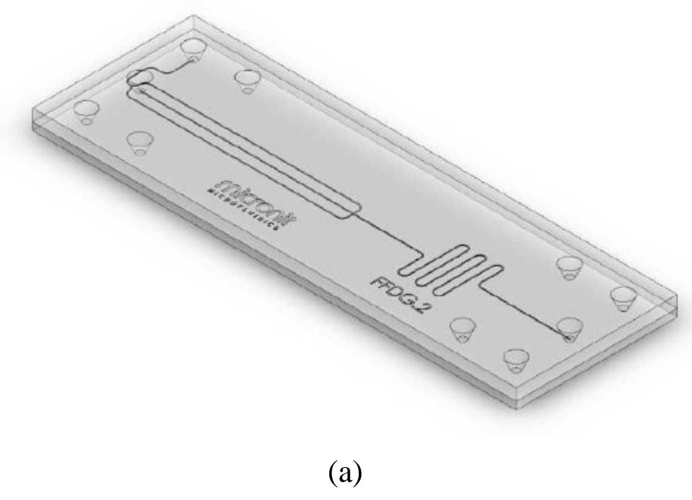

(a)

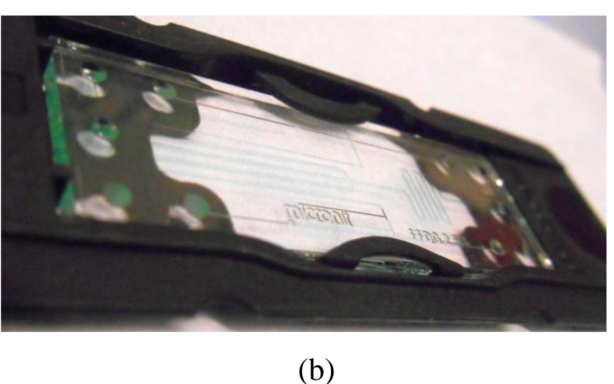

(b)

Figure 7.13. Focused-Flow Droplet Generator chip from Micronit microfluidics. (a) Scheme and (b) finalized chip of Single channel FFDG with a channel width and depth of 100 µm and 20 µm respectively and a restriction nozzle of 10 µm.

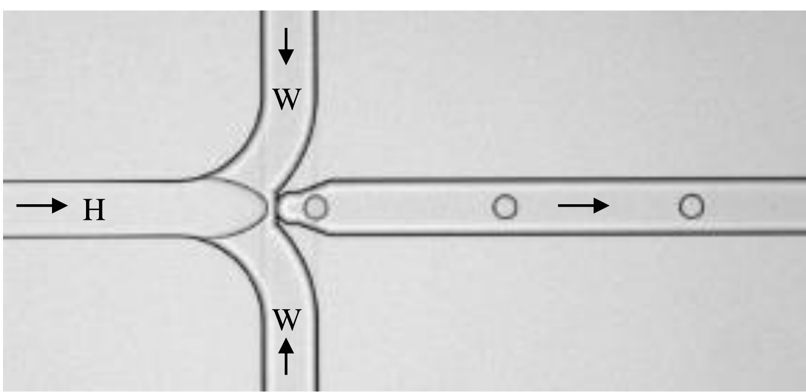

Figure 7.14. Hexadecane-in-water (O/W) droplet formation in a Focused-Flow Droplet Generator. The sheet flow is created ahead of the 10 µm restriction.

7.4.2. Droplet generation setup

The setup employed for the droplet generation comprises a packaging (Micronit microfluidics) to provide fluidic connection for water and hexadecane to the FFDG device (Figure 7.15.(a)), the LFCS previously detailed to precisely control the water flow rate, a syringe pump (Harvard PHD 2000) to accurately fix the hexadecane flow rate in a steady state, and a Leica DMI 5000M inverted microscope with a MotionBLITZ EoSens®mini2 high speed camera for recording the droplets in the FFDG device. The setup and the block diagram for the experiments can be seen in Figure 7.15.(b) and Figure 7.16.

(a.1)

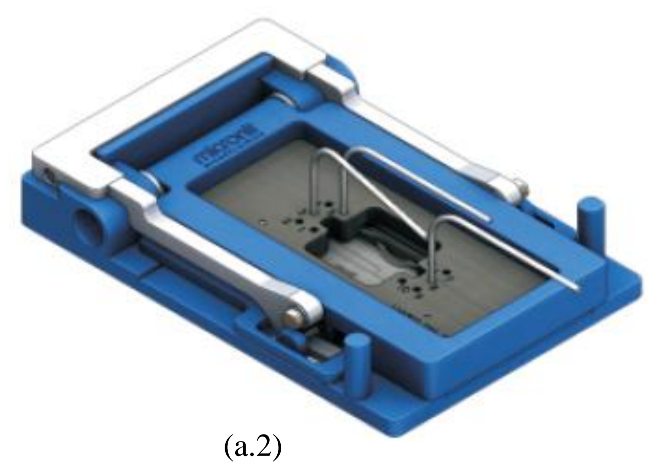

(a.2)

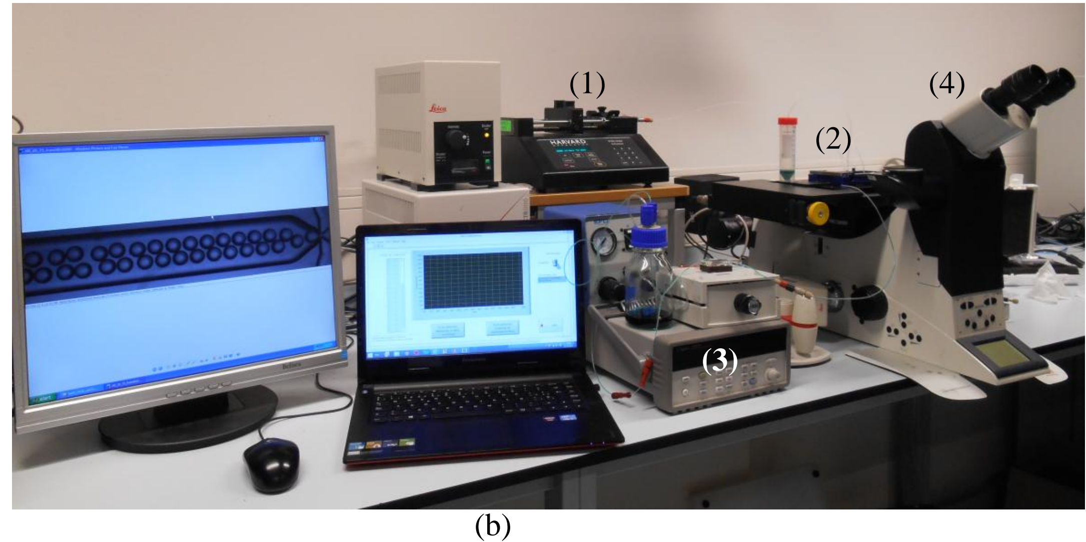

(b)

Figure 7.15. Setup employed for droplet generation experiments. (a) Packaging provided by Micronit to adequately connect the fluidic tubing to the flow-focused droplet generator. The bottom part possesses the chip holder and the top part brings the fluidic connections to the circuit. (b) Setup used for the hexadecane-in-water (O/W) droplet generation.

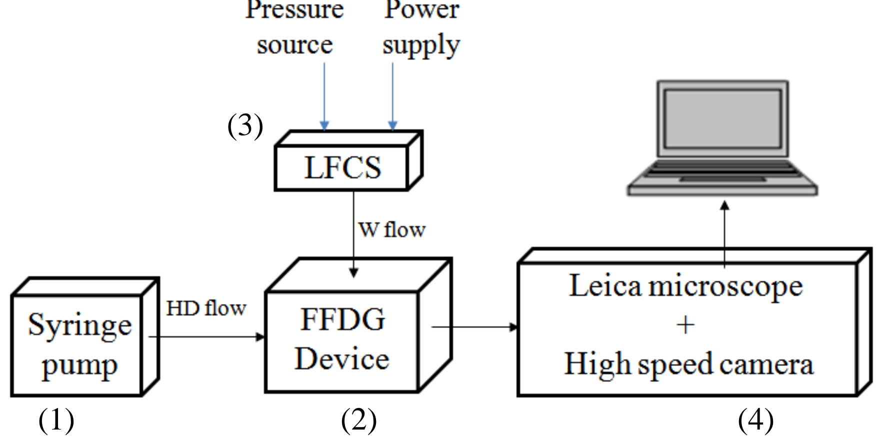

Figure 7.16. Block diagram of the setup employed for hexadecane-in-water droplet generation (O/W). The aqueous phase was controlled with the previously presented micro Liquid Flow Controlling System and the organic phase with a syringe micropump employing sufficiently high HD speeds to ensure pulse-free steady velocities. The droplets are formed within the droplet generator device with a focused-flow configuration and are recorded with a high speed camera mounted on a inverted Leica microscope.

7.4.3. Experiments

Hexadecane-in-water (O/W) droplet generation at different hexadecane and water velocities is investigated. Changing the flow rate of the two phases allows the size of the droplets to be increased or reduced. To generate hexadecane droplets in continuous water phase, the water flow rate must be higher than that of the hexadecane. During the experiments constant flow rates ranging from 0.1 µl/min to 20 µl/min are used for organic phase by a syringe pump (Q_{HD}), while the aqueous phase flow rate is varied from 3 µl/min to 200 µl/min by means of the LFCS (Q_W).

Prior to the assessment the stability of the droplets has been tested, for which several surfactants have been investigated so as to obtain immiscible droplets.

The waiting time for the system to be stabilized was determined to be 15 min. To define such stabilization time, fixed flow rate values were used for both phases and the diameters of the formed droplets were measured after 15 minutes. The same task was repeated after 30min, and the similar results indicated that the system had been stabilized after the first 15 minutes.

The generated droplets inside the channel were recorded with the high speed camera. Subsequently the fluid emerging from the chip was collected on a microscope slide in order to evaluate the size distribution and evidence monodispersity for the generated HD droplets.

Since the objective of this section is to evaluate the LFCS in droplet generation, prior to HD injection some experiments (results not shown) were carried out in order to guarantee that the syringe pump delivers a non-pulsating flow rate, observing that values higher than 0.1 µl/min should be used to avoid pulses in the employed syringe.

7.4.4. Droplet generation results

During the droplet stability tests, the generated HD droplets tended to merge. This was solved by adding 2%Tween80 (v/v) to the aqueous phase (W), avoiding the droplet merging.

The formation of hexadecane (O) droplets in water (W) is realized by maintaining the hexadecane flow rate (Q_{HD}) constant and varying the water flow rate (Q_W).

In Figure 7.17 the results for droplet diameter inside the channel (D_c), the droplet diameter on a slide (D_s) and frequency or velocity at which the droplets are generated (f) were plotted. The solid lines represent a stable system where single monodisperse droplets were formed (e.g. with Q_{HD}= 0.5 µl/min and Q_W= 7-50 µl/min), the dotted lines refer to a stable system where monodisperse droplets were generated in pairs and with the same diameter (e.g. with Q_{HD}= 0.1 and 0.2 µl/min and Q_W= 50 µl/min), the dashed lines indicate an unstable system where pairs or more droplets with different diameters were formed (e.g. with Q_{HD}= 5 µl/min and Q_W= 40-75 µl/min), and the solid lines containing a symbol show an unstable system where droplets were formed in pairs but being one droplet much bigger in comparison to the other (e.g. with Q_{HD}= 10 µl/min and Q_W= 100-150 µl/min).

Figure 7.18 shows the images obtained during the formation of hexadecane (HD) droplets in water (W), where the direction of the flow is from right to left. Droplets with diameters of 20 µm to75 µm inside the channel and 25 µm to 55 µm on a slide were generated depending on the flow rate of the two phases. Note that, since the channel height is 20 µm, the droplet inside the channel possesses a flattened sphere.

From Figure 7.17 it can be observed that for correct Q_{HD} and Q_W stable and monodisperse droplet formation is achieved. When the organic phase is too high in comparison with the carrier aqueous phase no droplets but slugs are formed, as can be observed for Q_{HD}/Q_W =1/5, Q_{HD}/Q_W =5/10 or Q_{HD}/Q_W =10/15, and which afterwards tend to merge because of their low surface energy compared to the droplet size (for

lower Q_W values no droplets were generated and two immiscible and laminar phases flow inside the channel).

When velocity of the aqueous phase (Q_W) is much higher than that of the organic phase (Q_{HD}), the droplets tend to form in pairs showing the same or very similar diameter when low Q_{HD} was used (depicted in dotted lines for Q_{HD}= 0.1-1 µl/min), but for increasing Q_{HD} pairs of droplets with different diameters were achieved being the first droplet larger than the second and consequently losing the monodispersity (depicted in dashed lines for Q_{HD}= 5-10 µl/min). For such Q_{HD} and higher Q_W the system becomes unstable, resulting in droplets with uncontrolled sizes and generating frequencies (depicted in solid lines with symbol for Q_{HD}= 10 µl/min).

For sufficiently high Q_{HD} (20µl/min) and Q_W (40-100 µl/min) a stable system with a high generating frequency was achieved until Q_W is too high and the system becomes unstable.

To summarize, it can be concluded that an increase in both phase flow rates increases the droplet generation frequency. In case of increasing Q_W for a fixed Q_{HD} leads to a decrease in the droplet diameter, and, on the contrary, increasing Q_{HD} for a fixed Q_W increases the droplet diameter. Finally, a stable system is obtained for high Q_{HD} (higher than 5 µl/min) until the aqueous phase flow rate is approximately five times higher than that of the organic phase (Q_W/Q_{HD}=5), after which monodispersity of droplet diameter is lost.

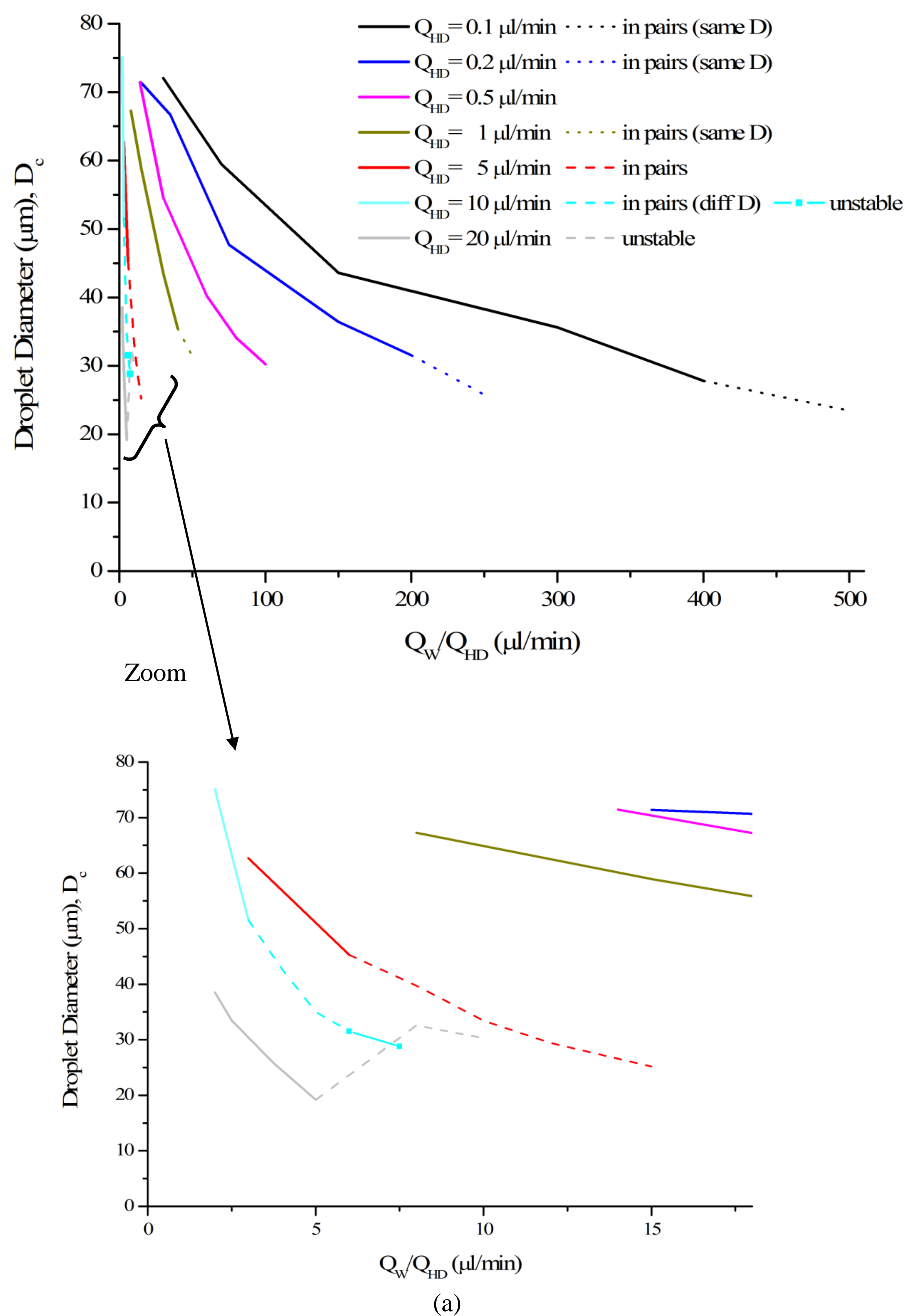

(a)

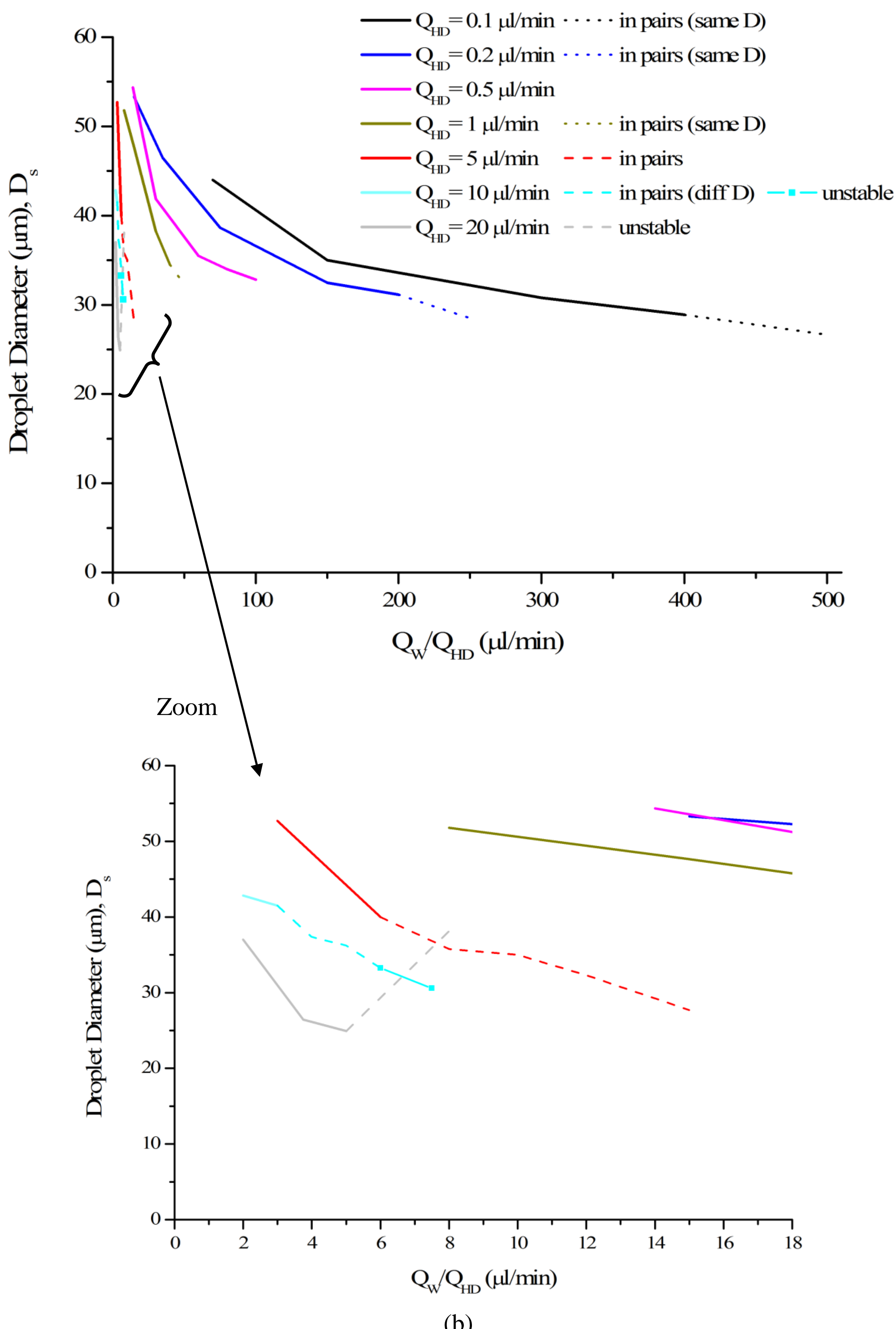

(b)

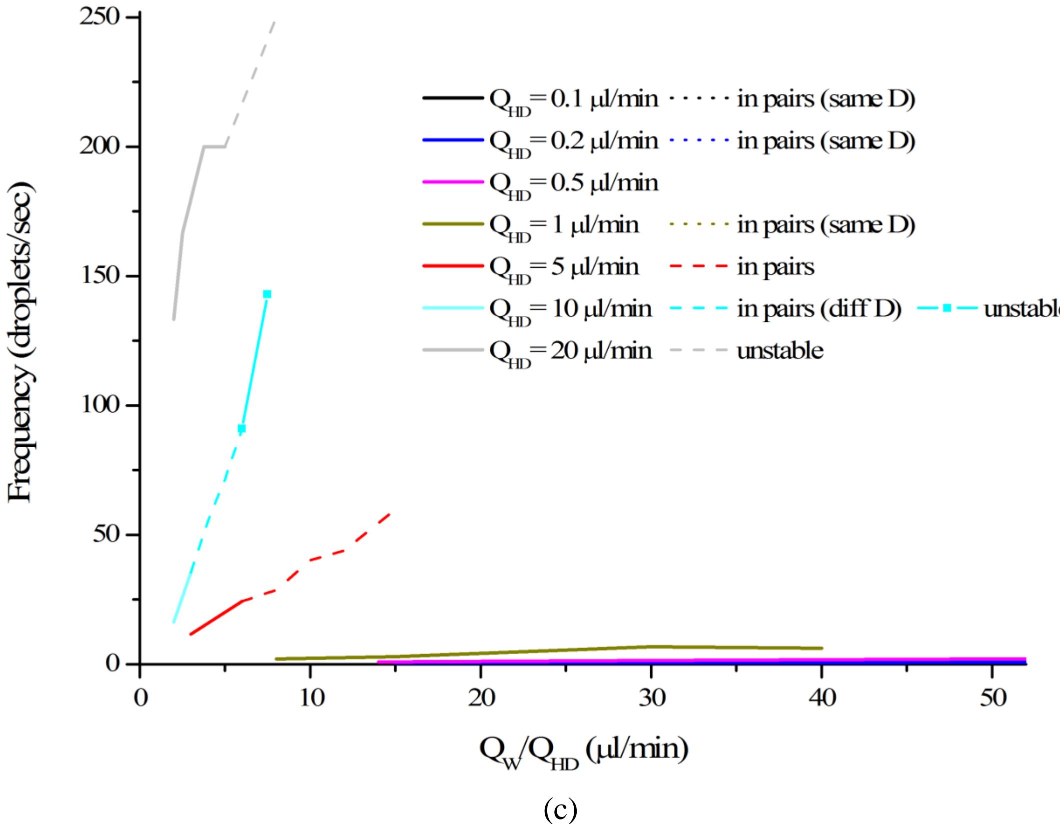

(c)

Figure 7.17. Hexadecane droplet generation in continuous water phase with a flow focused design at different HD and W flow rates. Different organic phase flow rates (Q_{HD}) were fixed employing a syringe while aqueous phase flow rate was changed with the LFCS for each Q_{HD}. (a) The generated droplet diameter inside the channel was measured with a high speed camera and plotted against flow rate ratio Q_W/Q_{HD}. (b) Droplet diameter on a slide plotted against flow rate ratio Q_W/Q_{HD} in order to further analyze the monodispersity of the droplets. (c) Frequency or velocity at which droplets are formed against flow rate ratio Q_W/Q_{HD}.

HD: 0.1 µl/min						
Water: 3 µl/min Dc= 72 µm f= 0.29 drop/sec Drops merge, they are too big?	Water: 7 µl/min Ds= 64.2 µm Dc= 59.4 µm f= 0.44 drop/sec	Water: 15 µl/min Ds= 39.6 µm Dc= 43.6 µm f= 0.63 drop/sec	Water: 30 µl/min Ds= 30.8 µm Dc= 35.6 µm f= 0.902 drop/sec	Water: 40 µl/min Ds= 28.9 µm Dc= 27.8 µm f= 0.85 drop/sec	Water: 50 µl/min In pairs, same D. Non-repetitive *f* Ds=26.6 µm Dc= 23.4 µm	
HD: 0.2 µl/min						
Water: 3 µl/min Ds= 53.3 µm Dc= 71.4 µm f= 0.32 drop/sec	Water: 7 µl/min Ds= 46.5 µm Dc= 66.7 µm f= 0.56 drop/sec	Water: 15 µl/min Ds= 38.7 µm Dc= 47.7 µm f= 0.93 drop/sec	Water: 30 µl/min Ds= 32.5 µm Dc= 36.4 µm f= 2.32 drop/sec	Water: 40 µl/min Ds= 31.1 µm Dc= 31.6 µm f= 2.71 drop/sec	Water: 50 µl/min In pairs, same D. Non-repetitive *f* Ds= 28.5 µm Dc= 25.8 µm	

HD: 0.5 µl/min						
Water: 7 µl/min Ds= 54.3 µm Dc= 71.4 µm f= 0.8 drop/sec	Water: 15 µl/min Ds= 41.9 µm Dc= 54.6 µm f= 1.5 drop/sec	Water: 30 µl/min Ds= 35.5 µm Dc= 40.2 µm f= 2.4 drop/sec	Water: 40 µl/min Ds= 34 µm Dc= 34.1 µm f= 4.2 drop/sec	Water: 50 µl/min Ds= 32.8 µm Dc= 30.25 µm f= 5 drop/sec		
HD: 1 µl/min						
Water: 5 µl/min slugs Ds=µm Dc=µm f= 0.7 drop/sec Slugs merged	Water: 8 µl/min Ds= 51.8 µm Dc= 67.3 µm f= 2 drop/sec	Water: 15 µl/min Ds= 47.6 µm Dc= 58.9 µm f= 2.9 drop/sec	Water: 30 µl/min Ds= 38.3 µm Dc= 43.5 µm f= 6.7 drop/sec	Water: 40 µl/min Ds= 34.5 µm Dc= 35.5 µm f= 6.3 drop/sec	Water: 50 µl/min In pairs, similar D. Non-repetitive f Ds= 32.3 µm Dc= 31.4 µm	

HD: 5 µl/min						
Water:10 µl/min	Water: 15 µl/min	Water: 30 µl/min	Water: 40 µl/min	Water: 50 µl/min	Water: 60 µl/min	Water: 75 µl/min
Slugs merged	Ds= 52.7 µm Dc= 62.7 µm f= 11.7 drop/sec	Ds= 40.0 µm Dc= 45.3 µm f= 24.3 drop/sec	In pairs, different D, constant *f* Ds= 35.8µm Dc= 39.3 ±3.7 µm 41.9 µm 36.7 µm f= 28.8 drop/sec	In pairs, different D, constant *f* Ds= 35.0 µm Dc= 33.4 ±4.7 µm 36.7 µm 30.1 µm f= 40.3 drop/sec	In pairs, different D, constant *f* Ds= 32.3 µm Dc= 29.4 ±3.7 µm 32 µm 26.8 µm f= 44 drop/sec	In pairs Ds= 27.7 µm Dc= 25.2 ±3.8µm 27.9 µm 22.5 µm f= 59.9 drop/sec

HD: 10 µl/min						
Water: 15 µl/min Ds=µm Dc= µm f= 5 drop/sec slugs merged Water: 100 µl/min In pairs, different D, Constant f Ds= 34.7 µm 18.5 µm Dc= 43.9 µm 19.2 µm	Water:20 µl/min Ds= 42.8 µm Dc= 75 µm f= 16.4 drop/sec Water: 150 µl/min In pairs, different D, constant f Ds= 26.7 µm 15.1 µm Dc= 28.1 µm 12.8 µm	Water: 30 µl/min Ds= 41.5 µm Dc= 51.5 µm f= 35.6 drop/sec	Water: 40 µl/min In pairs, different D, constant f Ds= 37.4 µm Dc= 42.7 ±4 µm 45.6 µm 39.9 µm f= 55.5 drop/sec	Water: 50 µl/min In pairs, different D, constant f Ds= 36.2 µm Dc= 43.6±5.1 µm 47.2 µm 40 µm f= 71.4 drop/sec	Water: 60 µl/min In pairs, different D, constant f Ds= 33.2 µm 28.7 µm Dc= 31.5±4.3 µm 34.5 µm 28.5 µm f= 90.9 drop/sec	Water: 75 µl/min 4/5 unstable Ds= 30.6 µm 27.6 µm Dc= 28.8±3 µm f= 142.8 drop/sec

Figure 7.18. Hexadecane droplet generation in water phase at different HD and W flow rates. Different organic phase flow rates (Q_{HD}) were fixed employing a syringe while aqueous phase flow rate (Q_W) was changed with the LFCS for each Q_{HD}. The generated droplet diameter inside the channel was measured with a high speed camera and the emerging fluid was subsequently collected on a microscope slide to analyze the monodispersity of the droplets. D_S, D_C and f mean droplet diameter on a microscope slide, droplet diameter in the channel and frequency at which the droplets are formed respectively.

7.5. CONCLUSIONS

- The proof of concept for the liquid meniscus-detector has been successfully verified for both approaches, being useful to detect a fluid passing a position of interest, which can be very useful know the completion of several steps in LOC protocols, and notice the presence of leakages in the fluidic circuit.

- The disposable meniscus detector sticker (PSA-detector) has been demonstrated to be feasible for simple, fast and cheap uses, without strict alignment requirements. The user can manually bond it against the interested device, with no need of any microscope or aligner, and its inexpensive fabrication allows its disposable use.

- The reusable meniscus detector membrane for POC platforms has also been successfully accomplished.

- In the validation of the flow sensor for cell culture applications, neither the materials used in the sensor fabrication nor the process of measurement were found to affect the viability of HUVEC cells culturing. This way, culturing has been realized dynamically, generating a shear stress of 0.1 dyna/cm^2 by means of flowing the nutrients under a constant flow rate of 50 µl/min for 20 hours.

  The low cost approach for the microfluidic chip and the miniaturized readout electronics allows the use of this technology for disposable flow sensor devices. Such feature is especially relevant in applications such as cell culture, where the equipment needs to be placed on a harsh environment (95% humidity and 5% CO_2).

- In the droplet generation system, the LFCS has been proved to be suitable to deliver stable and pulseless flow rates, achieving monodisperse droplet formation for a great range of flow rates. The COP material was found to be inappropriate for organic phases such as mineral oil, vegetable oil, hexadecane, etc. so the LFCS was only used to control the DIW phase. However, if applications require the control of

both phases, the technology could be easily transferred to other thermoplastics that can resist the organic phases.

8. MAIN CONCLUSIONS

A brief summary, with the main conclusions is provided as follows, extracted from the technical chapters presented in this thesis:

- In Chapter 3, a modular fabrication process has been successfully accomplished, using a simple and low-cost hot embossing method, which renders virtually defect-free devices with uniform contraction at all points of the replica, achieving values similar to those of industrial processes like injection moulding (0.67%). Two peculiarities of the embossing process distinguish it from the more conventional versions. First, a Pyrex-SU-8 mould without an anti-sticking coating can be used directly for the embossing, overcoming peeling-off during de-moulding step. Second, the de-moulding is carried out slightly above T_g, which provides excellent contraction uniformity and minimizes defects.

  The devices are sealed by solvent-bonding of the membrane, resulting in a monolithic component with excellent flatness at replica level, 0.024 % (±0.014 %) for the 3 mm diameter membrane, and unimpaired optical properties, allowing the fabrication of microvalves module with uniform gaps as low as 10 µm. The stress caused by the subsequent thin film metal deposition process reduces this flatness. However, the membranes retain a remarkable flatness and repeatability at chip level and wafer level, 0.470 % (±0.183 %), for the same diameter.

  The quality of the modular fabrication presented in this chapter evidence the enormous integration potential, owing to its monolithic construction in ordinary materials, which can simplify the complex task of embedding microfluidic control and other microfluidic operations in LOCs, which could be highly beneficial for the Lab-on-a-Chip community, since it is a real risk-reducer ahead of mass-production and it can be extrapolated to other thermoplastic polymer.

- In Chapter 4, a successful microvalve architecture has been presented, whereby three dimensions can be easily modified to tune the maximum flow rate and the

flow regulation profile. This microvalve provides improved performance for liquid flow regulation, from 200 nl/min up to 9 ml/min, ability to fully close the valve with instantaneous response time and negligible leakage of 0.2 µl/min, and excellent repeatability. This architecture allows highly versatile valving in rigid materials and it is a real alternative for microfluidic control, catering for varying flow control needs with a single valve concept and with high performance standards.

- In Chapter 5, the first approach towards an off-chip 100% polymer monolithic flow sensor has been described, which exhibits excellent resolution and reliability at low flow rates and low actuation temperatures. For the simple channel, excellent resolution of 30 nl/min in the range of 0-2000 nl/min and maximum error of 7% have been achieved. The introduction of a bypass has helped the sensor cover higher flow ranges, between 3 and 300 µl/min with an error less than 5%, with no dead volumes and no trapped bubbles. Owing to the previous fabrication process, the sensor can be easily integrated with other microfluidic components in complex LoC systems without affecting its performance.

  Some remarkable features include Ni electrodes, instead of the more common Pt, which enhances sensitivity and lowers cost, an off-chip, non-wetted configuration, which avoids undesired effects i.e. electroosmotic flow, corrosion of the sensing elements and deterioration of the sample, and total post-produced customization of the sensor location, which allows ubiquitous sensing of the microfluidic protocol and is compatible with industrial printing processes.

- In Chapter 6, a Liquid Flow Controlling System has been introduced, which integrates the previous components, namely, the valve and the off-chip flow sensor with a bypass. The LFCS shows great reproducibility and accuracy, achieving an error less than 5% in the range between 30-230 µl/min. The accuracy for a given flow range can be increased by integrating a bypass that is adequate for that particular range.

- In Chapter 7, the previous microfluidic components have been tested in new applications. First, a liquid meniscus-detector has been demonstrated, which is based on the flow sensor. This allows detection of the fluid past a position of interest as well as leakages. The objective is to enhance the robustness of the microfluidic protocol in the LoC, which is critical for its commercial success.

  Secondly, the flow sensor has been validated for HUVAC cell culture applications. In this case, the sensor has been integrated in an electronic board, programmed to maintain a closed-loop-regulated flow (50µl/min) that provides both nutrients and physiological stress levels to the cells. The viability of the culture is very high after 20 hours and similar to that obtained with commercial sensors. Futhermore, neither the sensor materials nor the measuring process have been found to affect the viability. Moreover, the low cost of the sensor and the electronics make this technology disposable, this feature being of especial relevance, since the equipment needs to be placed on a harsh environment (95% humidity and 5% CO_2).

  Finally, the LFCS has been proven to deliver stable and pulse-free flow for droplet generation systems.

The results of this thesis contribute primarily to a reduction in the risk associated with industrialization, by providing a highly performing LOC prototyping process, proven for typical microfluidic components and electrodes, all of them integrated in a single monolithic piece with industrial-like finish. This is further backed by the compatibility of the prototyping process with current industrial processes, such as injection moulding, and roll-to-roll embossing/printing. From the microfluidic point of view, this thesis contributes to the state of the art, by demonstrating a flow regulating microvalve architecture suitable for rigid materials (thermoplastics), a high-resolution flow sensor that can be scaled-up to the desired LOC flow rate range and a miniature LFCS in polymer with excellent regulation capabilities.

8.1. FURTHER WORK

In this section some prospective ideas are provided, which could help bring further the results of this thesis:

- Considering the current interest that some companies (undisclosed) have shown in implementing the LFCS technology, the peripherals should be miniaturized, namely valve actuators and electronics, to render a portable and automated flow controller, where the plastic device is disposable. For the miniaturization of the whole setup, the possibility of replacing the pneumatic actuator is contemplated, with a smaller and portable actuators such as micromotors with a centred pin, microcompressors, etc.

- Considering the excellent accuracy of the flow sensor for low flow rates, 0-2 μl/min, an appropriate LFCS for this range could be realized. For this, a new microvalve concept would be required. This may result challenging due to the limitations coming from the rigid material employed.

9. APPENDIX

APPENDIX SECTION II – Microvalve

i. Discussion on the effects caused by poor membrane flatness

Results for optimized manually bonded microvalves, where the rendered membrane flatness is not homogenous in the whole wafer neither between different batches.

The characterization results for microvalves of 40 µm *gap* are shown below in Figure II.1.

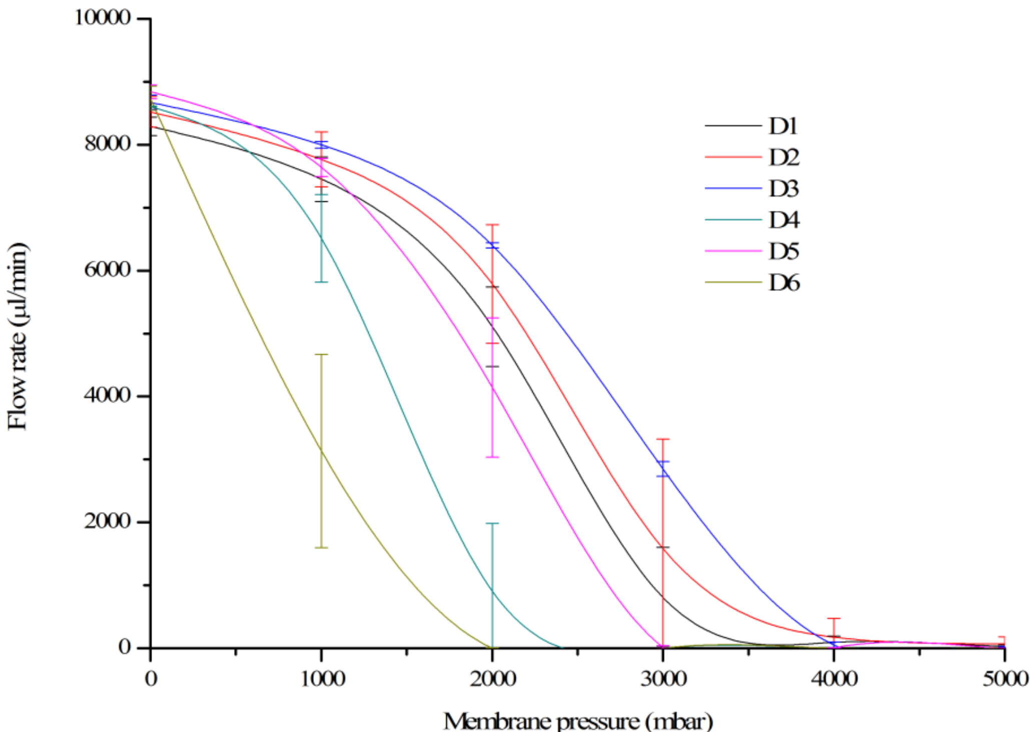

Figure II.1. Characterization results for manually solvent-bonded microvalves of 40 µm. The results seem to agree with the theoretical prediction, since as the seat diameter (*C*) decreases or the valve chamber's diameter (*D*) increases the closing pressure also decreases. Nevertheless, the repeatability between different chips of the same design is not acceptable for flow modulation. This lack of repeatability is considered to be the

consequence of non-uniform loads during the bonding of the membrane and COP wafer in the optimized solvent-bonding process by the aid of a manual roller.

Although the characterization results seem to agree the theoretical prediction, since as the seat diameter (*C*) decreases or the valve chamber's diameter (*D*) increases the closing pressure also decreases, the standard deviation obtained is not acceptable for flow modulation.

During the manual solvent-bonding process the membrane is putted in contact together with the structured wafer by the aid of a manual roller, which does not ensure uniform loads all over the wafer. Due to that, these non-uniform forces could render microvalves with membranes that could develop different mechanical tensions, and consequently could result in different membrane deformations.

In order to study this hypothesis and know the involvement of the membrane deformation on the microvalve response, three microvalves for two different designs (design 1 and 6) of 40 µm *gap* were selected and their membranes were measured with a profile meter. In regards to design 1, two microvalves with the same membrane deformation have been chosen, in order to see if both present the same response to actuation as is expected to happen, and the third one's deformation is different, but keeping in mind that the initial flow rate is equal or similar for all microvalves (in these case membrane plastic deformation does not decrease the fluidic path of the microvalve and therefore the initial flow rate is not reduced). For design 6, the three microvalves present different membrane deformation, so it is expected that three of them will behave different. The membrane profile measurements and the subsequent characterization results are illustrated in Figure II.2.

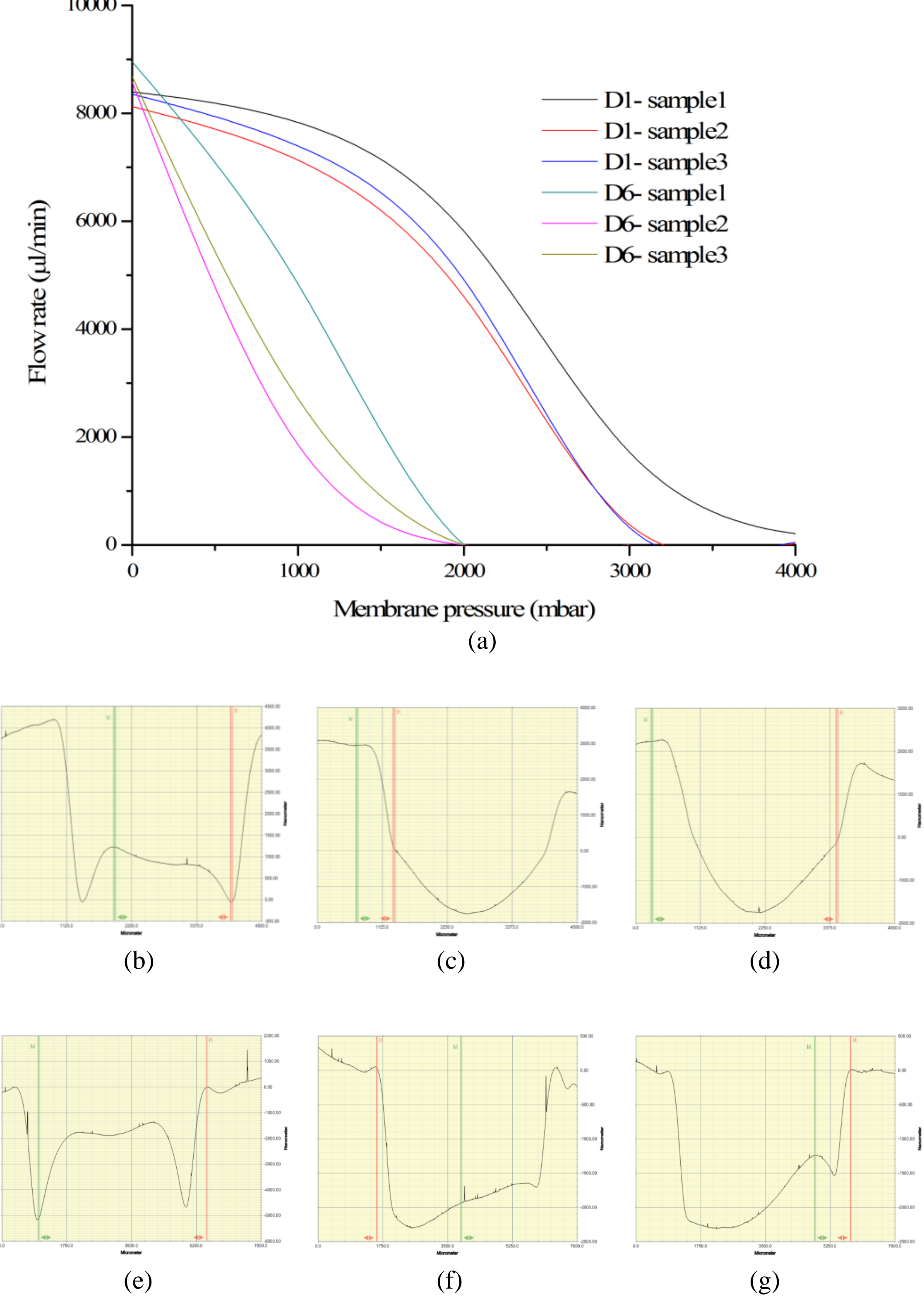

Figure II.2. Analysis of the involvement of initial membrane deformation choosing three microvalves of design 1, two with similar deformation (sample 2 and 3) and one with different (sample 1) in order to see if the same

deformation leads to same response to actuation, and another three microvalves of design 6, all of them with different membrane deformation. (a) Characterization curve for design 1 and 6 microvalves with 40 μm gap employing 1000 mbar fluid pressure and actuation pressures from 0 to 2500 mbar and from 0 to 4000 mbar, respectively. (b) Profile measurement of the initial membrane deformation for sample 1 of design 1, the peak is 1.2 microns respect to the horizontal plane and gap reduction is about 4 microns, (c) Membrane deformation measurement for sample 2 of design 1, the minimum peak is 1.8 microns and gap reduction is about 2.5 microns, (d) Membrane deformation measurement for sample 3 of design 1, the minimum peak is 1.6 microns and gap reduction is about 2 microns. (e) Membrane deformation measurement for sample 1 of design 6, the peak is 3.5 microns and gap reduction is about 5 microns, (f) Membrane deformation measurement for sample 2 of design 6, the deformation of the suspended membrane is negligible and gap reduction is about 3 microns, (g) Membrane deformation measurement for sample 3 of design 6, the peak at one edge is about 0.25 microns and gap reduction is about 2 microns.

As mentioned before, the employment of a manual bonding method resulted in a limited repeatability in microvalve's behaviour. And as expected, in Figure II.2 it can be seen that when membranes have a similar initial plastic deformation (samples 2 and 3 for design 1), this similarity also remains in the control behaviour of the microvalve, and actuation force for microvalve closure also changes. On the other hand, the difference on the reduction of the *gap* also provides different response as it can be seen when comparing the response for microvalves 5 and 6.

This result required an improvement of the solvent bonding method. Alternatively, a rolling laminator has been used to render planar microvalves with excellent flatness, Figure II.3. This later devices were measured in the profile meter, and only the flattest ones, presenting membrane deformation of less than 3 μm, were selected and fully characterized in Chapter 4, in order to analyze the effect of each design feature.

Figure II.3. The rolling laminator machine used in the solvent bonding method, designed by EVG® for the Lab On Foil Integrated Project.

APPENDIX SECTION III - Sensor

i. Electronic circuitries for heating and sensing (4w and Wheatstone Bridge)

The 4-w connection, allows measuring the resistance of the heater avoiding the intervention of the connectors resistance, as explained in Figure III.1. Thereby, it permits to set the needed heater's temperature with high accuracies.

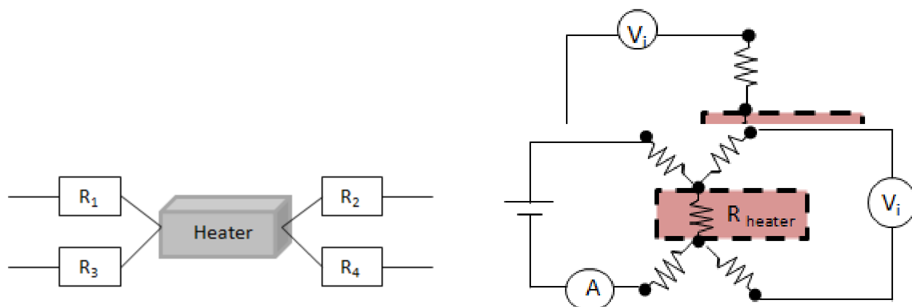

Figure III.1. Block diagram of the heater with its connectors, R1, R2, R3 and R4 (four wire connection method). The current is forced through the heater and two connectors (R1 and R3), while the voltage across the heater is measured through the other two connectors (R2 and R4). Although a small current needs to pass through the connector R2 and R3, it is usually negligible and can generally be ignored for practical purposes, since the voltage drop across these connectors is negligible, leading to voltage measurements essentially corresponding to the heater. As a result, the resistance value for the heater can be much more accurately measured than that when using a two wire method.

The Wheatstone bridge circuit, shown in Figure III.2, is commonly used in order to obtain accurate measurements of resistances, because it is a highly sensitive type of circuit.

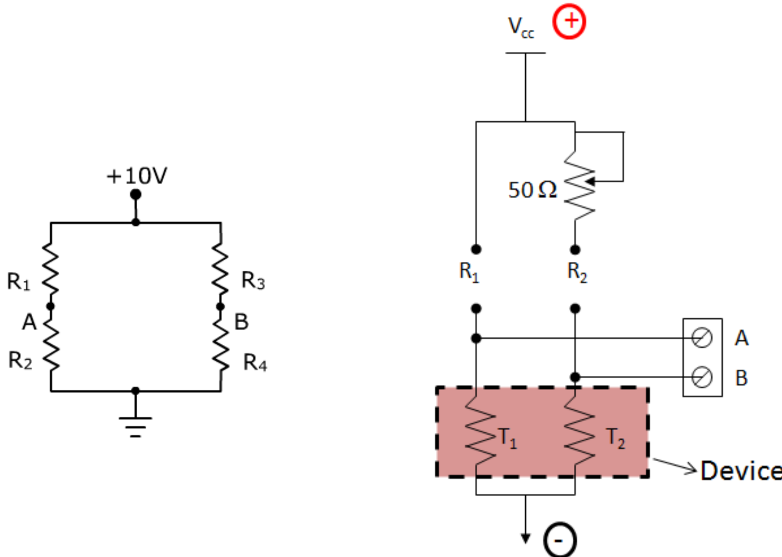

Figure III.2. Wheatstone bridge circuit scheme (left) and the circuitry used in the setup for characterization (right) of the device.

Although both sensors in a device should be identical, limitations in the fabrication process result in difficulties to maintain a constant thickness of the metal layer across the whole wafer. This leads to have different resistances in each sensor, and consequently an output voltage signal is measured for the stopped liquid. This measured voltage can be balances and set at zero by the tunable resistor shown in Figure III.2.

In the same way, since the sensitivity of the measurements is enhanced when T_1 and T_2 are as equal as possible to R_1 and R_2, respectively, R_1 and R_2 resistors were built in the way that they might be replaceable.

In order to enhance more the sensitivity of the measurements, it would be of great interest to only consider the resistance of the meandering parts which exactly match the area of the channel, and thus diminish the interference of the electrical connector's resistances. The best option for that is to construct also the sensors with 4-w configuration. This complicates the electronic and setup resources during the proof of

concept at laboratory scale. Alternatively, the connectors were designed much thicker than the sensing elements, so they can be negligible.

ii. Analysis of each design parameter for the calorimetric flow sensor

In the following Figure III.3, the results are compared as a function of each designing parameter, intending to determine the effect of each parameter separately in terms of sensing capability. The analyzed parameters are distance between the heater and the sensors (*D* in Figure III.3.(a)), length of the heater (*H* in Figure III.3.(b)), width of the heater (W_{heater} in Figure III.3.(c)), length of the sensing elements (*S* in Figure III.3.(d)) and width of sensing elements (W_{sensor} in Figure III.3.(e)).

For the designs with identical sensors (on the one hand D1, D5, D9, D2, D6, D10 and D13-D16; and on the other hand D3, D7, D11, D4, D8 and D12), if *H* increases so does the voltage signal measured due to the increase in the area of the heater, so the heat provided to the flowing DIW also increases and consequently, the sensors receive more heat. In this way, D2>D1, D6>D5, D10>D9 and D4>D3, D8>D7, D12>D11, as can be seen in Figure III.3.(b).

According to the heat transfer and what has been seen for *H*, augmenting W_{heater} might also provide a similar effect. But as depicted in Figure III.3.(c), a considerable improvement cannot be appreciated since the benefit of increasing the area of the heater is removed with an increase in cross-talk effect (heating of the sensing elements due to the conducted heat through the plastic). Accordingly, a slight improvement can be noticed when increasing *D* together with W_{heater}, as can be observed in Figure III.3.(a), especially when operating at 60ºC (D13≥D6, D14≥D10).

When W_{sensor} decreases, greater is the resistance of the sensors, and detection of small readout changes is expected to be enhanced. However, as can be seen in Figure III.3.(d), the voltage signal has decreased due to reduction of $\Delta T_{DIW\text{-}sensor}$, as a consequence of increase in the self-heating, resulting D8>D13 and D12>D14. Nevertheless, for designs

with lower W_{sensor} (D13-D16 for instance), the sensitivity does not tend to fall when augmenting *D*, meaning that the sensing elements are able to detect the changes in the resistance even if DIW may cool down with distance. In Figure III.3.(a) is shown that the sensitivity decreases only in the case of D16 when operating at 40ºC, which means that the distance of 100 µm is too high for that working temperature, and DIW cools down before reaching the downstream sensor.

For a larger length of the sensor (*S*), a similar effect of increasing the self-heating and decreasing the readout can be appreciated in Figure III.3.(a) and Figure III.3.(d).

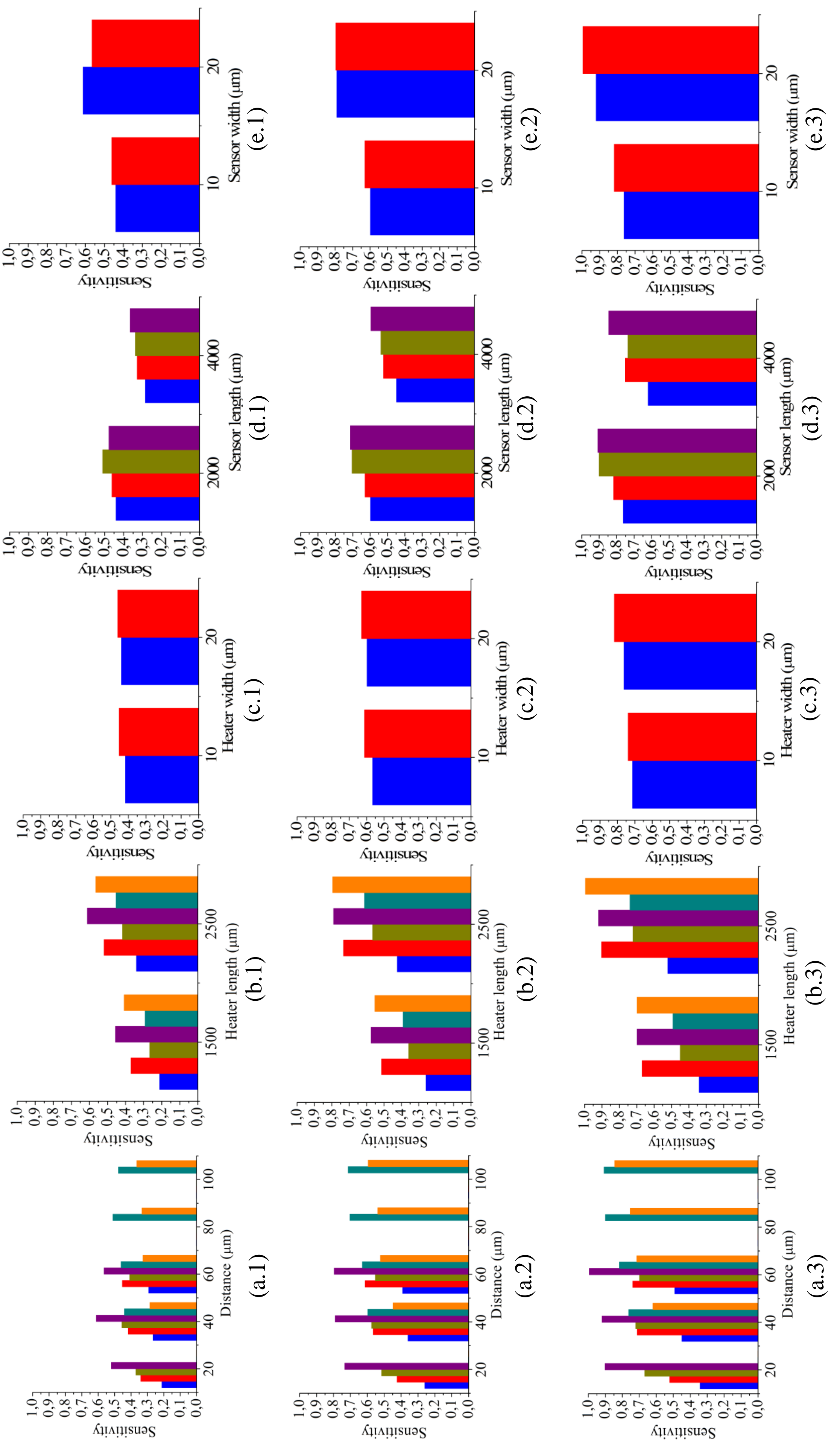

Sensitivity
Distance (µm)
(a.1)
(a.2)
(a.3)
Heater length (µm)
(b.1)
(b.2)
(b.3)
Heater width (µm)
(c.1)
(c.2)
(c.3)
Sensor length (µm)
(d.1)
(d.2)
(d.3)
Sensor width (µm)
(e.1)
(e.2)
(e.3)

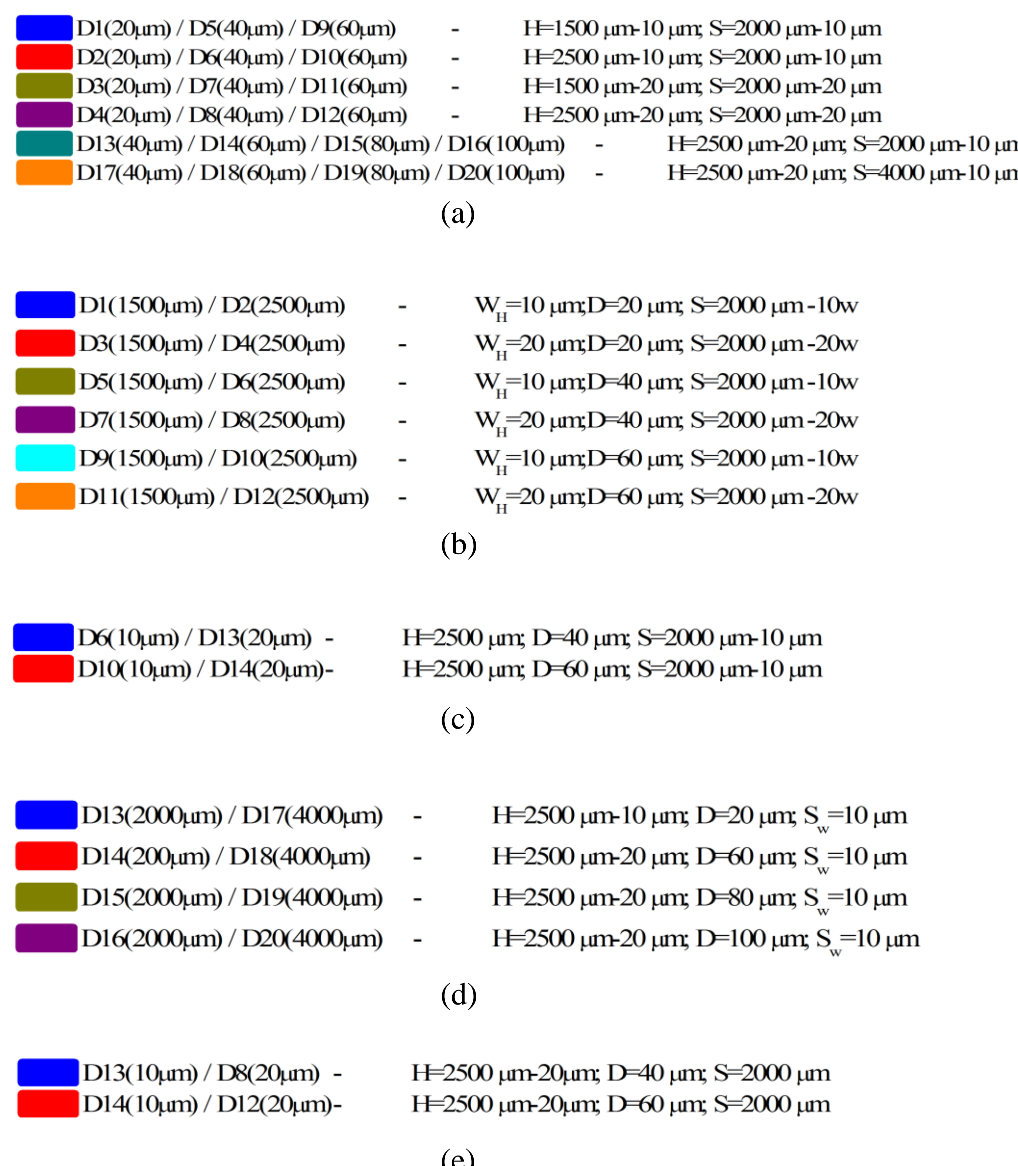

Figure III.3. Analysis of each designing parameter and its effect on the sensitivity for the micro flow sensor, in calorimetric configuration and CV mode. (a) Effect of D (distance between the heater and sensing elements) at 40ºC (a.1). 50ºC (a.2) and 60ºC (a.3); (b) Effect of H (length of the heater) at 40ºC (b.1). 50ºC (b.2) and 60ºC (b.3); (c) Effect of Wheater (width of the heater) at 40ºC (c.1). 50ºC (c.2) and 60ºC (c.3); (d) Effect of S (length of sensing elements) at 40ºC (d.1). 50ºC (d.2) and 60ºC (d.3); (e) Effect of Wsensor (width of the sensing elements) at 40ºC (e.1). 50ºC (e.2) and 60ºC (e.3).

iii. Effects caused by poor membrane flatness on the bypass-sensors

For the initial test with the bypass-sensor, 10 chips were subjected to increasing pressure driven flows of DIW, from 0 to 1 bar, while recording the total flow rate (Q_T) measured by the commercial flow sensor and the voltage signal measured by the data logger, when the heater operates at 50ºC. The results are depicted in Figure III.4.

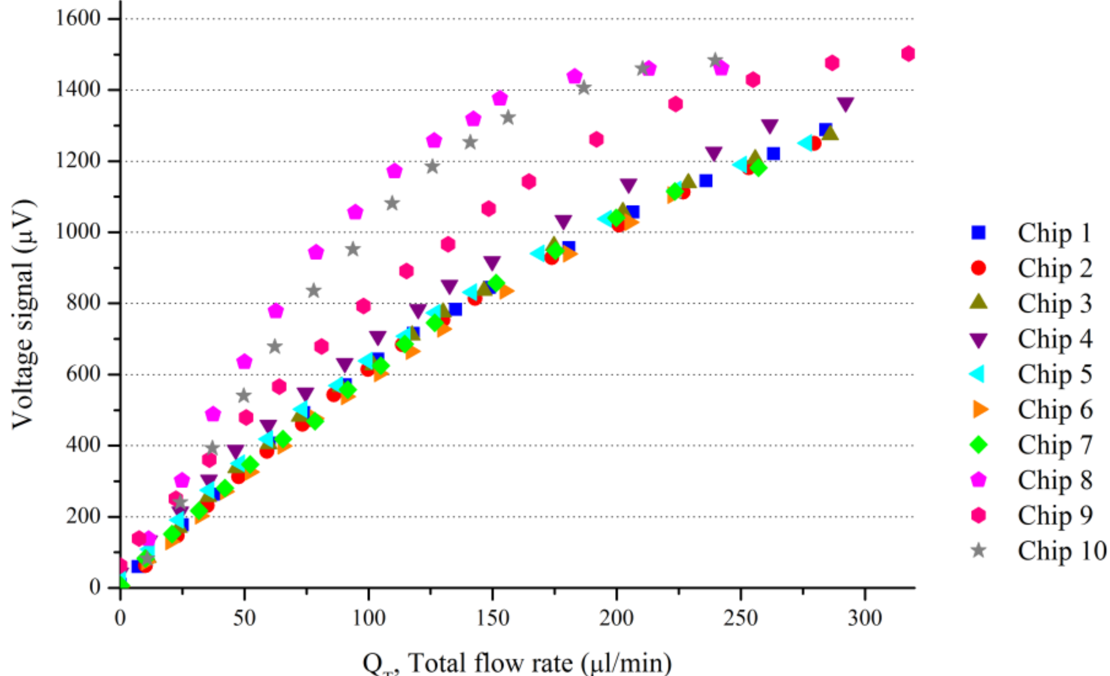

Figure III.4. Characterization results for ten different devices of bypass-sensor with W=2 mm and D12 sensor design, employed in calorimetric configuration and CV mode at 50ºC, where the readouts for increasing DIW flow rate are plotted.

From the characterization results, lack of repeatability was observed for 3 chips out of the 10 (chips 8, 9 and 10).

In order to investigate this in more detail, one representative condition of a system with a bypass construction has been considered, that as long as laminar flow condition is accomplished in both channels (sensing and bypass channels), the ratio of flow rates through these channels (Q_b/Q_s) has to be linear with the increasing pressure drop imposed. Moreover, as Q_b and Q_s depend exclusively on the geometry of the channels,

the derivative (slope) of curve that represents Q_b/Q_s vs. pressure drop must be constant from one device to another, whenever the geometry of the structures does not vary.

In Figure III.5, the flow rate through the bypass (Q_b) against the flow rate through the sensing channel (Q_s) has been depicted for an increasing pressure drop across the device. For this purpose, the data obtained from Figure III.4 has been used together with the characterization equation obtained for the simple-channel sensor of D12 at 50ºC. From there, flow rate through sensing channel (Q_S) has been calculated, and flow rate through bypass channel (Q_b) has been calculated by difference among Q_T and Q_S.

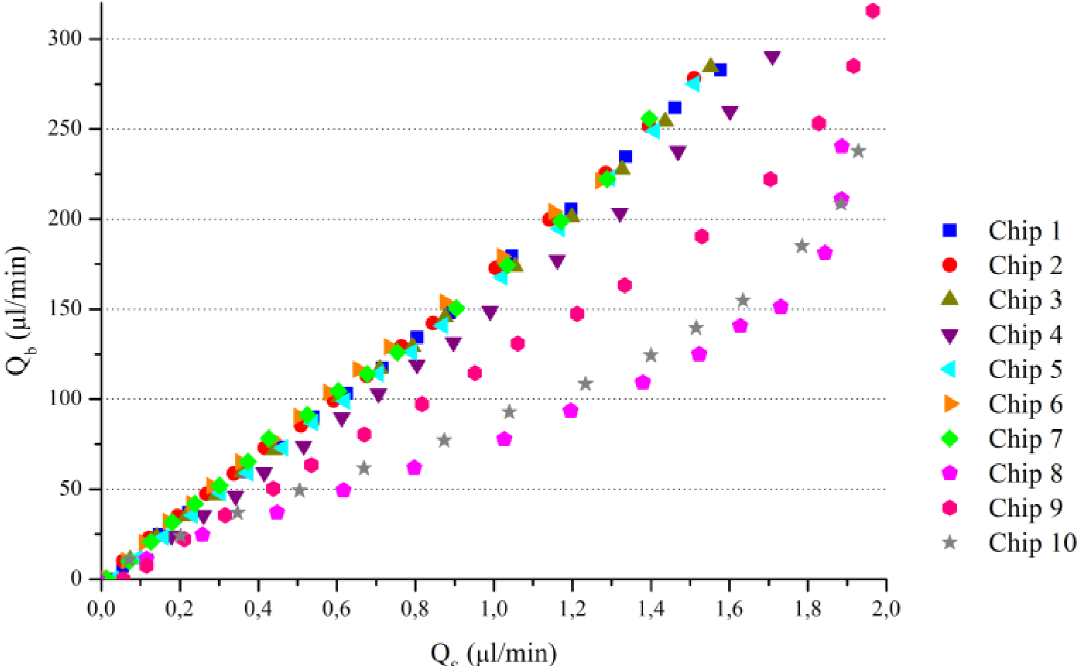

Figure III.5. Characterization data, where Qb vs. QS has been plotted for 10 different bypass-sensors with W=2 mm and D12 sensor design, employed in calorimetric configuration and CV mode. The flow rate through the sensing channel (QS) has been calculated converting the readouts into Qs using the characterization equation obtained for the simple channel flow sensor for 50ºC.(b). The flow rate through the bypass channel (Qb) has been achieved by difference between the total flow rate (QT), measured by a commercial sensor, and the calculated QS.

From Figure III.4 and Figure III.5 a noticeable lack of repeatability for chip 8, chip 9 and chip 10 can be appreciated, which coincides with the observation that the three devices had been produced by manual bonding, while the other seven devices were bonded employing the optimized bonding process and show much more similar behaviour between them.

It is further noticed that the linearity of curves for chips 8-10 disappear when saturation point of the sensor is reached around 150-200 µl/min of Q_T, in Figure III.4. For the devices accomplished with optimized bonding method, chips 1-7, the saturation point is shifted to around 300 µl/min, and more linear profile was achieved.

Moreover, for a fixed Q_S value, same or similar Q_b values were achieved for chips 1-7, whilst diversity was observed among chips 8-10, meaning that the bypass channel geometry is not repetitive for these three manually bonded chips.

The planarity of membranes has been measured in a surface profiler and depicted in Figure III.6. It can be observed that with the optimized bonding method, similar flatness is achieved from one chip to other. This is reflected in that the resulting slope for chips 1-7 is constant and similar, offering a clear resolution of the repeatability in the manufacturing of the devices. On the contrary, when the devices had been manually bonded, chips 8-10, the profile and magnitude of the planarity has vary from chip to chip, resulting in a different distribution of Q_T into Q_b and Q_S.

The earlier saturation of the sensor is also explained from the membrane deformations, because in Figure III.6.(h) for instance, the bypass channel's height results smaller, leading to a smaller Q_b/Q_S for a fixed Q_T.

Thereby, it has been demonstrated that the flatness of the membrane greatly affects the dimensions of the final channels, influencing notoriously the distribution of Q_T into Q_b and Q_S, and consequently the readouts between chips. Thereby, the detection range, accuracy and repeatability result notably affected.

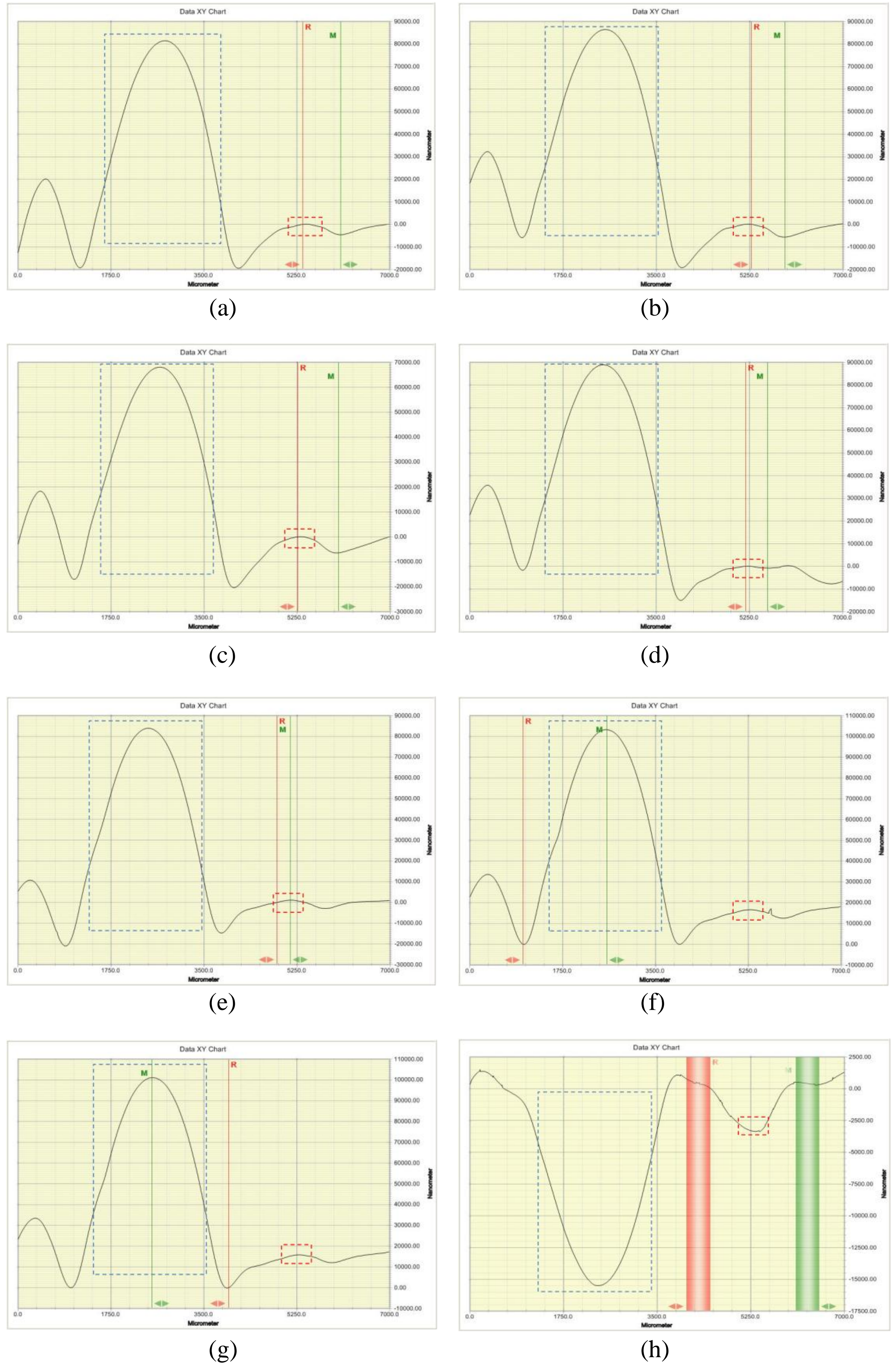

(a) (b)

(c) (d)

(e) (f)

(g) (h)

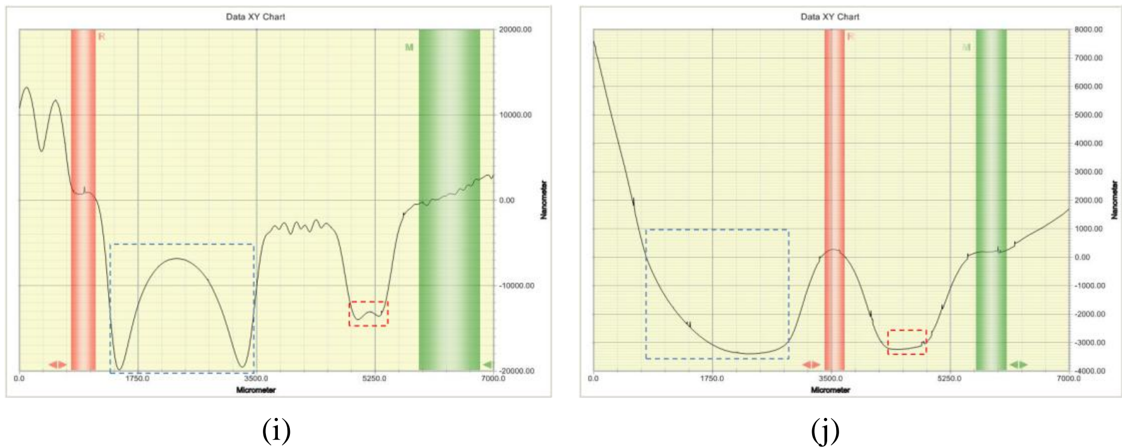

(i) (j)

Figure III.6. Surface profile of the COP membranes for bypass-sensor devices, whose characterization curve has been shown in Figure III.4 and Figure III.5. The measured plastic deformation belongs to the covering membrane of the structures. Whilst for the devices from (a) to (g) the COP membrane had been bonded with the optimized solvent bonding method, the devices (h)-(j) had been manually bonded.

APPENDIX SECTION IV - LFCS

i. PID control tool

For the accurate performance of the LFCS to precisely set the desired setpoint, a control loop feedback mechanism is required to properly communicate the flow sensor and the valve.

In this section, the used Labview programming software will be described in a very basic manner, focusing on the performance from the user's point of view.

The control and display program has been performed by implementing a State Machine, which is one of the fundamental programming architectures frequently used to build applications quickly and can be used to implement complex decision-making algorithms that can be described by state diagrams or flowcharts. It is used in applications where distinguishable states exist, and each state can lead to other state or multiple states, and it relies on user's interaction to determine which state to go next. Thus, Event Driven State Machine offers a way to create a program which considers user interactions, such as key strokes or mouse events, and then take appropriate actions based on this user's input.

The main states of the implemented machine are the Initialization State 1, Initialization State 2, Heater State, Measure State and Stop or Finish State. The actions for each state, with the respective control screen and the screen that the user displays, are as follows.

In Initialization State 1, the program asks to the user to input the calibration data for the calorimetric flow sensor. In this step, the user can introduce some data derived from the sensor's characterization, otherwise, the default data introduced in the program is used. In order to make a more accurate approach when converting the output voltage signal into the flow rate, the program uses the least square method to approximate the solution instead of the characterization equation obtained in Chapter 5. The programming interface and the screen viewed by the user are shown in Figure IV.1.

In Initialization State 2, the user needs to determine the scenario of the desired flow rates to be generated, that is whether to use a routine of flow rates or to skip this routine and determine a constant flow rate value. In case a routine is preferred, the user has to either choose a previously saved routine or define a new one, being able to save the generated ones for future applications. The respective screens to this state can be seen in Figure IV.2.

In Heater State, the user has to adequate the input voltage applied to the heater according to the TCR calibration curve previously obtained in order to achieve the desired working temperature in the heater. In this case constant voltage (CV) operation mode for the heater has been chosen to proof the concept of the automated LFCS so as to simplify the automated system and avoid complexity that would suppose the implementation of another closed-loop control system to correct the heater's temperature (needed in constant temperature mode, CT). In the previous chapter a working temperature of 50 ºC has been determined to be the best. In this stage, the user also needs to equilibrate the Wheatstone Bridge when the fluid flow is fully stopped by simply tuning the multi-turn potentiometer described in Chapter 6. These screens can be seen in Figure IV.3.

In Measure State the flow meter starts working under the order of a PID controller. Initially the microvalve is fully opened, since the pressure controller does not execute any action until the controller sends an order. Consequently, when a constant pressure drop of 1 bar is imposed across the device, the generated flow rate will be the maximum the system permits. Once the flow sensor notices the liquid flowing and measures its flow rate, the PID controller compares it to the one the user has defined and calculates the associated error. As a result, the PID controller sends a command to the pressure controller in order to actuate on the membrane and increase/decrease the fluidic resistance to correct the flow rate and deliver the proper amount of fluid. The flow controller program screen and real time flow rate monitoring can be observed in Figure IV.4.

Finally, in the Stop State the user finishes the execution of the flow controller by simply clicking on the STOP button placed in the flow rate real time monitoring interface. To finish the application the program gives the opportunity to save all the data measured during the application, such as measured flow rate, exerted pressure against the microvalve, voltage measured in the Wheatstone Bridge, the resistance of the heater, and so on. The respective program screen is depicted in Figure IV.5.

Regarding to PID control systems, a PID algorithm involves three constant parameters: the proportional (P), the integral (I) and the derivative (D).

The proportional gain (K_c) produces a control signal proportional to the error signal, enabling to reduce the steady-state error but does not eliminate it.

The integral time (T_i) provides a correction to offset the disturbance and maintain the controlled variable at the set point by eliminating the stationary errors. However, if T_i is too low it can destabilize the system.

The derivative time (T_d) anticipates the effect of the proportional action to stabilize more the controlled variable after a disturbance.

The controlling program includes the optimum constant parameters in order to obtain a good delivering response over the range that the LFCS covers. Nevertheless, in case the obtained overall response is not the desired, for instance because the response is too slow, it shows an increasing oscillation, etc, the user needs to manually adjust the control parameters. In principle, the proportional gain (K_c) adjusting improves the rise time, the integral time (T_i) eliminates the steady-state error and the derivative time (T_d) improves the overshoot.

In regards to manual adjusting, one tuning method is to first set T_i and T_d values to zero and increase K_c until the output oscillates. Then K_c should be set to approximately half of that value and increase T_i until the offset is corrected in sufficient time for the

process, taking into account that a too high K_i can render an unstable system. Finally, T_d is increased until the desired set point is reached in an affordable time.

In general terms, the effect of increasing each constant parameter independently has been resumed in the following Table IV.1.

Table IV.1. Effect of increasing independently each constant parameter involved in PID control

Parameter	**Rise time**	**Overshoot**	**Settling time**	**Steady-state**	**Stability**
K_c	Decrease	Increase	Small change	Decrease	Deteriorate
T_i	Decrease	Increase	Increase	Eliminate	Deteriorate
T_d	Small change	Decrease	Decrease	No change	Improve if T_d small

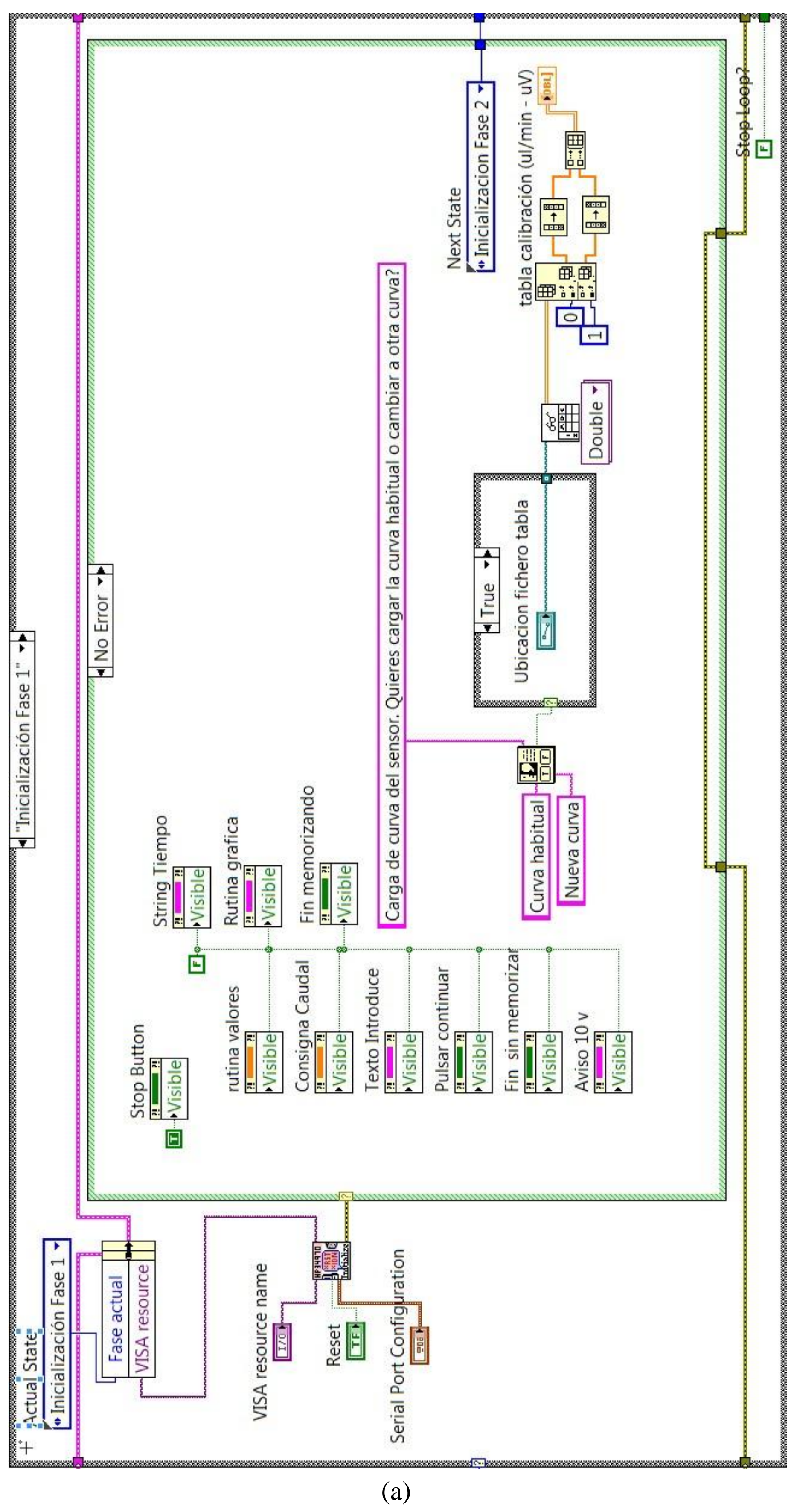

(a)

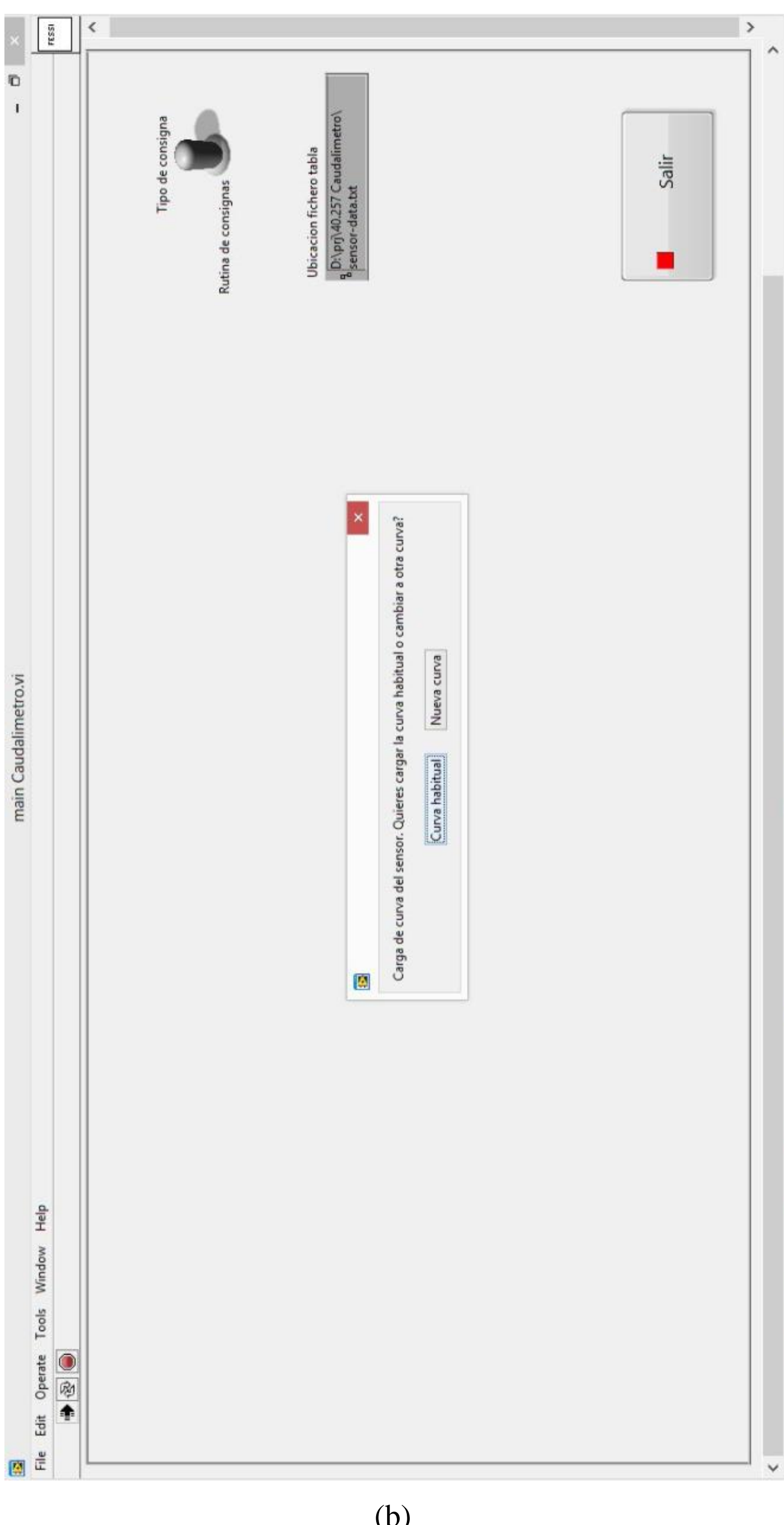

(b)

Figure IV.1. Initialization State 1, where the characteristic data for the calorimetric flow sensor must be defined to relate the generated flow rate with the output voltage signal. In this step the user has to determine either to use a default characterization data or define new values.

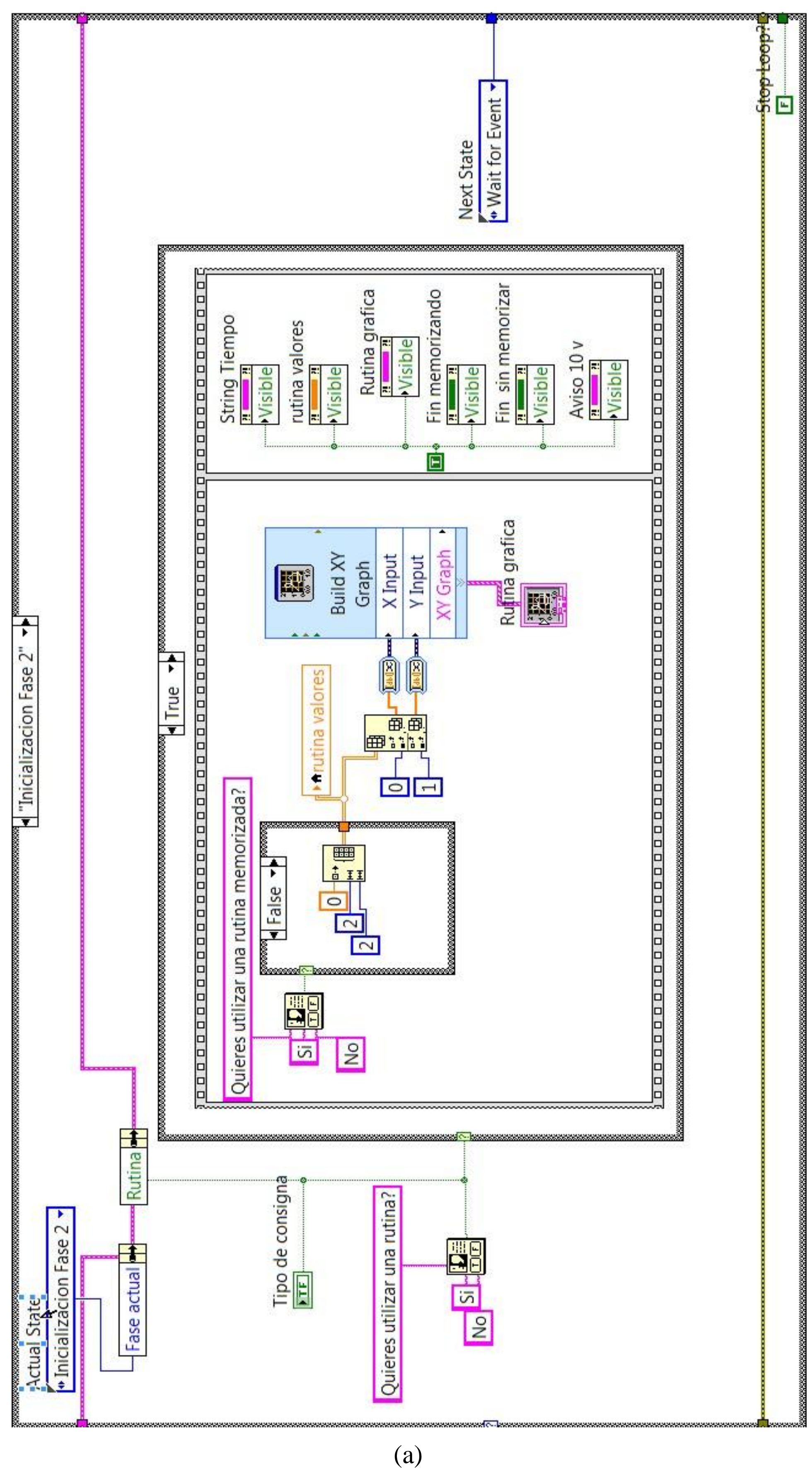

(a)

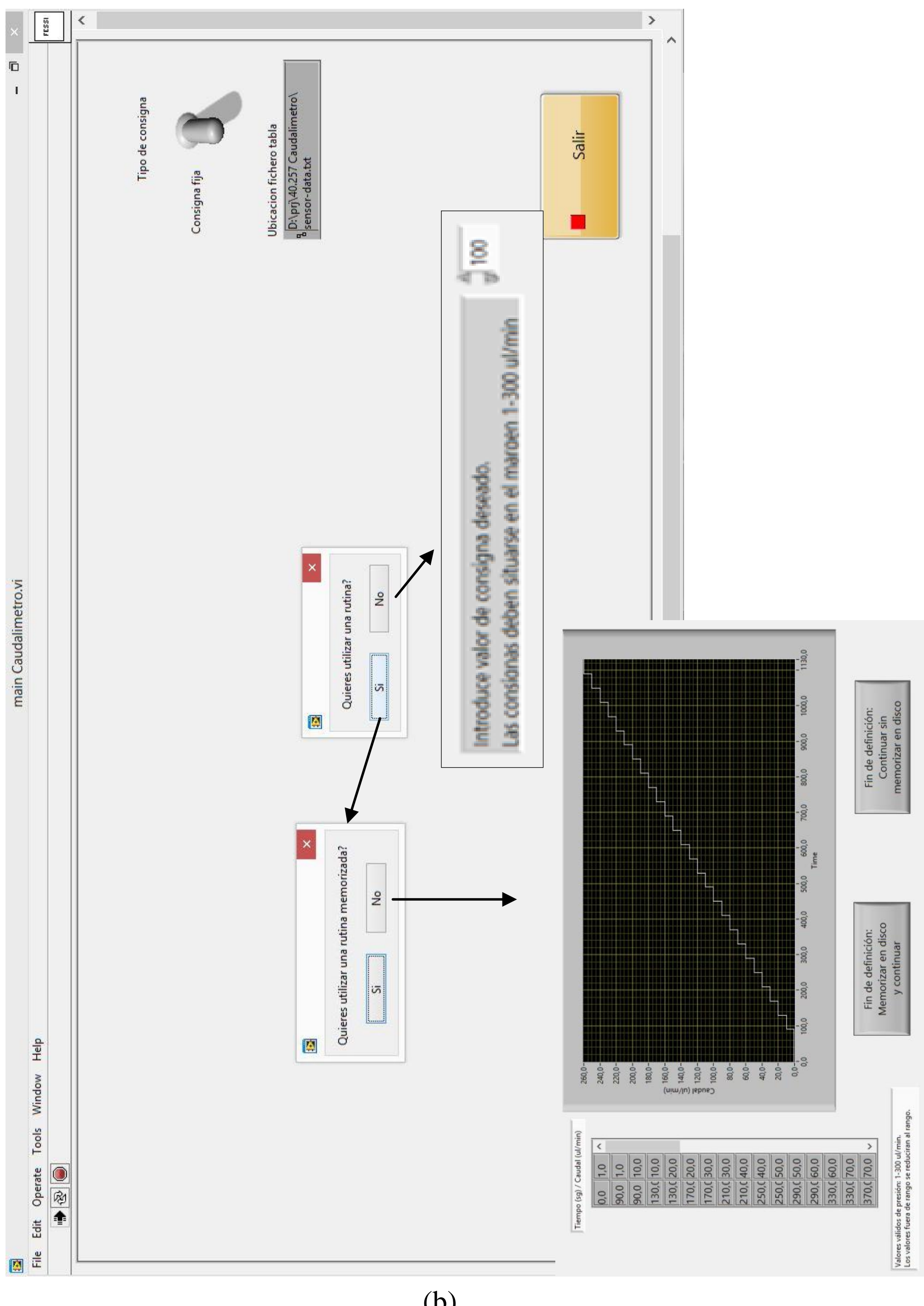

(b)

Figure IV.2. Initialization State 2, where the user has to determine to either use a routine to generate the desired flows along time, or define a precise and constant flow rate, whose value can be manually modified later on during the application. In case a routine option is selected, there is the option to open a previously memorized flow rate routine or to define a new one, which can be saved for future applications.

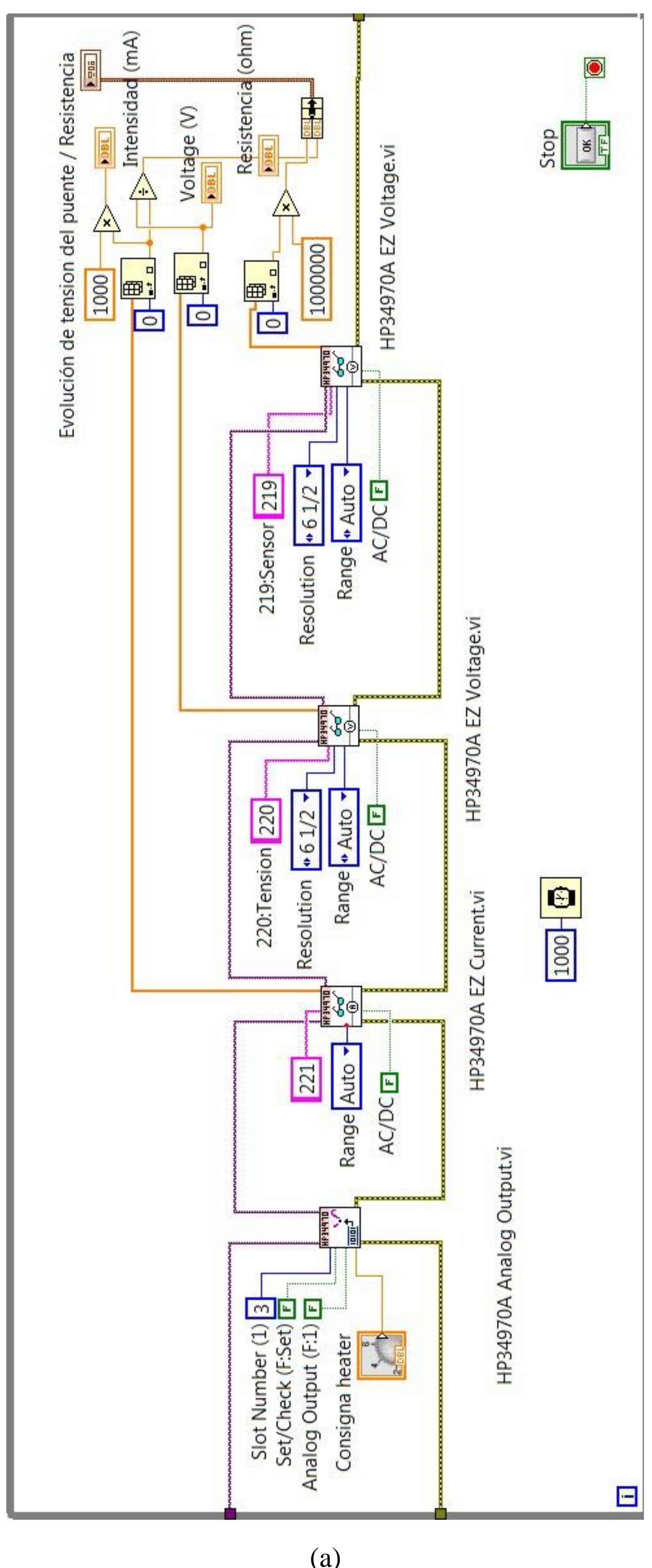

(a)

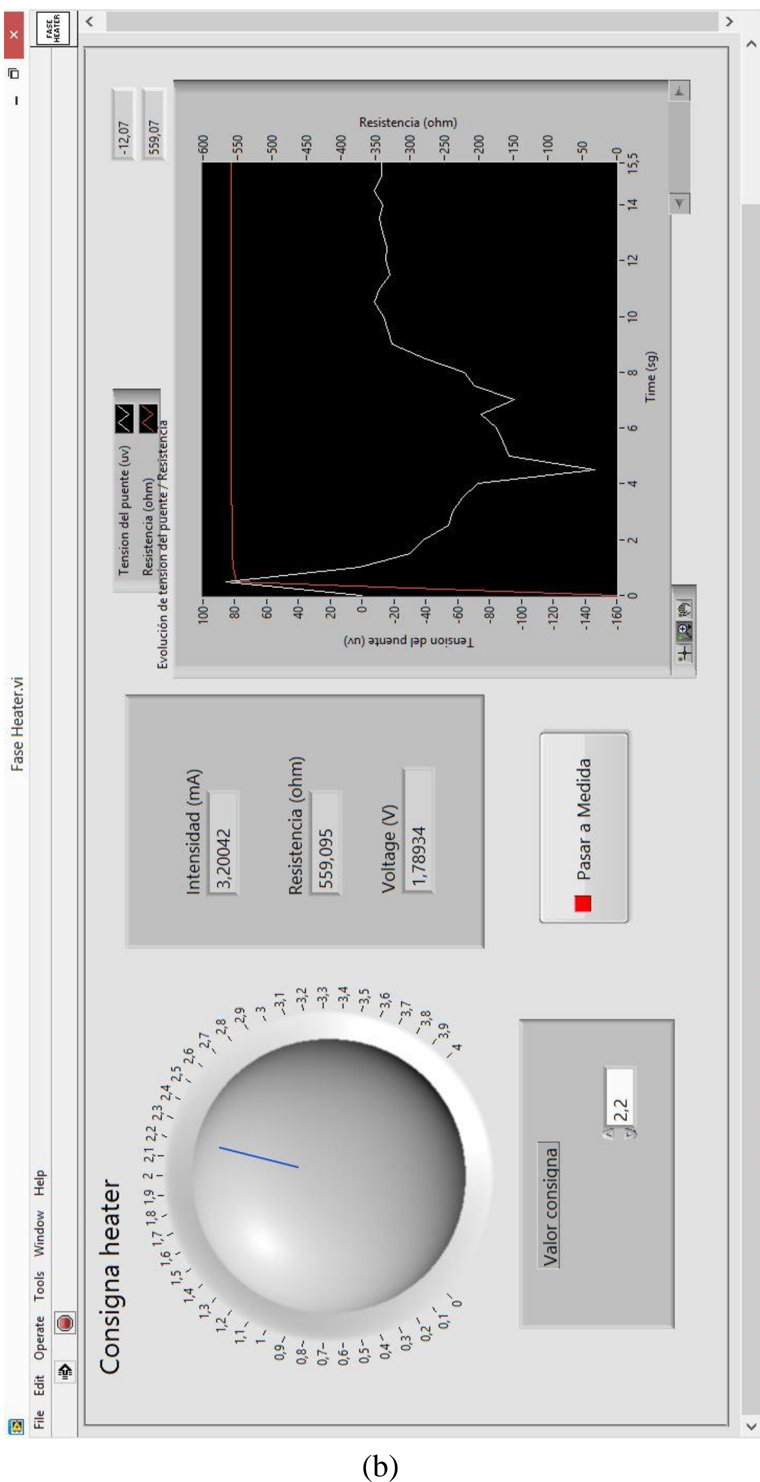

(b)

Figure IV.3. Heater State where the user sets the adequate conditions for the heater and sensors. First, the voltage needed to apply on the 4-wire heater is adjusted to maintain it at desired initial working temperature (50ºC), and then the Wheatstone Bridge needs to be balanced by tuning the multi-turn potentiometer in the electrical circuit.

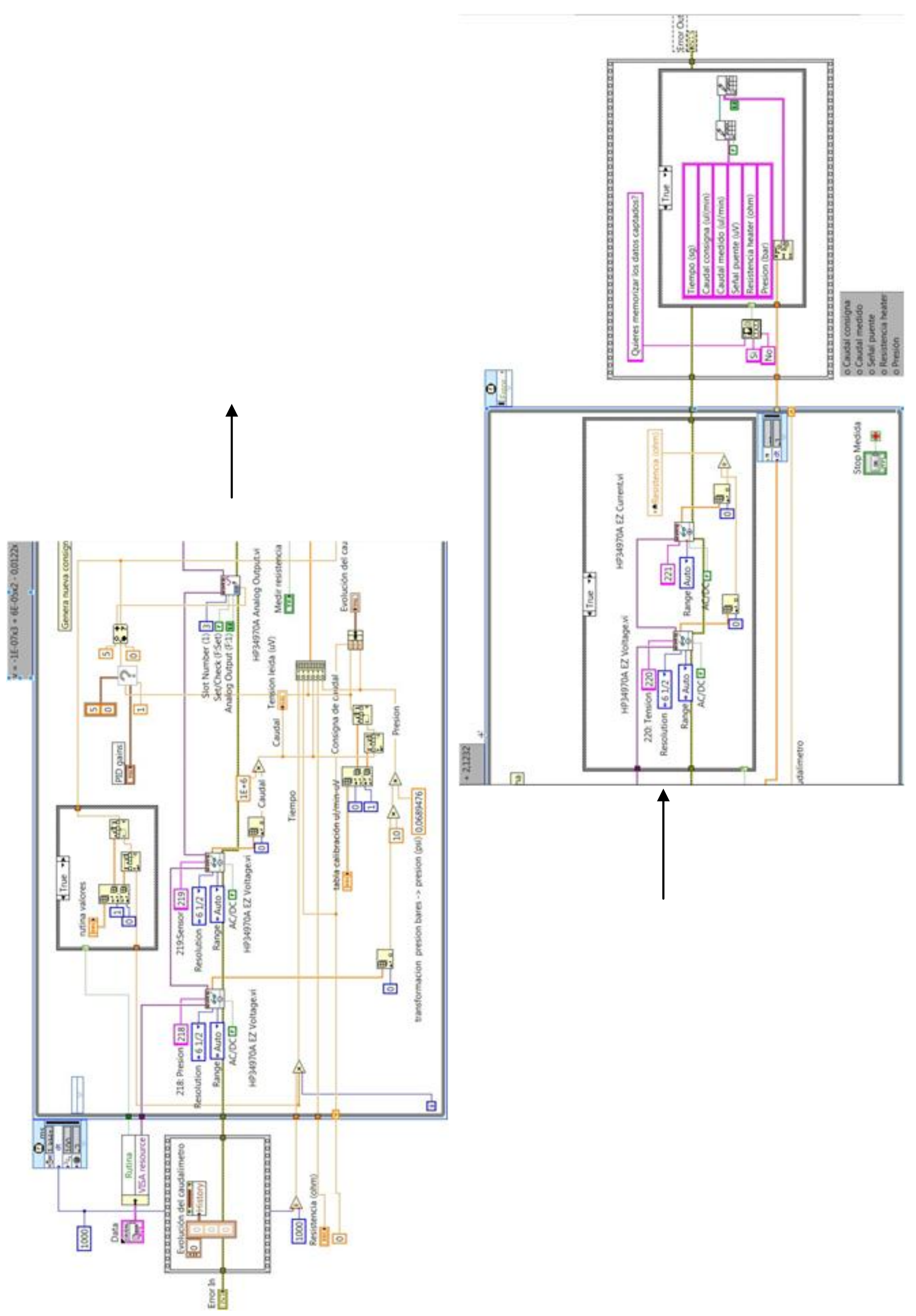

(a)

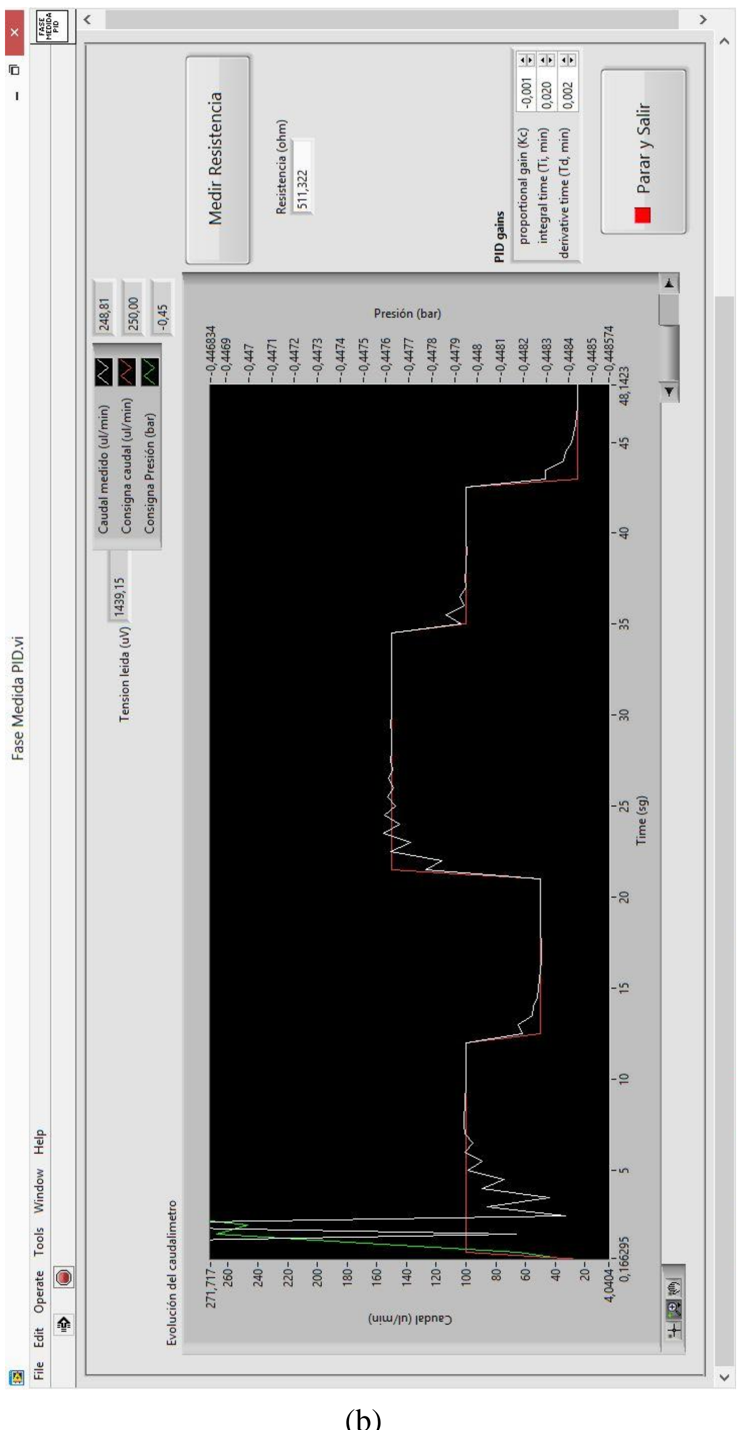

(b)

Figure IV.4. Measure State where the flow controller is working under the mandate of a PID controller in order to adequate the delivered flow rate to that of user's defined by increasing/decreasing the pressure exerted against the membrane depending on the flow rate measured in the flow sensor. The user can adjust the PID gains (Kc, Ti, Td) to improve the delivery, make the response faster, etc.

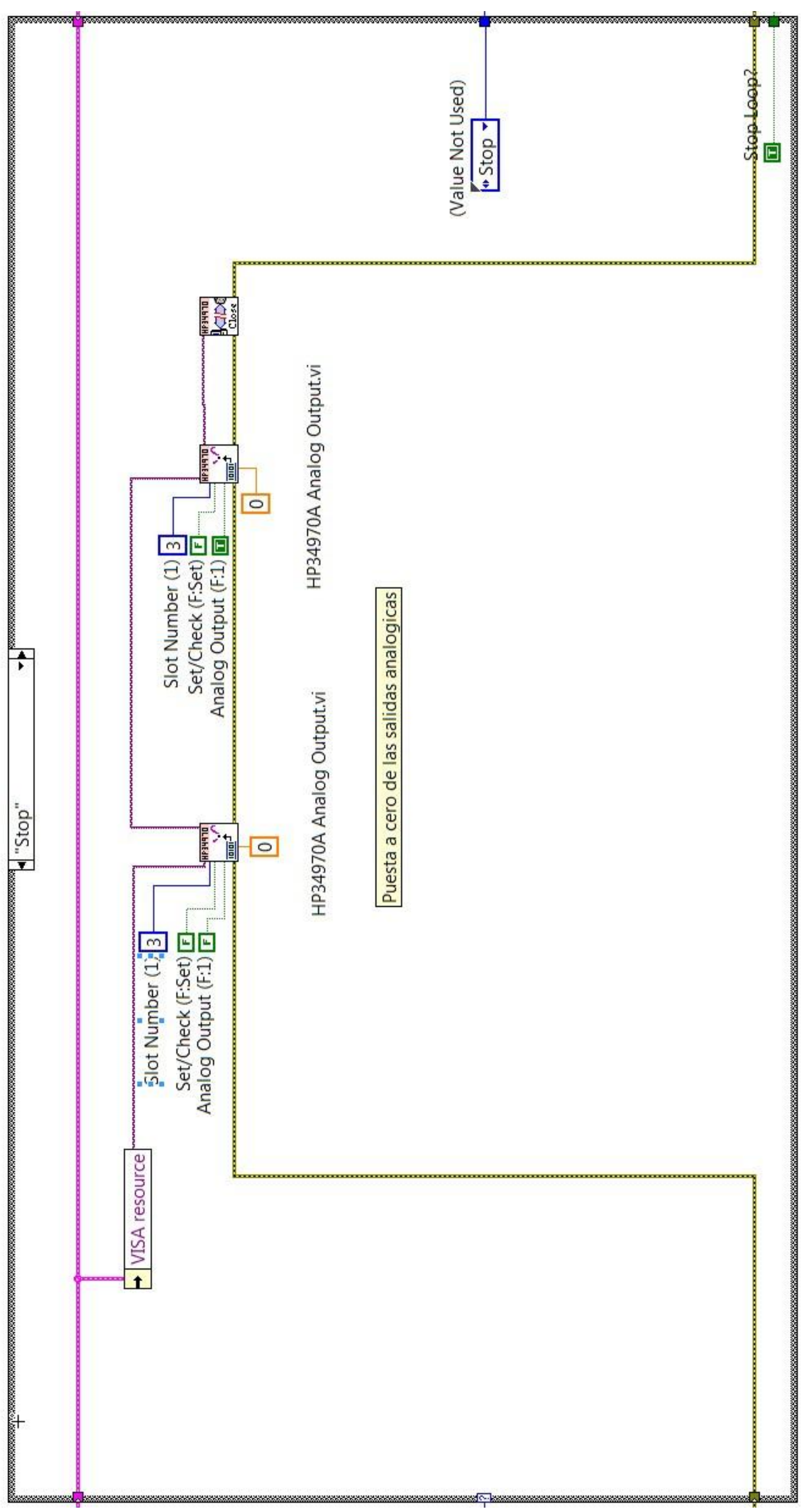

Figure IV.5. Stop State where the user finishes the execution of the flow controller and can save all the data captured during the real time flow rate monitoring.

10. List of PATENTS and PUBLICATIONS

- Publications in international journals:

J. Etxebarria, J. Berganzo, J. Anduaga, J. Besteiro, M. Brivio, H. Gardeniers, A. Ezkerra. *"Low cost highly integrated COP monolithic liquid flow controlling system"*. (Writing)

J. Etxebarria, J. Berganzo, J. Elizalde, G. Llamazares, I. Ochoa, L. J. Fernández, A. Ezkerra. *"Low cost off-chip flow sensor with nanoliter resolution for cell culture applications"*. (Lab on a Chip journal, under review)

J. Etxebarria, J. Berganzo, J. Elizalde, L. J. Fernández, A. Ezkerra. *"Highly integrated COP monolithic membrane microvalves by robust hot embossing"*. Sensors and Actuator B: Chemical 190 (2014) 451-458.

- Patents:

"PCT/ES2013/070746 – Aparato para el control del caudal en un dispositivo microfluídico" (Ikerlan 2013)

- Contribution to conferences:

J. Etxebarria, M. Tijero, R. Diez, F. Benito-Lopez, V. Castro, L. Basabe-Desmonts, A. Valero. *"Desarrollo de un dispositivo POC para la determinación cuantitativa y multiplex de biomoléculas en sangre"*. Anual Workshop CIC microGUNE, 2014, Arrasate-Mondragón, Spain.

J. Saez, J. Etxebarria, M. Antoñana, F. Benito-Lopez. *"In-situ Generated Biocompatible Alginate Actuators for Flow Control in Microfluidics"*. Anual Workshop CIC microGUNE, 2014, Arrasate-Mondragón, Spain.

J. Etxebarria, J. Berganzo, J. Elizalde, A. Ezkerra. *"Novel off-chip flow sensor and integration on polymeric by-pass for detection range widening"*. Anual Workshop CIC microGUNE, 2013, Arrasate-Mondragón, Spain.

J. Etxebarria, J. Berganzo, L. J. Fernández, A. Ezkerra. *"Microvalve and microflow sensor integrated in polymer material"*. 2012Cooperation Session, Advances in Rapid Diagnostic Technologies. CIC microGUNE. Arrasate-Mondragón, Spain.

11. BIBLIOGRAPHY

[1] P.A. Auroux, D. Iossifidis, D.R. Reyes, A. Manz, Micro total analysis systems. 2. Analytical standard operations and applications, Analytical Chemistry, 74(2002) 2637-52.
[2] P.S. Dittrich, K. Tachikawa, A. Manz, Micro total analysis systems. Latest advancements and trends., Analytical Chemistry, 78(2006) 3887-908.
[3] A. Manz, N. Graber, H.M. Widmer, Miniaturized total chemical analysis systems: A novel concept for chemical sensing, Sensors and Actuators B: Chemical, 1(1990) 244-8.
[4] D.R. Reyes, D. Iossifidis, P.A. Auroux, A. Manz, Micro total analysis systems. 1. Introduction, theory, and technology., Analytical Chemistry, 74(2002) 2623-36.
[5] T. Vilkner, D. Janasek, A. Manz, Micro total analysis systems. Recent developments., Analytical Chemistry, 76(2004) 3373-85.
[6] K.W. Oh, C.H. Ahn, A review of microvalves, Journal of Micromechanics and Microengineering, 16(2006) 13-39.
[7] A.K. Au, H. Lai, B.R. Utela, A. Folch, Microvalves and micropumps for BioMEMS, Micromachines, 2(2011) 179-220.
[8] P.K. Yuen, L.J. Kricka, P. Wilding, Semi-disposable microvalves for use with microfabricated devices or microchips, Journal of Micromechanics and Microengineering, 10(2000) 401-9.
[9] Y.C. Wang, M.H. Choi, J. Han, Two-dimensional protein separation with advanced sample and buffer isolation using microfluidic valves, Analytical Chemistry, 76(2004) 4426-31.
[10] M.A. Unger, H.P. Chou, T. Thorsen, A. Scherer, S.R. Quake, Monolithic microfabricated valves and pumps by multilayer soft lithography, Science, 288(2000) 113-6.
[11] M. Kanai, H. Abe, T. Munaka, Y. Fujiyama, D. Uchida, A. Yamayoshi, et al., Micro chamber for cellar analysis integrated with negligible dead volume sample injector, Sensors and Actuators A: Physical, 114(2004) 129-34.
[12] A. Luque, J.M. Quero, C. Hibert, P. Flückiger, A.M. Gana-Calvo, Integrable silicon microfluidic valve with pneumatic actuation, Sensors and Actuators A: Physical, 118(2005) 144-51.
[13] J.Y. Baek, J.Y. Park, J.I. Ju, T.S. Lee, S.H. Lee, A pneumatically controllable flexible and polymeric microfluidic valve fabricated via in situ development, Journal of Micromechanics and Microengineering, 15(2005) 1015-20.
[14] Z. Hua, Y. Xia, O. Srivannavit, J.M. Ruillard, X. Zhou, X. Gao, et al., A versatile microreactor platform featuring a chemical-resistant microvalve array for addressable multiplex syntheses and assays, Journal of Micromechanics and Microengineering, 16(2006) 1433-43.
[15] W. Zhang, S. Lin, C. Wang, J. Hu, C. Li, Z. Zhuang, et al., PMMA/PDMS valves and pumps for disposable microfluidics, Lab on a Chip, 9(2009) 3088-94.
[16] A. Toh, S. Ng, Z. Wang, Fabrication and testing of embedded microvalves within PMMA microfluidic devices, Microsystem Technologies, 15(2009) 1335-42.
[17] P. Gu, K. Liu, H. Chen, T. Nishida, Z.H. Fan, Chemical-assisted bonding of thermoplastics/elastomer for fabricating microfluidic valves, Analytical Chemistry, 83(2010) 446-52.
[18] H. Shanshi, H. Qiaohong, H. Xianqiao, C. Hengwu, Fabrication of micro pneumatic valves with double-layer elastic poly(dimethylsiloxane) membranes in rigid poly(methyl methacrylate) microfluidic chips, Journal of Micromechanics and Microengineering, 22(2012).
[19] X. Yang, C. Grosjean, Y.C. Tai, Design, fabrication, and testing of micromachined silicone rubber membrane valves, Journal of Microelectromechanical Systems, 8(1999).
[20] D. Baechi, R. Buser, J. Dual, A high density microchannel network with integrated valves and photodiodes, Sensors and Actuators A: Physical, 95(2002) 77-83.

[21] C.A. Rich, K.D. Wise, A high-flow thermopneumatic microvalve with improved efficiency and integrated state sensing, Journal of Microelectromechanical Systems, 12(2003) 201-8.
[22] J.H. Kim, K.H. Na, C.J. Kang, D. Jeon, Y.S. Kim, A disposable thermopneumatic-actuated microvalve stacked with PDMS layers and ITO-coated glass, Microelectronic Engineering, 73-74(2004) 864-9.
[23] P. Shao, Z. Rummler, W.K. Schomburg, Polymer micro piezo valve with a small dead volume, Journal of Micromechanics and Microengineering, 14(2004) 305-9.
[24] H.Q. Li, D.C. Roberts, J.L. Steyn, K.T. Turner, O. Yagliolu, N.W. Hagood, et al., Fabrication of a high frequency piezoelectric microvalve, Sensors and Actuators A: Physical, 111(2004) 51-6.
[25] C. Lee, E.H. Yang, S.M. Saeidi, J.M. Khodadadi, Fabrication, characterization and computational modeling of a piezoelectrically actuated microvalve for liquid flow control, Journal of Microelectromechanical Systems, 15(2006) 686-96.
[26] I. Chakraborty, W.C. Tang, D.P. Bame, T.K. Tang, MEMS micro-valve for space applications, Sensors and Actuators A: Physical, 83(2000) 188-93.
[27] M. Shikida, K. Sato, S. Tanaka, Y. Kawamura, Y. Fujisaki, Electrostatically driven gas valve with high conductance, Journal of Microelectromechanical Systems, 3(1994) 76-80.
[28] C. Goll, W. Bacher, B. Bustgens, D. Mass, R. Ruprecht, W.K. Schomburg, An electrostatically actuated polymer microvalve equipped with a movable membrane electrode, Journal of Micromechanics and Microengineering, 7(1997) 224-6.
[29] J.K. Robertson, K.D. Wise, A low pressure micromachined flow modulator, Sensors and Actuators A: Physical, 71(1998) 98-106.
[30] W. Van der Wijngaart, H. Ask, P. Enoksson, G. Stemme, A high-stroke, high-pressure electrostatic actuator for valve applications, Sensors and Actuators A: Physical, 100(2002) 264-71.
[31] M.M. Teymoori, E. Abbaspour-Sani, Design and simulation of a novel electrostatic peristaltic micromachined pump for drug delivery applications, Sensors and Actuators A: Physical, 117(2005) 222-9.
[32] J. Han, J. Yeom, G. Mensing, B. Flachsbart, M.A. Shannon, Characteristics of electrostatic gas micro-pump with integrated polyimide passive valves, Journal of Micromechanics and Microengineering, 22(2012).
[33] D. De Bhailís, C. Murray, M. Duffy, J. Alderman, G. Kelly, S.C.O. Mathúna, Modelling and analysis of a magnetic microactuator, Sensors and Actuators A: Physical, 81(2000) 285-9.
[34] B. Bae, H. Kee, S. Kim, Y. Lee, T. Sim, Y. Kim, et al., In vitro experiment of the pressure regulating valve for a glaucoma implant, Journal of Micromechanics and Microengineering, 13(2003) 613-9.
[35] X. Liu, S. Li, An electromagnetic microvalve for pneumatic control of microfluidic systems, Journal of Laboratory Automation, 1(2014).
[36] H. Suzuki, R. Toneyama, Integrated microfluidic system with electrochemically actuated on-chip pumps and valves, Sensors and Actuators B: Chemical, 96(2003) 38-45.
[37] D.T. Eddington, D.J. Beebe, A valved responsive hydrogel microdispensing device with integrated pressure source, Journal of Microelectromechanical Systems, 13(2004) 586-93.
[38] C. Yamahata, M. Chastellain, V.K. Parashar, A. Petri, H. Hoffmann, M.A.M. Gijs, Plastic micropump with ferrofluidic actuation, Journal of Microelectromechanical Systems, 14(2005) 96-102.
[39] L. Bousse, E. Dijkstra, O. Guenat, High-density arrays of valves and interconnects for liquid switching, Sensors and Actuators Workshop, (1996) 272-5.
[40] T. Ohori, S. Shoji, K. Miura, A. Yotsumoto, Partly disposable three-way microvalve for a medical micro total analysis system (µTAS), Sensors and Actuators A: Physical, 64(1998) 57-62.

[41] C. Vieider, O. Ohman, H. Elderstig, A penumatically actuated micro valve with a silicone rubber membrane for integration with fluid-handling systems, IEEE International Conference on Solid-State Sensors Actuators (Stockholm, Sweden), 2(1995) 284-6.
[42] X. Yang, C. Grosjean, Y.C. Tai, H. C.M., A MEMS thermopneumatic silicone rubber membrane valve, Sensors and Actuators A: Physical, 64(1998) 101-8.
[43] K. Hosokawa, R. Maeda, A pneumatically-actuated three-way microvalve fabricated with polydimethylsiloxane using the membrane transfer technique, Journal of Micromechanics and Microengineering, 10(2000) 415-20.
[44] X.Q. Ren, M. Bachman, C. Sims, G.P. Li, N. Allbritton, Electroosmotic properties of microfluidic channels composed of poly-(dimethylsiloxane), Journal of Chromatography B, 762(2001) 117-25.
[45] Y. Xia, G.M. Whitesides, Soft lithography, Annual Review of Material Science, 28(1998) 153-84.
[46] R.C. Anderson, X. Su, G.J. Bogdan, J. Fenton, A miniature integrated device for automated multistep genetic assys, Nucleic Acids Research, 28(2000).
[47] S. Bohm, W. Olthuis, P. Bergveld, A plastic micropump constructed with conventional techniques and materials, Sensors and Actuators A: Physical, 77(1999) 223-8.
[48] W.K. Schomburg, R. Ahrens, W. Bacher, J. Martin, V. Saile, AMANDA-surface micromachining, molding, and diaphragm transfer, Sensors and Actuators A: Physical, 76(1999) 343-8.
[49] S. Sjolander, C. Urbaniczky, Integrated fluid handling system for biomolecular interaction analysis, Analytical Chemistry, 63(1991) 2338-45.
[50] D.K. Armani, C. Liu, Microfabrication technology for polycaprolactone, a biodegradable polymer, Journal of Micromechanics and Microengineering, 10(2000) 80.
[51] Z.H. Fan, A. Ricco, Integrated plastic microfluidic devices for bacterial detection, Integrated Biochips for DNA Analysis, Springer New York(2007) 78-89.
[52] Z.H. Fan, Microfluidic devices with photodefinable pseudo-valves for protein separation, Micro and Nano Technologies in Bioanalysis, Humana Press(2009) 43-52.
[53] R.F. Boucher, Minimum flow optimization of fluidic flowmeters, Measurement and Science Technology, 6(1995) 872-9.
[54] Y. Ozaki, T. Ohyama, T. Yasuda, I. Shimoyama, An air flow sensor modeled on wind receptor hairs of insects, Proceedings MEMS 2000 (Miyazak), (2000) 631-7.
[55] J. Li, J. Chen, C. Liu, Micromachined biomimetic sensor using modular artificial hair cells, Nano Space 2000 (Houston), (2000).
[56] J. Zou, J. Chen, C. Liu, Plastic deformation magnetic assembly (PDMS) of out-of-plane microstructures: technology and application, Journal of Microelectromechanical Systems, 10(2001) 302-9.
[57] Z. Fan, J. Chen, J. Zou, D. Bullen, C. Liu, F. Delcomyn, Design and fabrication of artificial lateral line flow sensors, Journal of Micromechanics and Microengineering, 12(2002) 655-61.
[58] J. Chen, Z. Fan, J. Zou, J. Engel, C. Liu, Two dimensional micromachined flow sensor array for fluid mechanics studies, Journal of Aerospace Engineering, 16(2003) 85-97.
[59] M. Dijkstra, J.J. van Baar, R.J. Wiegerink, T.S.J. Lammerink, M. de Boer, J.J.M. Krijnen, Artificial sensory hairs based on the flow sensitive receptor hairs of crickets, Journal of Micromechanics and Microengineering, 15(2005) 132-8.
[60] C.M. Bruinink, R.K. Jaganatharaja, M.J. de Boer, E. Berenschot, M.L. Kolster, T.S.J. Lammerink, et al., Advancements in technology and design of biomimetic flow-sensor arrays, IEEE 22nd International Conference on Micro Electro Mechanical Systems, (2009).
[61] R.-H. Ma, C.-Y. Lee, Y.-H. Wang, H.-J. Chen, Microcantilever-based weather station for temperature, humidity and flow rate measurements, Microsystem Technologies, 14(2007) 971-7.

[62] R. Attia, D.C. Pregibon, P.S. Doyle, J.-L. Viovy, D. Bartolo, Soft microflow sensors, Lab on a Chip, 9(2009) 1213-8.
[63] M. Richter, P. Wackerle, P. Woias, B. Hillerich, A novel flow sensor with high time resolution based on differential pressure principle, IEEE International Conference on Micro Electro Mechanical Systems, (1999) 118-23.
[64] R.E. Oosterbroek, T.S.J. Lammerink, J.W. Berenschot, G.J.M. Krijnen, M.C. Elwenspoek, A. van de Berg, A micromachined pressure/flow-sensor, Sensors and Actuators A: Physical, 77(1999) 167-77.
[65] Y. Liu, L. Chen, L. Sun, Design and fabrication of a MEMS flow sensor and its application in precise liquid dispensing, Sensors, 9(2009) 4138-50.
[66] P. Enoksson, G. Stemme, E. Stemme, A silicon resonant sensor structure for coriolis mass-flow measurements, Journal of Microelectromechanical Systems, 6(1997) 119-25.
[67] J. Haneveld, T.S.J. Lammerink, M. Dijkstra, H. Droogendijk, M.J. de Boer, R.J. Wiegerink, Highly senstitive micro coriolis mass flow sensor, IEEE 21st International Conference on Electro Mechanical Systems, (2008) 920-3.
[68] J. Haneveld, T.S.J. Lammerink, M.J. de Boer, R.J. Wiegerink, Micro Coriolis mass flow sensor with integrated capacitive readout, IEEE 22nd International Conference on Micro Electro Mechanical Systems, (2009) 463-6.
[69] N.T. Nguyen, Micromachined flow sensors - A review, Flow measurements and instrumentation, 8(1997) 7-16.
[70] J.T.W. Kuo, L. Yu, E. Meng, Micromachined thernal flow sensors - A review, Micromachines, 3(2012) 550-73.
[71] H.H. Bruun, Hot-wire anemometry, Oxford University Press, UK(1995).
[72] G. Soundararajan, M. Rouhanizadeh, H.Y. Yu, L. De Maio, E.S. Kim, T.K. Hsiai, MEMS shear stress sensors for microcirculation, Sensors and Actuators A: Physical, 118(2005) 25-32.
[73] G. Kaltsas, A. Petropoulos, K. Tsougeni, D.N. Pagonis, T. Speliotis, E. Gogolides, et al., A novel microfabrication technology on organic substrates - Application to a thermal flow sensor, Journal of Physics: Conference Series, 92(2007).
[74] B.C. Kaanta, H. Chen, X. Zhang, Novel device for calibration-free flow rate measurements in micro gas chromatographic systems Journal of Micromechanics and Microengineering, 20(2010).
[75] S.C.C. Bailey, G.J. Kunkel, M. Hultmark, M. Vallikivi, J.P. Hill, K.A. Meyer, et al., Turbulence measurements using a nanoscale thermal anemometry probe, Journal of Fluid Mechanics, 663(2010) 160-79.
[76] Y. Ito, T. Higuchi, K. Takahashi, Submicroscale flow sensor employing suspended hot film with carbon nanotube fins, Journal of Thermal Science and Technology, 5(2010) 51-60.
[77] C.Y. Li, P.M. Wu, J. Han, C.H. Ahn, A flexible polymer tube lab-chip integrated with microsensors for smart microcatheter, Biomedical Microdevices, 10(2008) 671-9.
[78] H. Yu, L. Ai, M. Rouhanizadeh, D. Patel, E.S. Kim, T.K. Hsiai, Flexible polymer sensors for in vivo intravascular shear stress analysis, Journal of Microelectromechanical Systems, 17(2008) 1178-86.
[79] M. Dominguez, V. Jiménez, J. Ricart, L. Kowalski, J. Torres, S. Navarro, et al., A hot film anemometer for the Martian atmosphere, Planetary and Space Science, 56(2008) 1169-79.
[80] P. Liu, R. Zhu, R. Que, A flexible flow sensor system and its characteristics for fluid mechanics measurements, Sensors Journal, 9(2009) 9533-43.
[81] U. Budera, R. Petzb, M. Kittelb, M. Nitscheb, E. Obermeier, AeroMEMS polyimide based wall double hot-wire sensors for flow separation detection, Sensors and Actuators A: Physical, 142(2008) 130-7.
[82] R.J. Adamec, D.V. Thiel, Self heated thermo-resistive element hot wire anemometer, Sensors Journal, 10(2010) 847-8.

[83] R. Ahrens, M. Festa, Polymer-based micro flow sensor for dynamical flow measurements in hydraulic systems, Journal of Micromechanics and Microengineering, 20(2010).
[84] T.S.J. Lammerink, N.R. Tas, M. Elwenspoek, J.H.J. Fluitman, Micro-liquid flow sensor, Sensors and Actuators A: Physical, 37-38(1993) 45-50.
[85] W.C. Shin, R.S. Besser, A micromachined thin-film gas flow sensor for microchemical reactors, Journal of Micromechanics and Microengineering, 16(2006) 731.
[86] M. Dijkstra, M.J. de Boer, J.W. Berenschot, T.S.J. Lammerink, R.J. Wiegerink, M. Elwenspoek, Miniaturized thermal flow sensor with planar-integrated sensor structures on semicircular surface channels, Sensors and Actuators A: Physical, 143(2008) 1-6.
[87] Y. Tanaka, T. Akutsu, M. Terao, K. Isozaki, Micro flow sensor for microreactor, Yokogawa Technical Report English Eddition No 47, (2009).
[88] K. Palmer, H. Kratz, H. Nguyen, G. Thornell, A highly integratable silicon thermal gas flow sensor, Journal of Micromechanics and Microengineering, 22(2012) 065015.
[89] R. Vilares, C. Hunter, I. Ugarte, I. Aranburu, J. Berganzo, J. Elizalde, et al., Fabrication and testing of a SU-8 thermal flow sensor, Sensors and Actuators B: Chemical, 147(2010) 411-7.
[90] R.J. Rodrigues, R. Furlan, Design of microsensor for gases and liquids flow measurements, Microelectronics, 34(2003) 709-11.
[91] H. Berthet, J. Jundt, J. Durivault, B. Mercier, D. Angelescu, Time-of-flight thermal flowrate sensor for lab-on-a-chip applications, Lab on a Chip, 11(2010) 215-23.
[92] Y. Fournier, T. Maeder, G. Boutinard-Rouelle, A. Barras, N. Craquelin, P. Ryser, Integrated LTCC pressure/flow/temperature multisensor for compressed air diagnostics, Sensors (Basel), 10(2010) 11156-73.
[93] F. Hedrich, K. Kliche, M. Storz, S. Billat, M. Ashauer, R. Zengerle, Thermal flow sensor for MEMS spirometric devices, Sensors and Actuators A: Physical, 162(2010) 373-8.
[94] T.S.J. Lammerink, M. Elwenspoek, J.H.J. Fluitman, Integrated micro-liquid dosing system, Proceedings of IEEE-MEMS Workshop, (1993) 254-9.
[95] J. Xie, J. Shih, Y.C. Tai, Integrated surface-micromachined mass flow controller, IEEE Sixteenth Annual International Conference on Micro Electro Mechanical Systems, (2003).
[96] W. Xu, L.L. Wu, Y. Zhang, H. Xue, G.P. Li, M. Bachman, A vapor based microfluidic flow regulator, Sensors and Actuators B: Chemical, 142(2010).
[97] M. Kohl, Y. Liu, D. Dittmann, A polymer-based microfluidic controller, IEEE, (2004) 288-91.
[98] P. Gravesen, J. Branebjerg, O.S. Jensen, Microfluidics-a review, Journal of Micromechanics and Microengineering, 3(1993) 168-82.
[99] H. Becker, L.E. Locascio, Polymer microfluidic devices, Talanta, 56(2002) 267-87.
[100] J.-W. Choi, et al, Development and characterization of microfluidic devices and systems for magnetic bead-based biochemical detection, Biomed Microdevices, 3(2001) 191-200.
[101] B. Bilenberg, T. Nielsen, B. Clausen, A. Kristensen, PMMA to SU-8 bonding for polymer based lab-on-a-chip systems with integrated optics., Journal of Micromechanics and Microengineering, 14(2004) 814-8.
[102] K.B. Mogensen, J. El-Ali, A. Wolff, J.P. Kutter, Integration of polymer waveguides for optical detection in microfabricated chemical analysis systems, Applied Optics, 42(2003) 4072-9.
[103] S.K. Sia, G.M. Whitesides, Microfluidic devices fabricated in poly(dimethylsiloxane) for biological studies, Electrophoresis, 24(2003) 3563-76.
[104] J.C. Mac Donald, D.C. Duffy, J.R. Anderson, D.T. Chiu, H.K. Wu, O.J.A. Schueller, et al., Fabrication of microfluidic systems in poly(dimethylsiloxane), Electrophoresis, 21(2000) 27-40.
[105] P.S. Nunes, P.D. Ohlsson, O. Ordeig, J.P. Kutter, Cyclic olefin polymers: emerging materials for lab-on-a-chip applications, Microfluidics and Nanofluidics, 9(2010) 145-61.
[106] C.-W. Tsao, D.L. Devoe, Bonding of thermoplastic polymer microfluidics, Microfluidics and Nanofluidics, 6(2009) 1-16.

[107] M. Hansen, D. Nilsson, D.M. Johansen, S. Balslev, A. Kristensen, A nanoimprinted polymer lab-on-a-chip with integrated optics, Conference: Advancements in Polymer Optics Design, Fabrication, and Materials, 5872(2005) 76-82.
[108] A. Bhattacharyya, C. Klapperich, Thermoplastic microfluidic device for on-chip purification of nucleic acids for disposable diagnostics, Analytical Chemistry, 78(2006) 788-92.
[109] S.H. Choi, D.S. Kim, T.H. Kwon, Microinjection molded disposable microfluidic lab-on-a-chip for efficient detection of agglutination, Microsystem Technologies, 15(2009) 309-16.
[110] Topas Advances Polymers, http://wwwtopascom.
[111] Zeon Chemicals, http://wwwzeonexcom.
[112] Japan Synthetic, http://wwwjsrcojp/jsr/.
[113] Mitsui Chemicals America, http://wwwmitsuichemicalscom/.
[114] W.J. Huang, F.C. Chang, P.P.J. Chu, Functionalization and chemical modification of cyclo olefin copolymers (COC), Polymer, 41(2000) 6095-101.
[115] S.J. Hwang, M.C. Tseng, J.R. Shu, H.H. Yu, Surface modification of cyclic olefin copolymer substrate by oxygen plasma treatment, Surface and Coatings Technology, 202(2008) 3669.
[116] H. Steffen, K. Schröder, B. Busse, A. Ohl, K. Weltmann, Functionalization of COC surfaces by Microwave Plasmas, Plasma Process Polymer, 4(2007) 392-6.
[117] X.Q. Ren, M. Bachman, C. Sims, G.P. Li, N. Allbritton, Electroosmotic properties of microfluidic channels composed of poly-(dimethylsiloxane), J Chromatogr B 762(2001) 117-25.
[118] S. Hu, X. Ren, M. Bachman, C.E. Sims, G.P. Li, N. Allbritton, Surface modification of poly(dimethylsiloxane) microfluidic devices by ultraviolet polymer grafting, Analytical Chemistry, 74(2002) 4117-23.
[119] J. Steigert, S. Haeberle, T. Brenner, C. Muller, C.P. Steinert, P. Koltay, et al., Rapid prototyping of microfluidic chips in COC, Journal of Micromechanics and Microengineering, 17(2007) 333-41.
[120] B. Bilenberg, M. Hansen, D. Johansen, V. Ozkapici, C. Jeppesen, P. Szabo, et al., Topas-based lab-on-a-chip microsystems fabricated by thermal nanoimprint lithography, Journal of Vacuum Science and Technology, 23(2005) 2944.
[121] O. Rotting, W. Ropke, H. Becker, C. Gartner, Polymer microfabrication technologies, Microsystem Technologies, 8(2002) 32-6.
[122] P. Mela, A. Van den Berg, Y. Fintschenko, E.B. Cummings, B.A. Simmons, B.J. Kirby, The zeta potential of cyclo-olefin polymer microchannels and its effects on insulative (electrodeless) dielectrophoresis particle trapping devices, Electrophoresis, 26(2005) 1792-9.
[123] C.W. Tsao, J. Liu, D.L. Devoe, Droplet formation from hydrodynamically coupled capillaries for parallel microfluidic contact spotting, Journal of Micromechanics and Microengineering, 18(2008).
[124] Y.N. Yang, C. Li, J. Kameoka, K.H. Lee, H.G. Craighead, A polymeric microchip with integrated tips and in situ polymerized monolith for electrospray mass spectrometry, Lab on a Chip, 5(2005) 869-76.
[125] C.K. Fredrickson, Z. Xia, C. Das, R. Ferguson, F.T. Tavares, Z.H. Fan, Effects of fabrication process parameters on the properties of cyclic olefin copolymer microfluidic devices, Journal of Microelectromechanical Systems, 15(2006) 1060-8.
[126] Y.-J. Juang, L.J. Lee, K.W. Koelling, Hot embossing in microfabrication. Part I: Experimental, Polymer Engineering & Science, 42(2002) 539-50.
[127] A. Gerlach, G. Knebel, A.E. Guber, M. Heckele, D. Herrmann, A. Muslija, et al., High-density plastic microfluidic platforms for capillary electrophoresis separation and high-throughput screening, Sensor Mater, 14(2002) 119-28.
[128] P. Mosaddegh, D.C. Angstadt, Micron and sub-micron feature replication of amorphous polymers at elevated mold temperature without externally applied pressure, Journal of Micromechanics and Microengineering, 18(2008).

[129] D.A. Mair, M. Rolandi, M. Snauko, R. Noroski, F. Svec, J.M.J. Frechet, Room-temperature bonding for plastic high-pressure microfluidic chips, Analytical Chemistry, 79(2007) 5097-102.
[130] D. Sabbert, J. Landsiedel, H.D. Bauer, W. Ehrfeld, ArF-excimer laser ablation experiments on cycloolefincopolymer (COC), Applied Surface Science, 150(1999) 185-9.
[131] F. Bundgaard, G. Perozziello, O. Geschke, Rapid prototyping tools and methods for all-Topas (R) cyclic lefin copolymer fluidic microsystems, Institution of Mechanical Engineers Proceedings Part C: Journal of Mechanical Engineering Science, 220(2006) 1625-32.
[132] T.J. Johnson, E.A. Waddell, G.W. Kramer, L.E. Locascio, Chemical mapping of hot-embossed and UV-laser-ablated microchannels in poly(methyl methacrylate) using carboxylate specific fluorescent probes, Applied Surface Science, 181(2001) 149-59.
[133] H. Becker, C. Gärtner, Polymer microfabrication methods for microfluidic analytical applications, Electrophoresis, 21(2000) 12-26.
[134] J. Do, C.H. Ahn, A polymer lab-on-a-chip for magnetic inmunoassay with on-chip sampling and detection capabilities, Lab on a Chip, 8(2008) 542-9.
[135] J. Kameoka, H.G. Craighead, H.W. Zhang, J. Henion, A polymeric microfluidic chip for CE/MS determination of small molecules, Analytical Chemistry, 73(2001) 1935-41.
[136] O. Gustafsson, K.B. Mogensen, J.P. Kutter, Underivated cyclic olefin copolymer as substrate material and stationary phase for capillary and microchip electrochromatography, Electrophoresis, 29(2008) 3145-52.
[137] Y.N. Yang, C. Li, K.H. Lee, H.G. Craighead, Coupling on-chip solid-phase extraction to electrospray mass spectrometry through an integrated electrospray tip, Electrophoresis, 26(2005) 3622-30.
[138] P. Kettner, R.L. Pelzer, T. Glinsner, S. Farrens, D.G. Lee, New results on plasma activated bonding of imprinted polymer features for bio MEMS applications, Journal of Physics, 34(2006).
[139] C.W. Tsao, L. Hromada, J. Liu, P. Kumar, D.L. De Voe, Low temperature bonding of PMMA and COC microfluidic substrates using UV/ozone surface treatment, Lab on a Chip, 7(2007) 499-505.
[140] G.F. Chen, F. Svec, D.R. Knapp, Light-actuated high pressure resisting microvalve for lab-on-a-chip flow control based on thermoresponsive nanostructured polymer, Lab on a Chip, 8(2008) 1198-204.
[141] K. Faure, M. Albert, V. Dugas, G. Cretier, R. Ferrigno, P. Morin, et al., Development of an acrylate monolith in a cyclo-olefin copolymer microfluidic device for chip electrochromatography separation, Electrophoresis, 29(2008) 4948-55.
[142] J. Liu, K.W. Ro, R. Nayak, D.R. Knapp, Monolithic column plastic microfluidic device for peptide analysis using electrospray from a channel opening on the edge of the device, International Journal of Mass Spectrometry, 259(2007) 65-72.
[143] K.W. Ro, H. Liu, D.R. Knapp, Plastic microchip liquid chromatography-matrix-assisted laser desorption/ionization mass spectrometry using monolithic columns, Journal of Chromatography A, 1111(2006) 40-7.
[144] Thomas I. Wallow, Alfredo M. Morales, Blake A. Simmons, Marion C. Hunter, Karen Lee Krafcik, Linda A. Domeier, et al., Low-distortion, high-strength bonding of thermoplastic microfluidic devices employing case-II difusion-mediated permeant activation, Lab on a Chip, 7(2007) 1825-31.
[145] M. Koch, A. Evans, A. Brunnschweiler, Microfluidic Technology and Applications, Research Studies Press LTD.2000.
[146] Y. Hirai, T. Konishi, T. Yoshikawa, S. Yoshida, Simulation and experimental study of polymer deformation in nanoimprint lithography, Journal of Vacuum Science and Technology B: Microelectronics and Nanometer Structures, 22(2004) 3288-93.

[147] S. Miserere, G. Mottet, V. Taniga, S. Descroix, J.-L. Viovy, L. Malaquin, Fabrication of thermoplastics chips through lamination based techniques, Lab on a Chip, 12(2012) 1849-56.
[148] H. Becker, C. Gärtner, Polymer microfabrication technologies for microfluidic systems, Analytical and Bioanalytical Chemistry, 390(2008) 89-111.
[149] A.E. Guber, M. Heckele, D. Herrmann, A. Muslija, V. Saile, L. Eichhorn, et al., Microfluidic lab-on-a-chip systems based on polymers— fabrication and application, Chemical Engineering Journal, 101(2004) 447-53.
[150] M. Heckele, W.K. Schomburg, Review on micro molding of thermoplastic polymers Journal of Micromechanics and Microengineering, 14(2003) R1-R14.
[151] H.C. Scheer, H. Schulz, A contribution to the flow behaviour of thin polymers films during hot embossing lithography, Microelectronic Engineering, 56(2001) 311-32.
[152] Z. Herrasti, I. Etxabe, J.M. Mitxelena, M.P. Martínez, F. Martínez, Development and integration of an electrochemical system in a LOC device for DNA detection, Procedia Engineering, 47(2012) 25-8.
[153] Z. Herrasti, I. Etxabe, J.M. Mitxelena, I. Gabilondo, M.P. Martínez, F. Martínez, Development and integration of an electrochemical system in a LOC device for DNA detection, Sensors and Actuators B: Chemical, 189(2013) 66-70.
[154] M. Dirckx, H. Taylor, D. Hardt, High temperature de-molding for cycle time reduction in Hot Embossing, in Proc Society of Plastics Engineers Annual Technical Conference, (2007) 2972–6.
[155] Y.H. Guo, G. Liu, X.L. Zhu, Y.C. Tian, Analysis of the demolding forces during hot embossing, Microsystem Technologies-Micro-and Nanosystems-Information Storage and Processing Systems, 13(2007) 411-5.
[156] Y.J. Juang, L. Lee James, K.W. Koelling, Hot embossing in microfabrication. Part II: Rheological characterization and process analysis, Polymer Engineering and Science, 42(2002) 551-66.
[157] G. Yuhua, L. Gang, X. Yin, T. Yangchao, Study of the demolding process—implications for thermal stress, adhesion and friction control, Journal of Micromechanics and Microengineering, 17(2007) 9.
[158] J. Greener, W. Li, J. Ren, D. Voicu, V. Pakharenko, T. Tang, et al., Rapid, cost-efficient fabrication of microfluidic reactors in thermoplastic polymers by combining photolithography and hot embossing, Lab on a Chip, 10(2010) 522-4.
[159] C. Con, J. Zhang, Z. Jaheb, T.Y. Tsui, M. Yavuz, B. Cui, Thermal nanoimprint lithography using fluoropolymer mold, Microelectronic Engineering, 98(2012).
[160] J. Narasimhan, I. Papautsky, Polymer embossing tools for rapid prototyping of plastic microfluidic devices, Journal of Micromechanics and Microengineering, 14(2003) 96-103.
[161] M. Agirregabiria, F.J. Blanco, J. Berganzo, M.T. Arroyo, A. Fullaondo, K. Mayora, et al., Fabrication of SU-8 multilayer microstructures based on successive CMOS compatible adhesive bonding and releasing steps, Lab on a Chip, 5(2005) 545-52
[162] M.B. Esch, S. Kapur, G. Irizarry, V. Genova, Influence of master fabrication techniques on the characteristics of embossed microfluidic channels, Lab on a Chip, 3(2003) 121-7.
[163] X. Illa, O. Ordeig, D. Snakenborg, A. Romano-Rodriguez, R.G. Compton, J.P. Kutter, A cyclo olefin polymer microfluidic chip with integrated gold microelectrodes for aqueous and non-aqueous electrochemistry, Lab on a Chip, 10(2010) 1254-61.
[164] M. Worgull, J. Hétu, K. Kabanemi, M. Heckele, Modeling and optimization of the hot embossing process for micro- and nanocomponent fabrication, Microsystem Technologies, 12(2006) 947-52.
[165] A. Cattoni, J. Chen, D. Decanini, J. Shi, A.-M. Haghiri-Gosnet, Soft UV nanoimprint lithography: a versatile tool for nanostructuraion at the 20nm scale, Recent Advances in Nanofabrication Techniques and Applications, Prof Bo Cui (Ed), (2011).

[166] M. Dirckx, Demolding of hot embossed polymer microstructures, Massachusetts Institute of Technology Department of Mechanical Engineering, (2010).
[167] M. Worgull, M. Heckele, New aspects of simulation in hot-embossing, Design, Test, Integration and Packaging of MEMS/MOEMS 2003 Symposium on2003, pp. 272-4.
[168] L. Ressier, C. Martin, J.P. Peyrade, Atomic force microscopy study of micrometric pattern replica by hot embossing lithography, Microelectronic Engineering, 71(2004) 272-6.
[169] H. Takagi, M. Takahashi, R. Maeda, Y. Onishi, Y. Iriye, T. Iwasaki, et al., Experimental and numerical analyses on recovery of polymer deformation after demolding in the hot embossing process, Journal of Vacuum Science and Technology B: Microelectronics and Nanometer Structures, 26(2008) 2399-403.
[170] R.K. Jena, X. Chen, C.Y. Yue, Y.C. Lam, Rheological (visco-elastic behavoiur) analysis of cyclic olefin copolymers with application to hot embossing for microfabrication, Journal of Micromechanics and Microengineering, 21(2011).
[171] L.J. Fernández, I. Aranburu, M. Agirregabiria, J. Elizalde, J. Berganzo, J.M. Ruano-Lopez, et al., Method for producing microfluidic devices, in: Ikerlan (Ed.), B81C 3/00, F16K 99/00, F15C 5/00 ed.2013, pp. 1-12.
[172] H. Takao, M. Ishida, Microfluidic integrated circuits for signal processing using analogous relationship between pneumatic microvalve and MOSFET, Journal of Microelectromechanical Systems, 12(2003).
[173] S. Bohm, G.J. Burger, M.T. Korthorst, F. Roseboom, A micromachined silicon valve driven by a miniature bi-stable electro-magnetic actuator, Sensors Actuators A, 80(2000) 77-83.
[174] C. Fu, Z. Rummle, W. Chomburg, Magnetically driven micro ball valves fabricated by multilayer adhesive film bonding, Journal of Micromechanics and Microengineering, 13(2003) 96-102.
[175] K.W. Oh, R. Rong, C.H. Anh, In-line micro ball valve through polymer tubing, microTAS, (2001) 407-8.
[176] J. Sutanto, P.J. Hesketh, Y. Berthelot, Design, microfabrication and testing of a CMOS compatible bistable electromagnetic microvalve with latching/unlatching mechanism on a single wafer, Journal of Micromechanics and Microengineering, 16(2006) 266-75.
[177] C.R. Neagu, J.G.E. Gardeniers, M. Elwenspoek, J.J. Kelly, An electrochemical microactuator: principle and first results, Journal of Microelectromechanical Systems, 5(1996) 2-9.
[178] K. Takahashi, K. Yoshino, S. Hatano, K. Nagayama, T. Asano, Novel applications of thermally controlled microbubble driving system, IEEE, (2001) 286-9.
[179] A. Richter, D. Kuckling, S. Howitz, T. Gehring, K.-F. Arndt, Electronically controllable microvalves based on smart hydrogels: magnitudes and potential applications, Journal of Microelectromechanical Systems, 12(2003) 748-53.
[180] L.-M. Low, S. Seetharaman, K.-Q. He, M.J. Madou, Microactuators toward microvalves for responsive controlled drug delivery, Sensors and Actuators B, 67(2000) 149-60.
[181] J. Lee, H.S. Moon, J. Fowler, T. Schoellhammer, C.-J. Kim, Electrowetting and electrowetting-on-dielectric for microscale liquid handling, Sensors Actuators A, 95(2002) 259-68.
[182] P. Paik, V.K. Pamula, M.G. Pollack, R.B. Fair, Electrowetting-based droplet mixers for microfluidic systems, Lab on a Chip, 3(2003) 28-33.
[183] P.R.C. Gascoyne, J.V. Vykoukal, J.A. Schwartz, T.J. Anderson, D.M. Vykoukal, K.W. Current, et al., Dielectrophoresis-based programmable fluidic processors, Lab on a Chip, 4(2004) 299-309.
[184] V. Srinivasan, V.K. Pamula, R.B. Fair, An integrated digital microfluidic lab-on-a-chip for clinical diagnostics on human physiological fluids, Lab on a Chip, 4(2004) 310-5.

[185] S.P. Timoshenko, S. Woinowsky-Krieger, Theory of Plates and Shells, 2nd ed.: MacGraw-Hill; 1959.
[186] J. Berthier, P. Silberzan, Microfluidics for Biotechnology: Artech House Inc; 2006.
[187] M. Kohl, D. Dittmann, E. Quandt, B. Winzek, Thin film shape memory microvalves with adjustable operation temperature, Sensors and Actuators A: Physical, 83(2000) 214-9.
[188] J. Peirs, D. Reynaert, H. van Brussel, Design of miniature parallel manipulators for integration in a self-propelling endoscope, Sensors Actuators A, 85(2000) 409-17.
[189] C.M. Ho, X. Yang, C. Grosjean, Y.C. Tai, A MEMS thermopneumatic silicone rubber membrane valve, Sensors Actuators A, 64(1998) 101-8.
[190] L. Szekely, J. Reichert, R. Freitag, Non-invasive nano-flow sensor for application in microfluidic systems, Sensors and Actuators A: Physical, 113(2004) 48-53.
[191] T.K. Hsiai, S.K. Cho, P.K. Wong, M.H. Ing, A. Salazar, S. Hama, et al., Micro sensors: linking real-time oscillatory shear stress with vascular inflammatory responses, Annals of Biomedical Engineering, 32(2004) 189-201.
[192] J.T.W. Kuo, L.-Y. Chang, P.-Y. Li, T. Hoang, E. Meng, A microfluidic platform with integrated flow sensing for local chemical simulation of cells and tissue, Sensors and Actuators B: Chemical, 152(2011) 267-76.
[193] C. Liu, J.-B. Huang, Z. Zhu, F. Jiang, S. Tung, Y.-C. Tai, et al., A micromachined flow shear-stress sensor based on thermal transfer principles, Journal of Microelectromechanical Systems, 8(1999) 90-9.
[194] R. Ahrens, K. Schlote-Holubek, A micro flow sensor from a polymer for gases and liquids, Journal of Micromechanics and Microengineering, 19(2009).
[195] C. Li, P.M. Wu, J.A. Hartings, Z. Wu, C.H. Ahn, R.K. Narayan, Cerebral blood flow sensor with in situ temperature and thermal conductivity compensation, IEEE 25th International Conference on Micro Electro Mechanical Systems (MEMS), (2012) 1021-4.
[196] S.-T. Hung, S.-C. Wong, W. Fang, The development and application of microthermal sensors with a mesh-membrane supporting structure, Sensors and Actuators A: Physical, 84(2000) 70-5.
[197] Z. Tan, M. Shikida, M. Hirota, Y. Xing, K. Sato, T. Iwasaki, et al., Characteristics of on-wall in-tube flexible thermal flow sensor under radially asymmetric flow condition, Sensors and Actuators A: Physical, 138(2007) 87-96.
[198] Z. Tan, M. Shikida, M. Hirota, K. Sato, T. Iwasaki, Y. Iriye, Experimental and theoretical study of on-wall in-tube flexible thermal sensor, Journal of Micromechanics and Microengineering, 17(2007) 679-86.
[199] S. Wu, Q. Lin, Y. Yuen, Y.C. Tai, MEMS flow sensors for nano-fluidic applications, 13th Annual International Conference on MEMS, (2000).
[200] N. Sabaté, J. Santander, L. Fonseca, I. Gràcia, C. Cané, Multi-range silicon micromachined flow sensor, Sensors and Actuators A: Physical, 110(2004) 282-8.
[201] N.T. Nguyen, W. Dötzel, Assymetrical locations of heaters and sensors relative to each other using heater arrays: a novel method for designing multi-range electrostatic mass-flow sensors, Sensors and Actuators A: Physical, 62(1997) 506-12.
[202] P. Fürjes, G. Légradí, C. Düscó, A. Aszódi, Thermal characterisation of a direction dependent flow sensor, Sensors and Actuators A: Physical, 115(2004) 417-23.
[203] R.-H. Ma, D.-A. Wang, T.-H. Hsueh, C.-Y. Lee, A MEMS-based flow rate and flow direction sensing platform with integrated temperature compensation scheme, Sensors Journal, 9(2009) 5460-76.
[204] G.-P. Shen, M. Qin, Q.-A. Huang, H. Zhang, J. Wu, A FCOB packaged thermal wind sensor with compensation, Microsystem Technologies, 16(2010) 511-8.
[205] H. Ernst, A. Jachimowicz, G.A. Urban, High resolution flow characterization in Bio-MEMS, Sensors and Actuators A: Physical, 100(2002) 54-62.

[206] A.S. Cubukcu, E. Zernickel, U. Buerklin, A.G. Urban, A 2D thermal flow sensor with sub-mW power consumption, Sensors and Actuators A: Physical, 163(2010) 449-56.
[207] J. Branebjerg, O.S. Jensen, N.G. Laursen, O. Leistiko, A micromachined flow sensor for measuring small liquid flows, International Conference on Solid-State Sensors and Actuators, TRANSDUCERS '91, (1991) 41-4.
[208] C. Yang, H. Soeberg, Monolithic flow sensor for measuring millilitre per minute liquid flow, Sensors and Actuators A: Physical, 33(1992) 143-53.
[209] M. Elwenspoek, Thermal flow micro sensors, IEEE International Semiconductor Conference, (1999) 423-35.
[210] B.C. Kaanta, H. Chen, G. Lambertus, W.H. Steinecker, O. Zhdaneev, X. Zhang, High sensitivity micro-thermal conductivity detector for gas chromatography, Proceedings of the IEEE 22nd International Conference on Micro Electro Mechanical Systems, (2009).
[211] E. Meng, P.-Y. Li, Y.C. Tai, A biocompatible Parylene thermal flow sensing array, Sensors and Actuators A: Physical, 144(2008) 18-28.
[212] L.-Y. Chang, P.-Y. Li, L. Zhao, T. Hoang, E. Meng, Integrated flow sensing for local biochemical simulation, In Proceedings of the IEEE 3rd International Conference on Nano/Micro Engineered and Molecular Systems, (2008).
[213] H. Yu, L. Ai, M. Rouhanizadeh, R.A. Kloner, E.S. Kim, T.K. Hsiai, Flexible shear stress sensor for intravascular testing, In Proceedings of Society of Solid-State Sensors, Actuators Workshop, (2008).
[214] E.F.-C. Meng, MEMS technology and devices for microliquid dosing system., PhD dissertation, California Institute of Technology, Pasadena, CA, USA, (2003) 150.
[215] J.W. Gardner, Microsensors: Principles and Applications, 1st ed.1994.
[216] F. Mailly, A. Giani, R. Bonnot, P. Temple-Boyer, F. Pascal-Delannoy, A. Foucaran, et al., Anemometer with hot platinum thin film, Sensors and Actuators A: Physical, 94(2001) 32-8.
[217] D. Dittmann, R. Ahrens, Z. Rummler, K. Schlote-Holubek, W.K. Schomburg, Low-cost flow transducer fabricated with AMANDA-process, Springer-Verlag: Berlin, Germany, (2001).
[218] M. Terao, T. Akutsu, Y. Tanaka, Non-wetted thermal micro flow sensor, SICE, Annual Conference 2007, (2007) 2084-8.
[219] D.J. Quiram, I.M. Hsing, A.J. Franz, K.F. Jensen, M.A. Schmidt, Design issues for membrane-based, gas phase microchemical systems, Chemical Engineering Science, 55(2000) 3065-75.
[220] I. Sádaba Champetier de Ribes, J.A. Peón Eguiguren, Dispositivo microfluídico y método para la determinación del tiempo de coagulación sanguíneo, Iline Microsystems SL, Spain, (2011).
[221] F. Pourahmadi, W.A. McMillan, J. Ching, R. Chang, L.A. Christel, G.T.A. Kovacs, et al., Apparatus for the separation of preferential particles in fluid sample, Google Patents, (2003).
[222] J. Elizalde, M. Antoñana, L. Matthys, F. Laouenan, J.M. Ruano-Lopez, Rapid protyping of self aligned 3D microfluidic structures, μTAS, 1(2013).
[223] Goodfellow, http://wwwgoodfellowcom/.
[224] C.N. Baroud, F. Gallaire, R. Dangla, Dynamics of microfluidic droplets, Lab on a Chip, 10(2010) 2032-45.
[225] J.-W. Choi, D.K. Kang, H. Park, A.J. de Mello, S.I. Chang, High-throughput analysis of protein-protein interactions in picoliter-volume droplets using fluorescence polarization, Analytical Chemistry, 84(2012) 3849-54.
[226] H. Gu, M.H.G. Duits, F. Mugele, Droplets formation and merging in two-phase flow microfluidics, International Journal of Molecular Science, 12(2011) 2572-97.
[227] Y. Zhang, P. Ozdemir, Microfluidic DNA amplification: A review, Analytica Chimica Acta, 638(2009) 115-25.

[228] M.G. Pollack, A.D. Shenderov, R.B. Fair, Electrowetting-based actuation of droplets for integrated microfluidics, Lab on a Chip, 2(2002) 96-101.
[229] S.Y. Teh, R. Lin, L.H. Hung, A.P. Lee, Droplet microfluidics, Lab on a Chip, 8(2008) 198-220.
[230] A.S. Utada, E. Lorenceau, D.R. Link, P.D. Kaplan, H.A. Stone, D.A. Weitz, Monodisperse double emulsions generated from a microcapillary device, Science, 308(2005) 537-41.

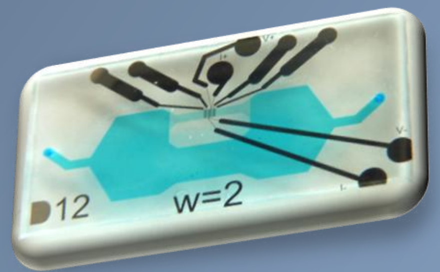
D12
w=2

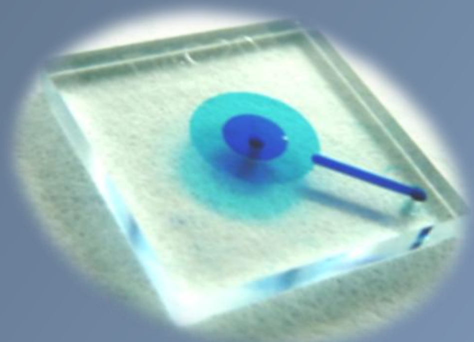

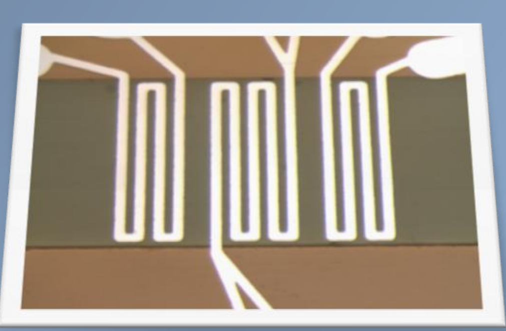

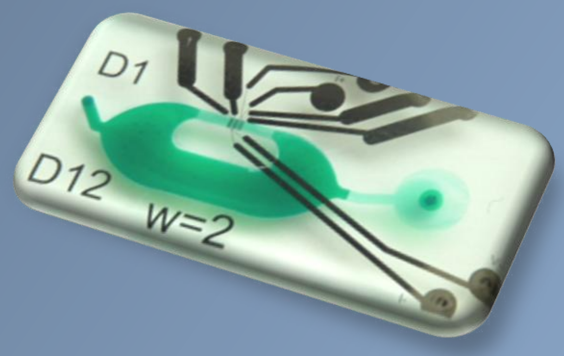
D1
D12
w=2

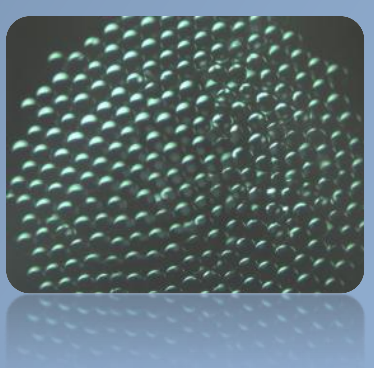

IK4 IKERLAN
Research Alliance